Metastable transition metal oxides, oxide nitrides, and nitrides

vorgelegt von

Diplom-Chemiker Tobias Clemens Lüdtke
geboren in Uccle, Belgien

von der Fakultät II – Mathematik und Naturwissenschaften
der Technischen Universität Berlin

zur Erlangung des akademischen Grades

Doktor der Naturwissenschaften
– Dr. rer. nat. –

genehmigte Dissertation

Promotionsausschuss:

Vorsitzender: Prof. Dr. Martin Kaupp
Gutachter: Prof. Dr. Martin Lerch
Gutachter: Prof. Dr. Holger Kohlmann

Tag der wissenschaftlichen Aussprache: 29. Juni 2017

Berlin 2017

Für meine Familie

It is recommended to view the digital version in "Two Page View" with the option "Show Cover Page in Two Page View". To enable this option in ADOBE ACROBAT READER, please check both of these items in the View menu:

English Version:

1) View > Page Display > Two Page View

2) View > Page Display > Show Cover Page in Two Page View

German Version:

1) Anzeige > Seitenanzeige > Zweiseitenansicht

2) Anzeige > Seitenanzeige > Deckblatt in Zweiseiten-ansicht einblenden

Preface

This present dissertation is a thesis by publication (article thesis, compilation thesis, cumulative thesis) and was processed within *ca.* three years from mid-November 2013 to March 2017 (including four months parental leave) under the supervision of Prof. Dr. Dr. Martin Lerch at the Technische Universität Berlin (TUB). In contrast to a monograph, the results are presented in form of published articles of established international journals. These contributions have already been examined and evaluated by the peer-review process of the respective journal.

The work was part of the research cluster "Synthesis, characterization, and theoretical description of metastable oxides and oxide nitrides of transition metals" of the priority program SPP 1415 "Crystalline non-equilibrium phases" of the Deutsche Forschungsgemeinschaft (DFG).[1] Other participants of this cluster were the research groups of Prof. Dr. Richard Dronskowski (RWTH Aachen), Prof. Dr. Thomas Bredow (Universität Bonn), and Prof. Dr. Thorsten Ressler (TUB).

An introduction (Part I) with the most important theoretical aspects and working methods for the personal contributions to the articles leads into the entire topic. The result section (Part II) includes all publications co-written with various partners. In the following, the publications are briefly described and cooperation partners outside of the cluster are presented.

1. Lüdtke, T.; Schmidt, A.; Göbel, C.; Fischer, A.; Becker, N.; Reimann, C.; Bredow, T.; Dronskowski, R.; Lerch, M. Synthesis and Crystal Structure of δ-TaON, a Metastable Polymorph of Tantalum Oxide Nitride. *Inorg. Chem.* **2014**, *53*(21), 11691–11698. DOI: 10.1021/ic501726m.

The synthesis of the bulk form of a new polymorph of tantalum oxide nitride, δ-TaON, was described in my diploma thesis "*Synthese und Charakterisierung neuer Verbindungen mit Anatasstruktur*" for the first time.[2] An improved synthesis and a comprehensive characterization of this substance is part of this work. A collaboration

with Prof. Dr. Anna Fischer (Technische Universität Berlin, now Albert-Ludwigs-Universität Freiburg) resulted in HRTEM images of the new substance.

2. Lüdtke, T.; Weber, D.; Schmidt, A.; Müller, A.; Reimann, C.; Becker, N.; Bredow, T.; Dronskowski, R.; Ressler, T.; Lerch, M. Synthesis and characterization of metastable transition metal oxides and oxide nitrides. *Z. Kristallogr.* **2017**, *232*(1–3), 3–14. DOI: 10.1515/zkri-2016-1961.

This article is intended to be one part of the final report for the research cluster of the SPP 1415. It contains a summary of already published results on the phase-pure synthesis of bixbyite-type V_2O_3 and γ-TaON by my predecessor Dr. Dominik Weber,[3] on the catalysis of vanadium oxide nitrides by Dr. Alexander Müller,[4] calculated band gaps of different TaON polymorphs by Dr. Christoph Reiman,[5] and exclusive novel information about improvements in the synthesis and characterization of δ-TaON.

3. Lüdtke, T.; Orthmann, S.; Lerch, M. Bixbyite-type phases in the system Ta-Zr-O-N. *Z. Naturforsch.* **2017**, *72b(4)*, 305–311. DOI: 10.1515/znb-2017-0014

Results about cation and anion substitution in TaON are presented in this article. The novel phases crystallizing in the bixbyite-type structure. In addition, one nitride, $TaZrN_3$, was synthesized as a stable analogue to metastable Ta_2N_3.

4. Becker, N.; Reimann, C.; Weber, D.; Lüdtke, T.; Lerch, M.; Bredow, T.; Dronskowski, R. A density-functional theory approach to the existence and stability of molybdenum and tungsten sesquioxide polymorphs. *Z. Kristallogr.* **2017**, *232*(1–3), 69–75. DOI: 10.1515/zkri-2016-1960.

The second part of the final reports by Nils Becker *et al.* is a theoretical study on possible metastable sesquioxides of molybdenum and tungsten. These investigations were supplemented by own experimental results on this topic.

5. Lüdtke, T.; Wiedemann, D.; Efthimiopoulos, I.; Becker, N.; Janka, O.; Seidel, S.; Pöttgen, R.; Dronskowski, R.; Koch-Müller, M.; Lerch, M. HP-MoO_2: A High-Pressure Polymorph of Molybdenum Dioxide. *Inorg. Chem.* **2017**, *56*(4), 2321–2327. DOI: 10.1021/acs.inorgchem.6b03067.

As a consequence of the results of publication 4 and other investigations, high-pressure experiments were carried out in cooperation with Prof. Dr. Monika Koch-Müller of the GeoForschungsZentrum Potsdam (GFZ), which resulted in a new metastable polymorph of molybdenum dioxide. Additional magnetic measurements and group-theoretical investigations were made by the research group of Prof. Dr. Rainer Pöttgen of the Westfälische Wilhelms-Universität Münster (WWU).

The contributions of each author are listed in detail at each publication. All journal articles have an individual introduction section; therefore some information may be redundant throughout this work. It should be noted that the presentation of the articles in this dissertation has been slightly altered in comparison to the original versions. Following adjustments have been made for a better reading experience and design consistency:

- Some chapters have been rearranged. All publications have now the consistent structure: Abstract – Introduction – Experimental Section (Theoretical Methodology) – Results and Discussion – Conclusion.
- All units have been standardized: *e.g.* °C was converted to K and g/cm^3 was unified to g·cm^{-3}. Non SI-conform units determined by cooperation partners (*e.g.* Oe) have not been converted.
- The different citation styles have been unified. Every publication has still its own reference list. No titles are included in the references of the publications.
- Figures and tables have a numeration according to the respective chapter.
- Graphics have been revised for a higher recognition value. A consistent color scheme is introduced for Rietveld refinement diagrams and crystal structure graphics to help the reader identify the various elements by their unique color. All modified graphics are marked with a star (*) at the end of the figure caption. No results have been changed or omitted. In fact, some figures with bond lengths (Figure 4.4 and Figure 5.11) have been supplemented with the respective errors. Figure 4.5 and Figure 7.1 were adapted with kind permission of Nils Becker.

A concluding chapter (Part III) at the end summarizes the major results of all publications and gives an outlook about possible developments on this research topic. The references for the parts I & III can be found in the Bibliography at the end of this work.

Abstract

In the present cumulative work the successful synthesis of new compounds of transition metals, with focus on metastable oxides and oxide nitrides of the vanadium and chromium group, is reported.

δ-TaON, a new polymorph of tantalum oxide nitride, besides the known β- and γ-phases, was extensively characterized by means of X-ray diffraction on powder samples, Rietveld refinement, anion composition, *etc*. The maximum yield was later increased to a mass fraction of about 82%. The product mixture contains secondary phases of γ-TaON and Ta_3N_5. The compound, crystallizing in the anatase-type structure, was also analyzed in detail by quantum-chemical calculations and HRTEM images by cooperation partners.

In the system Ta-Zr-O-N, various phase-pure new oxide nitrides and the nitride $TaZrN_3$ of the bixbyite type were prepared and comprehensively characterized. The variable anion composition showed significant changes in the lattice parameter and one cation position. The optical bandgaps of the light brown to black compounds were determined by means of UV-vis spectroscopy.

The attempts to synthesize new binary metastable oxides of molybdenum and tungsten by conventional syntheses routes were not successful. Quantum-chemical investigations of these systems support these observations and indicate high-pressure polymorphs as the next metastable compounds. A new high-pressure polymorph of molybdenum dioxide, HP-MoO_2, was prepared in cooperation with the GeoForschungsZentrum in Potsdam. A first study of X-ray powder data showed an isotypic relation to the high pressure compound of WO_2, which was subsequently confirmed by single-crystal diffraction. Furthermore, cooperation partners studied the magnetism, the relationship to the NiAs structure, and performed Raman measurements of the new compound.

Kurzfassung

In der vorliegenden kumulativen Arbeit wird über die erfolgreiche Synthese von neuen Verbindungen von Übergangsmetallen, mit Schwerpunkt auf metastabilen Oxiden und Oxidnitriden der Vanadium- und Chromgruppe, berichtet.

Mit δ-TaON konnte, nach der β- und der γ-Phase, eine neue Modifikation von Tantaloxidnitrid ausführlich charakterisiert werden (Röntgenbeugung an Pulverproben, Rietveld-Verfeinerung, Anionenzusammensetzung, *etc.*). Die Ausbeute konnte im weiteren Verlauf auf einen Massenanteil von *ca.* 82% erhöht werden. Das Produktgemenge enthält zusätzlich noch Nebenphasen von γ-TaON und Ta_3N_5. Die in der Anatasstruktur kristallisierende Verbindung wurde zudem umfassend durch quantenchemische Berechnungen und HRTEM Aufnahmen von Kooperationspartnern analysiert.

Im System Ta-Zr-O-N konnten verschiedene neue Oxidnitride und das Nitrid $TaZrN_3$ vom Bixbyit-Typ phasenrein dargestellt und umfassend charakterisiert werden. Durch die variable Zusammensetzung der Anionen sind messbare Veränderungen in dem Gitterparameter der kubischen Elementarzelle und einer Kationenposition zu beobachten. Die optischen Bandlücken der hellbraunen bis schwarzen Verbindungen wurden mittels UV-vis Spektroskopie bestimmt.

Die Darstellung neuer binärer und metastabiler Oxide von Molybdän und Wolfram mittels konventioneller Synthesemethoden blieb erfolglos. Quantenchemische Untersuchungen der betreffenden Systeme stützen diesen Sachverhalt und weisen Hochdruckpolymorphe als die nächst stabileren Formen aus. Eine neue Hochdruckmodifikation von Molybdändioxid HP-MoO_2 konnte in Kooperation mit dem GeoForschungsZentrum in Potsdam dargestellt werden. Eine erste Untersuchung an Röntgenpulverdaten zeigte eine Isotypie zur Hochdruckverbindung von WO_2, welche anschließend durch Einkristall-Röntgenstrukturanalyse bestätigt wurde. Weiterhin wurden von Kooperationspartnern der Magnetismus und die Beziehung zur NiAs Struktur untersucht sowie Raman-Messungen an der neuen Verbindung durchgeführt.

Acknowledgments

First and foremost, I would like to express my sincere gratitude and appreciation to Prof. Dr. Dr. Martin Lerch of the Technische Universität Berlin (TUB) for giving me the opportunity to work on the projects and to continue the research on the results achieved during my diploma thesis. His guidance and encouraged support was very inspiring for my development as a scientist, while giving me the freedom to work self-dependently. Thank you very much!

My thanks also go to Prof. Dr. Holger Kohlmann of the Universität Leipzig for the second review of this thesis and to the chairman of the examination board Prof. Dr. Martin Kaupp of the TUB.

Special thanks go to Prof. Dr. Wolfgang Bensch of the Christian-Albrechts-Universität Kiel and Prof. Dr. Josef Breu of the Universität Bayreuth for the initiation of the priority program SPP 1415 as well as to Dipl.-Chem. Christine Koch and Dipl.-Chem. Markus Krengel for the organization of the SPP. The funding of this project and my research by the Deutsche Forschungsgemeinschaft (DFG) is gratefully acknowledged.

Big thanks go to cooperation partners for the successful accomplishment of the priority program: Nils Becker, M.Sc., and Prof. Dr. Richard Dronskowski of the RWTH Aachen for quantum-chemical investigations on δ-TaON and HP-MoO_2. Dr. Christoph Reimann and Prof. Dr. Thomas Bredow of the Universität Bonn for additional calculations on δ-TaON. Dr. Alexander Müller and Prof. Dr. Thorsten Ressler of the TUB for the good partnership in the SPP 1415.

Additional research groups were involved in various projects of this work, whom I want to thank: Dr. Caren Göbel (TUB) and Prof. Dr. Anna Fischer (now Albert-Ludwigs-Universität Freiburg) for the HRTEM investigations of δ-TaON. Dr. Ilias Efthimiopoulos and Prof. Dr. Monika Koch-Müller of the GFZ Potsdam for the successful cooperation on the synthesis and characterization of HP-MoO_2. Dr. Oliver Janka, Dr. Stefan Seidel, and Prof. Dr. Rainer Pöttgen of the Westfälische Wilhelms-Universität Münster for magnetic measurements and the group-subgroup relationship in the HP-MoO_2 project.

My thanks go to the people of the TUB. In particular I want to bring out the help of Dr. Rafael Zubrzycki and Maika Stöbe, M.Sc., (research group Prof. Ressler) for RFA measurements, and Brigitte Hahn (research group Prof. Lerch) for additional N/O analyses. Prof. Dr. Arne Thomas and Dr. Hefeng Chen for providing the UV-vis spectrometer. Paula Nixdorf for single-crystal diffraction measurements. The glassblowers, Wiebke Matthes and Ralf Reichert, for the preparation of the reaction tubes with direct gas feed. The employees of the supply division, Edeltraud Böhme, Juana Krone, Franziska Rau, Alexander Billig, and Erik Neumann. Andrea Rahmel, Romy Klecker, and Mandy Prillwitz for administrative support during my time at the TUB. A big thanks goes to Claudia Benzin for her kind help with all administrative problems.

This work would not have been possible without the help of current and former colleagues. Thank you Abdullah, Alexander, André, Anna, Björn, Dennis, Dominik, Elisabeth, Eva, Gregor, Julia, Justus, Matthias, Sevilay, Stefan, Steven, and Suliman for the amazing working atmosphere and your help on various occasions. Some of them should be mentioned in detail: Alexander Schmidt for mentoring my diploma thesis and for showing me the first steps into solid state chemistry. Anna Ritscher for extensive proofreading and Zug! Björn Anke for the coffee and the assistance whenever needed. Dennis Wiedemann for the single-crystal X-ray analysis of HP-MoO_2. My predecessor Dominik Weber for his support on the final reports. Eva Heppke for being crystal godmother. Sevilay Cosgun for discussions on bixbyite-type phases and her investigations on my δ-TaON samples. Steven Orthmann for countless N/O measurements, the cooperation in the Nb/Ta-Zr/Hf projects, and the low temperature syntheses. Suliman Nakhal for the tireless help with crystallographic problems.

Best wishes and many thanks to my good friends for their support and encouragement throughout the years.

Moreover, big thanks to my family in Germany, Indonesia, Portugal, and Canada, especially my father and brother. “Aunt” Christine for babysitting so many times. My son Nicolas for many, many sleepless nights and the exciting adventure of growing up together. Last but not least, my beloved wife Yenny, a wonderful and devoted mother and my biggest support in all the time. Terima kasih!

Table of Contents

Preface i
Abstract iv
Kurzfassung v
Acknowledgments vi
Table of Contents viii

Part I Introduction 1

1 Motivation 3
1.1 Polymorphism and Metastability 3
1.2 Transition Metal Compounds 6
1.3 Intentions of the Thesis 7

2 Theoretical Background 9
2.1 Tantalum 9
2.1.1 Oxides 10
2.1.2 Nitrides 11
2.1.3 Oxide Nitrides 12
2.2 Zirconium 15
2.2.1 Oxides 15
2.2.2 Nitrides 16
2.2.3 Oxide Nitrides 17
2.3 The System Ta-Zr-O-N 17
2.4 Molybdenum 19
2.4.1 Oxides 19
2.5 Crystal Structures 20
2.5.1 Anatase Structure 21
2.5.2 Bixbyite Structure 27
2.5.3 HP-WO_2 Structure 32
2.6 Experimental Principles 36

2.6.1 Precursor 36
2.6.2 Ammonolysis Reaction 37
2.7 Powder X-ray Diffraction 38
2.7.1 Rietveld Refinement 39
2.8 Diffuse Reflectance UV-vis Spectroscopy 40

3 Methodology 43
3.1 Preparative Methods 43
3.1.1 Precursor Preparation 43
3.1.2 Tube Furnace 44
3.2 X-ray Diffraction 46
3.3 X-ray Fluorescence Analysis 46
3.4 UV-vis Spectroscopy 46
3.5 N/O-Analysis 47

Part II Publications 49

4 Publication 1 51
4.1 Abstract 53
4.2 Introduction 53
4.3 Experimental Section 54
4.4 Results and Discussion 57
4.5 Conclusions 66
4.6 Acknowledgements 66
4.7 References 67
4.8 Supporting Information 70

5 Publication 2 73
5.1 Abstract 75
5.2 Introduction 75
5.3 Experimental Section 77
5.4 Results and Discussion 78
5.4.1 Bixbyite-type V_2O_3 78
5.4.2 VO_2(B)-type γ-TaON 85
5.4.3 Anatase-type δ-TaON 90
5.4.4 Quantum-chemical Calculations 94

5.5 Conclusion 95
5.6 Acknowledgements 95
5.7 References 95

6 Publication 3 101
6.1 Abstract 103
6.2 Introduction 103
6.3 Experimental Section 105
6.4 Results and Discussion 106
6.5 Conclusion 113
6.6 Acknowledgement 113
6.7 References 113

7 Publication 4 119
7.1 Abstract 121
7.2 Introduction 121
7.3 Theoretical Methodology 122
7.4 Results and Discussion 123
7.5 Conclusion 130
7.6 Acknowledgement 131
7.7 References 131
7.8 Supporting Information 133

8 Publication 5 137
8.1 Abstract 139
8.2 Introduction 139
8.3 Experimental Section 140
8.4 Results and Discussion 143
8.5 Conclusion 154
8.6 Acknowledgement 154
8.7 References 154
8.8 Supporting Information 157

Part III Conclusion and Prospects **161**

9 Conclusion **163**
9.1 Outlook 166

A Appendices **169**
A.1 Additional Information 169
A.1.1 Chemicals 169
A.1.2 Software 169
A.2 Supplementary Material 170
A.3 Abbreviations, Variables, and Non-SI Units 172

B Bibliography **177**

List of Publications 203
List of Conference Contributions 204
List of Figures 205
List of Tables 211
Index 215

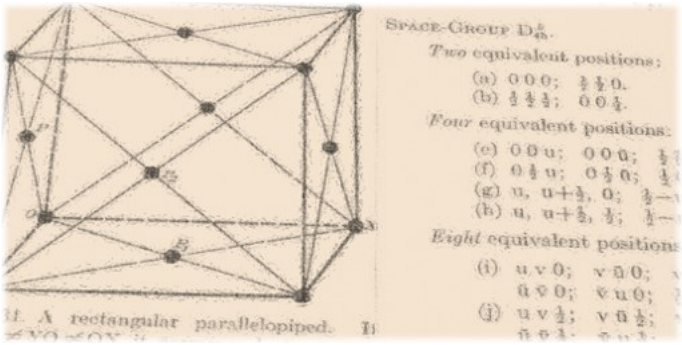

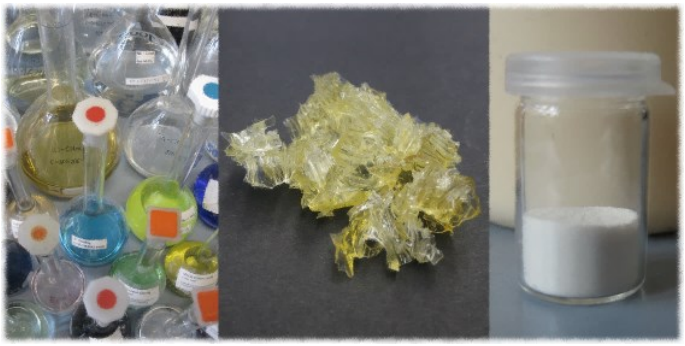

Part I

Introduction

1 Motivation 3

2 Theoretical Background 9

3 Methodology 43

Pictures on the cover sheet:

Top: Diamond rings on graphite powder, CD

Center: Cut-outs from the book: "*The analytical expression of the theory of space-groups*" by Ralph Walter Graystone Wyckoff.

Bottom: Metal-citrate solutions, Pechini gel, and amorphous Ta-oxide precursor.

1 Motivation

The priority program (Schwerpunktprogramm) SPP 1415 "Crystalline Non-equilibrium Phases – Preparation, Characterization, and *In situ*-studies of the Formation Mechanisms" of the German Science Foundation (Deutsche Forschungsgemeinschaft) DFG was initiated to attain a comprehensive understanding of the processes involved in the formation of metastable crystalline solids.[1] Up to now, the successful synthesis of such materials is mostly based on an aleatory trial and error process. The development of knowledge-based concepts for the rational synthesis of novel materials with interesting physical properties was one of the main intentions of this program, with participants from the fields of inorganic, analytical, physical, and theoretical chemistry, as well as experimental physics and geology. It has been funded for two periods of three years each.

The contributors of the cluster "Synthesis, characterization, and theoretical description of metastable oxides and oxide nitrides of transition metals", with focus on the elements of the vanadium and chromium groups, were the research groups of Prof. Dr. Bredow and Prof. Dr. Dronskowski, both specialized in quantum-chemical calculations (structure proposals, band gaps, thermodynamics, magnetism, *etc.*), Prof. Dr. Ressler for investigations on catalytic properties, and Prof. Dr. Lerch for synthesis and structural characterization of new compounds. Major achievements in the first period were the successful preparations of new metastable polymorphs of V_2O_3 and V_2O_5 by Dr. Dominik Weber[3,6,7] and its wide-ranging characterization.[5,8–10] Additional theoretical research on the sesquioxides of Nb, Ta,[9,11] and Cr[9,12] were also published.

1.1 Polymorphism and Metastability

Polymorphism is the existence of several different crystal structures of a compound and was probably first described by the German chemist Martin Heinrich Klaproth in the year 1788.[13] He discovered that both calcite and aragonite are forms of calcium carbonate. Such polymorphs (the term *polymorph* always relates to different crystal structures of a compound; *allotrope* describes different modifications of an element)[14–16] potentially exist for every crystalline compound. From a theoretical point of view, the num-

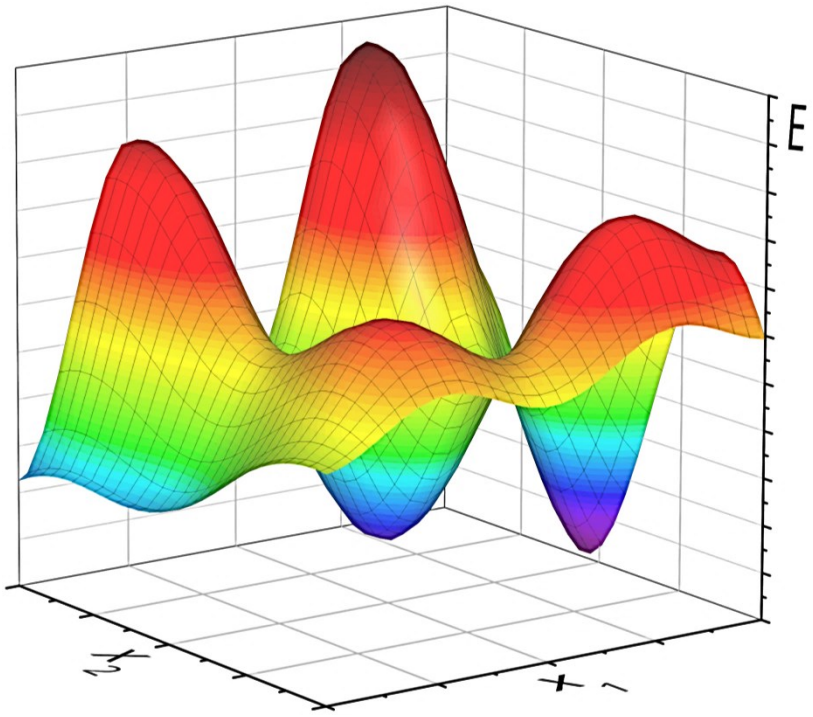

Figure 1.1. Schematic representation of an energy landscape for a one-component system depending on two arbitrary parameters x_1 and x_2. The minima in energy (blue and violet regions) indicate viable stable or metastable polymorphs.

ber of possible polymorphs is very high. The author Walter C. McCrone assumed that: "the number of forms known for a given compound is proportional to the time and money spent in research on that compound."[13, p 727] But only a small part of the existence range has been scientifically investigated. A computer software that analyzes the Cambridge Structural Database (CSD) of the Cambridge Crystallographic Data Centre (CDCC) showed that *ca.* 0.77% of the registered compounds in the year 2006 have one additional and only *ca.* 0.06% two or more crystalline structures.[17] A modern tool for the representation of the existence areas of a chemical system is the energy landscape.[18] Minima in energy of the hypersurface indicate a stable (or metastable) polymorph, respectively. Figure 1.1 shows a schematic representation of such a landscape for a system with one component and fictive coordinates, which would correlate, for example, to the Gibbs free energy of a system depending on pressure and temperature.

It is known for many elements and compounds that the crystal structure changes from the stable form at ambient conditions to other forms at elevated or lower temperatures. In these cases, the transformation is usually enantiotropic,[14,15] which means that it is reversible in both directions. If a phase transition to a more stable form is irreversible and can only occur in a specific direction, a monotropic transformation,[14–16] the starting compound is a metastable polymorph or allotrope. Metastable phases can be described by the concepts of non-equilibrium thermodynamics, which defines an open dynamical system

in exchange of energy and/or matter with the environment and, in addition to common equilibrium thermodynamics, its time-dependent change.[19,20] They exist in a configuration less favorable than the energetic ground-state, are therefore thermodynamically unstable, and are persistent because the transition is kinetically hindered or infinitely slow. In the example of Figure 1.1, the metastable state would correspond to the dark blue minimum, while the thermodynamically stable state would be represented by the violet minimum. The most common example of a metastable compound is diamond. This (high-pressure) allotrope of carbon exists besides graphite and is stable at ambient conditions, although the transformation reaction from diamond to graphite shows a negative change in Gibbs free energy and is therefore thermodynamically favorable. Other examples are amorphous substances (including glassy substances), supercooled liquids, and supersaturated solutions. Short-living intermediates of chemical reactions are not regarded as metastable, but as a transient species.[14–16]

The crystal structure of a solid has a significant influence on its properties. Many physical and chemical properties, such as the electronic structure, density, magnetism, thermal stability, conductivity, and optical properties are closely related to the arrangement of the atoms or ions. This phenomenon is easily illustrated by the above-mentioned example. Diamond is a colorless semiconductor with a high hardness, while the thermodynamically stable graphite is black, electrically conductive, and used as a soft lubricant.[1,13,19] An useful application of compounds with metastable polymorphs is, for example, the phase change memory (PCM). This type of a non-volatile random-access memory is based on the enantiotropic transition between a metastable amorphous and a metastable crystalline form by heating, irradiating of laser light or another excitation process.[21–23] These semiconducting materials based on Ge, Sb, and Te (GST, *e.g.* $Ge_2Sb_2Te_5$) are mainly used in data storage mediums, such as CDs and DVDs.

Not many rules or laws are established for the formation of metastable compounds. The Ostwald's step rule by the German chemist Friedrich Wilhelm Ostwald is the most frequently used rule. Based on his investigations on supersaturated solutions and subcooled melts, he found out that: "leaving any state and transitioning to a more stable one, it is not the state that is most stable under the existing conditions, but the closest one."[24, p 306] For example, in a crystallization process from a supersaturated solution, which is a highly metastable condition, the first formed solid is the least stable polymorph with the largest Gibbs free energy. The rule can be explained by irreversible thermodynamics or structural effects, but some examples show exceptions of this rule.[25,26] Ostwald also recommended the use of the term *metastable* as a more precise substitute for the

common word *labile*.[24] An additional interpretation of these observations is the Ostwald–Volmer rule which considers the densities of the various polymorphs. Often, the less stable polymorphs have lower densities.[19]

1.2 Transition Metal Compounds

Transition metals have characteristic features and properties with respect to their chemical, electrical, and magnetic behavior, which is a result of the filling of the second outermost d orbitals with electrons.[19] Those electrons have lower influence on the properties of the atom than the electrons in the valence orbital. A possible magnetic moment originates from partially occupied d orbitals with unpaired electron spins. Therefore, the elements can show ferromagnetic, ferrimagnetic, antiferromagnetic or paramagnetic behavior. All metals are characterized by high densities, melting and boiling points, and can often form colored complexes. Some elements can occur in different oxidation states and are able to form non-stoichiometric compounds.[19]

Oxides in general are among the mostly investigated materials in the history of chemistry. Since ancient times they are used in the form of minerals and ores as gemstones, pigments, raw materials for metallurgy, *etc.*[19] Newer fields of application are, for example, technical ceramics, catalysis, and nanotechnology. In contrast, oxide nitrides (sometimes referred to as oxidenitrides, oxynitrides, or nitride oxides) are a relatively new group of substances with some interesting features. The only natural occurring compound is the silicone oxide nitride Si_2N_2O in the mineral sinoite, which can be found in meteroids.[27] Semiconducting transition metal oxide nitrides are potential candidates for non-toxic color pigments,[28,29] anode-materials for photocatalytical water splitting under sunlight,[30–35] photocatalyst for oxidation of polycyclic aromatic hydrocarbons,[36] and as fast ion conductors.[37] Some of these properties can also be found in nitrides.[31,38–41] Besides the countless oxides in the earth's crust, only a few natural deposits of nitrides have been discovered so far (cubic-BN,[42] Si_3N_4,[43] TiN,[44] CrN,[45] iron nitrides,[46–49] and GaN[50]).

Another aspect of such compounds is the relative low structural complexity, which makes them predestined for the investigation of structure-property correlations. A good example is the polymorphism of tantalum oxide nitride, where the crystal structure has an influence on the optical properties, like the optical band gap and the resulting color of the substance (Chapters 2.1.3, 4, and 5).

In the previous chapter the reversible transformation of polymorphs, which are stable at different temperatures, has been mentioned. One key element in the preparation of metastable compounds can be the stabilization of such crystal structures by substitution with aliovalent ions. Cation substitution is a well-known tool for the stabilization of high-temperature forms. An applicable example is the stabilization of the cubic high-temperature form of ZrO_2 by small additions of other oxides like CaO or Y_2O_3 (Chapter 2.2.1). In tantalum oxide nitrides, small amounts of Mg,[51,52] Sc,[53–56] and Y[52,57] are responsible for the formation of anatase-, rutile-, bixbyite-, and fluorite-type phases, respectively. Oxide nitrides are prepared by anion substitution of nitrogen against oxygen or by partial oxidation of nitrides. Sometimes, nitrogen-poor compounds can be used as precursor for metastable oxides. Before the sesquioxide of vanadium with bixbyite-type structure was synthesized for the first time, the correspondent oxide nitride was already found.[6,58] The same approach was successfully applied to the vanadium oxide with anosovite-type structure.[7,59]

1.3 Intentions of the Thesis

The investigations in the present work concentrate on the development and progress on the preparative side, with focus on the synthesis and the comprehensive characterization of novel oxides and oxide nitrides. The aim of the research is, in cooperation with external partners, to gain a deeper insight into the formation of the metastable polymorphs and their transformation into thermodynamically stable forms.

A starting point is the comprehensive characterization of δ-TaON, a new polymorph of tantalum oxide nitride. The first synthesis of bulk material was described in my diploma thesis "*Synthese und Charakterisierung neuer Verbindungen mit Anatasstruktur*".[2] Increasing the phase purity of this compound is essential for the next step in a wide-ranging study. Additional cation substitutions experiments were planned for a further exploration of the existence range of other proposed TaON polymorphs.

The efforts to synthesize new oxides of molybdenum and tungsten are part of a further research area, which also includes the precursor preparation for high-pressure experiments and the investigation of the final results by means of powder X-ray diffraction. High-pressure polymorphs demand high standards on the synthesis apparatus and often show interesting chemical and physical properties, like an increased density and a higher coordination of the atoms.

2 Theoretical Background

This chapter provides information on the relevant transition metals and gives an overview of its most important binary oxides and nitrides, and ternary oxide nitrides. A detailed description of the mainly occurring crystal structures is also presented. In addition, major principles of synthesis routes and analyses methods are discussed.

2.1 Tantalum

The element tantalum (Ta) with the atomic number 73 has the electron configuration $[Xe]4f^{14}5d^{3}6s^{2}$ and is located in the 5^{th} group of the periodic system (vanadium group: vanadium, niobium, tantalum, and dubnium). It is a ductile and base metal with a blueish-gray color, a melting point of *ca.* 3273 K, a boiling point of *ca.* 5800 K, and a density of 16.68 $g \cdot cm^{-3}$.[19] It crystallizes in the bcc crystal structure of the α-W-type in space group $Im\bar{3}m$. The most important natural occurrences are minerals of the columbite group with the general composition AB_2O_6 (A = Fe^{2+}, Mn^{2+} and B = Nb^{5+}, Ta^{5+}).[60] Minerals with niobium as the dominant metal are called columbite (niobite) and tantalite (tapiolite) if tantalum is mainly located on the *B*-site. The prefixes *ferro* and *mangano* can be used according to the main element on the *A*-site. Ores containing both minerals columbite and tantalite are called coltan. Thoreaulith and mikrolith are rare minerals. Tantalum metal is prepared by chemical or electrochemical reduction of $K_2[TaF_7]$. The most important oxidation state is +5. It is used for medical prostheses and implants, in alloys, and as material for capacitors with very high capacitance in microelectronics.[19]

The discovery of tantalum is closely related to that of niobium. It was first discovered in 1802 by the Swedish chemist Anders Gustaf Ekeberg.[61,62] One year earlier, the English chemist Charles Hatchett found the element niobium which he originally named columbium.[63] For some time both elements were considered identical,[64] but the German chemist Heinrich Rose could prove that they were indeed two different elements.[65] The name derives from the Greek-mythological figure of Tantalus.

2.1.1 Oxides

Table 2.1 shows an overview of selected binary oxide compounds. According to a first characterization, the different oxides of tantalum can be divided in groups of α–ζ phases.[66] While the α- and β-phases are metallic and non-stoichiometric (solid solutions of oxygen in tantalum), the γ-phase is the monoxide of the rock salt type. Tantalum dioxide (δ-phase) crystallizes in the rutile-type structure.[66–69] The ε-phase is an intermediate TaO_2–Ta_2O_5 with no identifiable structure.[66]

The most important oxide is tantalum(V) oxide Ta_2O_5 (ζ-phase, according to the first characterization).[66] Due to its high refractive-index it is used as material for coatings and in the production of lithium tantalate single crystals, which are required for capacitors in mobile devices.[19] Hitherto, many different polymorphs or structure determinations of tantalum pentoxide can be found in literature.[70–74] In general, β-Ta_2O_5 is a colorless compound crystallizing in the orthorhombic crystal system. A natural occurrence is the mineral tantite.[75] In addition to the several reports on β-Ta_2O_5, a high number of low-temperature and high-temperature polymorphs are also known. All low-temperature polymorphs exhibit a hexagonal crystal structure and are stable at ambient conditions.[74,76,77] The numerous high-temperature polymorphs with tetragonal, orthorhombic, monoclinic, and triclinic crystal structure are not simply categorizable.[78–83]

Two different polymorphs are the outcome of high-pressure experiments.[84,85] The existence of a possible sesquioxide has only been discussed theoretically.[11] It should adopt the β-Ga_2O_3-type structure at pressures of 9 GPa with the dioxide and the metal as starting materials.

Table 2.1. Binary oxides of tantalum (sorted by ascending oxidation state of Ta).

Phase	Composition	Crystal structure	References
α	Ta–$TaO_{0.05}$	Bcc	66
β	Ta_4O	Orthorhombic	66
γ	TaO	NaCl (cubic)	66
δ	TaO_2	Rutile (tetragonal)	66–69
β-Ta_2O_5[a] (with L- and T-Ta_2O_5)	Ta_2O_5	Orthorhombic	70–74
Low-temperature polymorphs[b]	Ta_2O_5	Hexagonal	74,76,77
High-temperature polymorphs[b]	Ta_2O_5	Various	78–83
HP-Ta_2O_5[b]	Ta_2O_5	Monoclinic	84,85

[a] Different polymorphs and/or structure determinations.
[b] Group of different polymorphs.

2.1.2 Nitrides

An overview of selected binary nitrides can be found in Table 2.2. Like the oxides, nitrides of tantalum can be divided into different categories. The α- and β-phases are metallic solid solutions with a maximum of 10 mol % nitrogen.[86–88] A phase transformation to the γ-phase (β-Ta_2N) can be observed at approximately 33 mol % nitrogen. Phases with an 1:1 composition crystallizing in the cubic rock salt type (δ) or in the hexagonal CoSn-type structure (ε).[89–92] The latter transforms at higher pressures to the *θ*-phase of the WC-type. [93,94]

A series of nitrogen-rich compounds are also known: Ta_2N_3 crystallizes in the bixbyite-type structure (Chapter 2.5.2) and has only been obtained as thin film.[95–98] *η*-Ta_2N_3 is a high-pressure polymorph of the sesquinitride.[99,100] Ta_3N_5, the most important tantalum nitride, is a red colored compound and crystallizes in the orthorhombic anosovite-type structure of Ti_3O_5 in space group *Cmcm*.[91,101,102] Tantalum is coordinated by six nitrogen atoms and the distorted octahedra are linked three-dimensionally *via* edges and corners. It can be prepared by the reaction of $TaCl_5$ with NH_4Cl or by ammonolysis of Ta_2O_5.[101,102] It is used as color pigment, since it is toxicologically harmless, as photocatalyst for the oxidative water splitting, and as dielectric in microelectronics due to its large dielectric constant.[31,38,103] Ta_5N_6 and Ta_4N_5 are obtainable by heating Ta_3N_5 under ammonia.[91,104,105] High-pressure experiments on Ta_3N_5 can yield in a mixture of two polymorphs with U_3Se_5 and U_3Te_5 structure types, respectively.[106]

Table 2.2. Binary nitrides of tantalum (sorted by ascending oxidation state of Ta).

Phase	Composition	Crystal structure	References
α	Ta–$TaN_{0.04}$	Bcc	86–88,100
β	$TaN_{0.05}$	3 × 3 × 3 superstructure of α phase	86,91,100
γ (β-Ta_2N)	Ta_2N	V_2N (trigonal)	86,91,100,107
δ	TaN	NaCl (cubic)	89–91
ε	TaN	CoSn (hexagonal)	91,92
(HP) *θ*	TaN	WC (hexagonal)	93,94
Ta_5N_6	Ta_5N_6	Hexagonal	91,104,105
Ta_4N_5	Ta_4N_5	Tetragonal	91,104,105
Ta_2N_3	Ta_2N_3	Bixbyite (cubic)	95–98
η-Ta_2N_3	Ta_2N_3	U_2S_3 (orthorhombic)	99,100
Ta_3N_5	Ta_3N_5	Anosovite (orthorhombic)	91,101,102
HP-Ta_3N_5	Ta_3N_5	U_3Se_5, U_3Te_5 (orthorhombic)	106

2.1.3 Oxide Nitrides

An overview of the different TaON polymorphs can be found in Table 2.3 at the end of this chapter. Already in 1954, an investigation on non-stoichiometric metallic oxide nitrides of tantalum was presented.[108] A decade later, reports on the two phases α- and β-TaON, with tantalum in the oxidation state +5, were published.[109–111] Ionic-covalent oxide nitrides of tantalum can be considered as phases in the quasi-binary system of Ta_2O_5 and Ta_3N_5.

The α-TaON polymorph is allegedly formed by hydrolysis of Ta_2N_3Cl and is said to have a hexagonal crystal structure.[109,112] The existence of this polymorph was, however, clearly disproved by quantum-chemical investigations.[113]

The second polymorph, dubbed β-TaON, is prepared by ammonolysis of Ta_2O_5 at 1073 K.[110,111] It crystallizes in the monoclinic crystal system in space group $P2_1/c$ isotypically to the baddeleyite structure and can therefore be considered as a nitrogen-rich analogue to monoclinic ZrO_2 (Chapter 2.2.1). The crystal structure was initially determined by X-ray powder diffraction measurements and afterwards by neutron diffraction.[114] The results of the second method included the determination of an ordered anion arrangement. Tantalum is surrounded by three oxygen and four nitrogen ions in the first coordination sphere. This is consistent with the second rule of Pauling, which states that an anion in an ionic structure attempts to compensate the electrostatic binding strengths of the surrounding cations.[115] The three oxygen ions form a triangle and the four nitrogen ions form a square parallel to each other on opposing sides of tantalum.[114,116] Figure 2.1 shows the coordination polyhedra and the baddeleyite-type crystal structure of β-TaON according to neutron diffraction data.[114] The (TaN_4O_3) polyhedra have a zigzag-shaped arrangement parallel to (010).[117] Single-crystal investigations are also reported.[102,116] Quantum-chemical computations show a good agreement between experiment and theory.[113] Recent investigations indicate that β-TaON can form non-stoichiometric compounds with a variable N/O ratio.[118]

Sometimes, an olive colored product can be observed, which presumably results from impurities with the chemically related niobium or reduced tantalum.[52,56,119] A transformation into the yellow product occurs by brief heating in air at 1073 K.

Experimental investigations resulted in a range of 2.25–2.40 eV for the indirect band gap,[56,120] which classifies β-TaON as semiconductor.[121] The band gap decrease compared with Ta_2O_5 can be explained by the exchange of the O_{2p} orbitals in the oxide against N_{2p} orbitals with a higher potential energy, which leads to new orbitals with a higher-bound

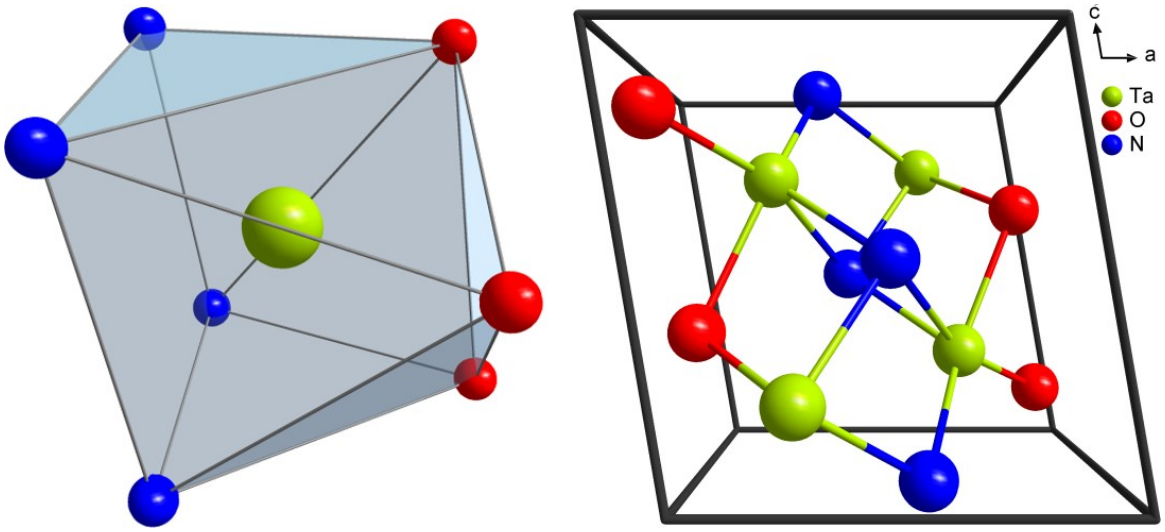

Figure 2.1. Coordination polyhedra (left) and unit cell (right) of the baddeleyite-type structure of β-TaON

state energy.[30,31,120,122] According to the theory of Phillips and van Vechten, the optical and electronic properties of a compound depend on the difference between the electronegativities of cations and anions.[123–125] Hence, the band gap of a semiconductor is influenced by the degree of the covalent bond and can be modified by altering the ratio of oxygen and nitrogen.

Quantum-chemical investigations on the structure and stability of β-TaON and other possible polymorphs with a AX_2 structure were carried out.[126] These calculations have confirmed the baddeleyite-type structure as the thermodynamically stable polymorph of tantalum oxide nitride and predicted possible polymorphs, in order of decreasing stability, with anatase, rutile, and fluorite-type structure. Later, this series was extended by the VO_2(B)-type structure with the discovery of the first metastable polymorph γ-TaON (*ca.* 17 kJ·mol^{-1} less stable than β-TaON),[52,127,128] which is located in the sequence between the baddeleyite- and the anatase-type structure.[128] Orange colored γ-TaON crystallizes in the monoclinic space group $C2/m$ and was initially obtained with impurities of β-Ta_2O_5.[52,127] Phase-pure products of a modified urea route[129,130] and phases with hollow urchin-like nanostructures[131] were presented later. A summary of an successful approach *via* a conventional synthesis route with a graphical representation of the crystal structure can be found in this thesis as a result of the work by Dr. Dominik Weber (Chapter 5.4.2).[3] In this structure, tantalum is 6-fold coordinated by anions and forms two different types of distorted octahedra. The Ta(O,N)$_6$ polyhedra around Ta1 are connected to

further polyhedra *via* four corners and five edges, while the Ta2 polyhedra are linked by only four corners and four edges to other polyhedra. On the basis of the X-ray powder diffraction, no statement could be made about the distribution of N and O over the four anion sites of the VO_2(B) structure. Quantum-chemical calculations for all possible occupancy variants revealed an ordered arrangement (see Chapter 6.4.2 for details).[128] This is also in agreement to the Pauling's second rule.[115] The coordination polyhedra form edge-intersected layers parallel to (001), which are linked by vertices. Cavities are traversing the three-dimensional structure. An irreversible phase transformation to β-TaON can be observed under an inert gas atmosphere at temperatures of *ca.* 1173 K.[127] In comparison with β-TaON and in agreement with the Ostwald–Volmer rule,[19] the density and the cell volume is larger due to the 6-fold coordination of tantalum. γ-TaON is also a semiconductor with an experimentally determined indirect band gap of 2.03 eV.[56]

Anatase-type δ-TaON was synthesized for the first time as thin film with a determined indirect band gap of 2.37 eV.[132,133] The synthesis and characterization of bulk material is one major scope of this work (Chapters 5 and 6). Another oxide nitride (Ta_3O_6N) is said to be obtainable by the ammonolysis of 1T-TaS_2 and crystallizing in the monoclinic $TiNb_2O_7$-type structure in space group $C2/m$.[134,135] $Ta_{5.00}N_{5.99}O_{0.01}$ and $Ta_{5.00}N_{4.79}O_{1.81}$ can be prepared using an iron catalyst.[136] Studies on a possible high-pressure polymorph with AX_2 composition were carried out independently by two research groups[137,138]. This polymorph, exhibiting the cotunnite type, was later synthesized at pressures of 33 GPa.[139]

Table 2.3. Ternary oxide nitrides of tantalum (sorted by ascending oxidation state of Ta).

Phase	Composition	Crystal structure	References
$TaO_{0.50}N_{0.50}$ – $TaO_{0.10}N_{0.90}$	$TaO_{0.50}N_{0.50}$ – $TaO_{0.10}N_{0.90}$	Superstructure of δ-TaN, ε-TaN	108
$Ta_{5.00}N_{5.99}O_{0.01}$ – $Ta_{5.00}N_{4.79}O_{1.81}$	$Ta_{5.00}N_{5.99}O_{0.01}$ – $Ta_{5.00}N_{4.79}O_{1.81}$	Hexagonal	136
(α-TaON)[a]	TaON	Hexagonal	109,112,113
β-TaON	TaON	Baddeleyite (monoclinic)	110
γ-TaON	TaON	VO_2(B) (monoclinic)	3,52,127,129,131
δ-TaON	TaON	Anatase (tetragonal)	132,133,this work
HP-TaON	TaON	Cotunnite (orthorhombic)	139
Ta_3O_6N	Ta_3O_6N	$TiNb_2O_7$ (monoclinic)	134,135

[a] Existence disproved.

2.2 Zirconium

The element zirconium (Zr) with the atomic number 40 has the electron configuration [Kr]$4d^2 5s^2$ and is located in the 4^{th} group of the periodic system (titanium group: titanium, zirconium, hafnium, and rutherfordium). It is a ductile and base metal with a greyish-white color, a melting point of *ca.* 2130 K, a boiling point of *ca.* 4570 K, and a density of 6.51 g·cm^{-3}.[19] It crystallizes in the hcp crystal structure of the α-Mg-type in space group $P6_3/mmc$. The most important occurrences of the metal are the silicate zircon ($Zr[SiO_4]$) and the dioxide zirconia (ZrO_2, see Chapter 2.2.1). Zirconium minerals generally contain 1–5 wt % hafnium as impurities. The oxidation state +4 is the most stable occurrence in chemical compounds. Zirconium metal is nowadays produced on an industrial scale by the Kroll process and purified by the van Arkel-de Boer process.[19,140,141] Zirconium is corrosion-resistant and therefore used as material for devices in chemical engineering. Furthermore, it is an excellent cladding material for nuclear reactors and fuel elements.[19]

The German chemist Martin Heinrich Klaproth succeeded in isolating the dioxide from zircon for the first time in 1789. He named it, in reference to the mineral, zirconia (Zirkonerde). Klaproth was also the discoverer of the elements Ce and U and could verify the discovery of Sr, Ti, and Te. Elementary zirconium metal was first obtained in 1824 by Swedish chemist Jöns Jacob Berzelius.

2.2.1 Oxides

Table 2.4 gives an overview of the binary oxide compounds. A solid solution of oxygen in zirconium can be formed within the compositional range $ZrO_x (0 \leq x \leq 0.4)$.[142,143] The most important oxide compound of Zr is the dioxide with the mineral baddeleyite as the main natural occurrence. At ambient pressure, the dioxide (zirconia) forms three polymorphs. A monoclinic (α-, m-) form at room temperature, designated as baddeleyite structure, is the thermodynamically stable form, which converts to a tetragonal (β-, t-) variant at temperatures above *ca.* 1373 K. Finally, cubic ZrO_2 (γ-, c-) with a fluorite-type structure is formed in a temperature range of *ca.* 2673 K and *ca.* 3073 K of the melting point.[19]

It is possible to stabilize the cubic high-temperature polymorph at ambient temperature by substituting the dioxide with aliovalent oxides like MgO_2, CaO_2, or Y_2O_3.[144–150] The substitution with Y_2O_3 can be described according to the Kröger–Vink notation:[151,152]

$$2\,Zr_{Zr}^{\times} + O_{O}^{\times} + Y_2O_3 = 2\,Y_{Zr}' + V_{O}^{\bullet\bullet} + 2\,ZrO_2\ (sf) \qquad (2.1)$$

As a result, vacancies in the anion substructure are generated, which are responsible for the oxygen conducting properties of the material. Such phases, like this yttria-stabilized zirconia (YSZ), have found a wide range of possible applications over the years and are used as membranes in oxygen sensors and fuel cells, as material for fire-resistant applications (crucibles and furnaces), and as gemstones in jewelry.[19]

At least two different high-pressure polymorphs have been discovered, namely brookite-type oI-ZrO_2[153–156] and cotunnite-type oII-ZrO_2.[157–160]

Table 2.4. Binary oxides of zirconium (sorted by ascending oxidation state of Zr).

Phase	Composition	Crystal structure	References
ZrO_x	ZrO_x ($x \leq 0.4$)	Hexagonal	142,143
m-ZrO_2	ZrO_2	Baddeleyite (monoclinic)	144–150
t-ZrO_2	ZrO_2	Tetragonal	144–150
c-ZrO_2	ZrO_2	Fluorite (cubic)	144–150
(HP) oI-ZrO_2	ZrO_2	Brookite (tetragonal)	153–156
(HP) oII-ZrO_2	ZrO_2	Cotunnite (orthorhombic)	157–160

2.2.2 Nitrides

Interestingly, there are not many different phases of zirconium nitrides (Table 2.5). Cubic ZrN crystallizes isotypically to δ-TaN in the rock salt type.[161–163] The exact space group of orthorhombic Zr_3N_4 (*Pnam* or *Pna*2_1) cannot be determined by powder diffraction methods.[164,165] A high-pressure polymorph of Zr_3N_4 adapting the cubic Th_3P_4-type has been successfully prepared at pressures greater than 18 GPa and temperatures greater than 3000 K in a laser-heated diamond anvil cell.[166]

Table 2.5. Binary nitrides of zirconium (sorted by ascending oxidation state of Zr).

Phase	Composition	Crystal structure	References
ZrN	ZrN	NaCl (cubic)	161–163
Zr_3N_4	Zr_3N_4	Eu_3O_4 (orthorhombic)	164,165
(HP) c-Zr_3N_4	Zr_3N_4	Th_3P_4 (cubic)	166

2.2.3 Oxide Nitrides

The most important ternary oxide nitride compounds are summarized in Table 2.6. Ionic-covalent zirconium oxide nitrides are generally described by the formula $ZrO_{2-2x}N_{4x/3}$ and belong to the quasi-binary system ZrO_2–Zr_3N_4. They are structurally derived from fluorite-type ZrO_2 (see Chapter 2.2.1). The three oxygen-rich phases are $Zr_7O_8N_4$ (β), $Zr_7O_{11}N_2$ (β'), and $Zr_{7.0}O_{9.5}N_{3.0}$ (β").[167–172] The nitrogen-rich Zr_2ON_2 (γ)[167–169,173–175] exhibits the cubic bixbyite-type structure. Another oxide nitride, the defect fluorite $Zr_4O_5N_2$, is formed by an intergrowth of ZrO_2 and Zr_2ON_2.[176]

Table 2.6. Ternary oxide nitrides of zirconium.

Phase	Composition	Crystal structure	References
β	$Zr_7O_8N_4$	Pr_7O_{12} (rhombohedral)	167–171
β'	$Zr_7O_{11}N_2$	$Sc_2Zr_5O_{13}$ (rhombohedral)	167–171
β''	$Zr_7O_{9.5}N_{3.0}$	Combination of β-phase and ZrO_2	167–171
γ	Zr_2ON_2	Bixbyite (cubic)	167–169,173–175
$Zr_4O_5N_2$	$Zr_4O_5N_2$	Defect fluorite (cubic)	176

2.3 The System Ta-Zr-O-N

The metallic solid solution of nitrogen and oxygen in the TaZr alloy of the general formula TaZrON crystallizes in the hexagonal crystal system.[163]

Hitherto, two phase-pure ionic-covalent oxide nitrides have been identified.[177–180] The first phase corresponds to a continuous transition of baddeleyite m-ZrO_2 to the homeotypic β-TaON with the general sum formula of $Ta_{1-x}Zr_xO_{1+x}N_{1-x}$ $(0 \le x \le 1)$.[177–180] The yellow color intensifies with increasing tantalum content. Similar results were obtained by incorporation of small amounts of Ta_2O_5 into zirconium oxide nitrides.[181] The formation of m-ZrO_2/β-TaON solid solutions has a positive influence on the photocatalytic activity,[182] but depends on the preparation method.[183] As a side note, a high-pressure polymorph of this compositional series with an even cation ratio ($TaZrO_3N$) has been postulated.[138] The second phase can be considered as a homeotype to anosovite-Ta_3N_5 with the general formula $Ta_{3-x}Zr_xO_xN_{5-x}$ $(0 \le x \le 0.66)$.[177–180] Due to the brilliant coloristic properties, these phases might be non-toxic replacements for orange pigments containing cadmium.[178]

Two additional side phases have been observed during the characterization of the system Ta-Zr-O-N.[177] The first phase in biphasic samples was indexed with an orthorhombic unit cell. Unfortunately, it was not possible to determine the exact crystal structure, but it was proposed that this phase has structural relationship to either the α-PbO_2-type or to a partially stabilized orthorhombic ZrO_2.[184] The second oxide nitride side phase was indexed with a cubic unit cell similar to the fluorite type. In some cases, weak superstructure reflections were observed and structural relationships to bixbyite-type Zr_2ON_2[167–169,173–175] or $Tb_{16}O_{36}$[185] were considered.

Surprisingly, ternary compounds with just one anion are not investigated in detail or are difficult to classify. Pure nitrides of Ta/Zr have only been realized as thin layers, *e.g.* as $Ta_xZr_{1-x}N$ films[186] or sputter-deposited nanocrystalline coatings.[187] The main interest for a mixed oxide is also the application as thin films.[188]

Bulk material oxides are reported rarely. The powder diffraction pattern of $TaZr_{2.75}O_8$ can be found in the ICDD filed as private communication (ICDD, PDF 00-042-0060)[189] with no space group provided. The classification in the orthorhombic crystal system and the cell parameters are the only information in this dataset. Another oxide with the sum formula $Ta_2Zr_8O_{21}$ is mentioned, too.[181,190] Additional literature about this topic does not provide further information about structural properties.[191–193] Supplementary data can be found by expanding the system to Hf-Ta[194,195] and especially to Nb-Zr oxides. The first report on an orthorhombic mixed Nb-Zr oxide is an investigation on solid solutions of the type $Nb_2O_5{\cdot}nZrO_2$ ($5 \le n \le 9$).[196] The structure was identified as a homeotype to α-PbO_2,[196,197] although the most referred compound $Nb_2Zr_6O_{17}$ and all other examples in the series are not trivially describable with a AX_2 structure type. Srilankit ($TiZrO_4$),[198] on the other hand, is a known Zr-containing substance exhibiting this structure type. A first theory described the crystal structure as a superstructure of a fluorite-type,[199] which itself has structural relationships to α-PbO_2.[200] It was proposed, that the compounds crystallizing in the orthorhombic crystal system with 6-, 7-, and 8-fold coordinated cations.[201] This model was described in more detail by defect structures.[202] An oxide nitride based on $Nb_2Zr_6O_{17}$ was synthesized successfully.[203] Although not all structural properties can be described adequate with this theory, an incommensurate modulated structure with a metal and an oxygen substructure was suggested.[204–207] An addition to this description is a frustrated two-dimensional *XY* model with chiral domains.[208,209]

2.4 Molybdenum

The element molybdenum (Mo) with the atomic number 42 has the electron configuration [Kr]$4d^5 5s^1$ and is located in the 6^{th} group of the periodic system (chromium group: chromium, molybdenum, tungsten, and seaborgium). It is a ductile and hard metal with a silvery-grey color, a melting point of *ca.* 2890 K, a boiling point of *ca.* 5100 K, and a density of 10.28 g·cm^{-3}.[19] It crystallizes in the bcc crystal structure of the α-W-type in space group $Im\bar{3}m$.The most important natural occurrence is the disulfide molybdenite (MoS_2). Other minerals are wulfenite ($PbMoO_4$) and powellite ($CaMoO_4$). The most stable compounds are those of hexavalent molybdenum (+6), but it also forms compounds in the oxidations state of +5, +4, +3, and +2. Molybdenum metal is produced by reduction of the trioxides with hydrogen at 1273 K. It is mainly used as electrode material, as catalyst in petrochemical processes, and mainly as ferromolybdenum for the production of hardened steel. Moreover, it is an essential element for humans and animals.[19]

The name molybdenum originates form the Greek word *mólybdos* (Μόλυβδος) meaning *lead*. Molybdenite has long been confused with galena (PbS) and graphite.[19] After the German-Swedish chemist Carl Wilhelm Scheele had succeeded in making molybdenum trioxide (MoO_3) from molybdenite with nitric acid in 1778,[210] it was the Swedish chemist Peter Jacob Hjelm who first reduced the oxide to elementary molybdenum with coal in 1782.[211]

2.4.1 Oxides

The binary oxides of molybdenum show a wide compositional range. An overview of selected phases can be found in Table 2.7. A metallic phase with a maximum of 20–30 mol % oxygen crystallizes in the same structure type as the pure metal.[212] Despite the high number of possible oxidation states of molybdenum, only the tri- and dioxide are known with Mo solely in one oxidation state. A theoretical investigation on a possible sesquioxide by Becker *et al.* is part of this work (Chapter 8). A first step to a Mo^V oxide might be the synthesis of an oxide nitride with the sum formula $Mo_2(N,O,\square)_5$.[3,213]

Colorless molybdenum trioxide (α-MoO_3) crystallizes in the orthorhombic crystal system.[214–217] It has a melting point of 1068 K and forms a yellow liquid in the molten state. A vapor of Mo_3O_9, Mo_4O_{12}, and Mo_5O_{15} amongst other oxides results from sublimation in vacuum at 1073 K. At 1273 K it decomposes under oxygen release.[19] A high-pressure polymorph is formed at 6 GPa.[218] Monoclinic β-[219,220] and β'-MoO_3[221,222] are

metastable polymorphs of the trioxide. The brownish-violet dioxide MoO_2 crystallizes in a distorted rutile-type structure in the monoclinic space group $P2_1/c$.[223–227] It is a metallic conducting and diamagnetic substance.[19] The existence of a tetragonal rutile-type variant is contradictory.[223,228,229]

Besides these two oxides, a series of suboxides with mixed cation valences exist. The γ-Mo_4O_{11} phase crystallizes in the orthorhombic crystal system.[224,230,231] The original proposed space group *Pnma* was later corrected to $Pn2_1a$.[232,233] Furthermore, a monocline variant derived from the ReO_3-type is reported.[231,234] This derivation can also be applied to the monoclinic oxides Mo_8O_{23} and Mo_9O_{26}.[235,236] The described Mo_5O_{14},[237–240] $Mo_{17}O_{47}$,[238,239,241–243] and hexagonal MoO_3[244–247] can only be stabilized by other cations and are no archetypally binary oxides.

Table 2.7. Binary oxides of molybdenum (sorted by ascending oxidation state of Mo).

Phase	Composition	Crystal structure	References
Mo_3O	Mo_3O	Bcc	212
MoO_2	MoO_2	Distorted rutile (monoclinic)	223–227
γ-Mo_4O_{11}	Mo_4O_{11}	Orthorhombic	224,230–233
η- Mo_4O_{11}	Mo_4O_{11}	Monoclinic	231,234
Mo_8O_{23} (β)	Mo_8O_{23}	Monoclinic	235,236
Mo_9O_{26} (β')	Mo_9O_{26}	Monoclinic	235,236
α-MoO_3	MoO_3	Orthorhombic	214–217
β-, β'-MoO_3	MoO_3	Monoclinic	219–222
HP-MoO_3	MoO_3	Monoclinic	218

2.5 Crystal Structures

This chapter offers more detailed information of the various structure types of the prepared compounds and its relations to existing basic types. Although this chapter cannot give a comprehensive introduction into crystallography and group theory, some major concepts are briefly elucidated.

A high-symmetric basis structure, the aristotype (Greek: ἄριστος, aristos "excellent"), can be transformed by symmetry reduction or expansion of the unit cell to less ordered arrangements within the same or in a different crystal system.[248,249] The affiliation of the resulting derivate structure, the hettotype, to its origin is sometimes barely recognizable. A formalism for these transformations was developed by the German chemist Hartmut

Bärnighausen by introducing genealogical-like trees for crystal structures.[250] In general, these Bärnighausen-trees take account of all intermediate steps, relevant types of transformations, and changes in the atomic positions.

Crystallographic transitions lead to maximal subgroups of lower symmetry, which are subdivided into three classes.[251,252] The *translationengleiche* non-isomorphic subgroups (t) still have the same translation lattice and the reduction of symmetry arises by elimination of symmetry elements or by symmetry reduction of the rotation, rotoinversion, and screw axes. This results in a transition to another crystal class. The index of the transformation is the quotient of the number of symmetry elements of the group and the subgroup. In contrast, a *klassengleiche* subgroup (k) is part of the same crystal class and the symmetry reduction corresponds to the loss of translation symmetry, caused by the omission of the centering (IIa, not possible for primitive cells), or an enlargement of the unit cell (IIb, non-isomorphic subgroups). The third option is the *isomorphic* subgroup (IIc), which belongs to the original space group type with the same Hermann–Mauguin symbol, but with an enlarged unit cell.

The different atoms are located on positions inside the unit cell, which are separated in general and special positions. Each of the 230 space groups has one general position were only the identity is the characteristic symmetry element. With exception of the lowest symmetric space group, 229 of them have additional higher symmetric special positions with coordinates related to the space group symmetry. The number of equivalent points for each position per unit cell is expressed by the multiplicity. Only one representative of the position is selected and the other positions arise by the oriented site-symmetry. Those Wyckoff positions are named after the American scientist Ralph Walter Graystone Wyckoff, who published a book with lists of all positional coordinates.[253] Modern and more advanced variants are the *International Tables for Crystallography, Vol. A*[254] and the *Bilbao crystallographic server*,[255–257] an online platform with several useful tools on crystallographic topics.

In the following, the representations of the final structure types are illustrated (as an anticipation of the results from Chapters 4, 5, 6, and 8) on the basis of the newly synthesized compounds.

2.5.1 Anatase Structure

In addition to the thermodynamically stable rutile and the rare brookite, the mineral anatase is a naturally occurring polymorph of titanium(IV) oxide TiO_2.[19] Metastable ana-

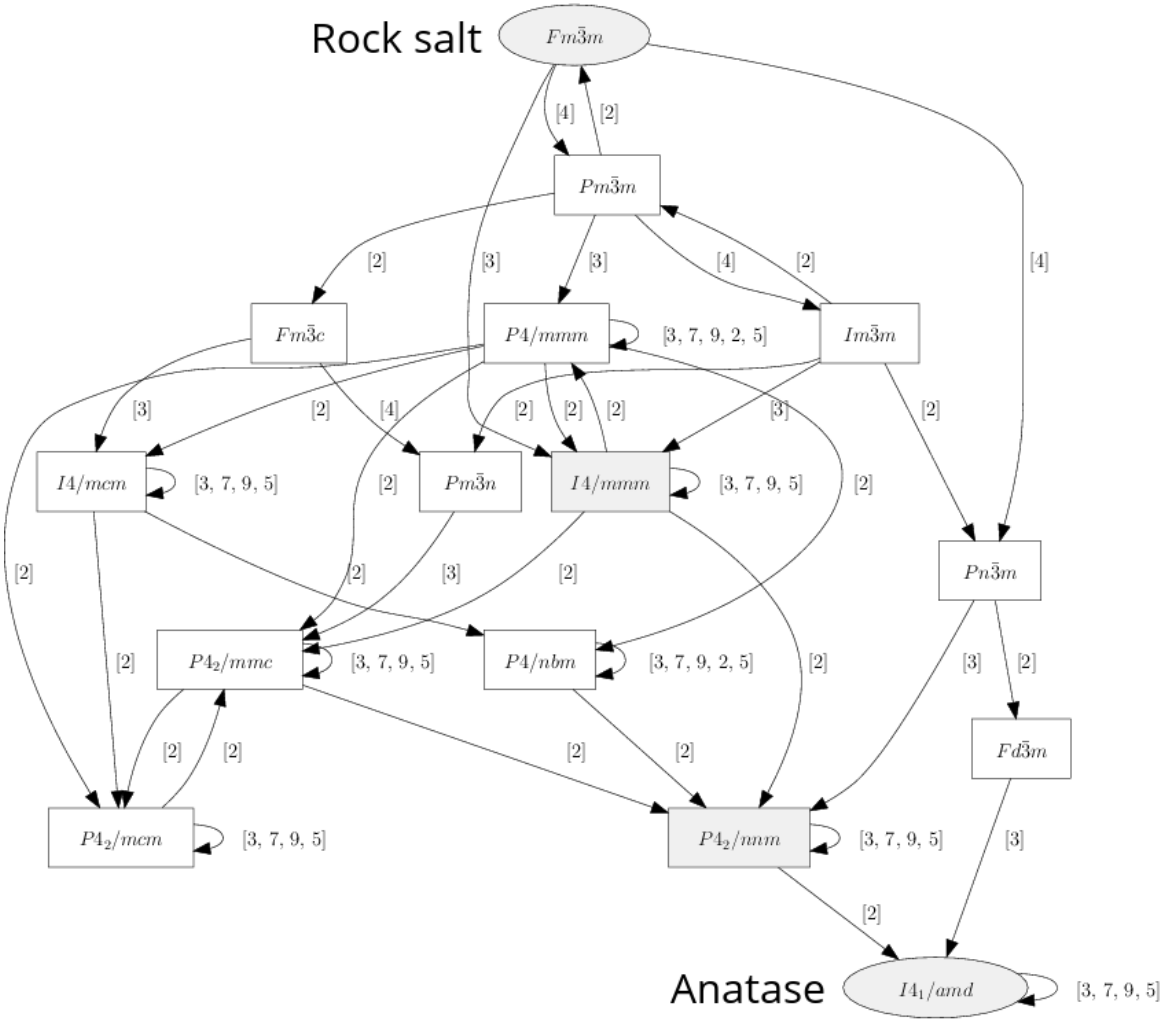

Figure 2.2. Group-subgroup relation of $Fm\bar{3}m$ and $I4_1/amd$ with possible transformation pathways.[261] The relevant transition steps are marked gray.

tase transforms irreversibly to rutile as a function of the crystallite size and impurities at about 873 K. All three crystal structures, named after the respective minerals, are constructed of (TiO_6) polyhedra and are distinguishable by the linkage. In rutile, the polyhedra are linked with two, in brookite with three, and in anatase with four other polyhedra.[19,258–260]

Anatase crystallizes in the tetragonal crystal system in space group $I4_1/amd$ and originates from the cubic rock salt structure ($Fm\bar{3}m$). The complete group-subgroup relationship between these two space groups is depicted in Figure 2.2.[261] Although the relations might get very complex, the complete transformation takes place in a total of only three steps. Two other possible three step routes ($Fm\bar{3}m$ – $Pn\bar{3}m$ – $Fd\bar{3}m$ or $P4_2/nnm$ –

$I4_1/amd$) do not result in the correct setup. The complete Bärnighausen-tree for the transition with a graphical development of the unit cell to the homeotype δ-TaON (Chapters 4 & 5) can be found in Figure 2.3.[250,252,254–256,262–264] Starting from the NaCl aristotype, which can be considered as two ccp lattices displaced relative to each other by ½ ½ ½, the first transition of index 3 to the tetragonal space group $I4/mmm$ is *translationengleich*. An alternative description of the newly formed space group is $F4/mmm$, but all tetragonal face-centered Bravais lattices can be converted under shrinkage of the unit cell to body-centered structures (see addition in Figure 2.3). The following symmetry reduction is a *klassengleiche* transition of index 2 and causes a decentering of the lattice, resulting in space group $P4_2/nnm$. Two of four possible conjugacy classes allow the correct splitting of the Wyckoff positions for the final *klassengleiche* transition of index 2. It includes a doubling of the *c* axis, a reinstatement of the body-centered lattice, and a splitting of the cation site to the special positions 4*a* and 4*b*. Nonetheless, only the 4*b* site is occupied by cations in the anatase structure, which can therefore be considered as a variant of the tetragonal $LiFeO_2$-type with vacancies on the 4*a* cation site.[262] The cation vacancies are included for demonstration purposes in the crystal structure in Figure 2.3. The other image shows the arrangement of the coordination polyhedra. The distortion of the octahedra is caused by the introduction of a *z* anion position not fixed by space group symmetry on the 8*e* site during the last transition. A characteristic property are the channels traversing the structure along the *a* and *b* axes.

Additional illustrations of δ-TaON can be found in Figure 4.4 and Figure 5.11. The first tantalum oxide nitride exhibiting the anatase type are olive green quaternary titanium-containing compounds with the general composition $Ti_xTa_{1-x}O_{1+x}N_{1-x}$ ($0.52 \leq x \leq 0.87$), which are formed by ammonolysis of Ti-Ta xerogels at temperatures between 873 and 973 K.[265] In the systems Mg-Ta-O-N and Sc-Ta-O-N, compounds with anatase structure can be isolated. A doping rate of 5 cation % Mg or 15 cation % Sc are required for phase pure results, respectively.[51–53,266] These are the first reported compounds exhibiting this structure type without the element titanium. The Mg-doped tantalum oxide nitride $Mg_{0.05}Ta_{0.95}O_{1.15}N_{0.85}$ (general formula: $Mg_xTa_{1-x}O_{1+3x}N_{1-3x}$) is a metastable compound, which irreversibly converts into the baddeleyite-type in a temperature range between 1173–1273 K.[51,52] The thin films of anatase-type δ-TaON are the first ternary compounds without titanium.[132]

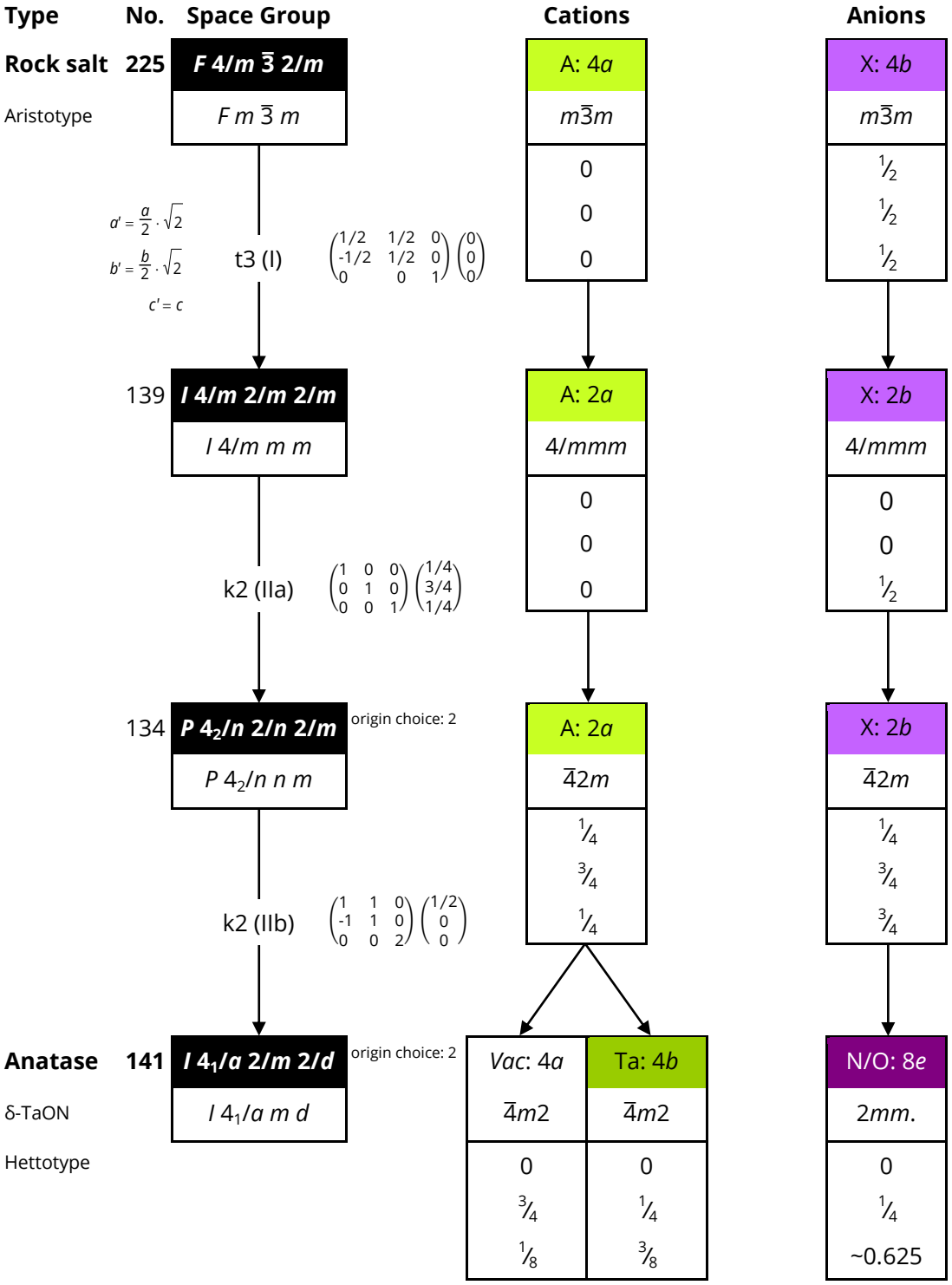

Figure 2.3. Group-subgroup scheme (Bärnighausen formalism) and graphical development of the unit cell for the group-theoretical relationship between rock salt (aristotype) and anatase-type δ-TaON (hettotype).[250,252,254–256,262–264] See Figure A.1 or Figure A.2 for legend.

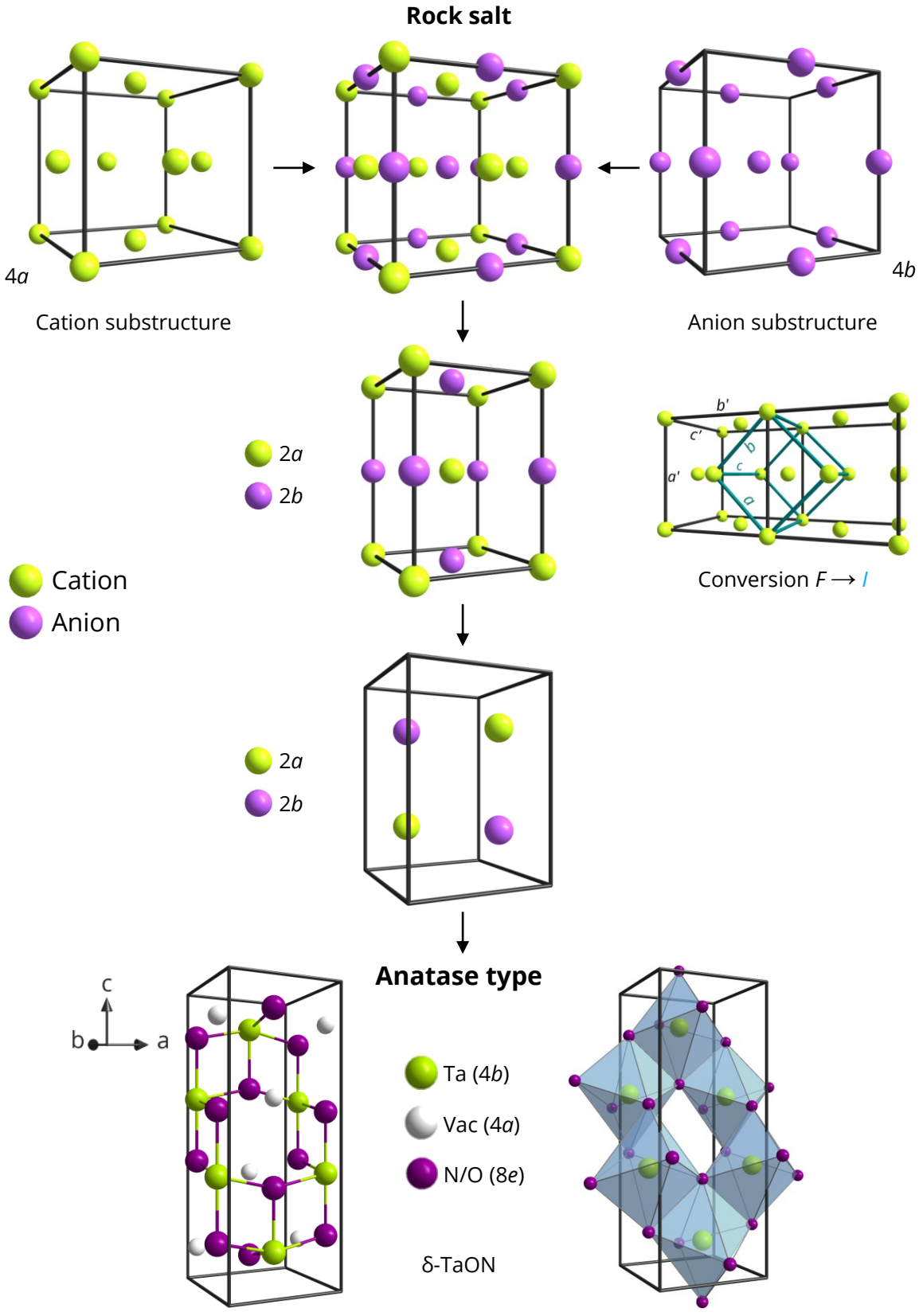
Rock salt
4a
4b
Cation substructure
Anion substructure
2a
2b
b'
c'
a'
b
c
a
Conversion F ⟶ I
Cation
Anion
2a
2b
Anatase type
c
b
a
Ta (4b)
Vac (4a)
N/O (8e)
δ-TaON

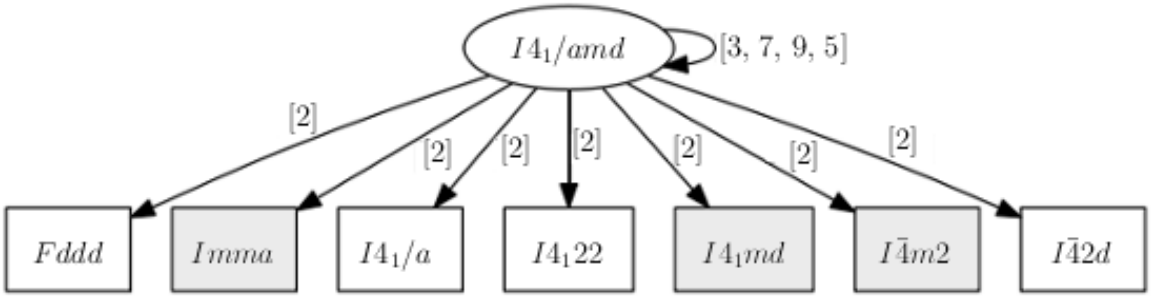

Figure 2.4. Maximal non-isomorphic subgroups (all *translationengleich*) of space group $I4_1/amd$. All subgroups allowing an ordered anion arrangement are marked gray.[261]

Several investigations regarding a possible anion ordering within this structure type have already been carried out. All seven maximal non-isomorphic *translationengleiche* subgroups of space group $I4_1/amd$ are represented in Figure 2.4.[254–257,261] Only the space groups *Imma* (No. 74), $I4_1md$ (No. 109), and $I\bar{4}m2$ (No. 119) tolerate an ordering of the anions with an index of 2.[51,52,262,266] In all variants, the cations are coordinated by the anions in a distorted octahedral configuration (see Figure 2.5 for all possible arrangements for δ-TaON). In case of $Mg_{0.05}Ta_{0.95}O_{1.15}N_{0.85}$, Rietveld refinements on neutron diffraction measurements were investigated. The best accordance between theoretical model and experimental results was obtained for space group $I4_1md$.[51,266] The ordered anion sites result from the splitting of the 8*e* Wyckoff position of the space group $I4_1/amd$ into two distinct 4*a* positions. This transformation, starting from origin choice 2, is described according to the Bärnighausen formalism in Figure 2.6.[250,254–257,261] The other transformations to *Imma* and $I\bar{4}m2$ are listed in the Appendices in Figure A.1.

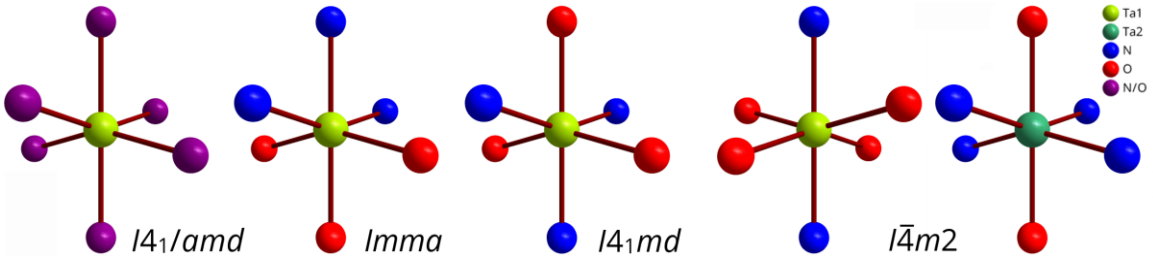

Figure 2.5. Coordination polyhedra and anion arrangement for δ-TaON in different space groups. Two different polyhedra are created during the transformation to space group $I\bar{4}m2$.[51,52,262,266]

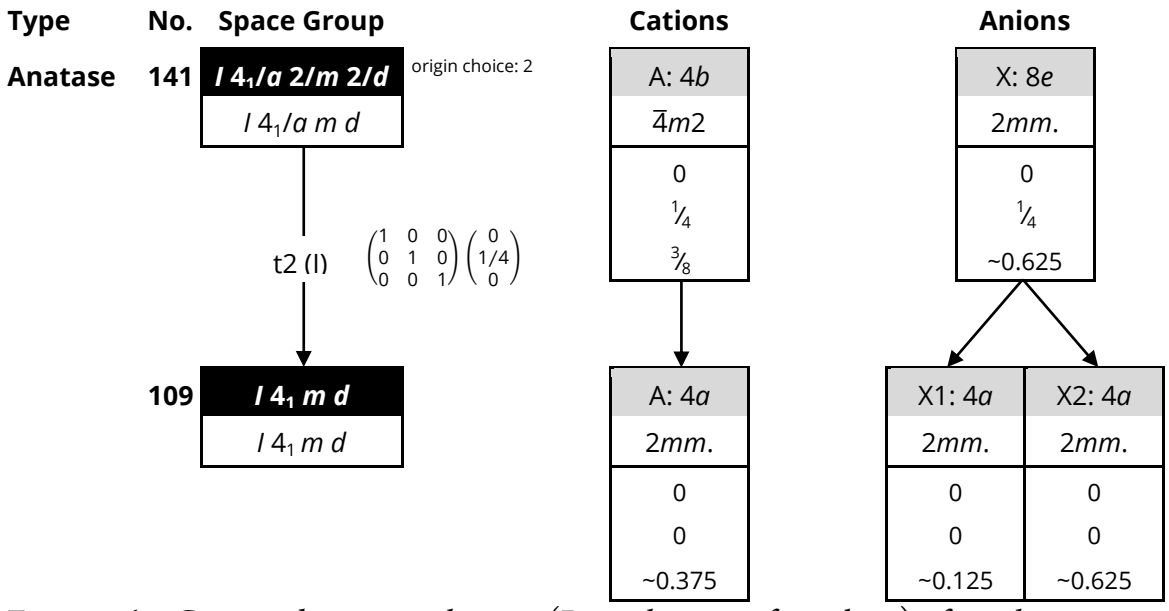

Figure 2.6. Group-subgroup scheme (Bärnighausen formalism) for the group-theoretical relationship between the anatase structure and the subgroup $I4_1md$.[51,52,250,252,254–256,263,267] See Figure A.1 or Figure A.2 for legend.

Quantum-chemical calculations on the model of undoped δ-TaON confirmed the experimental results. Compared w the statistical arrangement, a *ca.* 25 kJ·mol^{-1} more stable arrangement can be expected for space group $I4_1md$.[266] Additional quantum-chemical investigations are part of Chapter 4**.** By contrast, no ordering could be found in TiNF.[268]

2.5.2 Bixbyite Structure

This structure type was named after the mineral bixbyite[269] with the chemical formula $(Mn,Fe)_2O_3$,[223,270,271] which itself was named in honor after the American mineralogist Maynard Bixby.[272] It must not be confused with bixbite, a labeling for a red beryl, and also named after the mineralogist. Sometimes, the structure is also referred to as the cubic lanthanide sesquioxide type (C-Ln_2O_3),[97] C-type rare-earth-metal structure[177] or similar. Sesquioxides of Sc, Y, In, La, Tl, and many of the rare-earth elements exhibit this structure type. In bixbyite, at least 1.7 cation % Fe^{3+} are needed to stabilize the structure.[273]

The aristotype of the bixbyite structure ($Ia\bar{3}$) is the fluorite type ($Fm\bar{3}m$). The complete group-subgroup scheme between the two space groups is presented in Figure 2.7. There are at least two possible transformations with three steps, distinguishable by the sequence of transitions in the first two steps. In the following, one route is described in detail. The corresponding Bärnighausen-tree with a graphical evolution of the structure

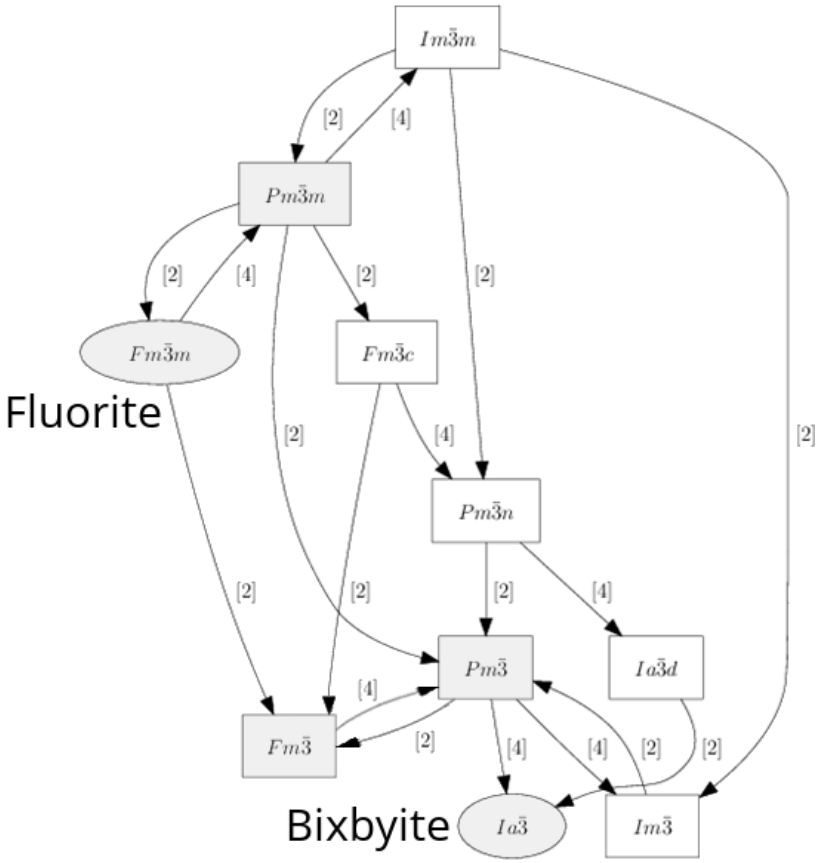

Figure 2.7. Group-subgroup relation of $Fm\bar{3}m$ and $Ia\bar{3}$ with possible transformation pathways.[261] The relevant transition steps are marked gray.

to the new tantalum zirconium oxide nitride (Chapter 7) is depicted in Figure 2.8. The other variant can be found in the Appendices in Figure A.2.

Starting from space group $Fm\bar{3}m$ of the AX_2 fluorite type, the first symmetry reduction, including a decentering of the lattice, goes to space group $Pm\bar{3}m$ *via* a *klassengleiche* transition of index 4 (k4). The cation sites are splitted into the 1*a* site on the cell corners and the 3*c* site on the centers of the cell faces. The smaller ideal anion cube with half edge length inside the unit cell is getting slightly distorted by loosening the fixed ¼ position. A *translationengleiche* transition of index 2 (t2) to $Pm\bar{3}$ is the second step. This progression does not have any consequences for the structure itself, but implies the loss of glide planes and the mirror planes perpendicular to the plane diagonals. The different symmetry elements are included in both interstages in Figure 2.8. For the final *klassengleiche* transition of index 4 to space group $Ia\bar{3}$, two different conjugacy classes are available, but only the class without an origin shift can be used for the correct splitting of the Wyckoff positions. After the conversion, the unit cell is doubled along all three axes, forming a 2 × 2 × 2 superstructure of the fluorite type with an 8-fold volume. By linking

eight formerly primitive cubes, a new body-centering is created at the central connection point.

Cations are finally located on the 8*a* and 24*d* sites, the latter one with a variable *x* parameter.[274] Anions are located on two crystallographically independent sites. In the ideal bixbyite structure, only the general site 48*e* is fully occupied and the empty special site 16*c* forms ordered vacancy positions. While the anions are coordinated tetrahedrally by cations, the cations at the 8*a* site are coordinated octahedrally by anions. The polyhedra around the 24*d* cations are distorted octahedra, caused by three different cation-anion distances. A picture of the different polyhedra and the corresponding bond length can be found in the discussion of the bixbyite-type vanadium sesquioxide in Figure 5.2 (Chapter 5.4.1). Graphics of this structure type can be found in Figure 2.8 and Figure 6.1, on the example of the new oxide nitrides of tantalum and zirconium.

With a total of 16 vacancies inside the unit cell, two of each original fluorite cube, the resulting composition for the ideal structure is A_2X_3. The positions, from which the vacancies arise, have been marked in the structure of space group $Pm\bar{3}$ in Figure 2.8. A special feature of the bixbyite type is the variable phase composition caused by a partially or fully occupation of the vacancies, forming compounds with a $A_2X_{3+\delta}$ ($\delta \leq 1$) composition. Nitrides of uranium with the composition $U_2N_{3+\delta}$ are known to cover the entire phase range up to the transition to fluorite-type UN_2.[275–277] Another example with a more limited compositional range is Zr_2ON_2.[173] In bixbyite-type V_2O_3, oxygen excess is theoretically possible, but hardly obtainable due to synthetic conditions.[6,10] Vanadium can occur in different oxidation states and the incorporation of excess oxygen on the 16*c* site could therefore be described according to the Kröger–Vink notation:[151,152]

$$2\,V_V^{\times} + \tfrac{1}{2}\,O_2 + V_i = 2\,V_V^{\bullet} + O_i'' \qquad (2.2)$$

Excess nitrogen in $V_2(O,N)_{3+\delta}$ is presumably located on the 16*c* site.[10,58] If a pure nitride compound with cations in just one oxidation state is oxidized, an occupation of the 16*c* site is inevitable:

$$2\,N_N^{\times} + \tfrac{3}{2}\,O_2 + V_i = 2\,O_N^{\bullet} + O_i'' + N_2\ (\mathrm{sf}) \qquad (2.3)$$

A complete cation ordering can be realized theoretically in space group $Ia\bar{3}$ for a cation ratio of 3:1 (there are 3 times as many cations on 24*d* compared with 8*a*) and is assumed for Cu_3TeO_6.[278,279] If other cation ratios show evidences for an ordering, they have to be analyzed in a non-isomorphic subgroup of the bixbyite-type structure. No evidence

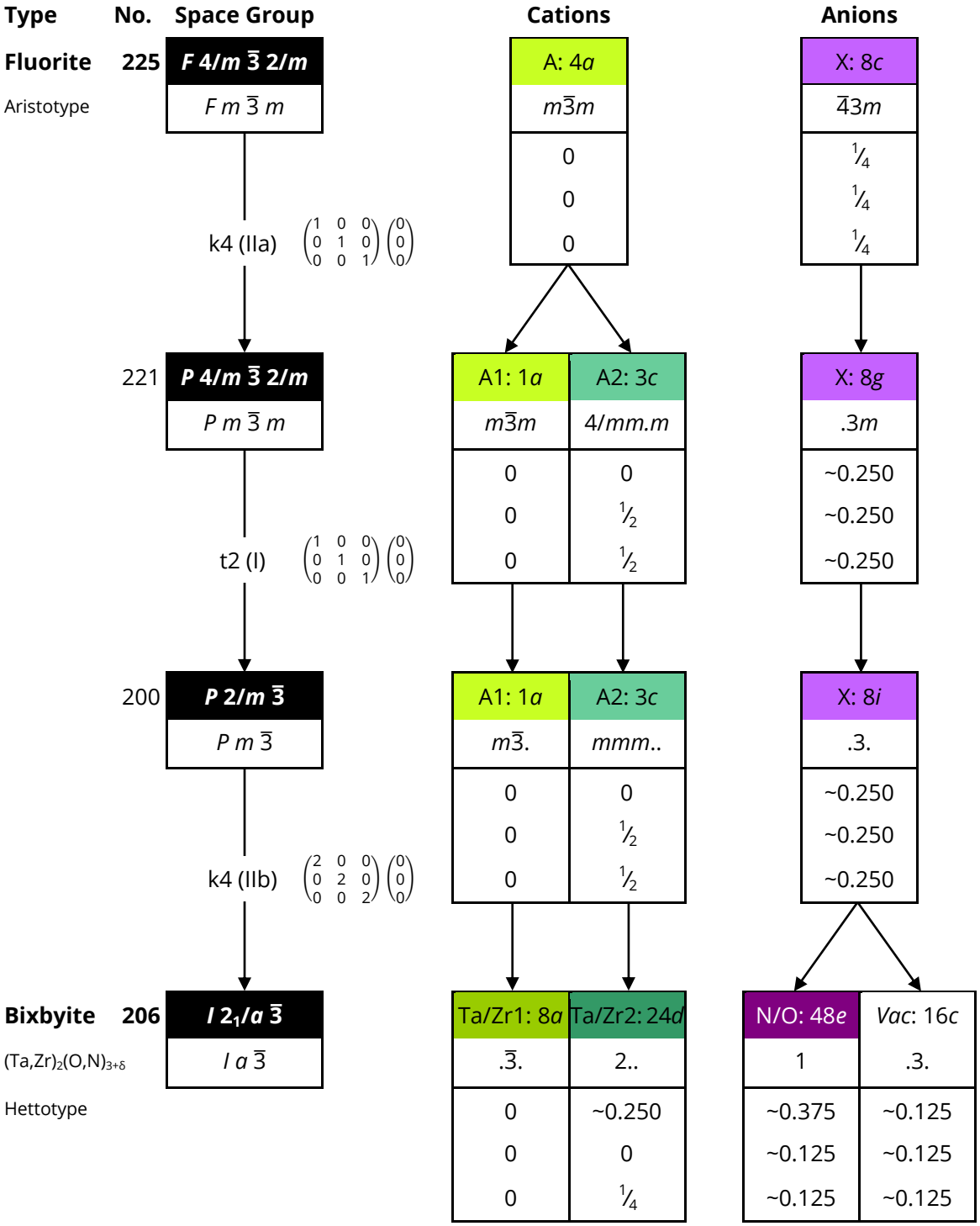

Figure 2.8. First variant of the group-subgroup scheme (Bärnighausen formalism) and graphical development of the unit cell for the group-theoretical relationship between fluorite (aristotype) and bixbyite-type $(Ta,Zr)_2(O,N)_{3+\delta}$ (hettotype).[250,252,254–256,263] See Figure A.1 or Figure A.2 for legend.

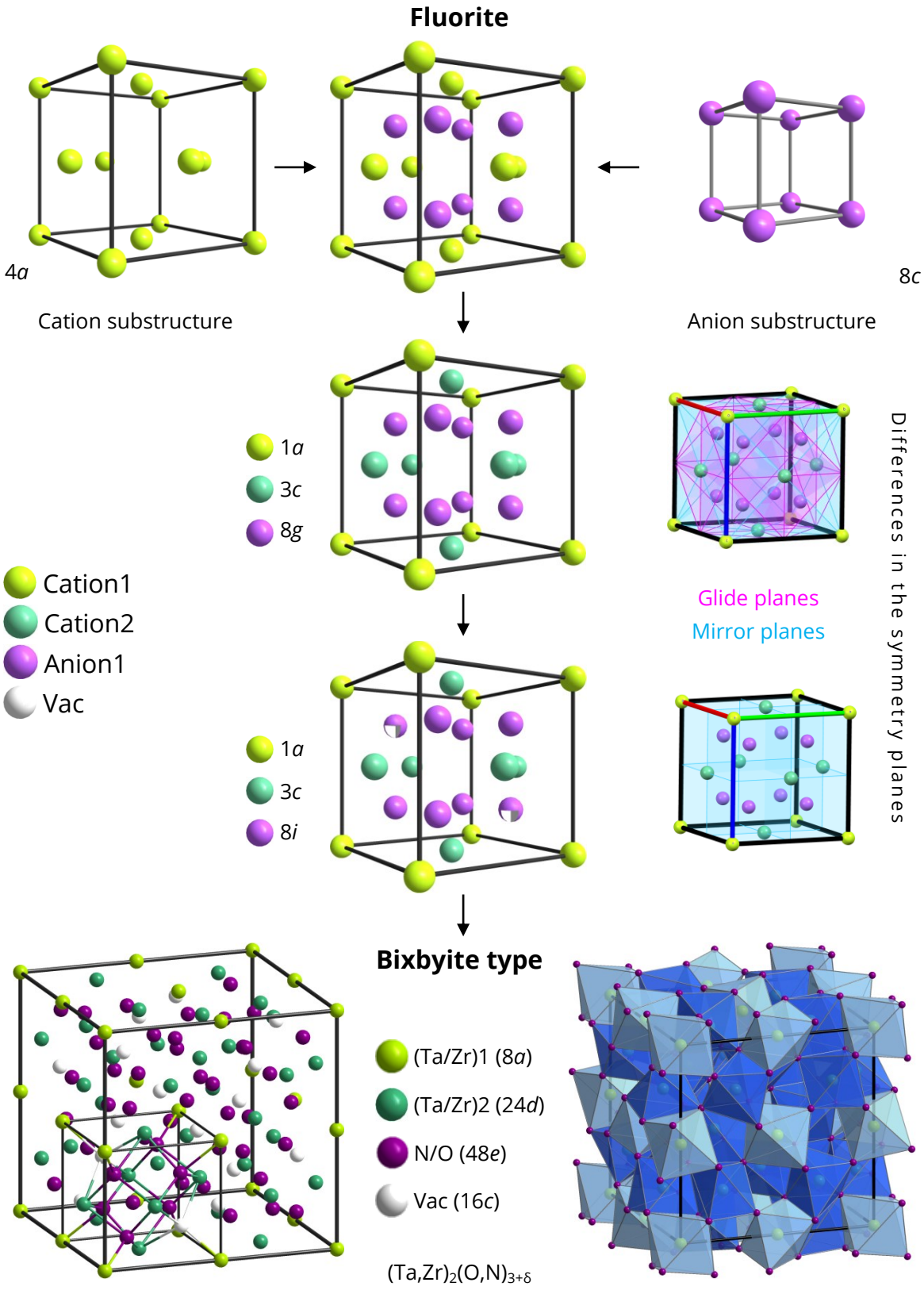
Fluorite
4a
8c
Cation substructure
Anion substructure
1a
3c
8g
Cation1
Cation2
Anion1
Vac
Glide planes
Mirror planes
Differences in the symmetry planes
1a
3c
8i
Bixbyite type
(Ta/Zr)1 (8a)
(Ta/Zr)2 (24d)
N/O (48e)
Vac (16c)
(Ta,Zr)2(O,N)3+δ

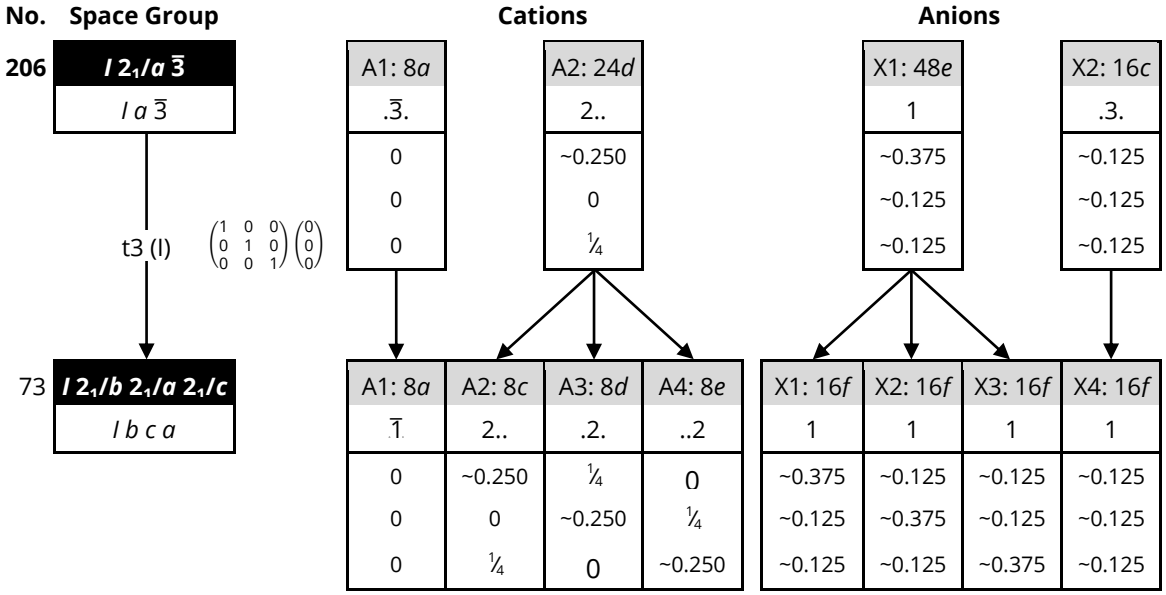

Figure 2.9. Group-subgroup scheme (Bärnighausen formalism) for the group-theoretical relationship between the bixbyite structure and the subgroup *Ibca*.[173,250,252,254–256,263] See Figure A.1 or Figure A.2 for legend.

for an ordering has been found for the mineral bixbyite ($FeMnO_3$).[280] An ordered arrangement of the anions is not possible for the ideal bixbyite type. Only the *translationengleiche* non-isomorphic subgroup *Ibca* offers four equivalent anion sites, in which a cation ordering is also possible.[173] The corresponding Bärnighausen-tree can be found in Figure 2.9. An ordered anion arrangement was first assumed for Zr_2ON_2,[173] but neutron diffraction experiments and quantum-chemical calculations favor a statistical distribution.[174,175]

A combination of a fully occupied 16*c* site and a cation ordering are compounds crystallizing in the anti-bixbyite-type, as a subgroup variant of the anti-fluorite-type, namely Li_3AlN_2,[281,282] Li_3GaN_2,[281–283] and Li_3ScN_2.[284]

2.5.3 HP-WO_2 Structure

Thus far, the now discussed structure type occurred only once in a high-pressure polymorph of tungsten dioxide.[285] HP-WO_2 crystallizes in the tetragonal crystal system in space group *Pnma*. Although the monoclinic space group $P2_1/c$ of the thermodynamic stable α-WO_2 is a direct subgroup of *Pnma*, both structures cannot be transformed into each other. The aristotype of the high-pressure polymorph is the NiAs structure (space

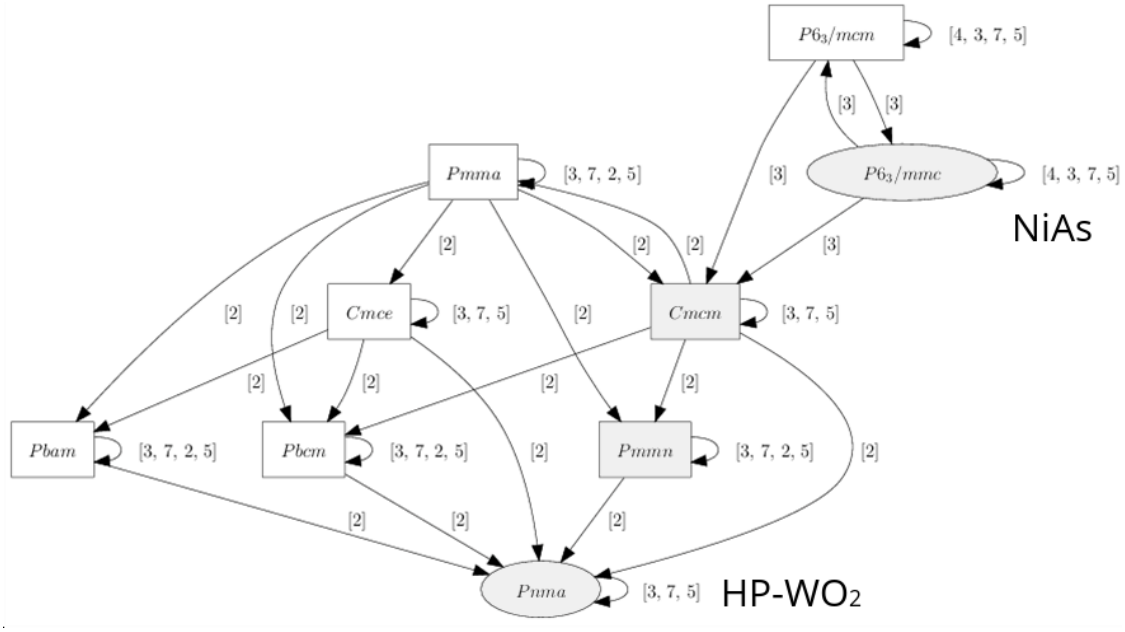

Figure 2.10. Group-subgroup relation of space groups $P6_3/mmc$ (NiAs, hcp) and *Pnma* (HP-WO_2) with possible transformation pathways.[261] The relevant transition steps are marked gray.

group $P6_3/mmc$) with an ideal hcp arrangement of arsenic and nickel occupying all octahedral sites. The complete structural relationship between aristotype and hettotype is depicted in Figure 2.10. The fastest transition route ($P6_3/mmc$ – *Cmcm* – *Pnma*) consists of two steps, but does not result in the final structure type. An additional step to space group *Pmmn* has to be inserted for the accurate setup.

A complete derivation of this structure type by the research group of Prof. Dr. Rainer Pöttgen is part of the characterization of the newly synthesized HP-MoO_2 in Chapter 8.4, including Figure 8.6. For a better understanding of the transformation process, this Bärnighausen-tree is depicted again in Figure 2.11 side by side with the development of the unit cell. It should be noted, that the final representatives for the atomic parameters of HP-MoO_2 in this overview do not match those listed in Figure 8.6. The values chosen here are the same representative coordinates as listed in Table 8.2.

The first transition (*translationengleich* of index 3) to space group *Cmcm* implicates an orthohexagonal setup of the unit cell by the changeover from the hexagonal to the orthorhombic crystal system.[254] A schematic representation of both alternative systems based on the hcp arrangement is embedded in picture Figure 2.11.

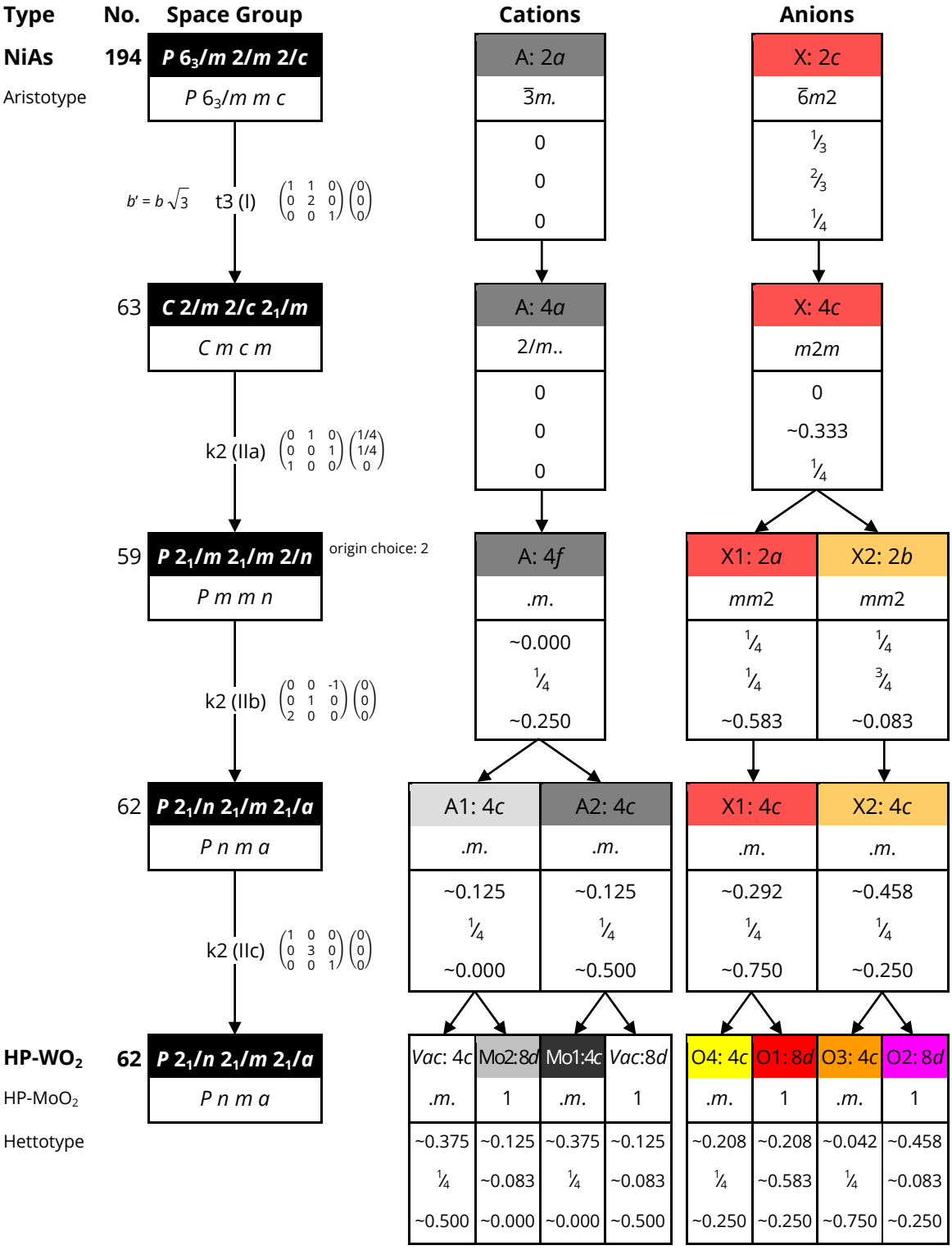

Figure 2.11. Group-subgroup scheme (Bärnighausen formalism) and graphical development of the unit cell for the group-theoretical relationship between NiAs (aristotype) and HP-WO_2-type HP-MoO_2 (hettotype).[250,252,254–256,263] See Figure A.1 or Figure A.2 for legend.

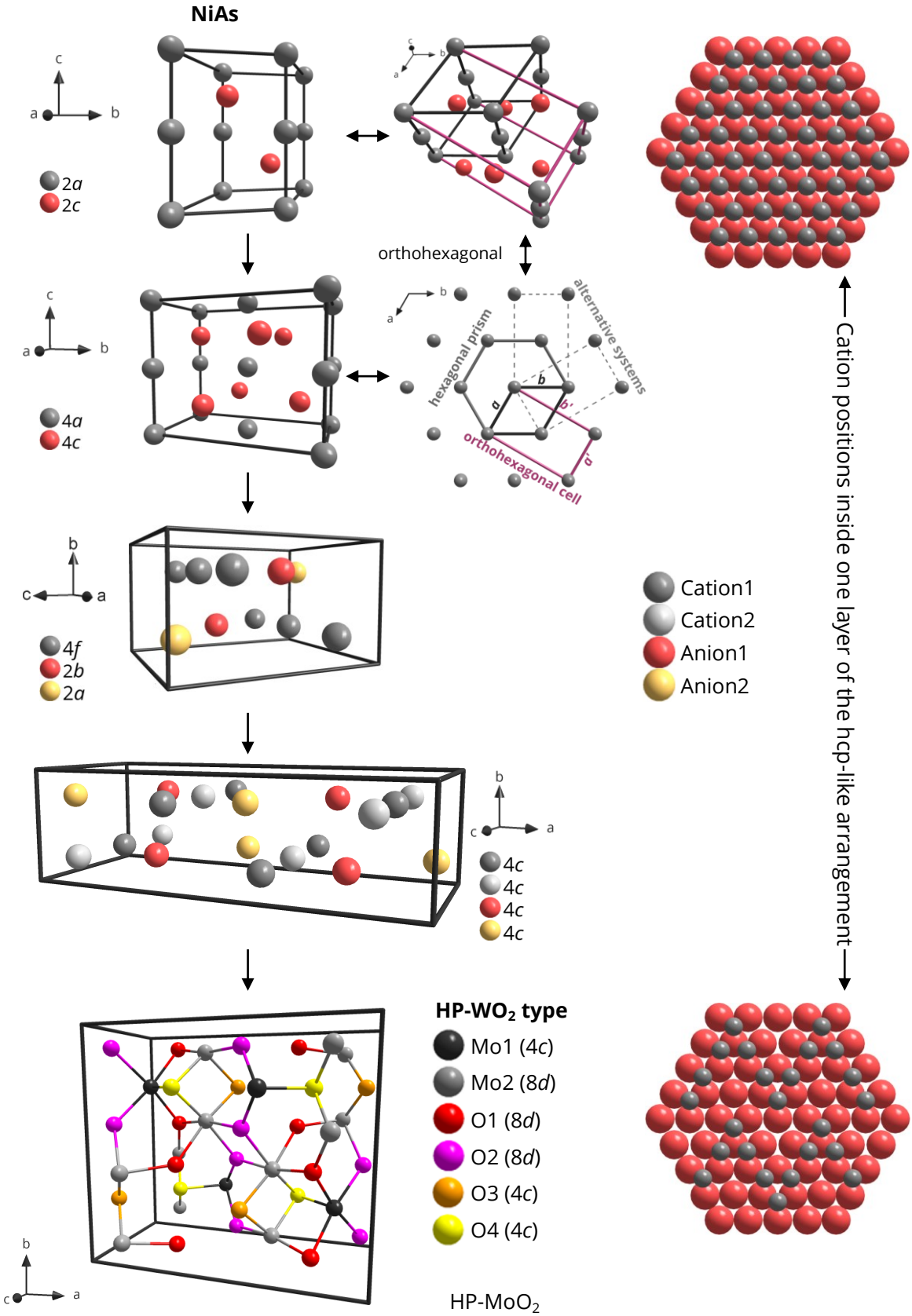
NiAs
2a
2c
orthohexagonal
4a
4c
hexagonal prism
alternative systems
orthohexagonal cell
4f
2b
2a
4c
4c
4c
4c
Cation1
Cation2
Anion1
Anion2
Cation positions inside one layer of the hcp-like arrangement
HP-WO2 type
Mo1 (4c)
Mo2 (8d)
O1 (8d)
O2 (8d)
O3 (4c)
O4 (4c)
HP-MoO2

The new orthorhombic cell has a *C*-centering with axes of the relation $b'/a' = \sqrt{3}$, while the *c* axis remains unaltered. As a consequence, the cell volume doubles in comparison to the primitive cell. A total of six right-handed systems can be defined; three of them are depicted in Figure 2.11 (the matching system to the provided transformation matrix is marked violet). Another set of three systems can be obtained by inversion of the *a*' and *b*' axes. All different options are part of one conjugacy class of transformations. The advantage of an orthorhombic setup is the presence of an orthogonal axis system at the expense of the loss of symmetry operations.

Four different conjugacy classes are available for the third transition. Two of them allow the accurate splitting of the Wyckoff positions to a diaspore-like structure and can be used adequately. The class selected here avoids an origin shift.

The setup of the structure with the special arrangement of the polyhedra is discussed in detail in Chapter 8.4. A similar polyhedral arrangement can be found in $Mg_2Mo_3O_8$.[234] In addition to the explanations given there, a simplified representation (without the distinguishable positions) of a view on the layers along the *c*-axis of the hcp and hcp-like structures of NiAs and HP-MoO_2, which shows the ordered cation arrangement of the hettotype compared with the ideal NiAs aristotype, is embedded in Figure 2.11.

2.6 Experimental Principles

The new tantalum based compounds were generally synthesized *via* an ammonolysis reaction of X-ray amorphous precursors obtained by a sol-gel route. The principles of these preparation methods are described in the following chapters.

2.6.1 Precursor

Dispersions of finely divided particles in solution are called sols.[286] Sol-gel processes are used in the production of ceramic or organoceramic materials. In general, educts are metal or non-metal alcoholates, which polymerize in a condensation reaction to oligomers. Further condensation reactions increase the viscosity of the solution and the agglomeration of the particles. These processes continue until a network has formed between the particles and the solution solidified into a gel. The gels can be further processed into powders, shaped bodies, fibers, or layers.

The Pechini method is a variant of the sol-gel process and was developed in 1967 by the American chemist Maggio Pechini.[287] It is used for the production of metal oxides

whose metals are not suitable for a conventional sol-gel process due to unsuitable hydrolysis properties. Hydroxycarboxylic acids are used as complexing agents for the metal. In combination with a suitable polyalcohol, they also functions as gelling agent. The hydroxycarboxylic acid acts as a chelate ligand, which makes the complexes highly resistant to oxidation and hydrolysis and stable over a wide pH range.

A suitable combination, particularly in terms of handling, workload, and toxicity, is the use of citric acid as the complexing agent and the dihydric alcohol ethylene glycol as the polymerization agent. A carboxyl group of the citric acid can react with a hydroxyl group of the ethylene glycol *via* an esterification reaction. Due to the multiplicity of functional groups, several molecules can polymerize to form a gel by polyesterification reactions.[288] The remaining organic constituents of the polymer are removed by a calcination process. The products are metal oxides powders. Through the use of different metal citrate solutions in the corresponding quantitative ratio, mixed oxides having a defined stoichiometric composition can thus be produced. Another consequence is a homogeneous phase formation during the synthesis, which is hardly achievable with classical solid-state reactions. Regulation of the calcination temperature also allows the degree of crystallization of the products. Metastable X-ray-amorphous powders can be prepared at low temperatures and used as precursors for subsequent reactions.

2.6.2 Ammonolysis Reaction

The reaction of a solid with gaseous ammonia is called ammonolysis. The grade of the ammonolysis can be controlled by various factors, such as reaction temperature, heating rate, reaction time, and gas composition. In contrast to the Mg- and Sc-doped tantalum oxide nitrides, which have been prepared with the aid of water-saturated ammonia gas,[51,53] a small amount of oxygen can be added to dry ammonia in order to control the equilibrium between the nitriding and reoxidation reactions. Without this balance, the educts would react completely to Ta_3N_5.[119]

As mentioned in the introduction, anion substitution is an useful tool for the synthesis of metastable compounds, as seen by the bixbyite- and anosovite-type vanadium oxide nitrides and matching oxides.[6,7,58,59] Only small amounts of nitrogen are required for the stabilization of the crystal structure in $V_2O_{3.08}N_{0.02}$[58] and $V_3O_{4.61}N_{0.27}$,[59] respectively. The incorporation of higher valent anions must be compensated with a corresponding removal of lower valence anions. In the present case, the insertion of two nitrogen ions has to be counterbalanced with three oxygen ions leaving the system. As a consequence, va-

cancies on formerly oxygen positions are generated. The whole process can be formulated according to the Kröger–Vink notation:[151,152]

$$3\ O_O^{\times} + 2\ NH_3 = 2\ N_O' + V_O^{\bullet\bullet} + 3\ H_2O\ (sf) \tag{2.4}$$

Those artificially generated defects can be, compared to the original material, responsible for new physical properties, such as ionic conductivity.

2.7 Powder X-ray Diffraction

X-ray (and neutron) diffraction is one of the most important analytical methods in solid-state chemistry. X-rays are suitable because of the comparable ratios between the wavelength and the distances of atoms in crystals. The photons interact with the electron shells of the crystal atoms and are diffracted, such as light on an optical grate. The relevant physical equation is the Bragg's law, which defines the requirements for constructive interference:[289]

$$2 d_{hkl} \cdot \sin \theta = n \cdot \lambda \tag{2.5}$$

d: Distance between atomic layers (hkl)
θ: Diffraction angle
n: Integer
λ: Wavelength of incident X-ray beam

Constructive interference occurs when the path length difference is an integer multiple of the wavelength. The crystal consists of various layers, indexed by the Miller indices (hkl), on which the radiation is reflected. The positions of these reflections in a diffractogram define the metrics of the various layers and the unit cell, while the intensities depend on the specific atomic positions and the space group. Another property, the crystallinity and the strain of a sample, can be extracted from the full width at half maximum (FWHM) of the reflections.

A disadvantage, compared with neutron diffraction experiments, is the problematic distinguishability of isoelectronic ions, like O^{2-}/N^{3-} or Hf^{4+}/Ta^{5+}. On the other hand, only a relatively small amount of substance and short measuring times are required for good results.

2.7.1 Rietveld Refinement

A technique for the evaluation of X-ray and neutron powder diffraction data is provided by the Rietveld refinement method.[290–292] In a first step of the general procedure, the data of an isotypically compound to the investigating substance is searched with the help of a database. The structural parameters adapted from the dataset are the starting point for calculated reflection positions and intensities, which are refined to the experimental data in an iterative mathematic process based on the least squares method. The refined parameters generally include the unit cell parameters (a, b, c, α, β, γ), the atomic positions (x, y, z) with temperature displacement factors (Debye-Waller factors), the profile parameters of the used mathematical function, asymmetry of the reflections, multiple background points, and parameters depending of the measuring device and method (*e.g.* displacement and transparency). All these parameters can be refined for multiple phases simultaneously. Overlapping reflexes of different phases can also be examined to a certain degree.

Numerical quality criteria of the refinement are the residual values (R-values) which specify the accordance of the calculated intensities with the measured diffractogram.[293,294] Low R-values indicate a good accordance. Due to the signal-to-noise ratio, the residual values are always greater than zero and can only converge to an expected value (R_{exp}).

$$R_{exp} = \sqrt{\frac{N-P+C}{\sum_{i=1}^{N} w_i \left[y_i^{obs}\right]^2}} \tag{2.6}$$

N: Number of measured points
P: Number of parameters
C: Number of parameter linkages
y_i^{obs}: Observed intensity at point i
w_i: Weighting factor at point i; $= (y_i^{obs})^2$

The statistically weighted R_{wp}-value is the most straightforward residual and indicates the mean deviation of the calculated intensities to the observed diffraction pattern.

$$R_{wp} = \sqrt{\frac{\sum_{i=1}^{N} w_i \left[y_i^{obs} - y_i^{calc}\right]^2}{\sum_{i=1}^{N} w_i \left[y_i^{obs}\right]^2}} \tag{2.7}$$

y_i^{calc}: Calculated intensity at point i

The quotient of R_{wp} and R_{exp} gives the goodness of fit S, which should be below 2 for a good refinement.

$$S = \frac{R_{wp}}{R_{exp}} \tag{2.8}$$

In addition to the above-mentioned parameters, the discrepancy index R_{Bragg} specifies the ratio from the observed and calculated integral intensities of the reflections.

$$R_{Bragg} = \sqrt{\frac{\sum_{k=1}^{N}\left(I_k^{obs} - I_k^{calc}\right)^2}{\sum_{k=1}^{N}\left(I_k^{obs}\right)^2}} \tag{2.9}$$

I_k^{obs}: Measured integral intensity of the k reflection
I_k^{calc}: Calculated integral intensity of the k reflection

Sometimes, an unambiguous interpretation of the collected data is not possible with the Rietveld method. This might be the case if, for example, a wrong structure model was chosen or the sample does not fulfill the requirements for powder diffraction analyses. The whole powder pattern decomposition method (WPPD), or the so called Le Bail method, allows a phase analyses without a distinct structure model.[295,296] The intensities of the reflections are based on the scaling, structure factors (depending on atomic positions), preferred orientation, and microstructure. The WPPD method fits these intensities by arbitrary values while the profile and cell parameters are still refined by the least squares process.

The raw data processing and the basic phase analysis were carried out with the software X'PERT HIGHSCORE PLUS from PANalytical, Almelo (NL). The software package FULLPROF was used for the Rietveld refinements and Le Bail decompositions.[297,298]

2.8 Diffuse Reflectance UV-vis Spectroscopy

The ultraviolet-visible spectroscopy (spectrophotometry) is a common tool for band gap determination of solids and is based on the interaction between matter and electromagnetic radiation of the ultraviolet and visible region. By excitation of electrons, the irradiated light is absorbed by the material. Unlike liquids, opaque solids cannot be analyzed with transmission experiments. An alternative technique is the measurement of the

diffuse reflected light spectra of the powder sample. These reflectance spectra can be converted by the Kubelka–Munk function to absorbance spectra.[299] In this case, the reflectance of a sample depends on an absorption component K and an abstract scattering component S. However, the function is only valid for low-absorbing and optically infinitely thick samples.

$$F(R_\infty) = \frac{K}{S} = \frac{(1-R_\infty)^2}{2R_\infty} \tag{2.10}$$

$F(R_\infty)$: Kubelka–Munk function
R_∞: Reflectance of an infinitely thick color layer
K: Absorption coefficient
S: Scattering coefficient

The Tauc plot method can be used for the determination of the direct and indirect optical band gaps. For this, the product of the Kubelka–Munk function and photon energy, modified with an exponent depending on the transition type, is plotted against the photon energy. A linear function is adjusted to this plot and its intersection point with the abscissa (x-axis) relates to the band gap energy.

$$\left[F(R_\infty)\cdot h\nu\right]^{\frac{1}{n}} = A(h\nu - E_{BG}) \tag{2.11}$$

$h\nu$: Photon energy
n: $n = ½$: direct band transition; $n = 2$: indirect band transition
A: Proportionality constant
E_{BG}: Band gap energy

In the case of a direct transition, the minimum of the conduction band corresponds to the same wave vector as the maximum of the valence band. On the other hand, the minimum of the conduction band relates to a change in the wave vector compared to the maximum of the valence band in the case of an indirect transition.

3 Methodology

General experimental proceedings and specifications of different synthesis and analysis devices used for this work are described in this chapter.

3.1 Preparative Methods

A successful synthesis depends on suitable educts and adequate equipment. All new tantalum compounds were prepared by ammonolysis reactions of amorphous oxide precursors in a tube furnace with direct gas feed. The MoO_2 precursor for high pressure synthesis was also prepared in such a furnace.

3.1.1 Precursor Preparation

Amorphous mixed oxides were prepared according to the modified Pechini method. The applied preparation procedure for the transition metal oxides was developed by Dr. Heikko Schilling.[52] The following example outlines the general technique for the preparation of a stock solution (500 mL): The precisely weighed metal salts (nitrates, chlorides, or oxides) are dissolved in a small amount of water or dilute HNO_3. For hydrolysis sensitive metals (*e.g.* tantalum), the corresponding chloride, enclosed in an ampoule, is transferred inside a glove box with inert gas atmosphere into a flask. The citric acid is dissolved in a 12-fold molar excess to the metal under heating in *ca.* 400 mL of absolute dry ethanol. Subsequently, this citric acid-ethanol solution is gently dripped into the flask (eventually under nitrogen atmosphere). The solvation process is supported by gentle stirring. The citrate solution is quantitatively transferred to a volumetric flask and filled to the mark with absolute ethanol. The metal content can be determined gravimetrically.

Most citrate solutions are resistant to moisture, light, and air. Some metals, *e.g.* tungsten, can form stable complexes with citric acid. A precipitate of this complex can be formed if the citric acid concentration of the solution is too high. The precipitate can sometimes be resolved in boiling ethylene glycol.

The amorphous mixed oxides were prepared according to the following procedure: For the required mixed oxides, the various citrate solutions are mixed in the appropriate volume ratio in a corundum crucible. Ethylene glycol in a 17-fold molar excess to the metal ions is added. First, ethanol is removed by heating the mixture to temperatures of *ca.* 373 K. Remaining water is evaporated at *ca.* 423 K and the polymerization process finalized at *ca.* 498 K. The resulting viscous gel is evaporated to dryness at temperatures of up to *ca.* 573 K. The final calcination is carried out in a batch furnace at 623–723 K for 72–168 h. X-ray fluorescence spectroscopy is used to verify the required cation ratio.

A slightly modified preparation method of the mixed oxides skips the production of the citrate stock solutions. The salts of the corresponding metals are appropriate weighed, mixed, and filled into the flask inside the argon glove box. The above mentioned method can now be applied in a smaller scale to the mixed metals without the gravimetric analyses and the storage difficulties.

3.1.2 Tube Furnace

Ammonolysis and reductions reactions were carried out in a tube furnace from Gero, Neuhausen (Germany), type SR-A-60-300/12 (Figure 3.1). The temperature is controlled by the external heating controller RES-E 230/3 from Gero, which is connected to a Ni/Cr-Ni thermocouple. A gas mixing system upstream of the furnace uses several mass flow controllers (MFC) of the type DeltaSmart MassFlow from Brooks Instrument, Ede (Netherlands), which are regulated *via* the LABVIEW program from National Instruments, Austin (USA). Controllers are available for reductive gases (NH_3 or H_2; maximum flow rate 25 $L{\cdot}h^{-1}$), for protective gases (N_2 or Ar; maximum flow rate 30 $L{\cdot}h^{-1}$), and for oxygen (maximum flow rate 1.2 $L{\cdot}h^{-1}$), respectively.

A washing bottle filled with polyol is connected to the end of the reaction tube. This device regulates the overall pressure and prevents the ingress of air into the reaction chamber. Additionally, it can be used as a bubble counter for a visual check of the gas flow. The precursors are placed in a corundum boat just below the outlet of the direct gas feed tube.

The reaction tube of amorphous silica glass is a custom-built fabrication. Its originate design was developed by Dr. Manop Huber[213] and it consists of two individual tubes fused together (Figure 3.2). A tube with a smaller diameter is connected directly to the gas mixing system and leads the gas directly onto the sample, which is usually placed in a corundum boat in the center of a larger tube. Due to the smaller radius of the tube, the

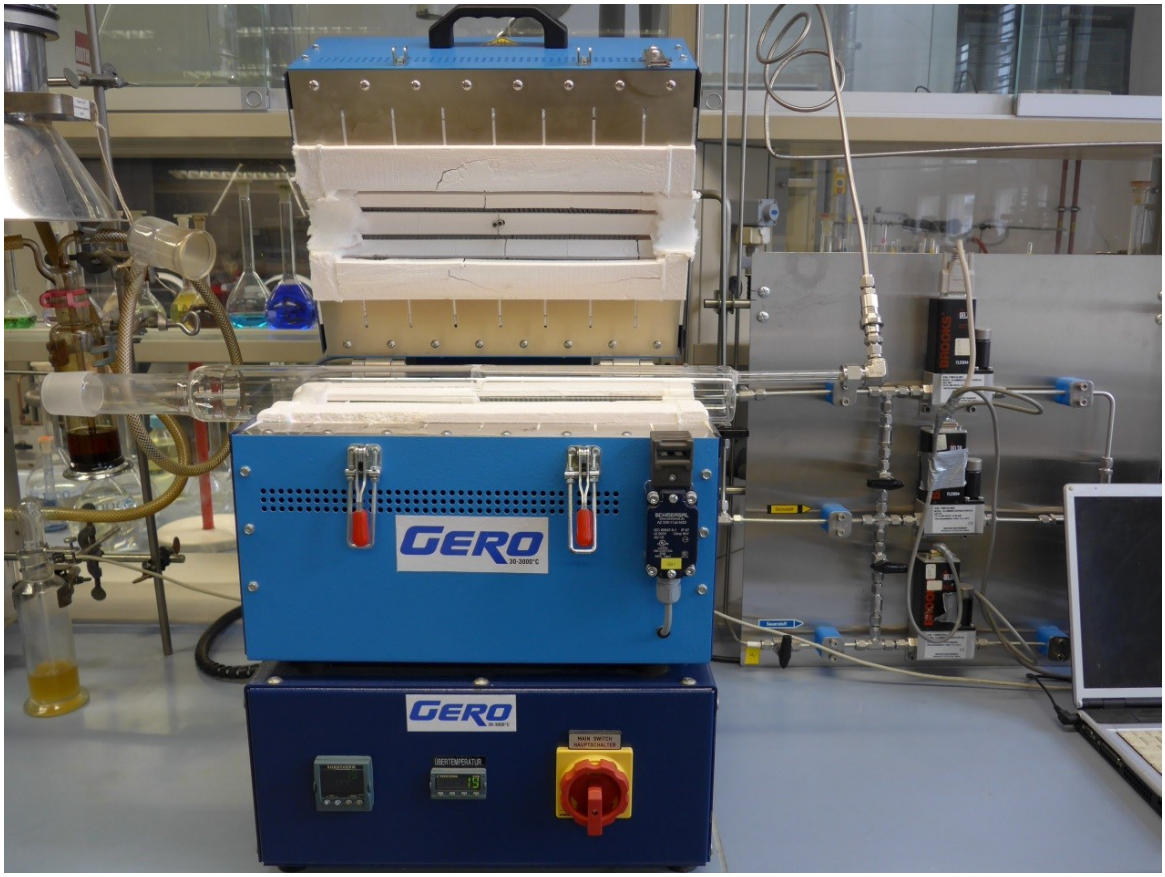

Figure 3.1. Synthesis apparatus with the gas mixing unit (right) and the tube furnace with the control unit (left).

gas flows into the reaction tube at a higher rate, thereby minimizing possible dissociation of the reaction gases. A similar version of the reaction tube made of corundum was developed by Dr. Dominik Weber and allows the chemical reaction of fluoride-containing precursors.[3]

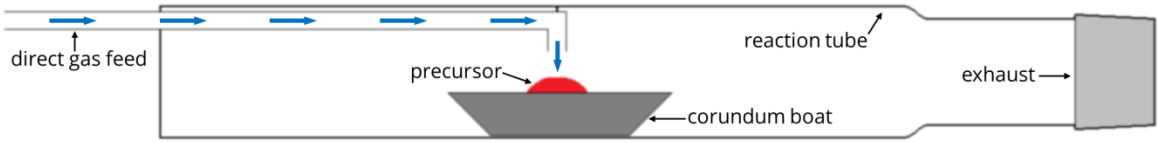

Figure 3.2. Schematic representation of the used reaction tube with direct gas feed.

3.2 X-ray Diffraction

Powder X-ray diffraction analyses were carried out on a X'Pert MPD Pro diffractometer from PANalytical, Almelo (Netherlands). It operates in Bragg-Brentano geometry with a θ/θ arrangement and generates the radiation in a X-ray tube with Cu anode. The Bremsstrahlung (braking radiation) and Cu-K_β radiation is filtered out by a nickel foil. No monochromator is mounted in the device. The characteristic radiations Cu-$K_{\alpha1}$ (λ = 154.060 pm) and Cu-$K_{\alpha2}$ (λ = 154.443 pm) are emitted with an intensity ratio of *ca.* 2:1. The sample holder consists of a Si single-crystal wafer. A PIXcel solid state sensor (Si-Li-semiconductor) is used for signal detection. The device is controlled *via* the software DATA COLLECTOR from PANalytical.

3.3 X-ray Fluorescence Analysis

A wave-dispersive X-ray fluorescence (WDXRF) spectrometer Axios from PANalytical, Almelo (Netherlands), was used for qualitative element analysis. The radiation is generated in a ceramic end-window SST X-ray tube (exit window made of Be) with a rhodium anode (Rh-K_α; λ = 61.4 pm) and a maximum power of 4 kW. After the X-ray radiation hits the sample, it passes through a collimator mask to filter out possible fluorescence radiation emitted from the sample holder. Subsequently, the primary collimator directs the fluorescence radiation from the sample in a planar-parallel beam onto the analyzer crystal (monochromator), of which several are installed in the device. The $\theta/2\theta$-goniometer aligns the crystals and the detector according to the Bragg condition (Equation 2.5). The radiation is detected by two different detectors (flow counter and scintillation). Light elements, in particular those of the first two periods, cannot be detected evaluable by the device. The spectrometer is controlled *via* the software SUPERQ (Version 5) with IQ PLUS from PANalytical. Measurements within the scope of this work were done by Dr. Rafael Zubrzycki and Maika Stöbe, M.Sc. (research group Prof. Ressler, TUB).

3.4 UV-vis Spectroscopy

UV-vis diffuse reflectance spectroscopy was carried out on a CARY 300 Scan spectrophotometer from VARIAN, Palo Alto (USA), (now AGILENT Technologies, Santa Clara (USA)) with a wavelength range of 190–900 nm. Visible light is emitted by a tung-

sten-halogen source and ultraviolet light by a deuterium-arc lamp, respectively. Monochromatic light is realized by a pre-monochromator and a Czerny-Turner monochromator. The monochromatic light is splitted into a primary and a reference beam by a chopper. The powder sample is mounted to a solid-state sample holder, which can be exchanged for a test arrangement for liquids. Barium sulfate was used as reference substance. A R928 photomultiplier tube detects the diffuse reflectance spectra. The CARY WINUV software converts the recorded spectra into absorbance spectra according to the Kubelka–Munk-function (Equation 2.10). The spectrometer was kindly provided by the research group of Prof. Thomas (TUB).

3.5 N/O-Analysis

Quantitative determination of the nitrogen and oxygen contents was carried out on a nitrogen/oxygen analyzer TC-300/EF-300 from LECO Corporation, St. Joseph (USA). The analyzer has the designation TC 300, the electrode furnace EF 300, respectively. A small amount (2–5 mg) of the sample is filled into a tin capsule, which itself is placed into a nickel capsule. The nickel serves as fluxing agent during the analysis. The nickel capsule and graphite powder is placed in a graphite crucible, which serves as a heating element for the furnace. The crucible is heated in a stream of helium over two electrodes to *ca.* 2973 K for less than one minute. This temperature is sufficient enough to set free elementary oxygen and nitrogen. Oxygen reacts with graphite to carbon monoxide and is further oxidized to carbon dioxide *via* a copper(II) oxide catalyst. CO_2 is detected by absorption spectroscopy in an infrared measuring cell. A thermal conductivity detector (Wheatstone bridge) is used to determine the nitrogen content, which is proportional to the change in electric resistance. Various substances with known nitrogen and oxygen contents are used for calibration. Nitrogen can be calibrated with steel (0.532 wt % N) or Si_3N_4 (40 wt % N). ZrO_2 (25.8 wt % O) or Ta_2O_5 (18.1 wt % O) are common standards for oxygen. The measuring accuracy of the method is *ca.* 2% of the presented values. All measurements were done by Dipl.-Chem. Steven Orthmann and Brigitte Hahn (both research group Prof. Lerch, TUB).

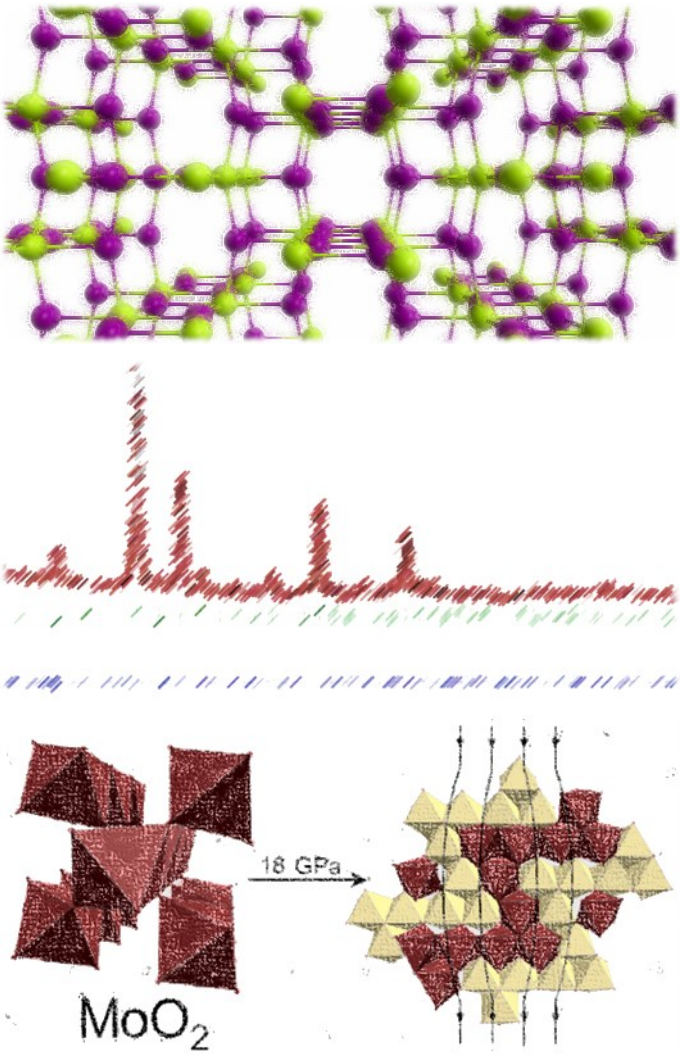

Part II

Publications

4 Publication 1 51
Synthesis and Crystal Structure of δ-TaON, a Metastable Polymorph of Tantalum Oxide Nitride
5 Publication 2 73
Synthesis and Characterization of Metastable Transition Metal Oxides and Oxide Nitrides
6 Publication 3 101
Bixbyite-type Phases in the System Ta-Zr-O-N
7 Publication 4 119
A Density-Functional Theory Approach to the Existence and Stability of Molybdenum and Tungsten Sesquioxide Polymorphs
8 Publication 5 137
HP-MoO_2: A High-Pressure Polymorph of Molybdenum Dioxide

Pictures on the cover sheet:

Top: Artistically modified crystal structure of δ-TaON.

Center: Artistically modified X-ray diffraction image of bixbyite-type $TaZrN_3$.

Bottom: Artistically modified graphical abstract of Publication 5.

4 Publication 1

Synthesis and Crystal Structure of δ-TaON, a Metastable Polymorph of Tantalum Oxide Nitride

Tobias Lüdtke, Alexander Schmidt, Caren Göbel, Anna Fischer, Nils Becker, Christoph Reimann, Thomas Bredow, Richard Dronskowski, Martin Lerch

Postprint
Inorganic Chemistry **2014**, *53(21)*, 11691–11698
DOI: 10.1021/ic501726m
http://pubs.acs.org/doi/abs/10.1021/ic501726m

Contribution to publication:

T. Lüdtke:	Sample preparation, characterization, writing.
A. Schmidt:	Evaluation.
C. Göbel:	Measurements (TEM), writing.
A. Fischer:	Measurements (TEM).
N. Becker:	Quantum-chemical calculations, writing.
C. Reimann:	Quantum-chemical calculations, writing.
T. Bredow:	General discussion, proofreading.
R. Dronskowski:	General discussion, proofreading.
M. Lerch:	General discussion, proofreading.

Overall contribution of T. Lüdtke to the publication: 40%

Authors. Tobias Lüdtke,[a] Alexander Schmidt,[a] Caren Göbel,[a] Anna Fischer,[a] Nils Becker,[b,c] Christoph Reimann,[d] Thomas Bredow,[d] Richard Dronskowski,[b,c] Martin Lerch [a,*]

(a) Institut für Chemie, Technische Universität Berlin, Straße des 17. Juni 135, D-10623 Berlin, Germany
(b) Institut für Anorganische Chemie, RWTH Aachen University, Landoltweg 1, D-52056 Aachen, Germany
(c) Jülich-Aachen Research Alliance (JARA-HPC), RWTH Aachen University, D-52056 Aachen, Germany
(d) Institut für Physikalische und Theoretische Chemie, Universität Bonn, Wegelerstraße 12, D-53115 Bonn, Germany

* Corresponding author

Keywords. Tantalum; Oxide nitrides; N/O order; Anatase; Quantum-chemical calculations

Dedication. Dedicated to Dr. Hans Boysen on the occasion of his 70th birthday.

Supporting Information. Crystallographic data in CIF format for the structure refinement of δ-TaON. Table with Gaussian-type basis sets for Ta, O, and N. This material is available free of charge *via* the Internet at http://pubs.acs.org.

Received: 06.08.2014
Accepted: 29.09.2014
Published online: 13.10.2014

4.1 Abstract

δ-TaON was prepared by reaction of gaseous ammonia with an amorphous tantalum oxide precursor. As a representative of the anatase structure (aristotype) it crystallizes in the tetragonal crystal system with lattice parameters $a = 391.954(16)$ pm and $c = 1011.32(5)$ pm. At temperatures between 1073 and 1123 K an irreversible phase transformation to baddeleyite-type β-TaON is observed. While quantum-chemical calculations confirm the metastable character of δ-TaON, its transformation to β-TaON is kinetically controlled. The anion distribution of the anatase-type phase was studied theoretically. In agreement with previous studies, it was found that a configuration with maximal N–N distances is most stable. The calculated band edge energies indicate that δ-TaON is a promising photocatalytic material for redox reactions, *e.g.*, water splitting.

4.2 Introduction

Transition metal oxide nitrides are a group of materials which attracted a lot of attention in recent years. In particular, tantalum-based compounds are, for example, suitable as nontoxic color pigments,[1,2] can be considered as fast ion conductors,[3] and are used as materials for photocatalytical water splitting under sunlight.[4,5] From a thermodynamical point of view, the most stable polymorph of tantalum oxide nitride is the so-called β-phase, reported first by Brauer and Weidlein.[6] It crystallizes in the well-known monoclinic baddeleyite-type structure also reported for ZrO_2 and exhibits a bright yellow color (optical band gap of *ca.* 2.6 eV). A metastable polymorph (γ-TaON) was reported by Schilling *et al.*[7] It shows an orange color (optical band gap of *ca.* 2.15 eV) and crystallizes similar to VO_2(B) in the monoclinic crystal system. For both β- and γ-TaON, an ordered distribution of oxygen and nitrogen was found. Another polymorph, α-TaON, was suggested by Buslaev *et al.*[8] but disproved by quantum-chemical calculations.[9] A possible high-pressure modification was predicted independently by two different groups.[10,11] Pressures of more than *ca.* 31 GPa should induce a phase transformation from β-TaON (7-fold coordination of Ta) to a cotunnite-type structure with 9-fold coordinated cations. In fact, this cotunnite phase has recently been found by high-pressure studies,[12] just as predicted. In addition, the relative stabilities of various structure types (including the anatase, rutile, and fluorite type) were calculated by quantum-chemical methods a couple of years ago.[13] Interestingly, and in clear contrast to TiO_2, the anatase type is energetically favored compared to the rutile type. With the small calculated stability difference of only

ca. 20 kJ·mol^{-1} between baddeleyite (most stable) and anatase type,[13] it is worth the effort trying to synthesize anatase-type TaON.

It should be mentioned that anatase-type phases have previously been prepared by incorporating lower-valent cations such as Mg^{2+} [14] or Sc^{3+} [15] into TaON. In particular, substitution of 5% tantalum by magnesium leads to a phase-pure material with the composition $Mg_{0.05}Ta_{0.95}O_{1.15}N_{0.85}$. This was the first example of an anatase-type structure not containing the element titanium. Interestingly, the preparation of 30–45 nm thin films of undoped anatase-type TaON on $(LaAlO_3)_{0.3}(SrAl_{0.5}Ta_{0.5}O_3)_{0.7}$ (LSAT) single crystals using nitrogen plasma-assisted pulsed laser deposition (NPA-PLD) was recently reported by Suzuki *et al.*[16] Epitaxial stress from the substrate stabilizes the anatase-type structure without additional elements such as magnesium or scandium. From a photocatalytical point of view, this material is of great interest due to its optical band gap of *ca.* 2.4 eV and its high charge carrier mobility which is comparable to that of anatase-type TiO_2.[16] Unfortunately, the quality of the X-ray diffraction patterns of the films is insufficient for a real structural refinement including atomic positions, bond lengths, *etc.* In the present Article we report, for the first time, the synthesis and crystal structure of tantalum oxide nitride powder with anatase-type structure without any additional cations. From now on we call this the δ-TaON phase.

4.3 Experimental Section

Synthesis. Amorphous tantalum oxide precursors were prepared *via* a modified Pechini route.[17] Tantalum chloride (99.999%, Alfa Aesar) was solved in an ethanol–citric acid solution. Citric acid was used in a molar excess of 12 times the $TaCl_5$. Ethylene glycol in a molar excess of 17 times the tantalum chloride was added for the gelling process. Ethanol, HCl, and water, the latter formed during the esterification, are evaporated at *ca.* 423 K. The polymerization can be finalized by heating the mixture to 473 K. The material was calcined at 673 K for 40 h. The products were colorless X-ray amorphous powders. The maximum yield of 43 wt % of anatase-type tantalum oxide nitride was obtained by ammonolysis of these amorphous precursors at 1033 K, a reaction time of 1 h, and flow rates of 12.50 L·h^{-1} ammonia and 0.02 L·h^{-1} oxygen. Additional phases were β-TaON, γ-TaON, and Ta_3N_5. Samples without γ-phase could be obtained using an increased ammonia flow rate of 23.75 L·h^{-1}, while the other parameters were unaltered. For the investigation of the high-temperature behavior in inert atmosphere the samples were heated at different temperatures for 1 h in closed copper capsules (nitrogen atmosphere).

After cooling down to ambient temperature the phase fractions were determined by X-ray diffraction.

Characterization. A PANalytical X'Pert Pro powder diffractometer (Cu-K_α radiation) was used for XRD measurements. Rietveld refinements including quantitative phase analyses were carried out using the program FULLPROF 2000.[18] Profiles were fitted with a pseudo-Voigt function.

The contents of nitrogen and oxygen were determined by hot gas extraction using a LECO TC-300/EF-300 N/O analyzer. ZrO_2 and steel were used as standard materials. The accuracy is *ca.* 2% of the N/O contents present. X-ray fluorescence spectrometry (XRF) was performed using a PANalytical Axios spectrometer with an Rh-tube. Crystallinity, phase composition (identification of δ-TaON, β-TaON, Ta_3N_5), and morphology of the particles were investigated by high-resolution transmission electron microscopy (HRTEM), selected area electron diffraction (SAED), and energy dispersive X-ray spectroscopy (EDX) analysis. For TEM analysis, powder samples were deposited on a holey carbon coated nickel grid. TEM and HRTEM measurements were performed at the Department of Electron Microscopy of the TU Berlin (ZELMI) on a Tecnai G^2 S-Twin transmission electron microscope (FEI Company, Eindhoven, Netherlands) equipped with a LaB_6-source operated at 200 kV. Images were recorded with a GATAN MS794 P CCD-camera. EDX-analysis were carried out with an r-TEM SUTW Detector from EDAX (Si (Li)-detector).

Quantum-Chemical Calculations. In order to investigate the thermodynamic properties of the TaON phases, periodic density functional theory (DFT) calculations were performed as implemented in the Vienna ab initio simulation package (VASP).[19,20] Projectoraugmented waves (PAW)[21] were used to separate the core and valence electrons. Exchange and correlation contributions were treated within the generalized-gradient-approximation as described by Perdew, Burke, and Ernzerhof (GGA-PBE).[22] An energy-cutoff of 500 eV and a Monkhorst–Pack *k*-point mesh of 20 × 20 × 8 were used for structure optimization, and ensured convergence.

Quasiharmonic phonon calculations were performed using the program PHONOPY.[23] In a first step, a supercell was constructed on the basis of the optimized crystal structure. All symmetry-inequivalent atoms of the previously created supercell were then slightly

shifted out of their equilibrium position to calculate the Hellman–Feynman forces. Subsequently, the force constants and then the dynamical matrix were computed. With a combination of its eigenvalues (phonon frequencies) with Bose–Einstein statistics, the free phonon energy was obtained.[24] Thermodynamic properties at finite temperatures are straightforwardly accessible from these data.

For the investigation of the high-pressure behavior, the cell volume was varied by scaling the cell parameters between 0.94 and 1.04 (with a fixed $a:b:c$ ratio and rectangular cell angles). The resulting energy versus volume data were fitted to the Birch–Murnaghan equation of state.[25] Thus, the pressure and, eventually, reaction enthalpies as a function of the pressure were calculated.

In order to investigate the dependence of the calculated properties on the basis set and functional, additional periodic calculations employing the PBE functional as well as the PBE026 DFT-Hartree–Fock hybrid method were conducted with the CRYSTAL program package (C09).[27] We used atom-centered Gaussian basis sets of valence double-ζ quality that have been optimized especially for the use in solid-state calculations (exponents and coefficients are listed in the Supporting Information, Chapter 4.8). For tantalum an effective core potential was employed (SD60MWB28) so that a total number of 13 electrons were kept in the semicore and valence region of each Ta atom, while all-electron basis sets were used for oxygen and nitrogen. The default values for the integral accuracy in CRYSTAL 09 have been increased by a factor of 10, and Monkhorst–Pack and Gilat grids have been generated using the shrinking factors (8,8). In order to obtain the Gibbs energies of the TaON polymorphs we performed frequency calculations at the Γ point.[29,30] Furthermore, we calculated the bulk modulus for the new phase by fitting the results of constant volume optimizations against the third-order isothermal Birch–Murnaghan's equation of state.

For the determination of the absolute electronic band edge positions with respect to the vacuum we performed periodic slab calculations with the PBE as well as the PBE0 functional. Since the Kohn–Sham gap as obtained from the PBE calculations is not a good approximation to the optical gap in solids,[31] we will follow the approach of Caspary Toroker *et al.* and merely calculate the band gap center from the hybrid calculations.[32] It has been shown that the band gap center is reproduced more reliably within the Kohn–Sham approach than the valence band maximum.[33]

In order to calculate the optical excitations, we employed the Bethe–Salpeter approach.[34] Therefore, we first calculated the quasiparticle gap with the GW0 method using

the VASP code.[35-38] The computational setup for these surface calculations has been described in detail elsewhere.[39] For these calculations, we used small-core PAWs developed for GW calculations as supplied with the VASP program package. In order to reduce the computational demands, a smaller Monkhorst–Pack *k*-point grid (6 × 6 × 6) has been chosen as well as a lower energy cutoff (400 eV) compared to the structure relaxations. Increasing these values in test calculations did not alter the results significantly.

4.4 Results and Discussion

The synthetic conditions, described in the Experimental Section, had to be respected carefully. Slightly increased reaction temperatures (*e.g.*, 1043 K instead of 1033 K) strongly preferred the formation of Ta_3N_5, while at lower temperatures (for example 1023 K) large parts of the amorphous tantalum oxide precursor did not react with ammonia but partially crystallized to β-Ta_2O_5. As mentioned above, we were successful in obtaining samples with a yield up to 43 wt % of the new δ-TaON polymorph as best result. With respect to the difficulties in refining the crystal structure of the disordered γ-phase,[7] we decided to choose a sample with a slightly smaller fraction of δ-TaON but without any γ-TaON for the Rietveld refinement. The red color of all prepared samples is likely dominated by the presence of dark-red Ta_3N_5. The red color also points to the absence of significant amounts of reduced tantalum resulting in black samples. XRF analysis proved the absence of other elements than tantalum, oxygen, and nitrogen.

Figure 4.1 presents the experimental powder XRD pattern with the results of the Rietveld refinement. Details are given in Table 4.1. The sample consists of three crystalline phases: anatase-type δ-TaON (35 wt %), Ta_3N_5 (45 wt %), and baddeleyite-type β-TaON (20 wt %). This is in good agreement with the results of chemical analysis (N = 7.6 wt %, O = 6.1 wt %), taking into account an additional content of amorphous tantalum oxide (assuming an overall content of 13 wt % amorphous Ta_2O_5 for the calculation gives the values from chemical analysis).

Additional TEM-investigations revealed that the sample consists of agglomerated crystalline nanoparticles assembled in sponge-like structures (Figure 4.2). Electron diffraction at those agglomerates as well as HRTEM analysis (see filtered images and corresponding FFT) of single nanoparticles revealed the presence of homogeneously intergrown δ-TaON, Ta_3N_5, and β-TaON particles on the nanometer scale (20–50 nm particle size, Figure 4.3). While δ-TaON and Ta_3N_5 are present as rounded "sintered" parti-

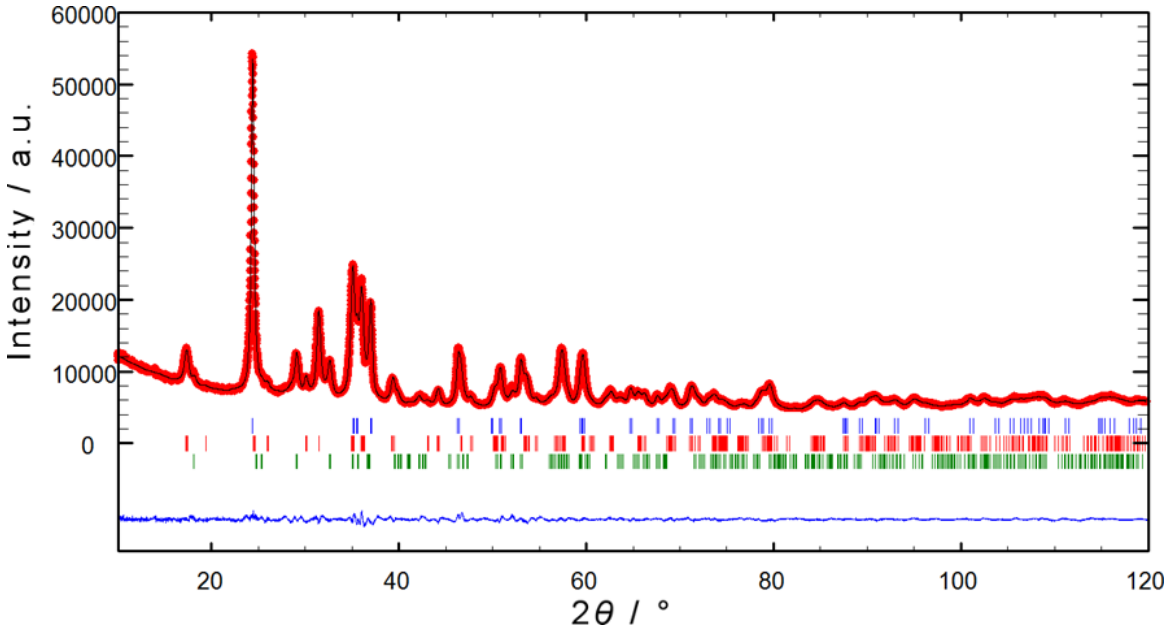

Figure 4.1. X-ray powder diffraction pattern (Cu-K_α radiation) with results of the Rietveld refinement (red: measured; black: calculated; blue: measured – calculated). The vertical bars indicate the reflection positions of anatase-type δ-TaON (top, blue), Ta_3N_5 (middle, red), and β-TaON (bottom, green).*

cles, β-TaON tends also to form angular aggregates. Unfortunately EDX analysis of single particles of identified phases could not be performed, due to intergrowth/overlapping of the nanoparticles. The observed overall ratio N/O of 1.23 is in very good agreement with the above-presented results of the chemical analysis (N/O = 1.24).

In comparison to $Mg_{0.05}Ta_{0.95}O_{1.15}N_{0.85}$, the lattice parameters determined for δ-TaON have very similar values (see Table 4.1). This can be easily explained by the similar ionic radii and the small amount of Mg^{2+} in the doped phase. In contrast, the calculated density of the undoped material is significantly larger due to the low mass of magnesium. It is remarkable that the density of the more stable γ-TaON phase (8.64 g·cm^{-3}) is clearly smaller which comes from the special structural features of the VO_2(B) type (huge tunnels, *etc.*, ref. 7).

Table 4.1. Results of the Rietveld refinement for δ-TaON in comparison with selected results for $Mg_{0.05}Ta_{0.95}O_{1.15}N_{0.85}$.

	δ-TaON	$Mg_{0.05}Ta_{0.95}O_{1.15}N_{0.85}$[13]
Structure type	Anatase	Anatase
Space group	$I4_1/amd$ (No. 141)	$I4_1/amd$ (No. 141)
Crystal system	Tetragonal	Tetragonal
a / pm	391.954(16)	391.986(6)
c / pm	1011.32(5)	1011.19(3)
c / a	2.58	2.58
V / 10^6 pm^3	155.367(12)	155.373(6)
Z	4	4
ρ_{calc} / g·cm^{-3}	9.02 g·cm^{-3}	8.71 g·cm^{-3}
Diffractometer	PANalytical X'Pert Pro	
2θ / °	10–120	
λ / pm	154.060, 154.443	
	$I(\lambda_2)/I(\lambda_1) = 0.5$	
Profile points	8839	
R_{wp}	0.0202	
R_{exp}	0.0115	
R_{Bragg}	0.0141	
S	1.75	

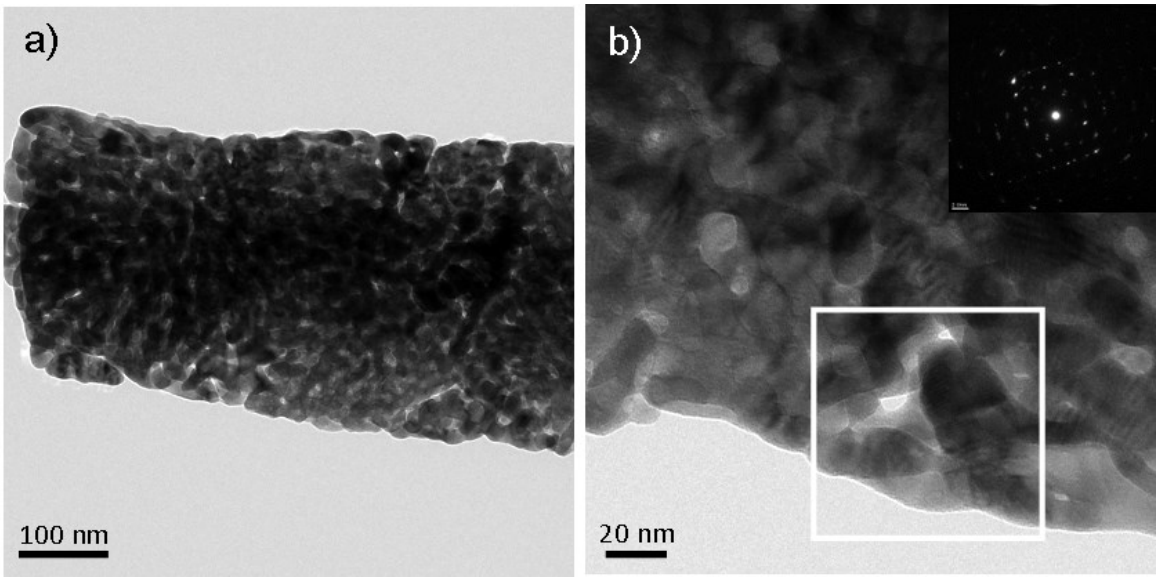

Figure 4.2. TEM-images of the as synthesized sample containing δ-TaON, β-TaON and Ta_3N_5: a), b) porous sponge-like structure. SAED pattern given as inset, demonstrate the presence of multiple crystal phases.

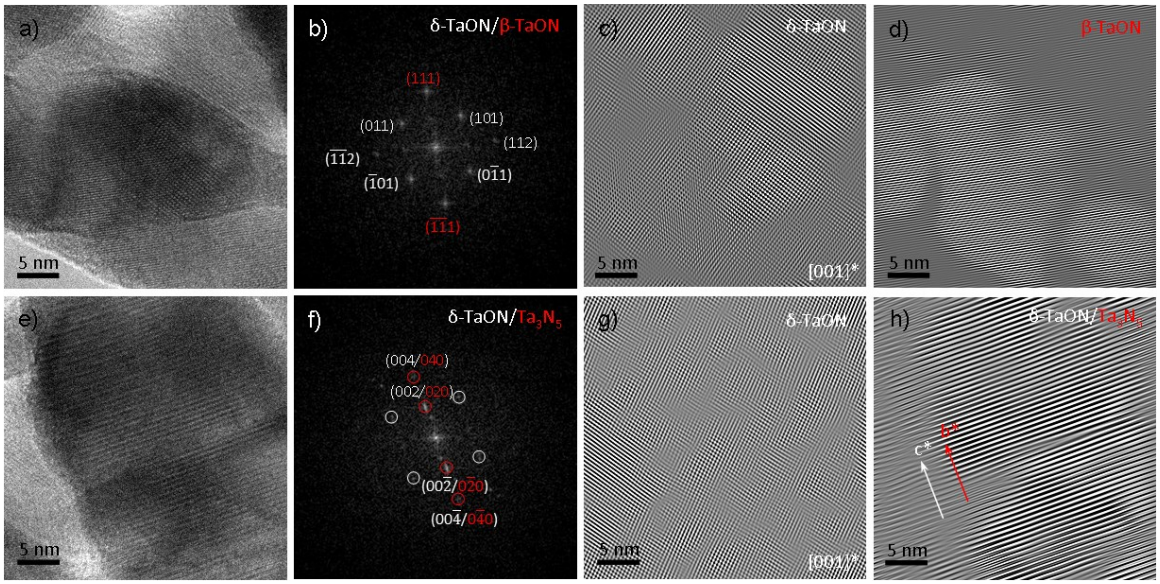

Figure 4.3. HRTEM-images (a,e) from the marked region in Figure 5.2 with corresponding FFT patterns (b,f). Filtered HRTEM-images of (a) evidencing the presence of δ-TaON (c) and β-TaON (d) and filtered HRTEM-images of (e) evidencing the presence of δ-TaON (g) and Ta_3N_5 (h).

The refined atomic parameters are presented in Table 4.2. The isotropic Debye-Waller factors were fixed to the results acquired from neutron diffraction experiments on the Mg containing phase.[14] Anatase-type TiO_2, which is structurally characterized by TiO_6-octahedra sharing four edges with neighboring octahedra and channels along the *a*- and *b*-axes, crystallizes in the tetragonal crystal system in space group $I4_1/amd$ (No. 141). Using this space group for the refinement of δ-TaON does not give the opportunity to respect an ordered arrangement of nitrogen and oxygen. In our case this is not a real problem because X-ray diffraction experiments do not allow distinguishing between these elements (ions with the same number of electrons).

Table 4.2. Refined atomic parameters for anatase-type TaON.

Atom	Wyckoff	*x*	*y*	*z*	S.O.F.[a]	B_{iso} / 10^4 pm^2
Ta	4*b*	0	¼	⅜	1	1.3[b]
O / N[c]	8*e*	0	¼	0.5789(7)	0.5/0.5	1.4[b]

[a] Site occupation factor.
[b] Fixed to the results from neutron diffraction, ref. 14.
[c] Not refined independently.

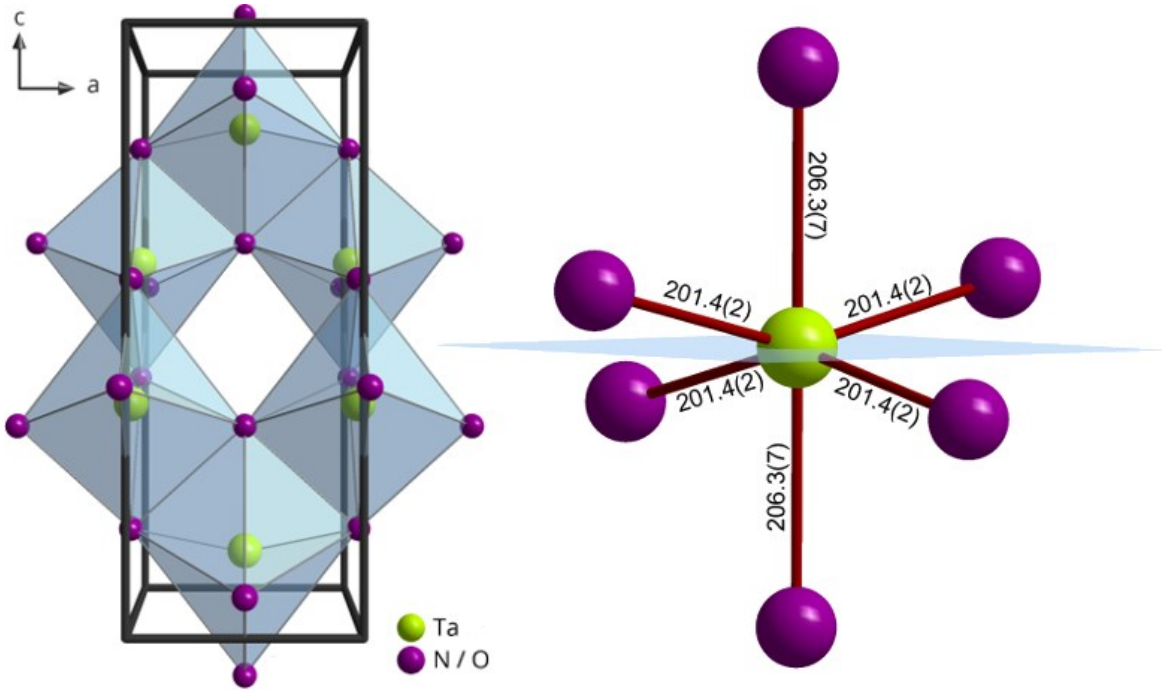

Figure 4.4. Crystal structure of anatase-type TaON. Left: unit cell with coordination octahedra. Right: Ta–O/N bond lengths in pm.*

Figure 4.4 depicts the crystal structure of anatase-type TaON with the above-mentioned aristotype setting with just one kind of anion position. The calculated bond lengths of the octahedra are also presented in Figure 4.4 and are in good agreement with the ionic radii expected from the corresponding ions[40] and that of $Mg_{0.05}Ta_{0.95}O_{1.15}N_{0.85}$.[14] Possible anion arrangements have already been studied theoretically on a quantum-chemical level[13] and experimentally using $Mg_{0.05}Ta_{0.95}O_{1.15}N_{0.85}$[14,41] with consistent results. There are three maximal non-isomorphic subgroups (all *translationengleich*) providing two nonequivalent anion sites: $I\bar{4}m2$ (No. 119), $I4_1md$ (No. 109), and *Imma* (No. 74). It was shown that space group $I4_1md$ is the most preferred for tantalum oxide nitrides with anatase-type structure. Unfortunately, the amount of material (*ca.* 100 mg) is hitherto not sufficient for a neutron diffraction investigation which is the method of choice for the experimental determination of the N/O distribution. Larger amounts of material and an increase of the fraction of the δ-phase are in the focus of our work in the near future.

The effect of different N/O configurations in the conventional unit cell of δ-TaON has already been investigated using periodic quantum-chemical calculations.[13] Since we used different density functionals in this work, we nevertheless performed structure re-

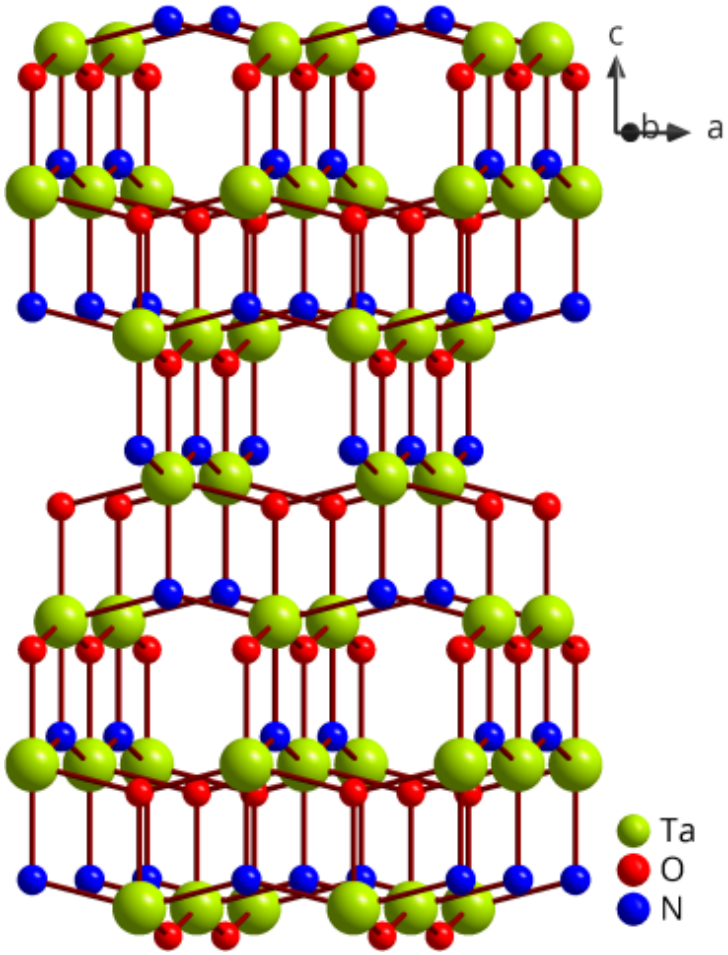

Figure 4.5.
Supercell of δ-TaON with the most stable N/O distribution.*

laxations at the GGA (PBE) and DFT-HF hybrid (PBE0) level for different distributions of N and O atoms over the 8*e* Wyckoff position. With both functionals, almost identical results were obtained that confirm the previously found structure. In the most stable configuration, N–Ta–N and O–Ta–O chains in *a* or *b* direction alter along the *c* direction (see Figure 4.5). This crystal structure can be described in the space group $I4_1md$ (No. 109) with all atoms residing on the Wyckoff position 4*a* (VASP/PBE: Ta: 0,0,0.5; O: 0,0,0.299; N: 0,0,0.701).

The relative stability of the different anatase-type phases with respect to each other is linked to the N–N distance. In the most stable phase with $I4_1md$ symmetry, two N^{3-} ions are separated by at least 323 pm. In all other configurations under consideration the smallest N–N distance was reduced by more than 8% compared to this value, which leads to energy differences up to 24 kJ·mol^{-1} per TaON formula unit due to the larger Coulomb repulsion between the N^{3-} anions. Nevertheless a large number of anion configurations were higher in energy by only 5–10 kJ·mol^{-1} and might thus be accessible at the

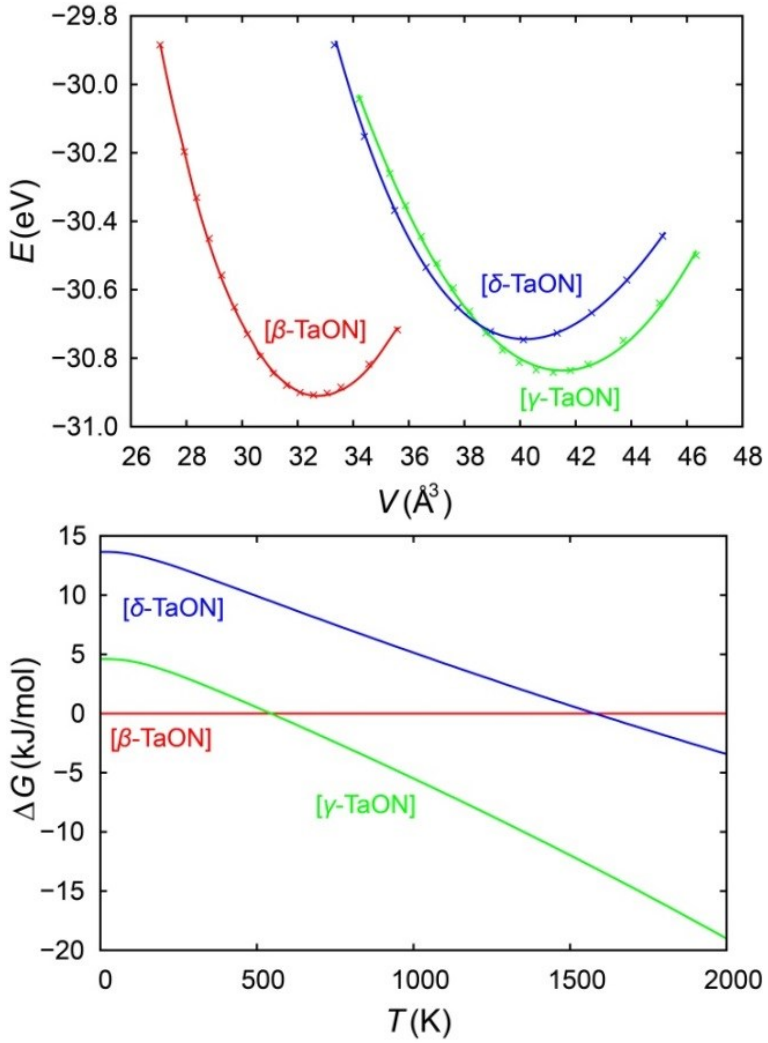

Figure 4.6.
Energy per formula unit versus volume of the three known phases of TaON at ambient pressure (top), and relative Gibbs energy versus temperature for the different TaON phases (VASP/PBE) (bottom).

applied conditions during the synthesis. The theoretical Ta–O/N bond lengths differ from the experimentally assigned values as the octahedral coordination is more strongly distorted due to the reduced symmetry. At the PBE0 level we found a single short Ta–N (d = 195 pm) and two Ta–O bond lengths (d = 197 pm), two N atoms (d = 205 pm) at intermediate distances, and one O atom with a greater displacement (d = 232 pm). The slightly shorter Ta–N bond lengths as compared to Ta–O nicely reflect the larger covalency in the Ta–N combination, as also found in other studies.[42]

In order to compare δ-TaON with the well-known β- and γ-phases, the energy per formula unit was plotted against the cell volume (Figure 4.6, VASP/PBE). Anatase-type TaON is energetically less favored than the thermodynamically stable baddeleyite-type by about 0.18 eV whereas the VO_2(B)-type is less stable by only 0.07 eV.

From the constant volume optimizations, we calculated the bulk moduli for the three phases from the Birch–Murnaghan equation of state. The value for β-TaON (B^{PBE} = 259 GPa, B^{PBE0} = 286 GPa) is in good agreement with the results from earlier theoretical work (G^{LDA} = 280 GPa,[43] B^{PW91} = 278 GPa[44]), whereas the previously calculated bulk modulus for the more open γ-TaON ($B^{\mathrm{VASP\text{-}PBE}}$ = 181 GPa) is less well-reproduced using atom-centered basis functions (B^{PBE} = 210 GPa, B^{PBE0} = 227 GPa). For δ-TaON we find a lower value compared to the other TaON phases (B^{PBE} = 186 GPa, B^{PBE0} = 216 GPa).

Metastable polymorphs, according to the Ostwald–Volmer rule, are usually characterized by low densities and transform to stable modifications at elevated temperatures.[45] These empirical findings are apparent in Figure 4.6 where δ-TaON phase has a larger volume per formula unit than β-TaON. At the same time, γ-TaON which is more stable than the δ-phase has a slightly smaller density [C09/PBE0: ρ(γ-TaON) = 8.6 g·cm^{-3}, ρ(δ-TaON) = 8.9 g·cm^{-3}]. Both values are in good agreement with the experimental results [ρ(γ-TaON) = 8.6 g·cm^{-3}, ρ(δ-TaON) = 9.0 g·cm^{-3}].

In air, all nitrogen-containing phases reacted to tantalum oxide at 773 K. In contrast, in nitrogen atmosphere anatase-type TaON undergoes a phase transition between 1073 and 1123 K to the baddeleyite-type β-TaON with a density of 11.0 g·cm^{-3}. This phase is preserved after cooling to room temperature, indicating an irreversible phase transformation. No formation of γ-TaON was observed during these experiments.

The calculated relative Gibbs energies as a function of the temperature (Figure 4.6, right, VASP/PBE results) clearly show that δ-TaON is thermodynamically unstable up to about 1600 K, and a phase transition to β-TaON should occur at lower temperatures. Experimentally, however, the δ to β phase transition is found between 1073 and 1123 K although ΔG is then much smaller compared to room temperature. Hence, kinetics is controlling the transition from δ to β.

In order to investigate the dynamic stability of δ-TaON we calculated the phonon density of states (PDOS) at ambient pressure. As can be seen in Figure 4.7 the PDOS does not exhibit any imaginary modes. Hence, the dynamic stability of the phase is assured, and anatase-type TaON is classified as a metastable solid-state material.

For the calculation of absolute band positions with respect to the vacuum, it is necessary to perform two-dimensional calculations of the TaON surface in order to circumvent the self-interaction problem in the Ewald summation. Therefore, several low-index surfaces have been investigated by performing periodic slab calculations (C09/PBE0)

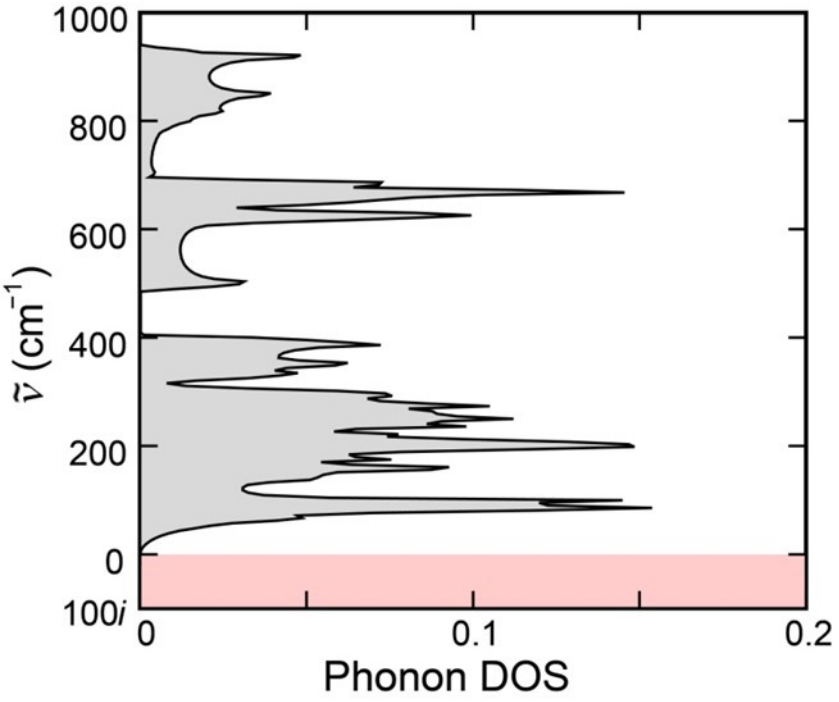

Figure 4.7. Phonon density of states of δ-TaON at ambient pressure calculated *via* density-functional theory.

which are treated as truly two-dimensional systems in CRYSTAL. By calculating the surface energies E_S it was found that the (100) surface is most stable ($E_S^{PBE} = 1.1$ J·m^{-2}, $E_S^{PBE0} = 1.2$ J·m^{-2}). The surface energies were converged for slab models consisting of eight or more stoichiometric layers. In order to obtain a value for the optical gap, we first calculated the quasiparticle gap using the GW0 approach for the δ-TaON bulk system (VASP/PBE). After five iterations where only the single particle Green's function was updated whereas the Coulomb interaction was kept fixed, we obtained a value of $E_g = 3.2$ eV for the quasiparticle gap which agrees very well with the PBE0 result for the bulk. The subsequent BSE calculation gave an excitation energy for the first optical transition of 2.7 eV which is in good agreement with the experimentally determined value for thin films of anatase-type TaON (2.4 eV).

To predict the applicability of δ-TaON as a photocatalyst in redox reactions it is necessary to determine whether tabulated redox potentials lie in between the material's valence and conduction band edges.[32] Therefore, we calculated the absolute values for the valence band maximum (VBM) and the conduction band minimum (CBM) according to

$$E_{VBM} = E_{VBM}^{(100)} - \tfrac{1}{2} E_g^{BSE}; \quad E_{CBM} = E_{BGC}^{(100)} + \tfrac{1}{2} E_g^{BSE} \tag{4.1}$$

Here E_g^{BSE} is the optical band gap in contrast to ref. 32 where the quasiparticle gap was used. This way we obtained the band edge energies $E_{VBM} = -6.6$ eV and $E_{CBM} = -3.9$ eV with respect to the vacuum level. Thus, in a photocatalytical setup δ-TaON can possibly support redox reactions like the H_2O/O_2 couple ($E = -5.7$ eV, $pH = 0$) that have potentials in this range.

4.5 Conclusions

We were successful in synthesizing a new polymorph of tantalum oxide nitride with anatase-type structure by an ammonolysis reaction. The measured density is higher than the one of the thermodynamically more stable γ-TaON phase exhibiting the VO_2(B) structure. δ-TaON is metastable and undergoes a phase transformation to baddeleyite-type β-TaON between 1073 and 1123 K. The absolute band edge positions were calculated by combining the results from periodic slab calculations with the lowest optical excitation energy for the bulk crystal, obtained with the BSE method. The resulting band edge energies ($E_{VBM} = -6.6$ eV, $E_{CBM} = -3.9$ eV) indicate that δ-TaON is a promising photocatalytic material for redox reactions, *e.g.*, water splitting. With the enormous interest in tantalum oxide nitride phases for solar fuel production *via* photo- or photoelectrochemical water splitting, additional work to prepare a phase-pure material is planned. Moreover, also the synthesis of a rutile-type metastable TaON phase, which is calculated to be at most 13 kJ·mol^{-1} (C09/PBE0, $T = 0$ K) less stable than the here presented anatase-type phase, is ongoing work.

4.6 Acknowledgements

This work is supported by the German Science Foundation (DFG) within the priority programs SPP 1415 (T. L., N. B., C. R., T. B., R. D., M. L.) and SPP 1613 (A. F., M. L.). XRF analysis by Rafael Zubrzycki and N/O analysis by Brigitte Hahn are gratefully acknowledged. The authors thank Dr. Dennis Wiedemann for compiling the CIF file. Access to the TEM facilities at the ZELMI (TUB) and equipment funding by the DFG Excellenz Cluster UniCat are gratefully acknowledged. We appreciate support and provisioning of computational resources by the Paderborn Center for Parallel Computing.

4.7 References

(1) Jansen, M.; Letschert, H. P. *Nature* **2000**, *404*, 980–982.

(2) Aguiar, R.; Logvinovich, D.; Weidenkaff, A.; Rachel, A.; Reller, A.; Ebbinghaus, S. G. *Dyes and Pigments* **2008**, *76*, 70–75.

(3) Lerch, M.; Lerch, J.; Hock, R.; Wrba, J. *J. Solid State Chem.* **1997**, *128*, 282–288.

(4) Hitoki, G.; Takata, G.; Kondo, J. N.; Hara, M.; Kobayashi, H.; Domen, K. *Chem. Commun.* **2002**, *16*, 1698–1699.

(5) Hara, M.; Hitoki, G.; Takata, T.; Kondo, J. N.; Kobayashi, H., Domen, K. *Catalysis Today* **2003**, *78*, 555–560.

(6) Brauer, G.; Weidlein, J. R. *Angew. Chem. Int. Ed.* **1965**, *4*, 875–875.

(7) Schilling, H.; Stork, A.; Irran, E.; Wolff, H.; Bredow, T.; Dronskowski, R.; Lerch, M. *Angew. Chem. Int. Ed.* **2007**, *46*, 2931–2934.

(8) Buslaev, Yu. A.; Safronov, G. M.; Pakhomov, V. I.; Glushkova, M. A.; Repko, V. P.; Ershova, M. M.; Zhukov, A. N.; Zhdanova, T. A. *Neorg. Mat.* **1969**, 5, 45-48; *Neorg. Mat., Int. Ed. Engl.* **1969**, *5*, 37–39.

(9) Lumey, M.-W.; Dronskowski, R. *Z. Anorg. Allg. Chem.* **2003**, *629*, 2173–2179.

(10) Lumey, M.-W.; Dronskowski, R. *Z. Anorg. Allg. Chem.* **2005**, *631*, 887–893.

(11) Lowther, J. E. *J. Phys. Rev. B* **2005**, *72*, 172105-1–4.

(12) Woodhead, K.; Pascarelli, S.; Hector, A. L.; Briggs, R.; Alderman, N.; McMillan, P. F., *Dalton Trans.* **2014**, *43*, 9647–9654.

(13) Bredow, T.; Lumey, M.-W.; Dronskowski, R.; Schilling, H.; Pickardt, J.; Lerch, M. *Z. Anorg. Allg. Chem.* **2006**, *632*, 1157–1162.

(14) Schilling, H.; Lerch, M.; Börger, A.; Becker, K.-D.; Wolff, H.; Dronskowski, R.; Bredow, T.; Tovar, M.; Baehtz, C. *J. Solid State Chem.* **2006**, *179*, 2416–2425.

(15) Stork, A.; Schilling, H.; Wessel, C.; Wolff, H.; Börger, A.; Baehtz, C.; Becker, K.-D.; Dronskowski, R.; Lerch, M. *J. Solid State Chem.* **2010**, *183*, 2051–2058.

(16) Suzuki, A.; Hirose, Y.; Oka, D.; Nakao, S.; Fukumura, T.; Ishii, S.; Sasa, K.; Matsuzaki, H.; Hasegawa, T. *Chem. Mater.* **2014**, *26 (2)*, 976–981.

(17) Okubo, T.; Kakihana, M. *Journal of Alloys and Compounds* **1997**, *256*, 151–154.

(18) Rodriguez-Carvajal, J. *Abstracts of the Satellite Meeting on Powder Diffraction of the XV Congress of the IUCr* **1990**, 127.

(19) (a) Kresse, G.; Hafner, J. *Phys. Rev. B* **1993**, 47, 558–561. (b) Kresse, G.; Hafner, J. *Phys. Rev. B*, **1994**, *49*, 14251–14269.

(20) (a) Kresse, G.; Furthmüller, J. *Comput. Mater. Sci.* **1996**, *6* (1), 15–50. (b) Kresse, G.; Furthmüller, J. *Phys. Rev. B* **1996**, *54*, 11169–11186.

(21) Blöchl, P. E. *Phys. Rev. B* **1994**, *50* (24), 17953–17979.

(22) Perdew, J. P.; Burke, K.; Ernzerhof, M. *Phys. Rev. Lett.* **1996**, *77* (7), 3865–3868.

(23) Togo, A.; Oba, F.; Tanaka, I. *Phys. Rev. B* **2008**, *78* (13), 134106-1–9.

(24) Stoffel, R. P.; Wessel, C.; Lumey, M.-W.; Dronskowski, R. *Angew. Chem. Int. Ed.* **2010**, *49* (31), 5242–5266.

(25) Birch, F. *Phys. Rev.* **1947**, *71* (11), 809–824.

(26) Adamo, C.; Barone, V. *J. Chem. Phys.* **1999**, *110*, 6158–6170.

(27) Dovesi, R.; Saunders, V. R.; Roetti, R.; Orlando, R.; Zicovich-Wilson, C. M.; Pascale, F.; Civalleri, B.; Doll, K.; Harrison, N. M.; Bush, I. J.; D'Arco, P.; Llunell, M. *CRYSTAL09 (CRYSTAL09 User's Manual)*, University of Torino, Torino, 2009.

(28) Andrae, D.; Häußermann, U.; Dolg, M.; Stoll, H.; Preuss, H. *Theor. Chim. Acta* **1990**, *77*, 123–141.

(29) Pascale, F.; Zicovich-Wilson, C. M.; Lopez, F.; Civalleri, B.; Orlando, R.; Dovesi, R. *J. Comput. Chem.* **2004,** *25*, 888–897.

(30) Zicovich-Wilson, C. M.; Pascale, F.; Roetti, C.; Saunders, V. R.; Orlando, R.; Dovesi, R. *J. Comput. Chem.* **2004**, *25*, 1873–1881.

(31) Baerends, E. J.; Gritsenko, O. V.; van Meer, R. *Phys. Chem. Chem. Phys.* **2013**, *15*, 16408–16425.

(32) Caspary Toroker, M.; Kanan, D. K.; Alidoust, N.; Isseroff, L. Y.; Liao, P.; Carter, E. A. *Phys. Chem. Chem. Phys.* **2011**, *13*, 16644–16654.

(33) Perdew, J. P., Levy, M. *Phys. Rev. Lett.* **1983**, *51*, 1884–1887.

(34) Ramos, L. E.; Paier, J.; Kresse, G.; Bechstedt, F. *Phys. Rev. B.* **2008**, *78*, 195423-1–9.

(35) Shannon, R. D.; Prewitt, C. T. *Acta Crystallogr. Sect. B* **1969**, *25* (5), 925–946.

(36) Wolff, H.; Lerch, M.; Schilling, H.; Bähtz, C.; Dronskowski, R. *J. Solid State Chem.* **2008**, *181*, 2684–2689.

(37) Wolff, H.; Dronskowski, R. *J. Comput. Chem.* **2008**, *29*, 2260–2267.

(38) Lowther, J. E. *Phys. Rev. B* **2006**, *73*, 134110-1–8.

(39) Fang, C. M.; Orhan, E.; de Wijs, G. A.; Hintzen, H. T.; de Groot, R. A.; Marchand, R.; Saillard, J.-Y.; de With, G. *J. Mater. Chem.* **2001**, *11*, 1248–1252.

(40) Hollemann, A. F.; Wiberg, N. *Lehrbuch der anorganischen Chemie*, 102th ed., de Gruyter, Berlin, 2007.

(41) Shishkin, M.; Kresse, G. *Phys. Rev. B* **2006**, *74*, 035101-1–13.

(42) Shishkin, M.; Kresse, G. *Phys. Rev. B* **2007**, *75*, 235102-1–9.

(43) Fuchs, F.; Furthmüller, J.; Bechstedt, F.; Shishkin, M.; Kresse, G. *Phys. Rev. B* **2007**, *76*, 115109-1–8.

(44) Shishkin, M.; Marsman, M.; Kresse, G. *Phys. Rev. Lett.* **2007**, *99*, 246403-1–4.

4.8 Supporting Information

Table 4.3. Gaussian-type basis sets for Ta, O, and N.

Element	Shell type	Exponent	Coefficient
Ta (SD60MWB)	5s	13.92894522	-0.65530133
		11.99334000	0.99999851
		5.13783577	-0.75340391
	6s	0.81369698	1.00000000
	7s	0.20617834	1.00000000
	5p	7.39668050	0.58299598
		5.71622490	-0.99750066
	6p	1.11480608	0.53922059
		0.48684871	0.43278257
	7p	0.20000020	1.00000000
	5d	3.89501783	-0.07125693
		1.54623255	0.18750222
		0.78972687	0.33933435
		0.39161871	0.46423064
	6d	0.20001481	1.00000000
	4f	0.69700000	1.00000000
O	1s	17236.81829238	0.00074182
		2751.75465497	0.00535982
		644.13976274	0.02693106
		186.54606980	0.10368114
		62.05370174	0.30631113
		22.40522705	0.63919506
		8.63211071	0.69861249
		3.43665812	0.23444923
	2s	31.23086387	-0.03031382
		8.75022651	-0.16427606
		0.99708039	0.97908082
	3s	0.29679220	1.00000000
	2p	37.97017643	0.01498951
		8.81023497	0.09235816
		2.57513767	0.29875716
		0.80224337	0.49916591
	3p	0.23077580	1.00000000

Element	Shell type	Exponent	Coefficient
O	3d	0.28447631	1.00000000
N	1s	19610.14142999	0.00067103
		2918.28119664	0.00524937
		662.82669961	0.02721870
		188.48972830	0.10851369
		61.86476194	0.33759047
		22.40189484	0.75710716
		8.70806179	1.04888702
		3.43054032	0.59027045
	2s	19.83643370	0.75107092
		5.74154083	3.14684949
		0.85051883	-14.22933913
	3s	0.26704755	1.00000000
	2p	40.95912588	0.01123324
		9.12783302	0.08265355
		2.53467765	0.31399797
		0.78249957	0.62944112
	3p	0.20016341	1.00000000
	3d	0.51431751	1.00000000

5 Publication 2

Synthesis and Characterization of Metastable Transition Metal Oxides and Oxide Nitrides

Tobias Lüdtke, Dominik Weber, Alexander Schmidt, Alexander Müller,
Christoph Reimann, Nils Becker, Thomas Bredow,
Richard Dronskowski, Thorsten Ressler, Martin Lerch

Postprint
Zeitschrift für Kristallographie - Crystalline Materials **2017**, *232*(1–3), 3–14
DOI: 10.1515/zkri-2016-1961
https://www.degruyter.com/view/j/zkri.2017.232.issue-1-3/
zkri-2016-1961/zkri-2016-1961.xml

Contribution to publication:

T. Lüdtke:	Sample preparation (δ-TaON), characterization, writing.
D. Weber:	Sample preparation (V_2O_3, γ-TaON), characterization.
A. Schmidt:	Sample preparation (γ-TaON).
A. Müller:	Catalytic measurements and interpretation.
C. Reimann:	Quantum-chemical calculations.
N. Becker	Quantum-chemical calculations.
T. Bredow:	General discussion, proofreading, writing (quantum-chemical calculations).
R. Dronskowski:	General discussion, proofreading.
T. Ressler:	General discussion, proofreading, writing (catalysis).
M. Lerch:	General discussion, proofreading.

Overall contribution of T. Lüdtke to the publication: 50%

Authors. Tobias Lüdtke,[a] Dominik Weber,[a] Alexander Schmidt,[a] Alexander Müller,[a] Christoph Reimann,[b] Nils Becker,[c] Thomas Bredow,[b] Richard Dronskowski,[c] Thorsten Ressler,[a] Martin Lerch [a,*]

(a) Institut für Chemie, Technische Universität Berlin, Straße des 17. Juni 135, D-10623 Berlin, Germany
(b) Mulliken Center for Theoretical Chemistry, Institut für Physikalische und Theoretische Chemie, University of Bonn, Beringstraße 4, D-53115 Bonn, Germany
(c) Chair of Solid-State and Quantum Chemistry, Institute of Inorganic Chemistry, RWTH Aachen University, Landoltweg 1, D-52056 Aachen, Germany

* Corresponding author

Keywords. Metastable compounds; Solid state chemistry.

Received: 24.05.2016
Accepted: 25.06.2016
Published online: 21.07.2016

5.1 Abstract

New routes to vanadium sesquioxide and tantalum oxide nitride (γ- and δ-phase) are presented. Phase pure V_2O_3 with bixbyite-type structure, a metastable polymorph, was obtained from vanadium fluoride hydrates at *ca.* 750 K. It crystallizes in the cubic crystal system in space group $Ia\bar{3}$ with lattice parameter $a = 939.30(5)$ pm. The catalytical properties of the corresponding oxide nitride phases and their oxidation and reduction solid-state kinetics were investigated. The preparation of γ-TaON as a phase pure sample can be realized by ammonolysis of X-ray amorphous tantalum oxide precursors at 1073 K. This metastable tantalum oxide nitride crystallizes in the monoclinic VO_2(B)-type structure in space group $C2/m$. The same precursors can be used to synthesize the δ-modification with an anatase-type structure at 1023 K. It crystallizes in the tetragonal crystal system in space group $I4_1/amd$. A maximum yield of 82 wt % could be obtained. The fundamental band gaps of the synthesized and of other metastable TaON polymorphs were calculated from first principles using the GW method. The present results are compared to experimental data and to previous calculations at hybrid DFT level.

5.2 Introduction

The physical properties of solids strongly depend on the arrangement of the atoms. For a deeper understanding of the correlations between crystal structure and physical properties investigations using simple compounds such as binary oxides or ternary oxide nitrides are most promising. In particular the syntheses of metastable polymorphs of such compounds pave the way to deeper insights into these nexuses. In the frame of the 'priority program' SPP 1415, funded by the German Science Foundation (DFG), synthesis routes to novel polymorphs of vanadium sesquioxide and tantalum oxide nitride were developed, backed by quantum-chemical calculations. In most cases it is very difficult to obtain phase pure materials important for an unambiguous interpretation of the data from the properties measurements. During the last years we published on synthesis and characterization of four new metastable phases: bixbyite-type V_2O_3,[1] anosovite-type V_3O_5,[2] VO_2(B)-type TaON,[3] and anatase-type TaON.[4] Unfortunately, only anosovite-type V_3O_5 can be synthesized as single phase.[2] All other samples contained large amounts of side phases leading to severe problems concerning the investigation of physical properties. However, the crystal structures could be determined,

also in combination with quantum-chemical methods.[1–4] Recently, we optimized the preparation techniques and in this contribution we present simple routes to phase pure bixbyite-type V_2O_3 and VO_2(B)-type TaON (γ-TaON).[5] The phase purity of anatase-type TaON (δ-TaON) is now increased from 42 wt % to 82 wt %. Moreover, structure-property relationships were studied with respect to selective oxidation of light alkenes. Mixed oxide catalysts containing, for instance, vanadium or molybdenum, are active heterogeneous oxidation catalysts. Bixbyite-type oxide nitrides and corundum-type V_2O_3 were used as model catalysts for selective oxidation of propene. Therefore, oxidation of the materials was studied time-resolved under oxidation reaction conditions. Solid-state kinetics were evaluated by model-dependent and model-independent methods and the results correlated to structural and compositional properties.

Transition metal oxides and oxide nitrides are considered as interesting materials for photocatalyis. The photocatalytic activity of the solid compounds is to a large extent determined by their fundamental and optical band gaps. Their experimental determination is not in all cases possible, in particular if the synthesized materials are not phase-pure. In this case theoretical calculations of band gaps have proven to be an indispensable tool to analyse the electronic structure of solid compounds. Furthermore, quantum-chemical methods allow predictions of structural, thermodynamic and electronic properties for metastable phases that have not yet been synthesized. In previous studies[4,6,7] we have calculated fundamental band gaps of TaON polymorphs with hybrid functionals in order to account for the self-interaction error of standard density-functional theory (DFT) using the semilocal generalized gradient approximation (GGA). The advantages and limitations of hybrid functionals for the study of the electronic properties of solid catalysts have been discussed recently.[8] In principle they are semi-empirical methods because the amount of Hartree–Fock exchange that is used in the exchange functional is not strictly determined from first principles. Additionally, the interpretation of Kohn–Sham single-particle energies as ionization potentials and electron affinities has been questioned.[9] A nonempirical and physically correct description of fundamental band gaps is provided by the GW methodology which combines a Green function approach with a screened Coulomb potential (W) to calculate the quasi-particle energies. Polarization effects in the environment of holes and electrons are taken into account. It has been shown that the GW method provides an accurate description of band gaps for a large variety of solids.[10] Several approximations of GW theory exist, *e.g.* non-self-consistent G0W0, GW0, or self-consistent GW. In the present study we apply the plasmon-pole approximation to GW as implemented in the

GPAW program[11–13] to calculate the fundamental band gaps of those TaON polymorphs that have been studied here and in our previous works.

5.3 Experimental Section

X-ray diffraction. A PANalytical X'Pert MPD Pro (Cu-K_α radiation) and a Siemens D5000 (Cu-$K_{\alpha1}$ radiation) powder diffractometer were used for XRD measurements at room temperature. Rietveld refinements including quantitative phase analyses were carried out using the program FULLPROF 2000.[14,15] Profiles were fitted with a pseudo-Voigt function.

In situ XRD experiments were carried out in a θ-θ scattering geometry on a STOE diffractometer equipped with a PAAR reaction chamber using Cu-K_α radiation (40 kV, 40 mA). Isothermal experiments were performed from 613 K through 653 K. Prior to isothermal measurements under reaction conditions the samples was heated to the corresponding temperature in helium (25 ml·min^{-1}). Subsequently, flow conditions were changed to 25 ml·min^{-1} propene (10 vol % propene in helium) and 2.5 ml·min^{-1} oxygen. The gas-phase composition at the *in situ* cell outlet was analyzed online with a mass spectrometer (Pfeifer Omnistar). The VO_2(R) (110) main peak was measured between 26.6° and 28.8° (2θ) in steps of 0.012° (2θ) and at a sampling time of 9 s·step^{-1}. For a solid-state kinetic analysis, the program package WINXAS v3.2[16] was used. Quantitative analysis of the phase composition was performed with the Rietveld program package FULLPROF 2000.[14,15]

X-ray absorption spectroscopy. *In situ* transmission X-ray absorption spectroscopy (XAS) was measured at the V *K* edge (5.465 keV, Si(111), beam line C, measuring time *ca.* 3.5 min/scan), at the Hamburg Synchrotron Radiation Laboratory, HASYLAB. *In situ* XAS measurements were performed in an *in situ* measuring cell. Samples were mixed with boron nitride (Alfa Aesar, 99.5%) and pressed to a self-stabilized 5 mm diameter pallet.[17] The sample mass was calculated to obtain an edge jump of $\Delta\mu(d) \approx 0.4$.[17] XAS data analysis was performed using the software WINXAS v3.2.[16]

Elemental analyses. The contents of nitrogen and oxygen were determined by hot gas extraction using a LECO TC-300/EF-300 N/O analyzer. ZrO_2 and steel were used as

standard materials. The accuracy is ~2% of the N/O contents present. Hydrogen and carbon contents were measured using a Thermo Fisher Scientific Flash EA1112, which can also detect nitrogen and sulfur (CHNS-analysis).

Quantum-chemical calculations. The fundamental band gaps of TaON polymorphs were calculated with GPAW.[8] The Kohn–Sham wave functions were represented by real-space grids with converged grid size parameters $h = 0.12$-0.15. The Monkhorst–Pack grids were chosen as dense as possible within the limits of the computational resources. For example the irreducible Brillouin zone of γ-TaON was sampled with a $2 \times 6 \times 4$ grid. PBE wavefunctions were used as basis for GW quasi-particle energy calculations. The plasmon-pole GW approximation was applied in order to reduce the computational effort. A cut-off energy of 400 eV was used which gave converged results for the band gaps within 0.05 eV. The number of bands was restricted to twice the number of occupied bands again due to limitations of computer resources. Test calculations for selected compounds showed only small changes <0.1 eV if the number of bands was further increased.

5.4 Results and Discussion

5.4.1 Bixbyite-type V_2O_3

Vanadium oxide-based ceramics are used versatile. Possible application areas are, for example, catalysis,[18,19] chemical sensors,[20] batteries,[21] and optical and electric devices.[22] At ambient conditions, vanadium sesquioxide usually crystallizes in the rhombohedral corundum-type structure.[23] At 170 K, it shows a so called Mott–Hubbard transition [24,25] to the monoclinic M1 phase, which is antiferromagnetically ordered and an electric insulator.[26–29] In a previous publication we presented the synthesis of bixbyite-type V_2O_3 with a maximum yield of about 82 wt % with corundum-type V_2O_3 as side phase.[1] In addition, the electronic structure and thermodynamics have already been discussed.[30] Later on, phase pure nanocrystals with a diameter of 5–30 nm were successfully synthesized by Bergerud *et al.*[31] Calculations predict Sc-, Y-, and especially Mg-doped bixbyite-type V_2O_3 to be promising *p*-type semiconductors.[32] With the adjusted synthesis conditions mentioned below we were able to isolate a phase pure sample as a grayish-black powder:[5] $V_2F_6{\cdot}4H_2O$ and $V_2F_6{\cdot}6H_2O$[33] were used as precursors for an optimized

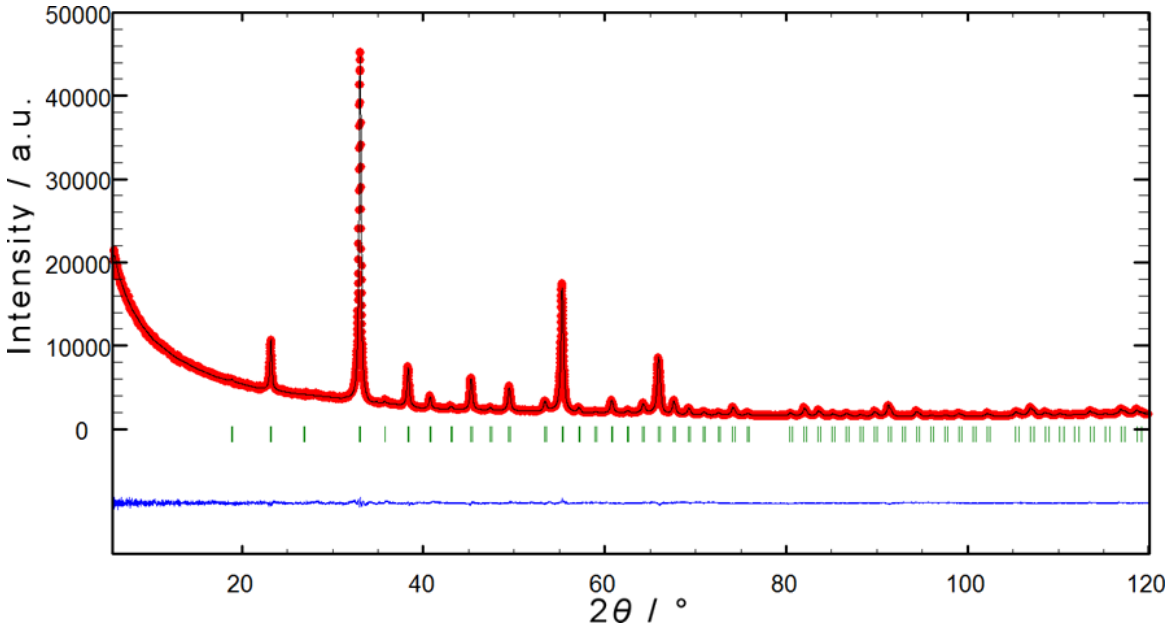

Figure 5.1. X-ray powder diffraction pattern (Cu-K_α radiation) of bixbyite-type V_2O_3 with results of the Rietveld refinement (red: measured; black: calculated; green: Bragg-reflection positions; blue: measured – calculated).*

synthesis. Those metal fluoride hydrates can be obtained by treating vanadium powder with hexafluorosilic acid and heating the mixture to *ca.* 353 K until a dry powder is formed. The new vanadium oxide was prepared in a tube furnace with a corundum tube at temperatures between 748 and 758 K for 2 h with a heating rate of 300 $K \cdot h^{-1}$. A flow rate of 10 $L \cdot h^{-1}$ of the reaction gas (40–60 vol % H_2 in Ar, gas stream piped through a water-filled washing flask) was used. The samples were cooled down in dry argon atmosphere.

The bixbyite-type polymorph of vanadium sesquioxide crystallizes in the cubic space group $Ia\bar{3}$ with the lattice parameter $a = 939.30(5)$ pm. The X-ray diffraction pattern with the results of the Rietveld refinement is shown in Figure 5.1. Details and refined parameters are presented in Table 5.1 and Table 5.2.

Description of crystal structure: vanadium is coordinated by oxygen in two different ways. Both octahedra-derived arrangements with the corresponding V–O-bond lengths are depicted in Figure 5.2 The perfect octahedron around V1 shows bond lengths of 200.8 pm, while for the $(V2)O_6$-polyhedra bond lengths between 197.7 and 210.4 pm (average 203.3 pm) are observed. All these values are in good agreement with the ionic radii of vanadium and oxygen.[34]

Table 5.1. Results of the Rietveld refinement for bixbyite-type V_2O_3.

	V_2O_3
Structure type	Bixbyite
Space group	$Ia\bar{3}$ (No. 206)
Crystal system	Cubic
a / pm	939.30(5)
V / 10^6 pm^3	828.72(7)
Z	16
ρ_{calc} / g·cm^{-3}	4.805
Diffractometer	PANalytical X'Pert MPD Pro
2θ / °	5–120
λ / pm	154.060, 154.443
	$I(\lambda_2)/I(\lambda_1) = 0.5$
Profile points	8845
Refined parameters	47
R_{wp}	0.022
R_{exp}	0.019
R_{Bragg}	0.038
S	1.15

Table 5.2. Refined atomic parameters of bixbyite-type V_2O_3.

Atom	Wyckoff	x	y	z	B_{iso} / 10^4 pm^2
V1	8*a*	0	0	0	0.70(4)
V2	24*d*	0.28174(5)	0	¼	0.77(3)
O	48*e*	0.1422(2)	0.1281(2)	-0.0954(2)	0.77(3)

The ideal bixbyite-type structure can be described as a 2 × 2 × 2 superstructure of the fluorite-type by removing ¼ of the anions. This new unit cell has doubled cell parameters and ordered anion vacancies. One of the remarkable characteristics of this structure type is the possible partially occupation of these vacancies by additional anions leading to compositions with an oxygen excess: A_2X_{3+x}. This is described for the sesquinitride of uranium U_2N_3[35,36] and the corresponding oxide nitrides of zirconium[37] and vanadium.[38] The oxygen content of vanadium sesquioxides prepared by our new route was determined by hot gas extraction: 31.8–32.2 wt %. Taking into account the error range (the accuracy is *ca.* 2% of the N/O contents present), these results are in good agreement with the ideal V_2O_3 composition for the sesquioxide (32.0 wt % oxygen). Calculations on

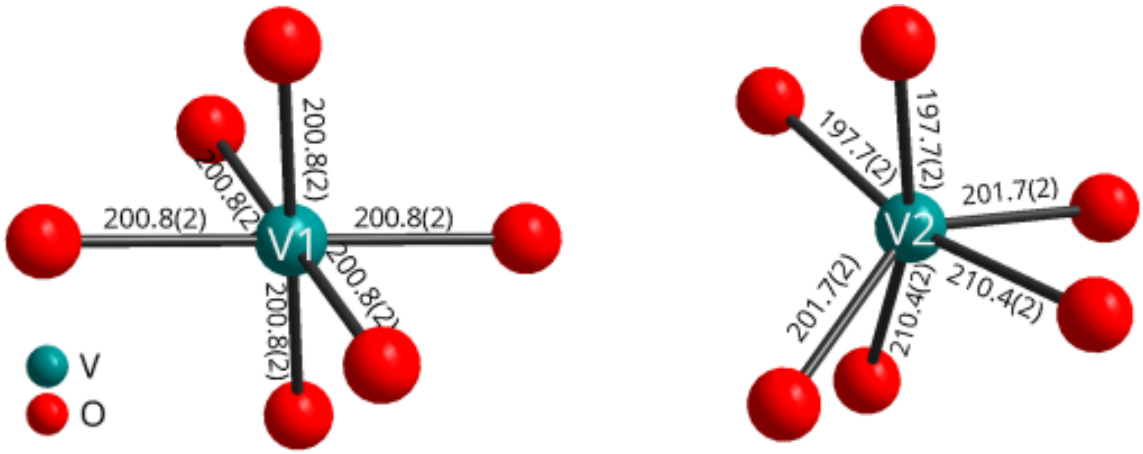

Figure 5.2. Coordination polyhedra of bixbyite-type V_2O_3. Bond lengths are presented in pm.

DFT level show that a formation of nonstoichiometric V_2O_{3+x} phases by incorporation of excess oxygen is possible, depending on the oxygen activity during synthesis.[39] No hydrogen was detectable using combustion analysis. The absence of remaining precursor-fluoride was proved by EDX, WDX, and XFA. The new vanadium oxide is metastable (about 9 $kJ \cdot mol^{-1}$ less stable than the thermodynamically stable polymorph[1] and largely independent from the quantum-mechanical method) and transforms to corundum-type V_2O_3 at *ca.* 823 K in argon atmosphere. An oxidation to V_2O_5 can be observed in air at *ca.* 523 K. At ambient conditions it oxidizes to VO_2 in a period of 3 weeks.

Additionally, the synthesis of phase pure bulk material allows the investigation of the physical properties. Neutron diffraction experiments and the determination of magnetic properties have already been carried out.[5]

Moreover, vanadium oxides are active and selective heterogeneous catalysts for partial oxidation of light alkanes and alkenes with gas-phase oxygen. Structure-function correlations of bixbyite-type vanadium sesquioxide were studied for the heterogeneous selective oxidation of propene to acrolein. Here, bixbyite-type vanadium oxide nitrides were employed permitting an additional variation of electronic and structural properties as a function of nitrogen content. Preparation conditions and materials characterization are described in ref. 38.

Corresponding vanadium oxide nitrides and corundum-type V_2O_3 oxidized under catalytic conditions to rutile-type VO_2. Hence, oxidation behavior under catalytic conditions was investigated by *in situ* X-ray absorption spectroscopy (XAS) measurements at

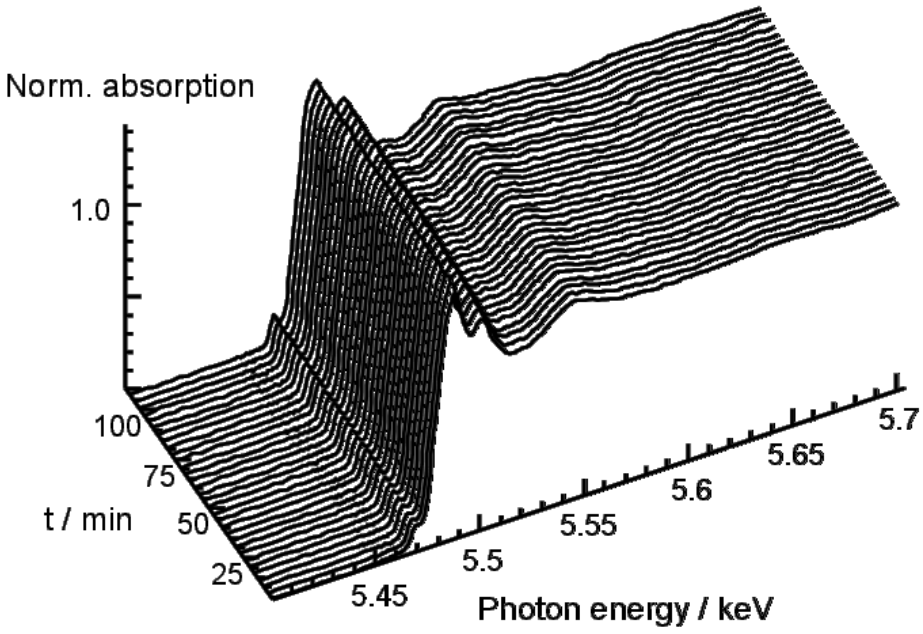

Figure 5.3. *In situ* V *K* edge XANES spectra measured during isothermal treatment of corundum-type V_2O_3 under catalytic conditions (5 vol % propene, 5 vol % oxygen in helium) at 633 K.

the V *K* edge. Evolution of V *K* edge XANES spectra of corundum-type V_2O_3 during isothermal treatment under catalytic conditions at 633 K is shown in Figure 5.3. The distinct XANES features of the various vanadium oxides permitted a quantitative analysis of the evolution of the phase composition during oxidation. Thus, the amount of VO_2(R) was extracted from a linear combination analysis (LCA) using reference spectra of corundum-type V_2O_3 and VO_2(B). Principal component analysis indicated these two references spectra to be sufficient to describe the experimental spectra excluding the formation of significant amounts of crystalline or amorphous intermediates or by-products. This makes the studied oxide nitrides and oxides suitable model systems for investigating solid-state kinetics under reaction conditions.

In situ X-ray diffraction experiments under catalytic condition (5 vol % propene, 5 vol % oxygen in helium) were performed for oxide nitrides with the composition $V_2O_{3.03}N_{0.02}$, $V_2O_{3.08}N_{0.06}$ and $V_2O_{3.04}N_{0.07}$ and for corundum-type V_2O_3. Figure 5.4 shows the oxidation degree α traces for the isothermal treatment of oxide nitride with the composition $V_2O_{3.08}N_{0.06}$ under catalytic conditions (5 vol % propene, 5 vol % oxygen in helium) measured by isothermal *in situ* X-ray diffraction. Isothermal measurements were performed at temperatures of 623 K, 633 K, 643 K, and 653 K. Similar to the oxidation degree α traces of $V_2O_{3.03}N_{0.02}$, the shape of the oxidation degree α traces of $V_2O_{3.08}N_{0.06}$ was characterized by an exponentially limited increase with reaction times. An induction period for the early stage of oxidation was not observed.

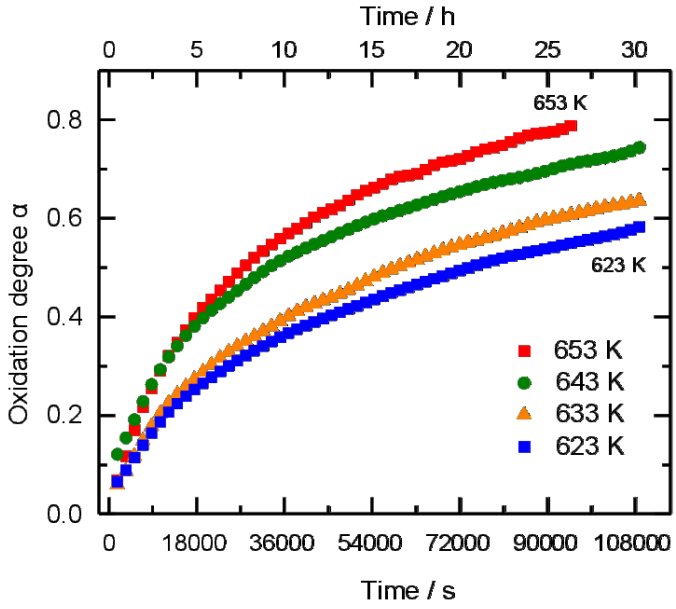

Figure 5.4.
Evolution of oxidation degree during isothermal oxidation as a function of time during isothermal oxidation of oxide nitride with bixbyite structure with the stoichiometry $V_2O_{3.08}N_{0.06}$ in 5 vol % propene, 5 vol % oxygen in helium at 623 K, 633 K, 643 K, and 653 K. Traces were extracted from *in situ* X-ray diffraction measurements.

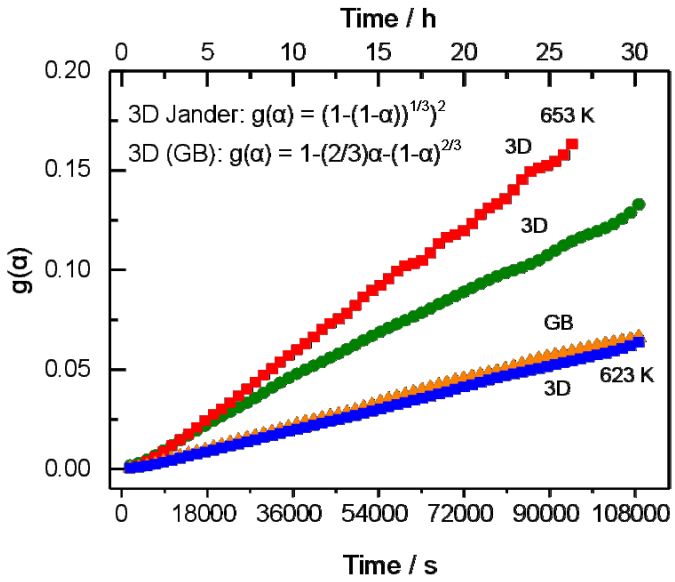

Figure 5.5.
Linearization of oxidation degree *α* traces for isothermal oxidation of $V_2O_{3.08}N_{0.06}$ with bixbyite to VO_2(R) using three-dimensional diffusion models (D3, Jander; D4, Ginstling-Brounshtein). Isothermal measurements were performed under catalytic conditions (5 vol % propene, 5 vol % oxygen in helium) at 623 K, 633 K, 643 K, and 653 K.

Oxidation degree *α* traces were evaluated by several solid-state kinetic reaction models. The model-dependent analysis suggested that oxidation of $V_2O_{3.08}N_{0.06}$ to VO_2(R) under catalytic conditions (5 vol % propene, 5 vol % oxygen in helium) was governed by three-dimensional diffusion. Figure 5.5 shows the linearized oxidation degree *α* traces using the Jander[40] and Ginstling–Brounshtein[41] solid-state reaction models that assume three-dimensional diffusion as rate-determining step. Apparently, the *α* traces can be sufficiently described by a single rate-determining step. Schematically, three-dimensional Jander and Ginstling–Brounshtein diffusion solid-state reaction models assume a spheri-

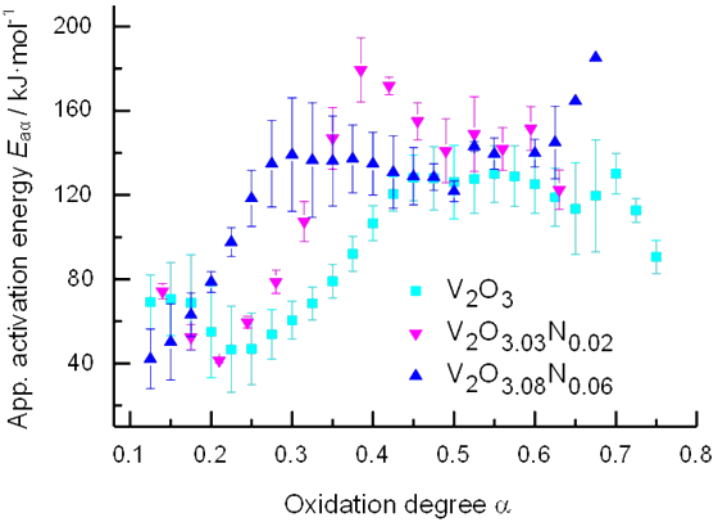

Figure 5.6.
Evolution of apparent activation energies $E_{a\alpha}$ of the rate determining step g(α) for the oxidation of oxide nitrides $V_2O_{3.03}N_{0.02}$, $V_2O_{3.08}N_{0.06}$, and corundum-type V_2O_3 under catalytic conditions (5 vol % propene, 5 vol % oxygen in helium).

cal particle consisting of a V_2O_3 core and a VO_2(R) shell. With ongoing oxidation, the shell is growing until the initial reactant in the core is consumed. The reaction rate is limited by diffusion of O^{2-} species through the product shell to the core-shell interface and conduction of electrons from the interface to the particle surface. Similar results were obtained from a model-dependent kinetic analysis of data measured during isothermal oxidation of $V_2O_{3.08}N_{0.02}$ and corundum-type V_2O_3. Hence, various amounts of nitrogen did not induce a change in the rate determining step g(α) for the oxidation reaction. Apparent activation energies for the rate-determining step in the oxidation of $V_2O_{3.08}N_{0.02}$, $V_2O_{3.08}N_{0.06}$, and corundum-type V_2O_3 amounted to 150 kJ·mol^{-1}, 122 kJ·mol^{-1}, and 87 kJ·mol^{-1}, respectively.

Model-independent (isoconversional) analysis of solid-state kinetic data measured for oxidation of oxide nitrides with bixbyite structure and corundum-type V_2O_3 yielded the evolution of the apparent activation energy with oxidation degree α (Figure 5.6). The obtained traces showed an increase of the apparent activation energy $E_{a\alpha}$ at α values below 0.4. The increase of the apparent activation energy $E_{a\alpha}$ for the oxidation of $V_2O_{3.08}N_{0.06}$ shifted to lower oxidation degree α values compared to $V_2O_{3.03}N_{0.02}$ and corundum-type V_2O_3 (Figure 5.6). In contrast to $V_2O_{3.03}N_{0.02}$ and corundum-type V_2O_3, an initial decrease of the apparent activation energy $E_{a\alpha}$ was not observed for $V_2O_{3.08}N_{0.06}$. The maximum value for the apparent activation energies $E_{a\alpha}$ for both, oxide nitrides and corundum-type V_2O_3, were similar (Figure 5.6). For the oxide nitrides, the apparent activation energy at higher α values agreed well with the results of the model-dependent analysis. Conversely, the lower apparent activation energy obtained for corundum-type V_2O_3 appeared to correspond to an average over the entire α range.

Mechanistically, the increasing apparent activation energy $E_{a\alpha}$ may correspond to the generation of VO_2(R) nuclei in the early stage of oxidation under catalytic conditions. This was followed by a transition into a diffusion-controlled stage according to the three-dimensional diffusion models identified by the model-dependent analysis. With increasing amount of nitrogen in the samples, the change in regimes was shifted to lower α values (Figure 5.6). Apparently, nucleation, formation of a VO_2(R) product layer, and transition into a diffusion-controlled stage were facilitated by incorporation of nitrogen. With respect to catalytic properties and according to the mechanism of selective oxidation of light hydrocarbons on metal oxide catalysts, oxygen vacancies were generated at the surface of the catalysts and subsequently diffused into the bulk during the catalytic cycle. Formation of VO_2(R) during oxidation depended on the density of oxygen vacancies in the bulk of oxide nitrides and corundum-type V_2O_3. For oxide nitrides, the refinement of V *K* edge FT($\chi(k)\cdot k^3$) revealed an increasing V–O disorder parameter σ^2 with an increasing amount of nitrogen. Because σ^2 scales with the density of oxygen vacancies in the solid, this indicated an increased O^{2-} mobility under catalytic conditions. The latter in turn resulted in facilitated oxidation and the observed shift of $E_{a\alpha}$ to lower α values for oxidation of $V_2O_{3.08}N_{0.06}$ compared to $V_2O_{3.03}N_{0.02}$.

5.4.2 VO_2(B)-type γ-TaON

More than 50 years ago, Brauer and Weidlein reported the first tantalum(V) oxide nitride: yellow β-TaON. Crystallizing in the well-known monoclinic baddeleyit-type structure, it is the most stable phase in this system.[42] Reports of a nearly simultaneous discovered α-polymorph[43,44] have been rebutted by quantum-chemical calculations.[45] A high-pressure modification with cotunnite-type structure and 9-fold coordinated cations was predicted independently by two different groups[46,47] and synthesized by Woodhead *et al.*[48] γ-TaON is the first metastable polymorph and was described almost a decade ago by Schilling *et al.*[3] The main side phase in our previous publication was β-Ta_2O_5 and the maximum yield was determined to 85 wt %.[3] Single phase material with hollow urchin-like nanostructures have been analyzed in terms of photocatalytic activity by Wang *et al.*[49] Another preparation method *via* a modified urea route has also been reported by Gao *et al.*[50] Based on the work of Schilling *et al.*,[3] optimized synthesis conditions allow us to obtain a phase pure sample of orange colored γ-TaON *via* a classical ammonolysis reaction.[5]

Amorphous tantalum oxide precursors were prepared *via* a modified Pechini route.[51] Tantalum chloride (99.999%, Sigma-Aldrich) was solved in an ethanol–citric acid solu-

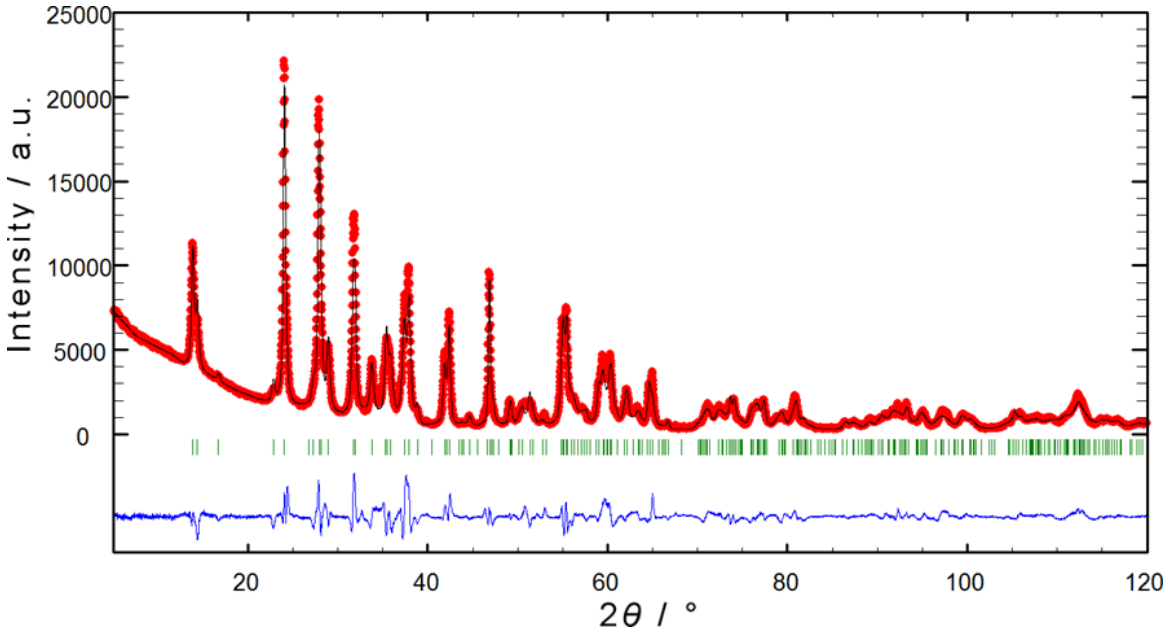

Figure 5.7. X-ray powder diffraction pattern (Cu-$K_{\alpha 1}$ radiation) of γ-TaON with results of the Rietveld refinement. The vertical bars indicate the positions of the Bragg reflections (red: measured; black: calculated; green: Bragg-reflection positions; blue: measured – calculated).*

tion. Citric acid was used in a molar excess of 12 times the $TaCl_5$. Ethylene glycol in a molar excess of 17 times the tantalum chloride was added for the gelling process. The polymerization was finalized by heating the mixture up to 473 K. The material was calcined at 623–773 K until a colorless X-ray amorphous powder was formed. γ-TaON was synthesized by ammonolysis of these amorphous precursors in a SiO_2 tube at 1073 K for 3 h and a heat rate of 400 $K \cdot h^{-1}$. The volume flow rate of NH_3 was 7 $L \cdot h^{-1}$ and of O_2 0.03 $L \cdot h^{-1}$.

It should be mentioned that possible applications of tantalum oxide nitrides are fast ion conductors,[52] the usage as nontoxic color pigments[53] or as anode-materials for photocatalytical water splitting under sunlight.[54] Our optical measurements on the phase pure samples gave an indirect optical band gap of 2.03 eV and a direct band gap of 2.59 eV, respectively.[55] Thus also this material might be a candidate for photocatalytical water splitting. It crystallizes in the monoclinic VO_2(B)-type structure in space group $C2/m$. The X-ray powder diffraction pattern with results of the Rietveld refinement is shown in Figure 5.7. Table 5.3 and Table 5.4 summarize the refined parameters.

Table 5.3. Results of the Rietveld refinement for γ-TaON.

	γ-TaON
Structure type	VO_2(B)
Space group	$C2/m$ (No. 12)
Crystal system	Monoclinic
a / pm	1293.1(2)
b / pm	387.37(5)
c / pm	669.80(10)
β / °	107.442(6)
V / 10^6 pm^3	320.08(8)
Z	8
ρ_{calc} / g·cm^{-3}	8.756
Diffractometer	Siemens D5000
2θ / °	5–120
λ / pm	154.051
Profile points	6144
Refined parameters	66
R_{wp}	0.111
R_{exp}	0.022
R_{Bragg}	0.061
S	5.03

Table 5.4. Refined atomic parameters of γ-TaON.

Atom	Wyckoff	x	y	z	B_{iso} / 10^4 pm^2
Ta1	4i	0.3075(2)	0	0.2027(4)	0.94(7)
Ta2	4i	0.6014(2)	0	0.2052(4)	1.08(7)
O1 (X1)	4i	0.390(2)	0	0.505(4)	0.91[a]
O2 (X2)	4i	0.142(2)	0	0.173(3)	0.91[a]
N1 (X3)	4i	0.456(3)	0	0.127(5)	0.4(5)[b]
N2 (X4)	4i	0.764(3)	0	0.199(5)	0.4(5)[b]

[a] Manually refined parameters.
[b] Not refined independently.

The density of this metastable polymorph (8.756 g·cm^{-3}) is smaller than the density of baddeleyite-type β-TaON (11.02 g·cm^{-3}).[56] According to the Ostwald–Volmer rule, metastable polymorphs are usually characterized by lower densities and transform to

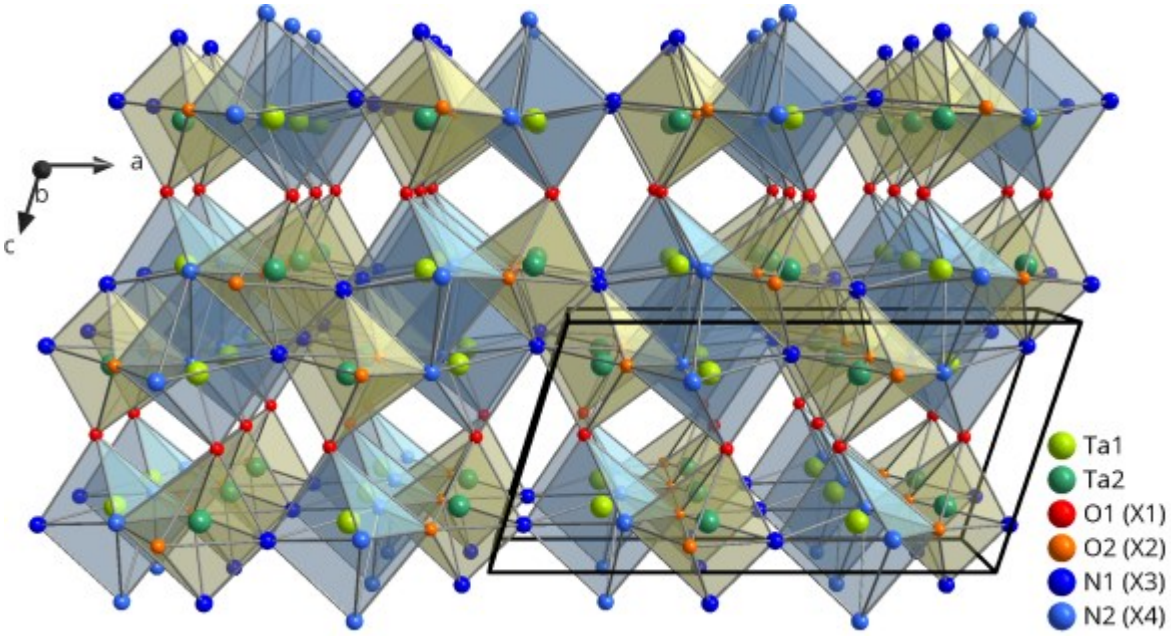

Figure 5.8. Crystal structure with eight unit cells of γ-TaON.*

more stable modifications at increased temperatures.[57] A discrepancy of this rule will be discussed later.

The crystal structure and the Ta coordination polyhedra are depicted in Figure 5.8 and Figure 5.9. Oxygen and nitrogen are occupying four different anion sites, marked as X1 to X4. The corresponding coordination numbers are increasing from 2 for X1 to 3 for X2 and X3 up to 4 for the X4 position. Investigations regarding the precise anion ordering are impossible due to the fact that N and O are not distinguishable in X-ray diffraction experiments. DFT calculations using a large variety of methods not only determined the most probable of the six possible arrangements (oxygen occupying the X1 and X2 positions, nitrogen the other two anion sites X3 and X4)[3,6] but also provided theoretical standard deviations for all structural parameters.

Besides the poor quality of the fit, the presented bond lengths in Figure 5.9 are a further hint for insufficient structural parameters. Ta1 is coordinated by anions with an average distance of 211.2 pm, which is considerably larger than the calculated value based on quantum-chemical calculations (207.4 pm).[6] A better agreement can be found for the Ta2 polyhedron: the average bond length (203.0 pm) is slightly shorter than the calculated length (203.4 pm). Especially the disproportionately large Ta1-N2 bond length of 260.5 pm and the short Ta2-N1 length of 187.3 pm are not reasonable in respect to the corresponding ionic radii of tantalum and nitrogen (sum of radii: 210.0 pm).[34,58]

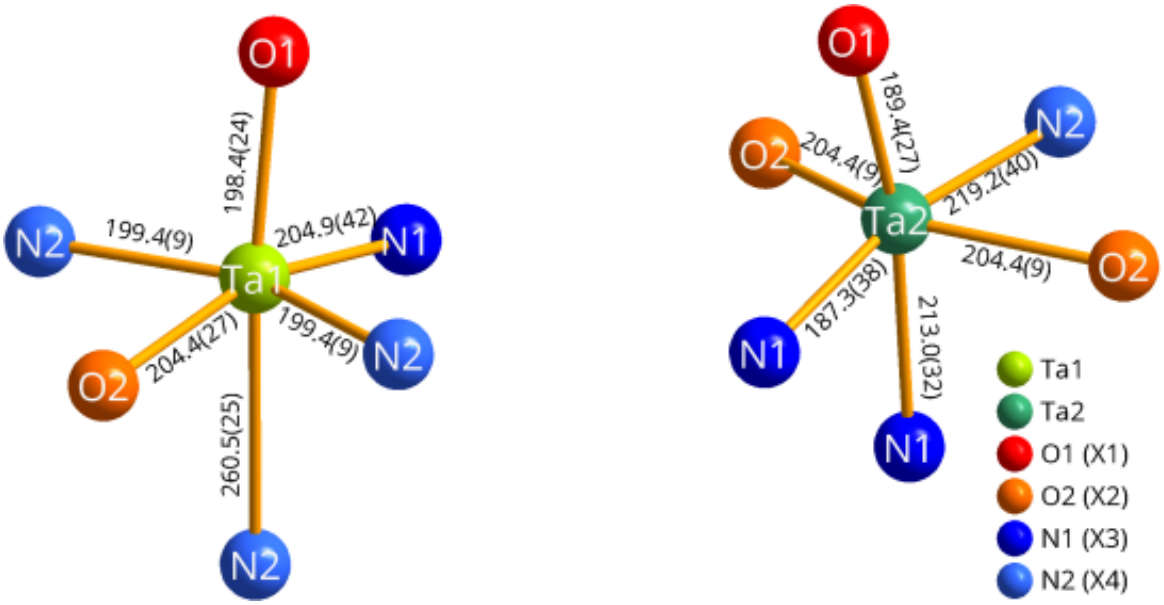

Figure 5.9. Coordination polyhedra of γ-TaON. Bond lengths are presented in pm.*

As mentioned above, the difference plot, the residuals, and the goodness of fit S are indicating a not satisfying accordance between experimental data and theoretical structure model. A more detailed look at the powder diffraction diagram shows that the deviations mainly come from intensity problems together with reflection shifts. All this is probably caused by the presence of shear planes in the layer-like VO_2(B)-type crystal structure. There are no indications for severe anisotropic reflection broadening. These observations are already known from previous investigations regarding γ-TaON.[3] Furthermore, the determination of the anion positions is very difficult besides the heavy scattering Ta atoms. The Rietveld refinement provided always negative values for B_{iso} for the anion positions. Consequently, the isotropic Debye-Waller factors for oxygen were altered manually until those factors for oxygen and nitrogen were positive and therefore reasonable under physical aspects. Interestingly, the same refinement problems can be observed for the single phase material with hollow urchin-like nanostructures[49] pointing to a general problem in the structural description of γ-TaON.

Quantitative N/O analysis resulted in 8.1 wt % oxygen and 6.2 wt % nitrogen, resulting in a composition of $TaO_{1.07}N_{0.93}$. Respecting the experimental accuracy of 2% this is in an acceptable accordance with the expected ideal stoichiometry TaON. It should be mentioned that investigations regarding non-stoichiometric phases of β-TaON and Ta_3N_5 have been published recently.[59] From these results a deviation from the ideal anion composition should not be completely ruled out. *In situ* temperature-dependent X-ray

diffraction experiments show a transformation to β-TaON in nitrogen atmosphere at *ca.* 1173 K. Calculations show that this metastable polymorph is *ca.* 17 kJ·mol^{-1} less stable than β-TaON.[3]

A comparison to our first publication on this phase could be misleading. The provided weighted residual ($R_{wp} = 0.089$)[3] of the Rietveld refinement is better than the value in this new investigation ($R_{wp} = 0.111$). The presence of Ta_2O_5 as a side phase, which can be better refined than the oxide nitride, has impact on the overall phase analysis. Besides the unsatisfying refinement results, the successful preparation of phase pure bulk material is the first step to solve most of the discussed problems. A more detailed analysis with the help of neutron diffraction measurements is strongly advised and an objective for future studies. Besides, the anion ordering has only been discussed theoretically,[3] which can be analyzed with this method.

5.4.3 Anatase-type δ-TaON

First discoveries of an anatase-type structure in tantalum oxide nitride phases have been made by incorporating small amounts of Mg^{2+} [60] or Sc^{3+} [61] ions. In fact, $Mg_{0.05}Ta_{0.95}O_{1.15}N_{0.85}$ was the first example for this particular structure type without the element titanium. Relative stabilities for pure TaON in different crystal structures have been determined by quantum-chemical calculations, resulting in the following order of structure types with decreasing stability: baddeleyite – VO_2(B) – anatase.[7] The latter has already been synthesized as thin film by Suzuki *et al.*[62,63] The optical band gap has been determined to 2.37 eV. Analyses on bulk material has been published recently (indirect band gap: 1.73 eV, direct: 2.06 eV).[55] It should be noted that those measurements have not been carried out on phase pure samples.

In our previous work we were able to synthesize a sample of anatase-type δ-TaON with a maximum yield of 43 wt %.[4] Structural refinements were performed on a sample (35 wt % δ-TaON) without γ-TaON as a side phase to avoid the above mentioned difficulties in the structure refinement. With our new synthesis conditions (ammonolysis of amorphous precursors mentioned above in an SiO_2 tube at 1023 K, reaction time of 0.75 h, heat rate of 400 K·h^{-1}, and flow rates of 12.50 L·h^{-1} ammonia and 0.03 L·h^{-1} oxygen) it was possible to increase the yield of the desired phase up to 82 wt %, but it was unavoidable to get γ-TaON (6 wt %) as a side phase in addition to the always present dark red Ta_3N_5 (12 wt %). The latter has a significant influence on the red color of the product.

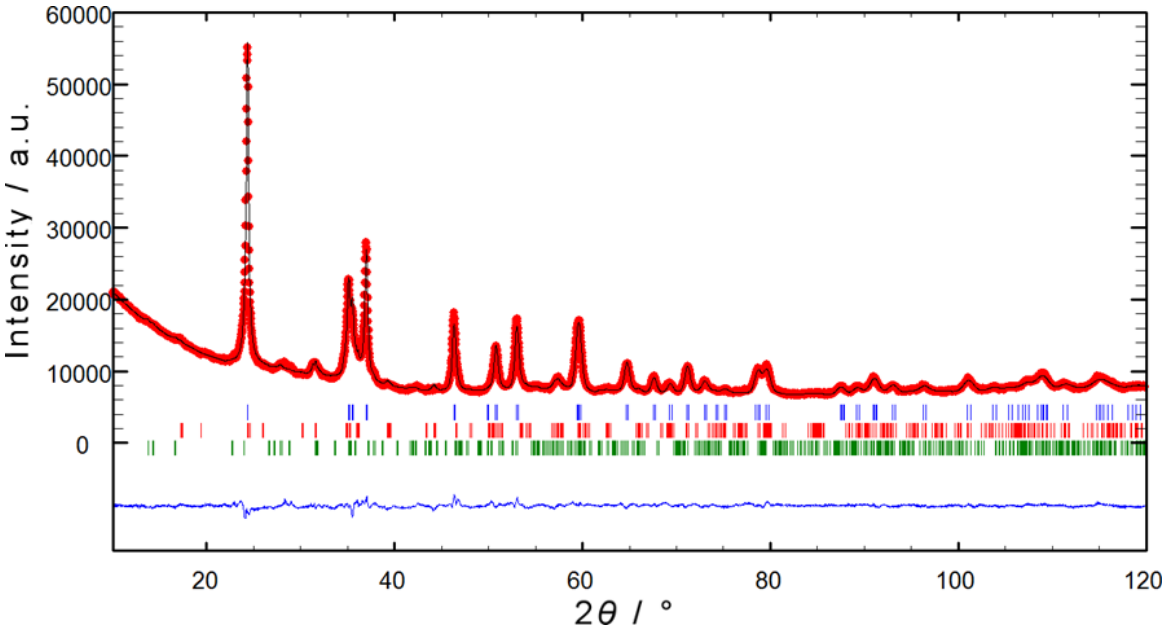

Figure 5.10. X-ray powder diffraction pattern (Cu-K_α radiation) of δ-TaON with results of the Rietveld refinement. The vertical bars indicate the positions of the Bragg reflections (blue: δ-TaON 82 wt %, red: Ta_3N_5 12 wt %, green: γ-TaON 6 wt %).

The powder diffraction pattern is shown in Figure 5.10. The Rietveld refinement was carried out using the tetragonal space group $I4_1/amd$, which does not allow an ordered anion arrangement. This problem has already been discussed elsewhere multiple times.[4,7,60,64] Refined parameters are listed in Table 5.5 and Table 5.6.

The presence of two side phases with strongly overlapping reflections has a noticeable influence on the Rietveld refinement, which is indicated by a relatively high R_{Bragg} value of 0.047 for the main phase. At an angular region of 2θ = ~24°, for example, the strongest reflections of both metastable TaON modifications and Ta_3N_5 are located. Additionally, the difficulties regarding the refinement of the γ-phase mentioned above must also be taken under consideration. This was the main reason to choose a sample without this side phase in the previous publication.[4] The isotropic Debye-Waller factors have been fixed to values from neutron diffraction experiments on $Mg_{0.05}Ta_{0.95}O_{1.15}N_{0.85}$.[60]

Table 5.5. Results of the Rietveld refinement for δ-TaON.

	δ-TaON
Structure type	Anatase
Space group	$I4_1/amd$ (No. 141)
Crystal system	Tetragonal
a / pm	391.872(17)
c / pm	1010.66(5)
V / 10^6 pm^3	155.201(13)
Z	4
ρ_{calc} / g·cm^{-3}	9.028
Diffractometer	PANalytical X'Pert Pro
2θ / °	10–120
λ / pm	154.060, 154.443
	$I(\lambda_2)/I(\lambda_1) = 0.5$
Profile points	4224
Refined parameters	36
R_{wp}	0.022
R_{exp}	0.010
R_{Bragg}	0.047
S	2.18

Table 5.6. Refined atomic parameters of δ -TaON.

Atom	Wyckoff	x	y	z	B_{iso} / 10^4 pm^2
Ta	4b	0	¼	⅜	1.3[a]
O / N[b]	8e	0	¼	0.5875(6)	1.4[a]

[a] Fixed to the results from neutron diffraction, ref. 60.
[b] Not refined independently.

In contrast to the Ostwald–Volmer rule,[57] this metastable polymorph of tantalum oxide nitride has a slightly larger density ($\rho = 9.029$ g·cm^{-3}) than the more stable γ-TaON ($\rho = 8.756$ g·cm^{-3}) with its huge tunnels. Anatase-type structures are also characterized by tunnels along the *a*- and *b*-axes (Figure 5.11), but the cavities are not as distinctive as in the VO_2(B)-type structure. Just one type of coordination polyhedron can be found in the anatase-type structure (Figure 5.11). Tantalum marks the center of an elongated and slightly distorted octahedron with anions on its edges. The four nearest anions with a distance of 199.6 pm are tilted out of the ideal equatorial plane by an angle

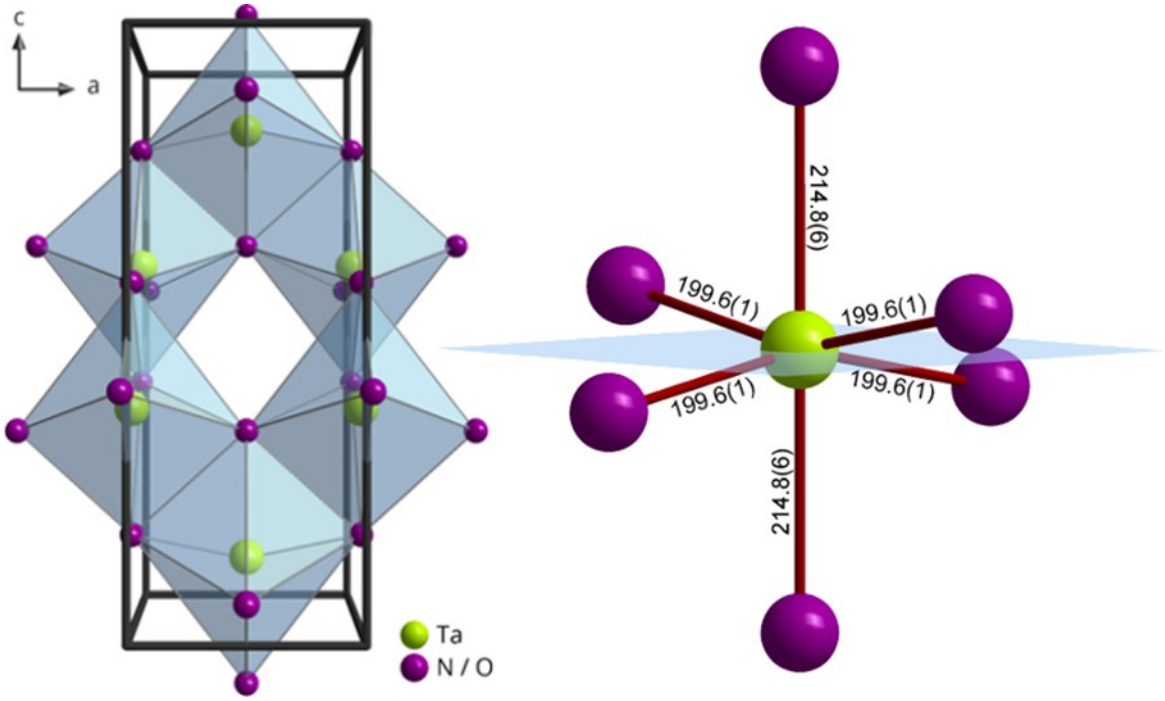

Figure 5.11. Crystal structure of anatase-type TaON. Left: unit cell with coordination polyhedra. Right: Ta–O/N bond lengths. Bond lengths are presented in pm.*

of ±11°, whereas the bonds in the axial direction are noticeably larger (214.8 pm). In comparison to $Mg_{0.05}Ta_{0.95}O_{1.15}N_{0.85}$ the bond lengths are in a good agreement with experimental (200.3–211.3 pm)[60] and calculated (200.0–214.0 pm)[64] values of the Mg-containing compound. Such deformed octahedra are also well known from anatase-type TiO_2 (193.4–197.9 pm).[65]

A phase transition to β-TaON can be observed at temperatures between 1073 and 1123 K. δ-TaON is a metastable polymorph and about 20 $kJ \cdot mol^{-1}$ less stable than the thermodynamically stable β-polymorph.[7] No intermediate phase was observed during the experiments. It should be mentioned that thermoanalytical measurements (DTA/TG) were performed for all described compounds. No significant thermal effects (exo- or endothermic) or mass changes were observed in the relevant temperature regions.

A comparison of this work and formerly presented results might be difficult due to diversity and amount of side phases. Those problems were discussed above. The coordination polyhedra are now more conformable with experimental and theoretical data of the Mg-containing compound. A detailed study on physical properties, especially photocatalytic activity, might be difficult due the insufficient phase purity. A severe problem for

neutron diffraction studies, important for the experimental determination of the anion distribution, is the small product yield (*ca.* 10 mg) per reaction.

5.4.4 Quantum-chemical Calculations

The calculated fundamental band gaps of the synthesized TaON β-, γ-, and δ-polymorphs and the hypothetical rutile, fluorite and t-ZrO_2 polymorphs are summarized in Table 5.7. For the δ-polymorph the experimental structure parameters reported in this study were used. For all other polymorphs the lattice parameters optimized at DFT level in previous works were used. In all cases the smallest band gap energy corresponds to an indirect transition.

Table 5.7. Fundamental band gaps (eV) of TaON polymorphs calculated with the plasmon-pole approximation to GW implemented in GPAW. All calculated gaps obtained in this work correspond to indirect transitions. The corresponding direct gaps are given in parentheses.

Polymorph	This work	Previous studies	Experimental
β-TaON	2.99 (3.20)	3.2[b]	2.4, 2.8[b]
γ-TaON	2.38 (2.59)	2.9[c]	2.03 (2.58)[a]
δ-TaON	2.52 (3.01)	2.85[b], 3.2[d]	1.73 (2.06)[a], 2.4[d]
Rutile	1.85 (2.21)	2.3[b]	
Fluorite	1.78 (2.50)	2.46[b]	
t-ZrO_2	1.57 (1.77)		

[a] Optical band gaps, ref. 56.
[b] Experimental and theoretical study using the hybrid functional PW1PW, ref. 7
[c] Theoretical study using the hybrid functional PW1PW, ref. 6.
[d] Combined experimental and theoretical study using the hybrid functional PBE0, ref. 4.

Compared to the band gaps obtained in our previous hybrid DFT calculations, the GW gaps are systematically smaller, by 0.2–0.7 eV. Where comparison with experimental values is possible, this decrease corresponds to an improvement of the theoretical results. As a general trend, the band gaps decrease with decreasing stability of the polymorphs, in nice accord with the principle of maximum hardness[66]. It has to be noted that optical and fundamental band gaps differ by the exciton energy which is typically in the order of a few hundred meV for oxides. It is therefore not surprising that the calculated gaps are in all cases larger than the experimental values. In order to correct for the excitonic effects, so-

lution of the Bethe–Salpeter equations is necessary, which was beyond the scope of the present study. Based on the present results it can be concluded that the plasmon-pole GW approximation is useful as a computationally efficient screening method.

5.5 Conclusion

After the first publications on bixbyite-type V_2O_3, γ-TaON, and δ-TaON powders we were able to improve the preparation conditions of all these metastable polymorphs. In the first two cases phase pure products were obtained and the yield of δ-TaON was almost doubled to a phase purity of 82 wt %. This clearly shows that new metastable polymorphs of simple compounds can be prepared by classical synthesis routes, pointing to additional new phases in the future. Moreover, metastable polymorphs may show structure-function correlations distinctly different from those of the corresponding stable phases. These features will make them suitable model systems to advance our understanding of the properties and the design of improved functional materials. A first-principles quantum-chemical method was used to study the electronic structures of TaON polymorphs and their excitations. A semiquantitative agreement with measured optical spectra was obtained, so that it can be expected that this approach can be used for predictions of photocatalytic activity of solid compounds.

5.6 Acknowledgements

This work is supported by the German Science Foundation (DFG) within the priority program SPP 1415. XRF analysis by Dr. Rafael Zubrzycki (TU Berlin) and N/O analysis by Brigitte Hahn and Steven Orthmann (TU Berlin) are gratefully acknowledged. The Hamburger Synchrotron Radiation Facility, HASYLAB, is acknowledged for providing beamtime. We thank Sigrid Imme and Barbara Dunker (TU Berlin) for CHNS-analysis.

5.7 References

(1) Weber, D.; Stork, A.; Nakhal, S.; Wessel, C.; Reimann, C.; Hermes, W.; Müller, A.; Ressler, T.; Pöttgen, R.; Bredow, T.; Dronskowski, R.; Lerch, M. *Inorg. Chem.* **2011**, *50* (14), 6762–6766.

(2) Weber, D.; Wessel, C.; Reimann, C.; Schwickert, C.; Müller, A.; Ressler, T.; Pöttgen, R.; Bredow, T.; Dronskowski, R.; Lerch, M. *Inorg. Chem.* **2012**, *51* (15), 8524–8529.

(3) Schilling, H.; Stork, A.; Irran, E.; Wolff, H.; Bredow, T.; Dronskowski, R.; Lerch, M. *Angew. Chemie Int. Ed.* **2007**, *46* (16), 2931–2934.

(4) Lüdtke, T.; Schmidt, A.; Göbel, C.; Fischer, A.; Becker, N.; Reimann, C.; Bredow, T.; Dronskowski, R.; Lerch, M. *Inorg. Chem.* **2014**, *53* (21), 11691–11698.

(5) Weber, D. A. *Synthese und Charakterisierung neuer Oxide und Oxidnitride der Elemente der 5. und 6. Gruppe des Periodensystems*; Technische Universität Berlin: Berlin, 2014.

(6) Wolff, H.; Bredow, T.; Lerch, M.; Schilling, H.; Irran, E.; Stork, A.; Dronskowski, R. *J. Phys. Chem. A* **2007**, *111* (14), 2745–2749.

(7) Bredow, T.; Lumey, M.-W.; Dronskowski, R.; Schilling, H.; Pickardt, J.; Lerch, M. *Z. Anorg. Allg. Chem.* **2006**, *632* (7), 1157–1162.

(8) Paier, J. *Catal. Letters* **2016**, *146* (5), 861–885.

(9) Baerends, E. J.; Gritsenko, O. V.; van Meer, R. *Phys. Chem. Chem. Phys.* **2013**, *15* (39), 16408–16425.

(10) Grüneis, A.; Kresse, G.; Hinuma, Y.; Oba, F. *Phys. Rev. Lett.* **2014**, *112* (9), 96401-1–5.

(11) Enkovaara, J.; Rostgaard, C.; Mortensen, J. J.; Chen, J.; Dułak, M.; Ferrighi, L.; Gavnholt, J.; Glinsvad, C.; Haikola, V.; Hansen, H. A.; Kristoffersen, H. H.; Kuisma, M.; Larsen, A. H.; Lehtovaara, L.; Ljungberg, M.; Lopez-Acevedo, O.; Moses, P. G.; Ojanen, J.; Olsen, T.; Petzold, V.; Romero, N. A.; Stausholm-Møller, J.; Strange, M.; Tritsaris, G. A.; Vanin, M.; Walter, M.; Hammer, B.; Häkkinen, H.; Madsen, G. K. H.; Nieminen, R. M.; Nørskov, J. . K.; Puska, M.; Rantala, T. T.; Schiøtz, J.; Thygesen, K. S.; Jacobsen, K. W. *J. Phys. Condens. Matter* **2010**, *22* (25), 253202-1–24.

(12) Rostgaard, C.; Jacobsen, K. W.; Thygesen, K. S. *Phys. Rev. B* **2010**, *81* (8), 85103-1–10.

(13) Hüser, F.; Olsen, T.; Thygesen, K. S. *Phys. Rev. B* **2013**, *87* (23), 235132-1–14.

(14) Rodríguez-Carvajal, J. In Abstracts of the Satellite Meeting on Powder Diffraction of the XV IUCr Congress; 1990; p 127.

(15) Rodríguez-Carvajal, *J. Phys. B Condens. Matter* **1993**, *192*, 55–69.

(16) Ressler, T. J. *Synchrotron Radiat.* **1998**, *5* (2), 118–122.

(17) Ressler, T. *Anal. Bioanal. Chem.* **2003**, *376* (5), 584–593.

(18) Haber, J. *Catal. Today* **2009**, *142* (3–4), 100–113.

(19) Hess, C. *ChemPhysChem* **2009**, *10* (2), 319–326.

(20) Liu, P.; Lee, S.-H.; Cheong, H. M.; Tracy, C. E.; Pitts, J. R.; Smith, R. D. *J. Electrochem. Soc.* **2002**, *149* (3), H76–H80.

(21) Prosini, P. P.; Xia, Y.; Fujieda, T.; Vellone, R.; Shikano, M.; Sakai, T. *Electrochim. Acta* **2001**, *46* (17), 2623–2629.

(22) Muster, J.; Kim, G. T.; Krstić, V.; Park, J. G.; Park, Y. W.; Roth, S.; Burghard, M. *Adv. Mater.* **2000**, *12* (6), 420–424.

(23) Zachariasen, W. H. *Geol. Foereningan i Stock. Foerhandlingar* **1929**, *51* (1), 123–123.

(24) Mott, N. F. *Metal-Insulator Transition*, 1st ed.; Taylor and Francis: London, 1974.

(25) Held, K.; Keller, G.; Eyert, V.; Vollhardt, D.; Anisimov, V. I. *Phys. Rev. Lett.* **2001**, *86* (23), 5345–5348.

(26) Finger, L. W.; Hazen, R. M. *J. Appl. Phys.* **1980**, *51* (10), 5362–5367.

(27) McWhan, D. B.; Remeika, J. P. *Phys. Rev. B* **1970**, *2* (9), 3734–3750.

(28) Dernier, P. D.; Marezio, M. *Phys. Rev. B* **1970**, *2* (9), 3771–3776.

(29) Moon, R. M. *Phys. Rev. Lett.* **1970**, *25* (8), 527–529.

(30) Wessel, C.; Reimann, C.; Müller, A.; Weber, D.; Lerch, M.; Ressler, T.; Bredow, T.; Dronskowski, R. *J. Comput. Chem.* **2012**, *33* (26), 2102–2107.

(31) Bergerud, A.; Buonsanti, R.; Jordan-Sweet, J. L.; Milliron, D. J. *Chem. Mater.* **2013**, *25* (15), 3172–3179.

(32) Sarmadian, N.; Saniz, R.; Partoens, B.; Lamoen, D. *J. Appl. Phys.* **2015**, *117* (1), 15703-1–6.

(33) Nakhal, S.; Weber, D.; Irran, E.; Lerch, M.; Schwarz, B.; Ehrenberg, H. *Z. Krist.* **2013**, *228* (8), 347–350.

(34) Shannon, R. D.; Prewitt, C. T. *Acta Crystallogr. Sect. B* **1969**, *25* (5), 925–946.

(35) Rundle, R. E.; Baenziger, N. C.; Wilson, A. S.; McDonald, R. A. *J. Am. Chem.* Soc. **1948**, *70* (1), 99–105.

(36) Masaki, N.; Tagawa, H. *J. Nucl. Mater.* **1975**, *57* (2), 187–192.

(37) Füglein, E.; Hock, R.; Lerch, M. *Z. Anorg. Allg. Chem.* **1997**, *623* (1–6), 304–308.

(38) Nakhal, S.; Hermes, W.; Ressler, T.; Pöttgen, R.; Lerch, M. *Z. Naturforsch.* **2009**, *64b*, 281–286.

(39) Reimann, C.; Weber, D.; Lerch, M.; Bredow, T. *J. Phys. Chem. C* **2013**, *117* (39), 20164–20170.

(40) Carter, R. E. *J. Chem. Phys.* **1961**, *34* (6), 2010–2015.

(41) Ginstling, A. M.; Brounshtein, B. I. *J. Appl. Chem. USSR* **1950**, *23*, 1327.

(42) Brauer, G.; Weidlein, J. R. *Angew. Chemie Int. Ed.* **1965**, *4* (10), 875–875.

(43) Buslaev, Y. A.; Glushkova, M. A.; Ershova, M. M.; Shustorovich, E. M. *Neorg. Mat.* **1966**, *2*, 2120–2123.

(44) Buslaev, Y. A.; Safronov, G. M.; Pakhomov, V. I.; Glushkova, M. A.; Repko, V. P.; Ershova, M. M.; Zhukov, A. N.; Zhdanova, T. A. *Neorg. Mat.* **1969**, *5*, 45–48.

(45) Lumey, M.-W.; Dronskowski, R. *Z. Anorg. Allg. Chem.* **2003**, *629* (1213), 2173–2179.

(46) Lumey, M.-W.; Dronskowski, R. *Z. Anorg. Allg. Chem.* **2005**, *631* (5), 887–893.

(47) Lowther, J. E. *Phys. Rev. B* **2005**, *72* (17), 172105-1–4.

(48) Woodhead, K.; Pascarelli, S.; Hector, A. L.; Briggs, R.; Alderman, N.; McMillan, P. F. *Dalton Trans.* **2014**, *43* (25), 9647–9654.

(49) Wang, Z.; Hou, J.; Yang, C.; Jiao, S.; Huang, K.; Zhu, H. *Energy Environ. Sci.* **2013**, *6* (7), 2134–2144.

(50) Gao, Q.; Liu, N.; Wang, S.; Tang, Y. *Nanoscale* **2014**, *6* (23), 14106–14120.

(51) Okubo, T.; Kakihana, M. *J. Alloys Compd.* **1997**, *256* (1–2), 151–154.

(52) Lerch, M.; Lerch, J.; Hock, R.; Wrba, J. *J. Solid State Chem.* **1997**, *128* (2), 282–288.

(53) Jansen, M.; Letschert, H. P. *Nature* **2000**, *404* (6781), 980–982.

(54) Hitoki, G.; Takata, T.; Kondo, J. N.; Hara, M.; Kobayashi, H.; Domen, K. *Chem. Commun.* **2002**, *2* (16), 1698–1699.

(55) Cosgun, S. *Synthese und Charakterisierung Tantaloxidnitrid-basierter Verbindungen für die photokatalytische Wasserspaltung*, Technische Universität Berlin: Berlin, 2015.

(56) Armytage, D.; Fender, B. E. F. *Acta Crystallogr.* **1974**, *B30* (3), 809–812.

(57) Hollemann, A. F.; Wiberg, N.; Wiberg, E. *Lehrbuch der Anorganischen Chemie*, 102th ed.; de Gruyter: Berlin, Boston, 2008.

(58) Shannon, R. D. *Acta Crystallogr. Sect. A* **1976**, *32* (5), 751–767.

(59) Harb, M.; Sautet, P.; Nurlaela, E.; Raybaud, P.; Cavallo, L.; Domen, K.; Basset, J.-M.; Takanabe, K. *Phys. Chem. Chem. Phys.* **2014**, *16* (38), 20548–20560.

(60) Schilling, H.; Lerch, M.; Börger, A.; Becker, K.-D.; Wolff, H.; Dronskowski, R.; Bredow, T.; Tovar, M.; Baehtz, C. *J. Solid State Chem.* **2006**, *179* (8), 2416–2425.

(61) Stork, A.; Schilling, H.; Wessel, C.; Wolff, H.; Börger, A.; Baehtz, C.; Becker, K.-D.; Dronskowski, R.; Lerch, M. *J. Solid State Chem.* **2010**, *183* (9), 2051–2058.

(62) Suzuki, A.; Hirose, Y.; Oka, D.; Nakao, S.; Fukumura, T.; Ishii, S.; Sasa, K.; Matsuzaki, H.; Hasegawa, T. *Chem. Mater.* **2014**, *26* (2), 976–981.

(63) Suzuki, A.; Hirose, Y.; Oka, D.; Nakao, S.; Fukumura, T.; Hasegawa, T. *Jpn. J. Appl. Phys.* **2015**, *54* (8), 80303-1–3.

(64) Wolff, H.; Lerch, M.; Schilling, H.; Bähtz, C.; Dronskowski, R. *J. Solid State Chem.* **2008**, *181* (10), 2684–2689.

(65) Burdett, J. K.; Hughbanks, T.; Miller, G. J.; Richardson, J. W.; Smith, J. V. *J. Am. Chem. Soc.* **1987**, *109* (12), 3639–3646.

(66) Pearson, R. G. *Chemical Hardness*, 1st ed.; Wiley-VCH: Weinheim, New York, 1997.

6 Publication 3

Bixbyite-type Phases in the System Ta-Zr-O-N

Tobias Lüdtke, Steven Orthmann, Martin Lerch

Postprint
Zeitschrift für Naturforschung **2017**, *72b(4)*, 305–311
DOI: 10.1515/znb-2017-0014
https://www.degruyter.com/view/j/znb.2017.72.issue-4/
znb-2017-0014/znb-2017-0014.xml

Contribution to publication:

T. Lüdtke:	Sample preparation, characterization, writing.
S. Orthmann:	Measurements (N/O analysis), proofreading.
M. Lerch:	General discussion, proofreading.

Overall contribution of T. Lüdtke to the publication: 80%

Authors. Tobias Lüdtke,[a] Steven Orthmann,[a] Martin Lerch [a,*]

(a) Institut für Chemie, Technische Universität Berlin, Straße des 17. Juni 135, D-10623 Berlin, Germany

* Corresponding author

Keywords. Tantalum, zirconium, oxide nitride, nitride, bixbyite

Supporting Information. Crystallographic data in CIF format for the structure refinement of $TaZrN_3$. This material is available *via* the Internet at https://www.degruyter.com/view/j/znb.2017.72.issue-4/znb-2017-0014/znb-2017-0014.xml

Received: 19.01.2017
Accepted: 02.02.2017
Published online: 07.04.2017

6.1 Abstract

Phase-pure tantalum/zirconium oxide nitrides and nitrides were synthesized by ammonolysis of amorphous oxide precursors. The nitrogen-rich oxide nitrides with variable anion composition and the nitride $TaZrN_3$ crystallize in the cubic bixbyite-type structure (space group $Ia\bar{3}$). The nitrogen content of these compounds has a significant influence on the cell parameters, the atomic positions, and the optical band gap. The results extend the already well-studied Ta-Zr-O-N system by new oxide nitrides in addition to the already known baddeleyite- and anosovite-type phases. $TaZrN_3$ can be considered as a thermodynamically stable ternary variant of metastable Ta_2N_3.

6.2 Introduction

Ternary transition metal oxide nitrides are interesting materials with relatively low complexity and therefore predestinated for investigations of structure-property correlations. In addition, they offer a wide range of applications. For example, tantalum- or zirconium-based oxide nitrides are promising photocatalysts,[1,2] non-toxic color pigments,[3] and fast ion conductors.[4] Consequently, the investigation of phases including both metals, oxygen, and nitrogen, may offer a wider range of interesting materials.

Ionic-covalent zirconium oxide nitrides belong to the quasi-binary system ZrO_2-Zr_3N_4. They are generally described by the formula $ZrO_{2-2x}N_{4x/3}$ and are structurally derived from fluorite-type ZrO_2, the high temperature polymorph of zirconia. A series of oxygen-rich β-type phases (β: $Zr_7O_8N_4$; β': $Zr_7O_{11}N_2$; β": $Zr_{7.0}O_{9.5}N_{3.0}$)[5–9] are supplemented by a nitrogen-rich γ-phase (Zr_2ON_2),[5–7] crystallizing in the cubic bixbyite-type structure. A more detailed overview concerning this system was conducted by Lerch (ref. 10). An intergrowth of ZrO_2 and Zr_2ON_2, resulting in the formation of $Zr_4O_5N_2$,[11] and the incorporation of small amounts of Ta_2O_5 into zirconium oxide nitrides have also been investigated.[12] The hitherto reported nitrides of zirconium are ZrN[13, 14] and Zr_3N_4.[15,16] A cubic high-pressure polymorph of Zr_3N_4 also exists.[17]

On the other hand, the ionic-covalent oxide nitride of tantalum(V), TaON, is more stoichiometrically restricted and crystallizes in various AX_2 structure types. The thermodynamically stable polymorph is called β-TaON, crystallizing in the monoclinic baddeleyite-type structure.[18] Sometimes it is referred to be a nitrogen-rich analogue to monoclinic ZrO_2 (m-ZrO_2). Two metastable polymorphs have been prepared so far: γ-TaON[19] crystallizes in the monocline crystal system in the VO_2(B)-type structure, and

δ-TaON, which exhibits the tetragonal anatase type.[20,21] A high-pressure polymorph with cotunnite-type structure has been synthesized as well.[22] In addition, the existence of a further tantalum(V) oxide nitride, Ta_3O_6N,[23] has been proposed. By contrast, the variety of the nitrides is significantly higher. The compounds Ta_3N_5,[24] Ta_4N_5,[25] Ta_5N_6,[25] and Ta_2N_3[26–29] belong to the group of nitrogen-rich nitrides. Ta_2N_3 crystallizes, comparable with Zr_2ON_2, in the bixbyite-type structure.[28,29] High-pressure polymorphs of Ta_3N_5 and Ta_2N_3 are also described in literature.[30,31] Additional nitrides can be separated into two different categories: solid solutions of nitrogen in tantalum metal (α phase) with a correlated superstructure of this type,[32–34] the β-Ta_2N phase,[32–36] and three different mononitrides (δ-, ε-, θ-TaN).[37–39]

It is remarkable that the quaternary system Ta-Zr-O-N has also been investigated in detail. The first publication about this topic was presented by Schönberg in 1954,[40] and the most comprehensive work was presented by Grins *et al.*[41] They reported on synthesis and characterization of phase-pure baddeleyite- and anosovite-type phases, which can be derived from m-ZrO_2/β-TaON and Ta_3N_5, respectively. In addition, a cubic and an orthorhombic phase, both obtained as side phases, have also been reported. Unfortunately, a detailed description of those phases was not possible. Investigations regarding the optical properties of the phase-pure baddeleyite- and anosovite-type compounds were presented later.[42,43] The existence of a high-pressure polymorph of $TaZrO_3N$ was studied theoretically.[44] Literature about ternary nitrides of tantalum and zirconium is restricted to (Ta,Zr)N thin films or alloys with an even lower nitrogen content (for examples see ref. 45,46). To our knowledge, ternary ionic-covalent nitrides have not been reported so far.

Obviously, a more detailed investigation of the system Ta-Zr-O-N should be worth the efforts. In particular, the search for new metastable compounds was one of the main intentions for the present work. Our synthesis of metastable δ-TaON powder was based on the preparation of partly cation-substituted compounds such as $Mg_{0.05}Ta_{0.95}O_{1.15}N_{0.85}$[47] or $Sc_{0.15}Ta_{0.85}O_{1.30}N_{0.70}$[48] with a similar crystal structure type. The preparation of these quaternary compounds was much easier compared to the ternary phase because the anatase structure is stabilized by small amounts of incorporated aliovalent cations. The development of synthesis routes to these quaternary phases has to be considered as an indispensable prerequisite for the successful preparation of TaON in the anatase type. Results of quantum-chemical calculations suggest the existence of at least two more polymorphs with rutile- and fluorite-type structures, respectively.[49] Rutile-type $ScTa_2O_5N$ has already been synthesized and might be a first step to the ternary

analogue.[50] Consequently, we expand this approach to zirconium as an additional cation, in a search of new ionic-covalent phases in the system Ta-Zr-O-N.

6.3 Experimental Section

Precursors were prepared by a modified Pechini sol-gel route.[51, 52] This method allows the synthesis of amorphous Ta-Zr oxides by using metal-citrate solutions and ethylene glycol as gelling agent. $TaCl_5$ (99.999%, Sigma Aldrich) and $ZrCl_4$ (99.99%, Sigma Aldrich) were mixed in the required ratios and dissolved in a citric acid-ethanol solution. Citric acid was used in a 12-fold molar excess to the cations. Ethylene glycol in a molar excess of 17 times the cations was added to the solutions. These mixtures were vaporized at temperatures up to 523 K. The formed gels were then calcined in a corundum crucible at temperatures up to 723 K, resulting in colorless X-ray amorphous powders of the mixed oxides.

Nitrides and oxide nitrides were synthesized *via* an ammonolysis reaction of these precursors in a tube furnace with dry ammonia at temperatures of 1073–1223 K for 3–12 h and ammonia flow rates of 10–20 $L \cdot h^{-1}$.

A PANalytical X'Pert MPD Pro instrument (Almelo, Netherlands) was used for XRD measurements at ambient temperature. This powder diffractometer operates with a Cu anode and without a monochromator (Cu-K_α radiation, $\lambda_1 = 154.060$ pm, $\lambda_2 = 154.443$ pm, $I(\lambda_2)/I(\lambda_1) = 0.5$) at 40 kV and 40 mA. Additional data were collected on a RIGAKU SmartLab 3 kW system equipped with a Cu anode X-ray tube (40 kV and 30 mA) and a $K_{\alpha 1}$-unit (Johansson-type Ge crystal) monochromator (Cu-$K_{\alpha 1}$ radiation, $\lambda = 154.060$ pm). Rietveld refinements were carried out using the program FULLPROF 2000.[53] Profiles were fitted with a pseudo-Voigt profile shape function. The backgrounds were fitted with various points with refinable heights.

A LECO TC-300/EF-300 N/O hot gas extraction analyzer (Saint Joseph, MI, USA) was used for the determination of nitrogen and oxygen contents of the samples. ZrO_2 and special steel (Saint Joseph, MI, USA) were used as standard materials. The accuracy is *ca.* 2% of the N/O contents present.

UV-vis measurements were performed on a VARIAN (Palo Alto, CA, USA) Cary 300 Scan UV-vis spectrophotometer in diffuse reflectance mode. Barium sulfate (Sigma-Aldrich) was used as reference. The measured diffuse reflectance spectra were converted

by the Kubelka–Munk function to absorbance spectra. The optical band gaps were determined by the Tauc plot method.[54,55]

6.4 Results and Discussion

As generally described in the experimental part, mixed amorphous Ta/Zr oxides consisting of 95, 85, 66.6, 50, or 33.3 cation % Ta were prepared. The cation ratios of these precursors were confirmed by X-ray fluorescence spectroscopy. Although the ammonolysis of precursors with low Zr contents resulted only in the formation of already known baddeleyite- and anosovite-type phases, some samples with low Ta contents show crystal structures yet unknown for this system.

Ammonolysis of precursors with Ta contents of 33.3, 50, or 66.6 cation %, performed at 1073 K, resulted in phase-pure powders of oxide nitrides or nitrides with cubic bixbyite-type structure ($Ia\bar{3}$). Structural similarities to bixbyite-type Zr_2ON_2 are apparent. Samples synthesized at lower temperatures contain side phases with baddeleyite-type structure. Additional tests with 70 cation % Ta were performed as well, but an anosovite-type phase was an unavoidable byproduct. It can be assumed that this series can be expanded to Ta contents lower than 33.3 cation % with Zr_2ON_2 as the final member.

The ideal bixbyite structure can be described as a $2 \times 2 \times 2$ superstructure of the fluorite type where one quarter of the anions is removed.[56–59] Cations are located on 8*a* and 24*d* sites, anions on a 48*e* site (and the vacancies on a 16*c* site). The cations are coordinated octahedrally by anions and the anions are tetrahedrally surrounded by cations. A graphical presentation is shown in Figure 6.1. One characteristic of this structure type is the possible partial occupation of the vacancies by anions, leading to $A_2X_{3+\delta}$ ($\delta \leq 1$) compositions. This observation has already been made for U_2N_3,[60,61] Zr_2ON_2,[62] and vanadium oxide nitrides.[63]

In the system Ta-Zr-O-N, compounds between Zr_2ON_2/ZrO_2 and $TaZrN_3/TaZrO_3N$ can be described with the general formula $Ta_{1-x}Zr_{1+x}O_{x+3y/2}N_{3-x-y}$ ($0 \leq x \leq 1$, $0 \leq y \leq 2$). From a formal point of view, it should be possible to prepare 1:1 phases in the range from $TaZrN_3$ ($\delta = 0$) to $TaZrO_3N$ ($\delta = 1$). For a Ta:Zr ratio of 1:2, the following range can be calculated: $Ta_{0.67}Zr_{1.33}O_{0.33}N_{2.67}$–$Ta_{0.67}Zr_{1.33}O_{3.33}N_{0.67}$. The range $Ta_{1.33}Zr_{0.67}N_{3.11}$–$Ta_{1.33}Zr_{0.67}O_{2.67}N_{1.33}$ can be expected for a ratio of 2:1, which can be generalized to the formula $Ta_{1+x}Zr_{1-x}O_{3y/2}N_{3+x/3-y}$ ($0 \leq x \leq 0.33$, $0 \leq y \leq 2–2x/3$). Without the *x*-restriction (no phase-pure samples could be obtained for $x > 0.33$), the series could be continued for

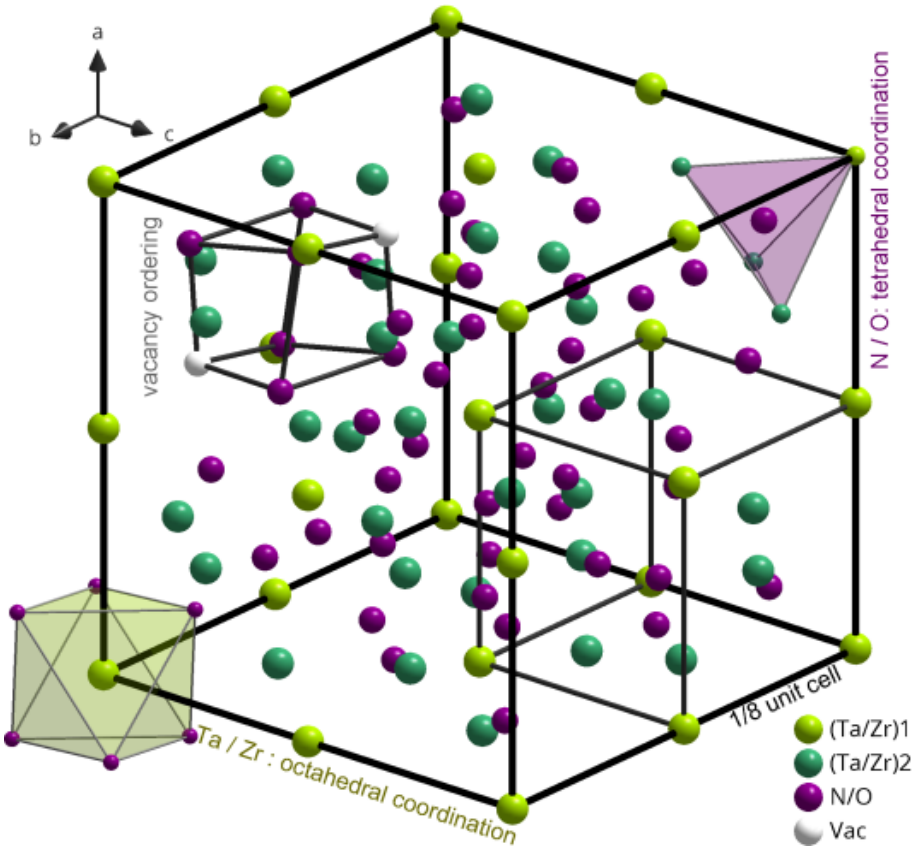

Figure 6.1. Crystal structure of the bixbyite-type tantalum zirconium oxide nitrides. Only two of 16 possible vacancies (Vac) have been marked.*

$x = 1$ to $Ta_{2.00}N_{3.33}$ ($y = 0$) and the corresponding phase $Ta_2O_2N_2$ ($y = 1.33$), or simply TaON. As mentioned above, quantum-chemical calculations indeed predict a metastable polymorph of TaON with fluorite-type structure.[49] This polymorph is expected to be *ca.* 80 kJ·mol^{-1} less stable compared with β-TaON, making a successful synthesis unlikely.

By variation of the synthesis parameters, it was possible to produce samples with different amounts of nitrogen and oxygen. For a 1:1 cation ratio, phase-pure phases in the range $Ta_{1.00}Zr_{1.00}O_{0.00}N_{3.00}$–$Ta_{1.00}Zr_{1.00}O_{1.67}N_{1.89}$ were found, corresponding to a y-range of $0 \le y \le 1.11$. For the other two ratios, compounds $Ta_{0.67}Zr_{1.33}O_{0.42}N_{2.61}$–$Ta_{0.67}Zr_{1.33}O_{1.89}N_{1.63}$ ($0.06 \le y \le 1.04$) and $Ta_{1.33}Zr_{0.67}O_{0.12}N_{3.03}$–$Ta_{1.33}Zr_{0.67}O_{0.30}N_{2.91}$ ($0.08 \le y \le 0.20$) were obtained. For simplicity, we mainly concentrate the following structural discussion on the compounds with a cation ratio of 1:1. Several reasons favor this choice: For Ta:Zr ratios larger than 1 it is not possible to prepare phases of the ideal A_2X_3 composition. Also the formation of anosovite-type side phases, which can be derived from Ta_3N_5, is favored by high amounts of tantalum. We do not focus on Ta-poor phases because exclusively the 1:1 series principally allows the synthesis of a pure nitride bixbyite-type compound with ideal A_2X_3 composition ($TaZrN_3$). This nitride was indeed

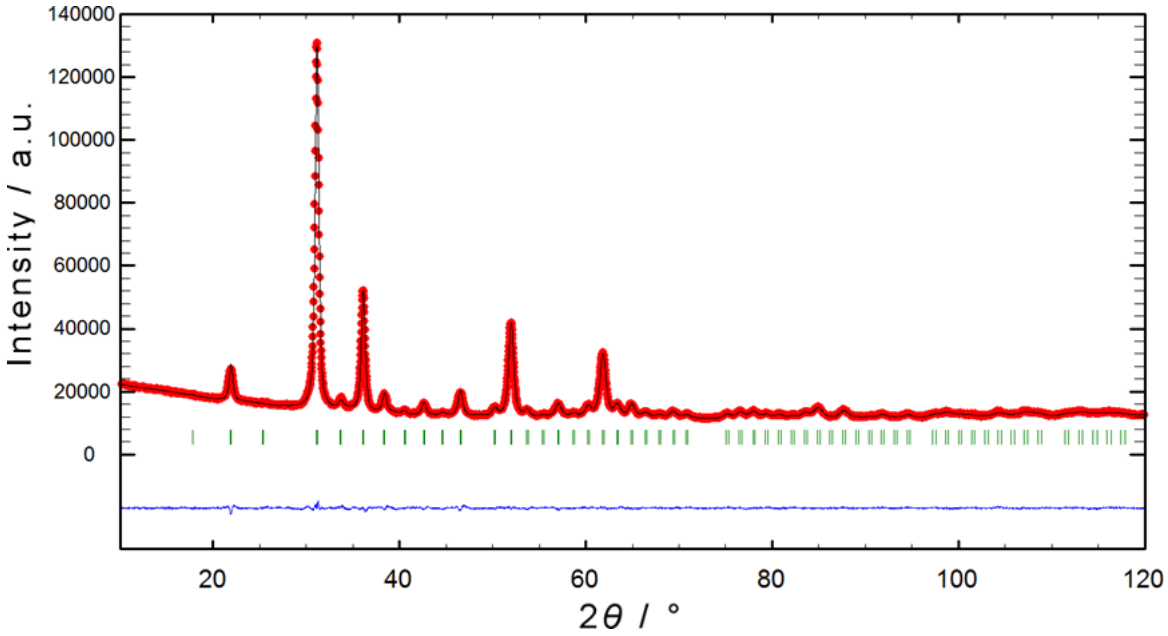

Figure 6.2. X-ray powder diffraction pattern (Cu-K_α radiation) of $TaZrN_3$ with results of the Rietveld refinement (red: measured; black: calculated; green: Bragg-reflection positions; blue: difference between measured and calculated).*

obtained in addition to various oxide nitrides. The X-ray powder pattern of $TaZrN_3$ together with the results of the Rietveld refinement is depicted in Figure 6.2. Refined structural parameters for the nitride and the phases with the highest nitrogen content obtained for the other investigated cation ratios (Ta:Zr) of 2:1 and 1:2 are presented in Table 6.1. For comparison, some details for Zr_2ON_2 are also implemented in this table.[62] The corresponding atomic parameters for $TaZrN_3$ are presented in Table 6.2.

Further details of the crystal structure investigation may be obtained from FIZ Karlsruhe, 76344 Eggenstein-Leopoldshafen, Germany (fax: +49 7247 808-666; e-mail: crysdata@fiz-karlsruhe.de), on quoting the deposition number CSD-432434.

In $TaZrN_3$, the octahedra around (Ta/Zr)1 have cation-anion bond lengths of 217.3(8) pm. By contrast, the (Ta/Zr)2$(O,N)_6$ polyhedra show values between 204.9(8) and 221.4(8) pm. The average bond length of 214.2 pm agrees with the sums of the ionic radii of the elements (Ta^{5+}: 64 pm; Zr^{4+}: 72 pm; N^{3-}: 146 pm)[64] and is almost exactly the average of the common Ta–N (210 pm) and Zr–N bonds (218 pm). It should be mentioned that no indication for Ta/Zr ordering was found. Consequently, a statistical distribution of the cations is assumed and the site occupations factors have been fixed for the refinements. N/O ordering in oxide nitrides cannot be investigated

using X-ray diffraction. Calculations on anion-excess vanadium oxide nitrides with bixbyite-type structure ($V_{2.000}O_{3.000}N_{0.125}$, $V_{2.000}O_{3.125}N_{0.125}$, and $V_{2.000}O_{3.067}N_{0.133}$) have shown that nitrogen is preferably located on the 48*e* and not on the 16*c* site.[63,65] This topic has already been discussed for Zr_2ON_2 with respect to neutron diffraction investigations[62,66] and based on quantum-chemical calculations.[67] The only possible maximal non-isomorphic *translationengleiche* subgroup allowing an ordered arrangement of oxygen and nitrogen is *Ibca*. However, an ordered anion arrangement was not found by both methods.

Table 6.1. Results of the Rietveld refinements for selected bixbyite-type phases in comparison with results for Zr_2ON_2.

Compound	Zr_2ON_2[62]	$Ta_{0.67}Zr_{1.33}O_{0.42}N_{2.61}$	$TaZrN_3$	$Ta_{1.33}Zr_{0.67}O_{0.12}N_{3.03}$
Ta:Zr		1:2	1:1	2:1
Structure type		Bixbyite		
Space group		$Ia\bar{3}$ (No. 206)		
Crystal system		Cubic		
Z		16		
a / pm	1013.32	1001.20(4)	995.17(4)	991.50(5)
V / 10^6 pm^3	1040.5	1003.62(7)	985.59(6)	974.73(8)
ρ_{calc} / g·cm^{-3}	5.78	7.54	8.47	9.58
Diffractometer	P1710	PANalytical X'Pert MPD Pro		
2θ / °	16.5–100	10–120		
λ / pm	154.060	154.060, 154.443		
		$I(\lambda_2)/I(\lambda_1) = 0.5$		
R_{wp}	0.073	0.0129	0.0126	0.0136
R_{exp}	0.051	0.0074	0.0080	0.0078
R_{Bragg}	0.025	0.0217	0.0146	0.0300
S	1.43	1.73	1.59	1.75

Table 6.2. Refined atomic parameters for TaZrN3.

Atom	Wyckoff	x	y	z	S.O.F.	B_{iso} / 10^4
Ta1	8*a*	0	0	0	0.5	0.89(7)
Zr1	8*a*	0	0	0	0.5	0.89(7)
Ta2	24*d*	0.28280(7)	0	¼	0.5	0.44(4)
Zr2	24*d*	0.28280(7)	0	¼	0.5	0.44(4)
N	48*e*	0.3549(8)	0.1340(9)	0.0942(7)	1	1

An overview of the prepared 1:1 samples is given in Table 6.3. The N/O ratio has a significant impact on the cell axis *a* and the *x* parameter of the 24*d* cation site, which is the only cation coordinate not fixed by space group symmetry.

Table 6.3. Cell parameter *a* and cation coordinate *x* of selected samples with a Ta:Zr ratio of 1:1.

Sum formula	Nitrogen content / anion %	*a* / pm	*x* (24*d*)
$Ta_{1.00}Zr_{1.00}O_{0.00}N_{3.00}$	100	995.17(4)	0.28280(9)
$Ta_{1.00}Zr_{1.00}O_{0.00}N_{3.00}$	100	995.60(4)	0.28363(8)
$Ta_{1.00}Zr_{1.00}O_{0.02}N_{2.99}$	99.3	995.74(5)	0.28422(10)
$Ta_{1.00}Zr_{1.00}O_{0.24}N_{2.84}$	92.2	995.96(5)	0.28380(10)
$Ta_{1.00}Zr_{1.00}O_{0.98}N_{2.35}$	70.6	1000.37(6)	0.27050(16)
$Ta_{1.00}Zr_{1.00}O_{1.67}N_{1.89}$	53.1	1007.93(5)	0.26324(15)

Taking a look at the present results, the *y* value of the general formula $TaZrO_{3y/2}N_{3-y}$ has the range of $0 \leq y \leq 1.11$. As it can be easily understood by reasons of charge neutrality, a consequence of increasing oxygen content is the increasing deviation from the ideal A_2X_3 composition ($A_2X_{3+\delta}$). While δ grows, more vacancies are occupied by anions and the crystal structure becomes more and more 'fluorite-like'. Therefore, the *x* (24*d*) coordinate is approaching ¼, which is the value for the cubic fluorite type. This is accompanied by lower intensities of the superstructure reflections in the X-ray diffraction patterns. With an increasing number of atoms inside the unit cell, the lattice parameter expands by *ca.* 12.75 pm. All this is depicted in Figure 6.3.

Phase-pure samples are predominantly nitrogen-rich. At higher oxygen contents, the formation of more than one phase is likely. It was not possible to cover the whole composition range up to the ideal fluorite-type (AX_2), as practiced for uranium nitride.[60, 61] Fluorite-type phases of tantalum oxide nitrides containing yttrium are known.[68] In the present system, the baddeleyite-type is the favored crystal structure for an AX_2 composition. The maximal 16*c* occupation in all our experiments ($\delta = 0.63$) was found for a sample with a Ta:Zr ratio of 1:2: $Ta_{0.67}Zr_{1.33}O_{2.22}N_{1.41}$.

A reamorphization of the samples can be observed at temperatures above 600 K in air. Under nitrogen atmosphere the sample is stable at least up to 1273 K.

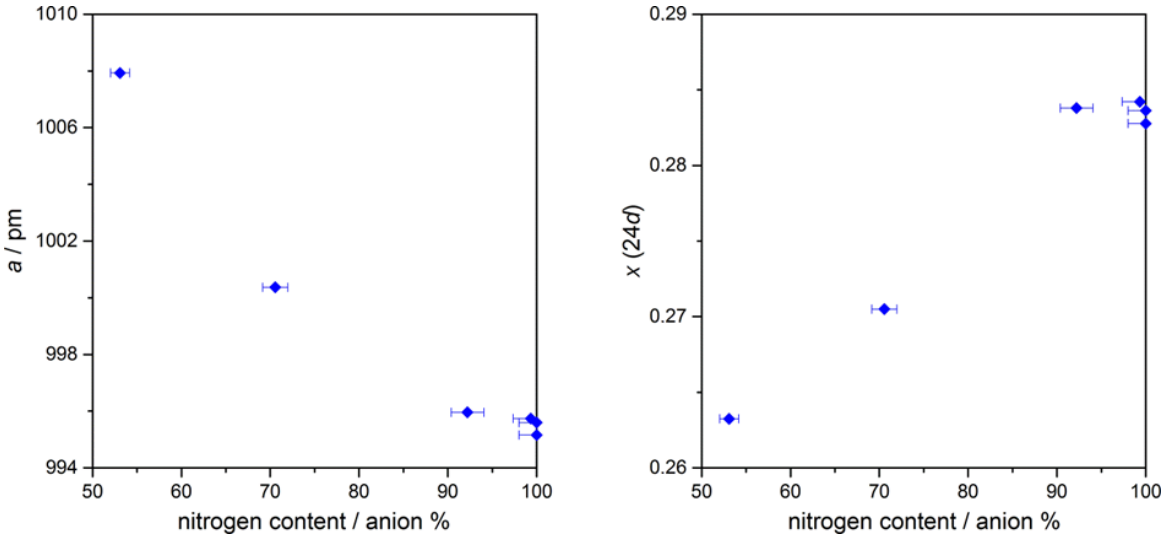

Figure 6.3. Dependency of unit cell parameter *a* and cation position *x* (24*d*) from the nitrogen content of the new bixbyite-type phases with an even cation ratio.

It can be expected that the nitrogen content should have an influence on the optical band gap. Products with an Ta:Zr ratio of 1:2 and a high oxygen content have a yellowish light-brown color and become darker with increasing nitrogen content. Five different samples were analyzed by UV-vis spectroscopy (diffuse reflectance geometry) in order to determine the optical band gaps. As an example, the Tauc plot of the absorbance spectra for the direct optical band gap of $Ta_{0.67}Zr_{1.33}O_{1.89}N_{1.63}$ (lowest nitrogen content) is depicted in Figure 6.4. The results for all investigated samples are summarized in Table 6.4.

Table 6.4. Optical band gaps of different bixbyite-type compounds.

Sum formula	Color	Direct band gap	Indirect band gap
$Ta_{0.67}Zr_{1.33}O_{1.89}N_{1.63}$	Light-brown	2.48 eV	1.87 eV
$Ta_{0.67}Zr_{1.33}O_{1.38}N_{1.97}$	Brown	2.31 eV	1.65 eV
$Ta_{0.67}Zr_{1.33}O_{0.42}N_{2.61}$	Red-black	1.93 eV	1.32 eV
$Ta_{1.00}Zr_{1.00}O_{0.00}N_{3.00}$	Black	1.72 eV	1.30 eV
$Ta_{1.33}Zr_{0.67}O_{0.12}N_{3.03}$	Black	1.71 eV	1.27 eV

A band gap of $E = 2.48$ eV should correspond to a yellowish colored product. Therefore, the direct band gaps are probably the most reliable values. Higher contents of nitrogen reduce the gap between valence and conduction band, which nicely corresponds to the theory of Phillips and Van Vechten.[69, 70]

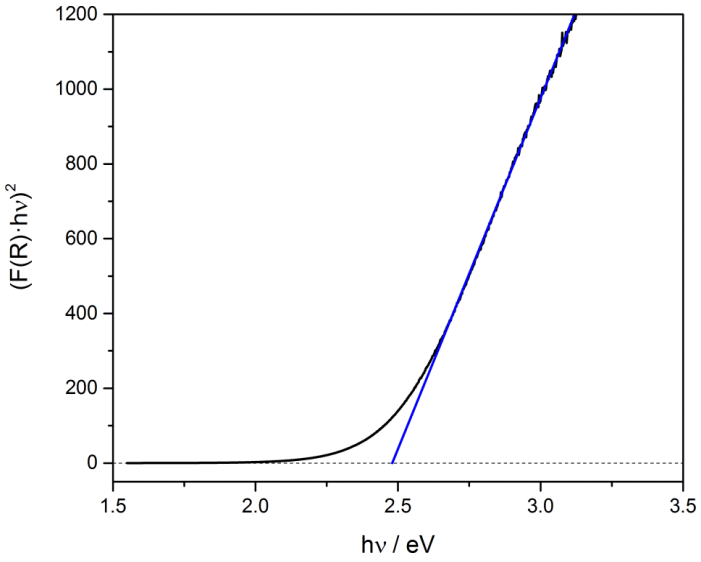

Figure 6.4.
UV-vis spectrum/Tauc plot (black) of $Ta_{0.67}Zr_{1.33}O_{1.89}N_{1.63}$ with Tauc plot determination of the direct optical band gap (blue).

These bixbyite-type phases are most likely the cubic side phases which have been reported by Grins *et al.*[41] No or only small superstructure reflections were observed in their powder XRD measurements. They excluded the bixbyite type as the adequate crystal structure. However, those superstructure reflections are clearly observable in the diffractograms presented here (see Figure 6.1).

Bixbyite-type phases containing tantalum are already known. Quaternary tantalum oxide nitrides with scandium also exhibit a dependency of the *a* and *x* (24*d*) parameters on the nitrogen content.[48] Because of the lower-valent scandium, the nitrogen content was far smaller (30–59 anion %) than in the Ta-Zr compounds presented here.[48,71]

The corresponding mixed-valent binary tantalum nitride Ta_2N_3 can only be realized by plasma-enhanced CVD at temperatures of 873–973 K[28] or sputter deposition[29] and has probably been synthesized several times before a definite phase identification was successful.[26,27,72] The cell parameter of $a = 982.05(4)$ pm[28] is consistent with our result of $a = 995.16(4)$ pm for the nitride compound, taking into account the smaller ionic radius of Ta^{4+} (68 pm) compared with the isovalent Zr^{4+} (72 pm).[64] Most recent investigations have shown a metastable behavior of these Ta_2N_3 films.[29] Transformation to δ-TaN_x-like phases can be observed at temperatures higher than 1123 K.

Sesquinitrides of lanthanides (Tb_2N_3, Dy_2N_3, Ho_2N_3, Tm_2N_3, and Lu_2N_3[73]) and actinides (U_2N_3[60], Np_2N_3[74]) are listed in databases. It should be noted that the final compositions of the lanthanide nitrides were not determined in the publication. Nitrides of other

metals, for example Be_3N_2,[75] Mg_3N_2,[76–78] Ca_3N_2,[79] Zn_3N_2,[76,78] and Cd_3N_2[80] exhibit the anti-bixbyite structure.

6.5 Conclusion

It was possible to complement the already well-studied system Ta-Zr-O-N by bixbyite-type compounds. The N/O ratio has a significant influence on the deviation δ from the ideal A_2X_3 bixbyite composition ($A_2X_{3+\delta}$), the cell parameter *a*, and the *x* coordinate of the 24*d* cation position. For a Ta:Zr ratio of 1:1, the ternary nitride $TaZrN_3$ could be prepared. Contrary to the main intention of this work, the search for metastable compounds, this new nitride phase can be considered as a stable analogue of the already known metastable Ta_2N_3. Experiments with lower Zr contents did not result in new phases.

6.6 Acknowledgement

This work was supported by the German Science Foundation (DFG) within the priority program SPP 1613. We thank Dr. Hefeng Cheng (research group Prof. Arne Thomas, TU Berlin) for assistance during UV-vis measurements.

6.7 References

(1) Hitoki, G.; Takata, T.; Kondo, J. N.; Hara, M.; Kobayashi, H.; Domen, K. *Chem. Commun.* **2002**, *2* (16), 1698–1699.

(2) Maeda, K.; Terashima, H.; Kase, K.; Domen, K. *Appl. Catal. A Gen.* **2009**, *357* (2), 206–212.

(3) Jansen, M.; Letschert, H. P. *Nature* **2000**, *404* (6781), 980–982.

(4) Lerch, M.; Lerch, J.; Hock, R.; Wrba, J. *J. Solid State Chem.* **1997**, *128* (2), 282–288.

(5) Gilles, J.-C. *Bull. Soc. Chim. Fr.* **1962**, *22*, 2118–2122.

(6) Gilles, J.-C. *Corros. Anticorros.* **1964**, *12*, 15–22.

(7) Collongues, R.; Gilles, J. C.; Lejus, A. M.; Perez y Jorba, M.; Michel, D. *Mater. Res. Bull.* **1967**, *2* (9), 837–848.

(8) Cheng, Y. B.; Thompson, D. P. *Spec. Ceram.* **1992**, *9*, 149–162.

(9) Lerch, M. *J. Am. Ceram. Soc.* **1996**, *79* (10), 2641–2644.

(10) Lerch, M. *J. Mater. Sci. Lett.* **1998**, *17* (6), 441–443.

(11) Michie, C. W.; Claridge, J. B.; Clarke, S. J.; Rosseinsky, M. J. *Chem. Mater.* **2003**, *15* (7), 1547–1553.

(12) Lerch, M.; Lerch, J. *J. Mater. Sci. Lett.* **1997**, *16* (17), 1454–1456.

(13) Van Arkel, A. E. *Phys. (The Hague)* **1924**, *4*, 286–301.

(14) Becker, K.; Ebert, F. *Z. Phys.* **1925**, *31* (1), 268–272.

(15) Juza, R.; Rabenau, A.; Nitschke, I. *Z. Anorg. Allg. Chem.* **1964**, *332* (1–2), 1–4.

(16) Lerch, M.; Füglein, E.; Wrba, J. *Z. Anorg. Allg. Chem.* **1996**, *622* (2), 367–372.

(17) Zerr, A.; Miehe, G.; Riedel, R. *Nat. Mater.* **2003**, *2* (3), 185–189.

(18) Brauer, G.; Weidlein, J. R. *Angew. Chem. Int. Ed.* **1965**, *4* (10), 875–875.

(19) Schilling, H.; Stork, A.; Irran, E.; Wolff, H.; Bredow, T.; Dronskowski, R.; Lerch, M. *Angew. Chem. Int. Ed.* **2007**, *46* (16), 2931–2934.

(20) Suzuki, A.; Hirose, Y.; Oka, D.; Nakao, S.; Fukumura, T.; Ishii, S.; Sasa, K.; Matsuzaki, H.; Hasegawa, T. *Chem. Mater.* **2014**, *26* (2), 976–981.

(21) Lüdtke, T.; Schmidt, A.; Göbel, C.; Fischer, A.; Becker, N.; Reimann, C.; Bredow, T.; Dronskowski, R.; Lerch, M. *Inorg. Chem.* **2014**, *53* (21), 11691–11698.

(22) Woodhead, K.; Pascarelli, S.; Hector, A. L.; Briggs, R.; Alderman, N.; McMillan, P. F. *Dalton Trans.* **2014**, *43* (25), 9647–9654.

(23) Nakhal, S.; Lumey, M.-W.; Bredow, T.; Dronskowski, R.; Lerch, M. *Z. Anorg. Allg. Chem.* **2010**, *636* (6), 1006–1012.

(24) Brauer, G.; Weidlein, J. R. *Angew. Chem. Int. Ed.* **1965**, *4* (3), 241–242.

(25) Gilles, J.-C. *C. R. Acad. Sci. Sér. C* **1968**, *266*, 546–547.

(26) Buvinger, E. A. *Appl. Phys. Lett.* **1965**, *7* (1), 14–15.

(27) Coyne, H. J.; Tauber, R. N. *J. Appl. Phys.* **1968**, *39* (12), 5585–5593.

(28) Ganin, A. Y.; Kienle, L.; Vajenine, G. V. *Eur. J. Inorg. Chem.* **2004**, *2004* (16), 3233–3239.

(29) Salamon, K.; Očko, M.; Radić, N.; Bogdanović Radović, I.; Despoja, V.; Bernstorff, S. *J. Alloys Compd.* **2016**, *682*, 98–106.

(30) Zerr, A.; Miehe, G.; Li, J.; Dzivenko, D. A.; Bulatov, V. K.; Höfer, H.; Bolfan-Casanova, N.; Fialin, M.; Brey, G.; Watanabe, T.; Yoshimura, M. *Adv. Funct. Mater.* **2009**, *19* (14), 2282–2288.

(31) Salamat, A.; Woodhead, K.; Shah, S. I. U.; Hector, A. L.; McMillan, P. F. *Chem. Commun.* **2014**, *50* (70), 10041–10044.

(32) Schönberg, N. *Acta Chem. Scand.* **1954**, *8*, 199–203.

(33) Brauer, G.; Zapp, K. H. *Naturwissenschaften* **1953**, *40* (23), 604–604.

(34) Brauer, G.; Zapp, K. H. *Z. Anorg. Allg. Chem.* **1954**, *277* (3–4), 129–139.

(35) Terao, N. *Jpn. J. Appl. Phys.* **1971**, *10* (2), 248–259.

(36) Conroy, L. E.; Christensen, A. N. *J. Solid State Chem.* **1977**, *20* (2), 205–207.

(37) Gatterer, J.; Dufek, G.; Ettmayer, P.; Kieffer, R. *Monatsh. Chem.* **1975**, *106* (5), 1137–1147.

(38) Christensen, A. N.; Lebech, B. *Acta Crystallogr. Sect. B* **1978**, *34* (1), 261–263.

(39) Brauer, G.; Mohr, E.; Neuhaus, A.; Skokan, A. *Monatsh. Chem.* **1972**, *103* (3), 794–798.

(40) Schönberg, N. *Acta Chem. Scand.* **1954**, *8*, 627–629.

(41) Grins, J.; Käll, P.-O.; Svensson, G. *J. Mater. Chem.* **1994**, *4* (8), 1293–1301.

(42) Guenther, E.; Jansen, M. *Mater. Res. Bull.* **2001**, *36* (7–8), 1399–1405.

(43) Pastrana-Fábregas, R.; Isasi-Marín, J.; Sáez-Puche, R. *J. Mater. Res.* **2006**, *21* (9), 2255–2260.

(44) Lowther, J. E. *Phys. Rev. B* **2006**, *73* (13), 134110-1–8.

(45) Aouadi, S. M.; Filip, P.; Debessai, M. *Surf. Coatings Technol.* **2004**, *187* (2–3), 177–184.

(46) Ruan, J.-L.; Huang, J.-L.; Lu, H.-H.; Chen, J. S.; Lii, D.-F. *Thin Solid Films* **2011**, *519* (15), 4987–4991.

(47) Schilling, H.; Lerch, M.; Börger, A.; Becker, K.-D.; Wolff, H.; Dronskowski, R.; Bredow, T.; Tovar, M.; Baehtz, C. *J. Solid State Chem.* **2006**, *179* (8), 2416–2425.

(48) Stork, A.; Schilling, H.; Wessel, C.; Wolff, H.; Börger, A.; Baehtz, C.; Becker, K.-D.; Dronskowski, R.; Lerch, M. *J. Solid State Chem.* **2010**, *183* (9), 2051–2058.

(49) Bredow, T.; Lumey, M.-W.; Dronskowski, R.; Schilling, H.; Pickardt, J.; Lerch, M. *Z. Anorg. Allg. Chem.* **2006**, *632* (7), 1157–1162.

(50) Cosgun, S.; Rohloff, M.; Göbel, C.; Gernert, U.; Fischer, A.; Lerch, M. *Z. Anorg. Allg. Chem.* **2014**, *640* (14), 2771–2775.

(51) Pechini, M. P. Method of Preparing Lead and Alkaline Earth Titanates and Niobates and Coating Method using the same to form a capacitor. USPTO 3330697, 1967.

(52) Okubo, T.; Kakihana, M. *J. Alloys Compd.* **1997**, *256* (1–2), 151–154.

(53) Rodríguez-Carvajal, J. In *Abstracts of the Satellite Meeting on Powder Diffraction of the XV IUCr Congress*; 1990; pp. 127.

(54) Tauc, J.; Grigorovici, R.; Vancu, A. *Phys. Status Solidi B* **1966**, *15* (2), 627–637.

(55) Tauc, J. *Mater. Res. Bull.* **1968**, *3* (1), 37–46.

(56) Zachariasen, W. *Z. Kristallogr.* **1928**, *67* (1–6), 455–464.

(57) Pauling, L.; Shappell, M. D. *Z. Kristallogr.* **1930**, *75* (1), 128–142.

(58) Marezio, M. *Acta Crystallogr.* **1966**, *20* (6), 723–728.

(59) Ramos-Gallardo, A.; Vegas, A. *J. Solid State Chem.* **1995**, *119* (1), 131–133.

(60) Rundle, R. E.; Baenziger, N. C.; Wilson, A. S.; McDonald, R. A. *J. Am. Chem. Soc.* **1948**, *70* (1), 99–105.

(61) Masaki, N.; Tagawa, H. *J. Nucl. Mater.* **1975**, *57* (2), 187–192.

(62) Füglein, E.; Hock, R.; Lerch, M. *Z. Anorg. Allg. Chem.* **1997**, *623* (1–6), 304–308.

(63) Nakhal, S.; Hermes, W.; Ressler, T.; Pöttgen, R.; Lerch, M. *Z. Naturforsch.* **2009**, *64b*, 281–286.

(64) Shannon, R. D.; Prewitt, C. T. *Acta Crystallogr. Sect. B* **1969**, *25* (5), 925–946.

(65) Reimann, C.; Weber, D.; Lerch, M.; Bredow, T. *J. Phys. Chem. C* **2013**, *117* (39), 20164–20170.

(66) Clarke, S. J.; Michie, C. W.; Rosseinsky, M. J. *J. Solid State Chem.* **1999**, *146* (2), 399–405.

(67) Bredow, T.; Lerch, M. *Z. Anorg. Allg. Chem.* **2004**, *630* (13–14), 2262–2266.

(68) Schilling, H.; Wolff, H.; Dronskowski, R.; Lerch, M. *Z. Naturforsch.* **2006**, *61b* (6), 660–664.

(69) Phillips, J. C. *Science* **1970**, *169* (3950), 1035–1042.

(70) Phillips, J. C.; Van Vechten, J. A. *Phys. Rev. B* **1970**, *2* (6), 2147–2160.

(71) Cosgun, S. *Synthese und Charakterisierung Tantaloxidnitrid-basierter Verbindungen für die photokatalytische Wasserspaltung*; Technische Universität Berlin: Berlin, 2015.

(72) Shin, C. S.; Kim, Y. W.; Gall, D.; Greene, J. E.; Petrov, I. *Thin Solid Films* **2002**, *402* (1–2), 172–182.

(73) Kieffer, R.; Ettmayer, P.; Pajakoff, S. W. *Monatsh. Chem.* **1972**, *103* (5), 1285–1298.

(74) Silva, G. W. C.; Weck, P. F.; Kim, E.; Yeamans, C. B.; Cerefice, G. S.; Sattelberger, A. P.; Czerwinski, K. R. *J. Am. Chem. Soc.* **2012**, *134* (6), 3111–3119.

(75) Reckeweg, O.; Lind, C.; Simon, A.; DiSalvo, F. J. *Z. Naturforsch.* **2003**, *58b* (2–3), 159–162.

(76) von Stackelburg, M.; Paulus, R. *Z. Phys. Chem.* **1933**, *B22*, 305–322.

(77) David, J.; Laurent, Y.; Lang, J. *Bull. la Soc. Fr. Mineral. Cristallogr.* **1971**, *94*, 340–346.

(78) Partin, D. E.; Williams, D. J.; O'Keeffe, M. *J. Solid State Chem.* **1997**, *132* (1), 56–59.

(79) Laurent, Y.; Lang, J.; Le Bihan, M. T. *Acta Crystallogr. Sect. B* **1968**, *24* (4), 494–499.

(80) Karau, F.; Schnick, W. *Z. Anorg. Allg. Chem.* **2007**, *633* (2), 223–226.

7 Publication 4

A Density-Functional Theory Approach to the Existence and Stability of Molybdenum and Tungsten Sesquioxide Polymorphs

Nils Becker, Christoph Reimann, Dominik Weber, Tobias Lüdtke,
Martin Lerch, Thomas Bredow, Richard Dronskowski

Postprint
Zeitschrift für Kristallographie - Crystalline Materials **2017**, *232*(1–3), 69–75
DOI: 10.1515/zkri-2016-1960
https://www.degruyter.com/view/j/zkri.2017.232.issue-1-3/
zkri-2016-1960/zkri-2016-1960.xml

Contribution to publication:

N. Becker	Quantum-chemical calculations, writing.
C. Reimann	Quantum-chemical calculations.
D. Weber	Conventional synthesis experiments.
T. Lüdtke:	Conventional synthesis experiments, writing.
M. Lerch:	General discussion, proofreading.
T. Bredow	General discussion, proofreading.
R. Dronskowski	General discussion, proofreading.

Overall contribution of T. Lüdtke to the publication: 10%

Authors. Nils Becker,[a,b] Christoph Reimann,[c] Dominik Weber,[d] Tobias Lüdtke,[d] Martin Lerch,[d] Thomas Bredow,[c] Richard Dronskowski [a,b,*]

(a) Institut für Anorganische Chemie, RWTH Aachen University, Landoltweg 1, D-52056 Aachen, Germany
(b) Jülich-Aachen Research Alliance (JARA-HPC), RWTH Aachen University, D-52056 Aachen, Germany
(c) Institut für Physikalische und Theoretische Chemie, Universität Bonn, Wegelerstraße 12, D-53115 Bonn, Germany
(d) Institut für Chemie, Technische Universität Berlin, Straße des 17. Juni 135, D-10623 Berlin, Germany

* Corresponding author

Keywords. DFT; high-pressure; molybdenum; sesquioxide; tungsten.

Supporting Information. DFT technicalities. Metal bonds in the corundum type. This material is available *via* the Internet at https://www.degruyter.com/view/j/zkri.2017.232.issue-1-3/zkri-2016-1960/zkri-2016-1960.xml.

Received: 25.05.2016
Accepted: 04.08.2016
Published online: 26.08.2016

Reprinted (adapted) with permission from Becker, N.; Reimann, C.; Weber, D.; Lüdtke, T.; Lerch, M.; Bredow, T.; Dronskowski, R. A density-functional theory approach to the existence and stability of molybdenum and tungsten sesquioxide polymorphs. *Z. Kristallogr.* **2017**, *232*(1–3), 69–75.

7.1 Abstract

The sesquioxides of molybdenum and tungsten have been reported as thin films or on surfaces as early as 1971, but the preparation of bulk materials and their crystal structures are still unknown up to the present day. We present a systematic *ab initio* approach to their possible syntheses and crystal structures applying complementary methods and basis-set types. For both compounds, the corundum structure is the most stable and does not display any imaginary frequencies. Calculations targeted at a high-pressure synthesis starting from the stable oxides and metals predict a reaction pressure of 15 GPa for Mo_2O_3 and over 60 GPa for W_2O_3.

7.2 Introduction

The distinct behavior of the d-block elements also applies within the chromium group. Accordingly, molybdenum and tungsten are the heavier atoms of this group and show similar atomic and ionic radii which also leads to an alike chemical behavior and is the result (at least in part) of the lanthanide contraction. Chromium as the lighter atom has a smaller radius and behaves differently, not too surprisingly. The difference between chromium and its heavier homologues molybdenum and tungsten, however, is not as significant as it is in the adjacent vanadium group.

It is quite puzzling to note that the inorganic crystal structure database (ICSD) does not list any sesquioxides of molybdenum or tungsten. Nonetheless, there is a first report on a cubic polymorph of both molybdenum and tungsten sesquioxide by Palatnik *et al.*,[1] which, however, only provides the lattice parameters for the proposed cubic structures, namely $a = 6.84$ Å for Mo_2O_3 and $a = 6.86$ Å for W_2O_3. Second, a composition dubbed Mo_2O_3 and W_2O_3 was also reportedly obtained on the surface of oxygen-implanted single crystals of molybdenum and tungsten.[2] The observed surface layers, however, were amorphous as a result of oxygen-ion bombardment. Third, the synthesis of tungsten(III) oxide was again claimed as a thin film *via* atomic layer deposition in 2006[3] but no details on the crystal structure could be given as the X-ray diffraction data indicated that the samples were amorphous.

As a first experimental attempt, a conventional synthetic approach inspired by the successful synthesis of the metastable sesquioxides of vanadium was used.[4] Different oxide (crystalline and amorphous) and oxide fluoride precursors were reduced with altered H_2/Ar flow rates. The usage of hexafluorides is difficult due to their liquid (Mo) and gas-

eous (W) aggregate state at ambient conditions. Additionally, experiments with oxide hydrates and oxide nitrides were performed as well. All results were more than underwhelming. Well-known phases such as MoO_2 and WO_2 were predominantly formed throughout all experiments. Other typical results were highly amorphous samples. Motivated by the lack of experimentally confirmed crystal structures, we used density-functional theory to present a first-principles approach to the crystal structures and possible synthetic routes to molybdenum and tungsten sesquioxide.

7.3 Theoretical Methodology

Periodic density-functional theory (DFT) calculations were performed as implemented in the Vienna ab initio simulation package (VASP).[5] Core and valence electrons were separated using projector-augmented waves (PAW),[6] and the generalized-gradient-approximation as described by Perdew, Burke and Ernzerhof (GGA-PBE)[7,8] was used to treat contributions of exchange and correlation. An energy-cutoff of 500 eV and an adapted *k*-point sampling ensured well-converged structures. The *k*-point grid was increased until the number of *k*-points multiplied with the number of atoms was >5000, a sufficient criterion in the past; numerical values are given in the Supporting Information (Chapter 7.8). All lattice parameters and atomic positions were allowed to relax until the ionic convergence criterion of 10^{-6} eV was reached. For selected cases (*i.e.* Al_2O_3 as the reference structure, La_2O_3 and Sb_2O_3) additional corrections for van der Waals forces were included, namely Grimme's "D3(BJ)" dispersion correction with Becke-Johnson damping[9,10] as implemented in VASP 5.3.5.

To investigate the unknown crystal structures of the hypothetical compounds Mo_2O_3 and W_2O_3, a set of 13 well-known A_2X_3 structures was chosen as starting structures, namely the same used in our previous studies on the sesquioxides of Cr, Nb and Ta. A full relaxation of the structures including atomic positions and cell parameters was performed to ensure the lowest-energy structure to be found. To speed up the calculations, symmetry was applied while iterating but no explicit symmetry reduction or change to subgroups was introduced, unless automatically occurring during optimization. To predict high-pressure polymorphs, the volume of the optimized structures at ambient pressure was varied by scaling the cell parameters from 94% to 104%, and the resulting energy vs. volume data were fitted to the Birch–Murnaghan equation of state.[11] Thus, the pressure and, eventually, the reaction enthalpies as a function of the pressure were calculated.

The dynamic stability of selected M_2O_3 candidates was investigated by calculating the phonon density of states (PDOS) using the program PHONOPY.[12] As a first step, supercells of the optimized structures were constructed. All symmetry-inequivalent atoms were then slightly shifted out of their equilibrium positions to numerically calculate the Hellmann–Feynman forces. Subsequently, the force constants and then the dynamical matrices were computed. Phonon frequencies and eigenvectors were calculated from the dynamical matrices. The PDOS can then be assessed by summing up over all phonon frequencies.[13]

As a complementary approach and in order to investigate the influence of exact exchange on the electronic ground states and the relative stabilities of the polymorphs, we also calculated the same set of 13 structures with the crystalline-orbital program CRYSTAL14.[14] Here, the Bloch functions are represented by atom-centered basis functions. The localized nature of the basis functions leads to an efficient calculation of exact exchange. For comparison with the VASP-PBE results, we employed the hybrid functional PW1PW which has been previously used in similar studies of thermodynamic and electronic properties of transition-metal oxides.[15,16] The Hartree–Fock contribution of this functional is 20%, and it was optimized towards the band gaps of MgO, NiO, and CoO.[17] The basis sets remained unmodified. Atomic basis sets of standard quality were selected for Mo,[18] W,[19] and O.[20] We then considered closed-shell diamagnetic (DM), open-shell ferromagnetic (FM) and antiferromagnetic (AFM) states. Full optimizations within the symmetry restrictions of the space groups and their magnetic subgroups were performed. In what follows in tabular form, only the relative energies of the lowest magnetic states of the polymorphs are given. Magnetic calculations with FM and AFM ordering resulted in zero magnetic moments and identical energy values for the stable corundum type structure when using VASP.

7.4 Results and Discussion

As said before, a set of 13 well-known A_2X_3 starting structures was first fully optimized for both compositions Mo_2O_3 and W_2O_3 with VASP-PBE and CRYSTAL-PW1PW. The resulting energies and volumes are listed in Table 7.1 for the molybdenum and Table 7.2 for the tungsten case. The corundum-type [Al_2O_3] starting structure resulted in the lowest total energy for both elements. The fully relaxed structure resembles the corundum starting structure quite well but with one significant difference: the previously slightly distorted hexagonal close packing (hcp) of the oxygen atoms becomes perfectly ordered

Table 7.1. Molar volumes and relative energies per formula unit for hypothetical molybdenum sesquioxide Mo_2O_3 polymorphs as a function of computational methodology and magnetic state (DM = diamagnetic, FM = ferromagnetic, AFM = antiferromagnetic). The listed structures represent the starting structures.

Structure	V(PBE) / Å^3	ΔE(PBE) / eV	ΔE(PBE-D3) / eV	ΔE(PW1PW) / eV
Al_2O_3[21]	54.02	0.00	0.00	0.00 (AFM)
V_2O_3[22]	54.02	0.00		0.00 (DM)
Ga_2O_3[23]	55.22	0.30		0.61 (DM)
Rh_2O_3[24]	53.51	0.51		0.51 (AFM)
Sm_2O_3[25]	57.15	0.69		1.21 (FM)
Sb_2O_3[26]	61.75	0.70	0.90	0.80 (AFM)
Au_2O_3[27]	53.54	0.95		2.12 (AFM)
Fe_2O_3[28,29]	57.56	1.04		1.93 (AFM)
Sb_2S_3[30]	58.08	1.39		1.01 (AFM)
$GdFeO_3$[31]	53.07	1.94		1.45 (AFM)
La_2O_3[32]	60.99	1.98	2.11	1.59 (AFM)
Bixbyite[33]	56.47	2.07		1.34 (AFM)
Ag_2O_3[34]	57.65	2.84		1.77 (AFM)

Table 7.2. Molar volumes and relative energies per formula unit for hypothetical tungsten sesquioxide W_2O_3 polymorphs as a function of computational methodology and magnetic state (DM = diamagnetic, FM = ferromagnetic, AFM = antiferromagnetic). The listed structures represent the starting structures.

Structure	V(PBE) / Å^3	ΔE(PBE) / eV	ΔE(PBE-D3) / eV	ΔE(PW1PW) / eV
Al_2O_3[21]	54.50	0.00	0.00	0.00 (AFM)
V_2O_3[22]	54.50	0.00		0.00 (AFM)
Rh_2O_3[24]	54.01	0.50		1.04 (AFM)
Sm_2O_3[25]	58.00	0.66		2.04 (AFM)
Ga_2O_3[23]	58.79	0.91		1.38 (AFM)
Fe_2O_3[28,29]	59.56	0.98		1.12 (AFM)
Au_2O_3[27]	53.98	1.23		0.49 (AFM)
Sb_2S_3[30]	59.47	1.66		0.42 (AFM)
Sb_2O_3[26]	57.37	1.77	0.14	0.34 (AFM)
$GdFeO_3$[31]	52.73	2.20		0.82 (AFM)
La_2O_3[32]	62.03	2.28	2.42	1.18 (AFM)
Bixbyite[33]	56.75	2.49		0.76 (AFM)
Ag_2O_3[34]	57.62	2.89		1.04 (AFM)

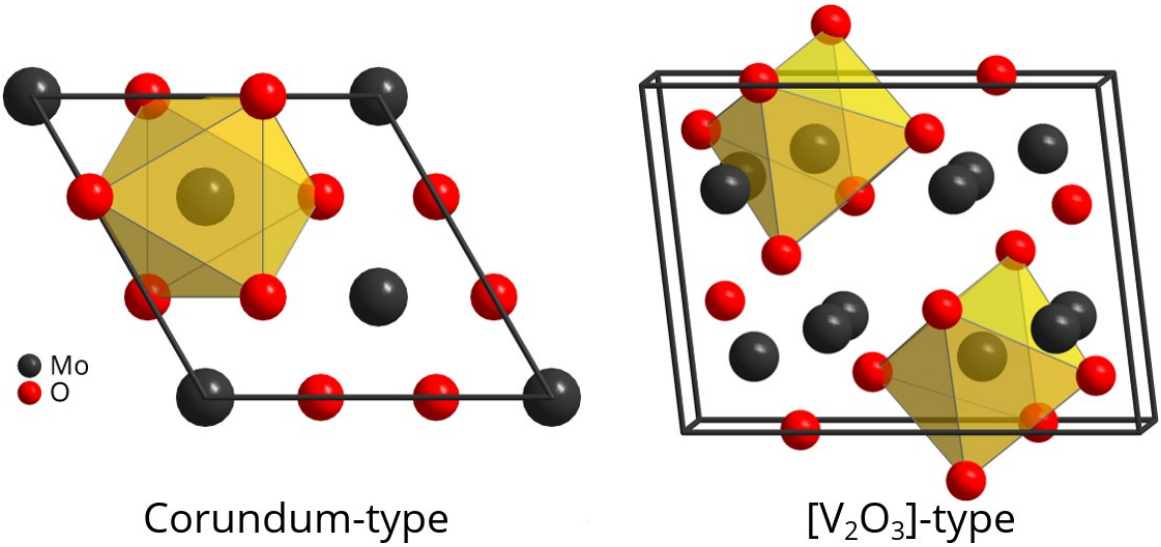

Figure 7.1. Relaxed crystal structure of Mo_2O_3 (and W_2O_3) in the corundum structure (left) displaying the lowest energy. The $[V_2O_3]$ starting structure (right) transforms into the corundum structure (left) upon structural relaxation.*

in the relaxed structure. The origin of this effect could not be determined yet, but a magnetic effect is unlikely, as a magnetic moment was unstable in the calculations. When performing the identical relaxation with Al_2O_3 in the corundum structure, the ordering phenomenon was not observed. Therefore, a temperature effect also seems unlikely. Furthermore, the monoclinic $[V_2O_3]$ starting structure (Figure 7.1, right) transforms into the corundum structure upon structural optimization and, thus, arrives at the same total energy.

Once again, this applies to both sesquioxides of molybdenum and tungsten which is why we only depict the structure of Mo_2O_3 in Figure 7.1. We also note that this behavior ($V_2O_3 \rightarrow Al_2O_3$) has previously been observed in a similar DFT investigation for chromium sesquioxide, in which the $[V_2O_3]$ starting structure also transformed into the corundum structure upon structural optimization. No starting structure type seems to be within a reasonable energetic range of about 0.2 eV ($\approx 20\ kJ{\cdot}mol^{-1}$ per formula unit) to the corundum structure type which is the energetically preferred structure for both investigated sesquioxides. This is also true when the CRYSTAL-PW1PW results are considered. Despite the fact that the magnetic ground states derived from VASP-PBE and CRYS CRYSTAL-PW1PW are different in many cases, which then leads to a different ordering of the less stable polymorphs, the corundum and $[V_2O_3]$-derived structures are clearly preferred over all the others. The stability differences between these structures and other

phases increases even more whenever London dispersion interactions (needed in particular for layered structures) are taken into account. Therefore, and for reasons of computational efficiency, we will continue our investigation only with the corundum structure type. The calculated cell parameters and atomic positions for Mo_2O_3 and W_2O_3 are listed in Table 7.3.

Table 7.3. Structural details and molar volumes of molybdenum and tungsten sesquioxide in the corundum structure based on VASP-PBE calculations.

Mo_2O_3	$R\bar{3}c$ (No. 167)	Atom	x	y	z
a	4.710 Å	Mo	0	0	0.163
c	16.874 Å	O	⅓	0	¼
Z	6				
V	54.01 Å^3				
W_2O_3	$R\bar{3}c$ (No. 167)	Atom	x	y	z
a	4.663 Å	W	0	0	0.163
c	17.366 Å	O	⅓	0	¼
Z	6				
V	54.50 Å^3				

For the most stable corundum polymorphs of both Mo_2O_3 and W_2O_3 the electronic density of states was calculated with CRYSTAL-PW1PW. This is because, quite generally, hybrid methods provide a more accurate description of the electronic structure compared to semilocal GGA functionals. In Figure 7.2, the projected density of states of the highest valence and lowest conduction bands are shown for the AFM ground states.

The electronic structures of the two compounds are rather similar. In both cases, the valence band and the conduction band predominantly consist of metal 4d (5d) orbitals, respectively, but with significant contributions from the O 2p states, indicating a partially covalent bonding. The upper part of the valence band of W_2O_3 (right frame) is split into two domains from 0 to −2 eV and between −2 and −4 eV below the Fermi energy. Mo_2O_3 (left frame) only shows one domain between 0 and −2 eV. This is possibly due to a smaller distortion from octahedral site symmetry of the metal ions in Mo_2O_3 so that the splitting of the t_{2g} orbitals is smaller in this compound. The fundamental band gap of Mo_2O_3 (2.39 eV) is slightly larger than that of W_2O_3 (1.84 eV) at PW1PW level of theory. If the calculated electronic band gaps are a reasonable approximation to the optical band gaps, i.e. if the excitonic effects are small, then molybdenum sesquioxide could be a

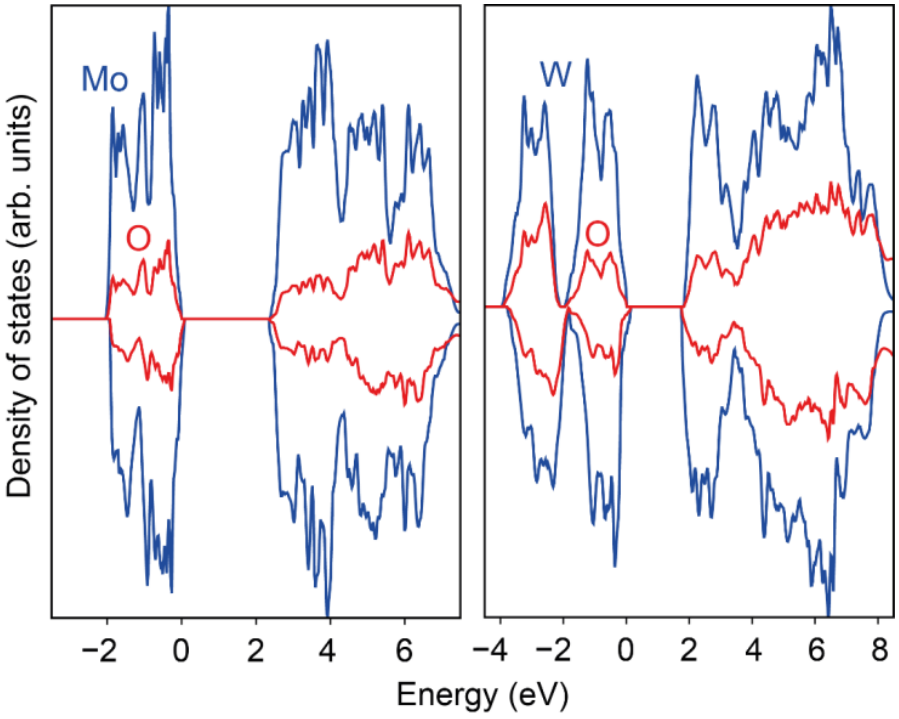

Figure 7.2. Projected density of states for both sesquioxides in the corundum structure according to CRYSTAL-PW1PW. The orbital energy is given relative to the Fermi energy.

promising candidate for photocatalytical applications since the gap is in the optimal region, *e.g.* for water splitting.

Prior to an investigation of possible synthetic routes, we performed phonon calculations on the sesquioxides of molybdenum and tungsten with VASP-PBE taking the corundum structure. The calculated phonon densities of states (PDOS) depicted in Figure 7.3 show no imaginary modes for both sesquioxides and thereby verify their dynamic stability.

Having identified the corundum structure as the most likely one for Mo_2O_3 and W_2O_3, we then considered various reaction routes to estimate the feasibility of their syntheses. The selected pathways are limited to solid-state materials and only include the metals and their different oxides. Molybdenum and tungsten both only form two oxides with an integer oxidation state, namely the dioxide and the trioxide, and therefore allowing only two simple reaction routes to be computationally explored:

(I) $M + MO_3 \rightarrow M_2O_3$

(II) $^1/_2\ M + {}^3/_2\ MO_2 \rightarrow M_2O_3$

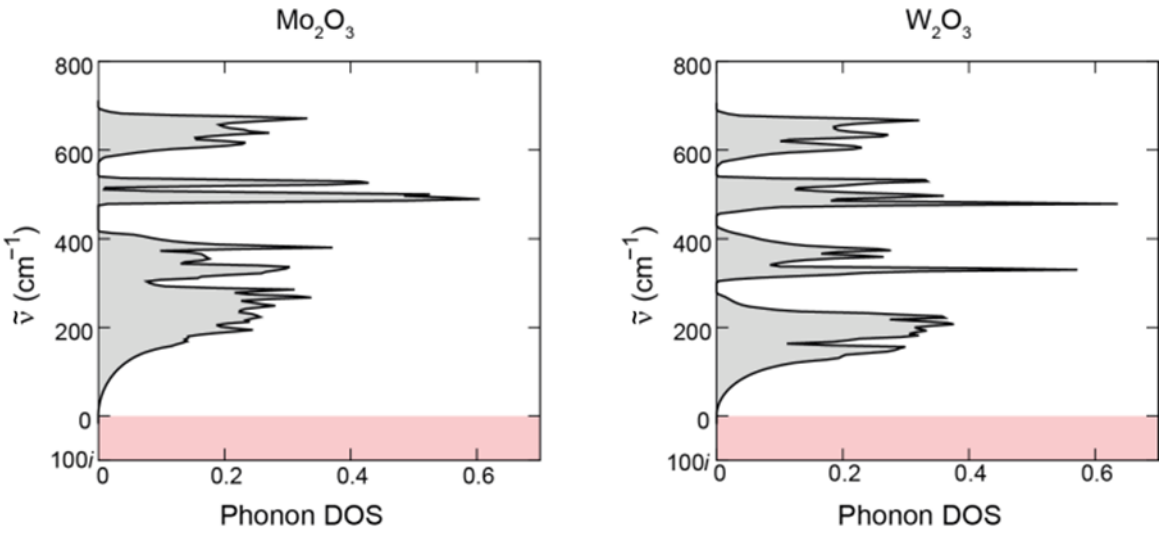

Figure 7.3. Calculated phonon DOS of both sesquioxides in the corundum structure based on VASP-PBE results.

The corresponding reaction enthalpies and volumes relative to the reactants are listed in Table 7.4.

Table 7.4. Relative theoretical reaction enthalpies and volumes of M_2O_3 for the hypothetical reaction routes I and II based on VASP-PBE results.

Synthesis	Mo_2O_3		W_2O_3	
	ΔV / Å^3	ΔH_R / kJ·mol^{-1}	ΔV / Å^3	ΔH_R / kJ·mol^{-1}
(I) $M + MO_3 \rightarrow M_2O_3$	−20.30	−89.26	−19.38	105.91
(II) $\frac{1}{2}M + \frac{3}{2}MO_2 \rightarrow M_2O_3$	−4.56	37.06	−4.16	104.62

When investigating such reaction enthalpies, one has to be aware of two key issues: first, the reactions are always equilibrium reactions and, second, they compete with each other. For example: if reaction (I) is exothermic, the reactants will yield the product of route (I). This product, however, will decay into the reactants of reaction (II) in case the latter is endothermic. As a consequence, all possible reaction routes must show exothermic reaction enthalpies for the proposed synthetic conditions.

The synthesis of Mo_2O_3 *via* the trioxide route (I) is exothermic while route II shows a positive reaction enthalpy of ca. 37 kJ·mol^{-1}. Also, the large volume loss of the product relative to the reactants calls for a high-pressure synthesis. For W_2O_3, both reaction routes show very similar reaction enthalpies of about 105 kJ·mol^{-1}and a negative relative

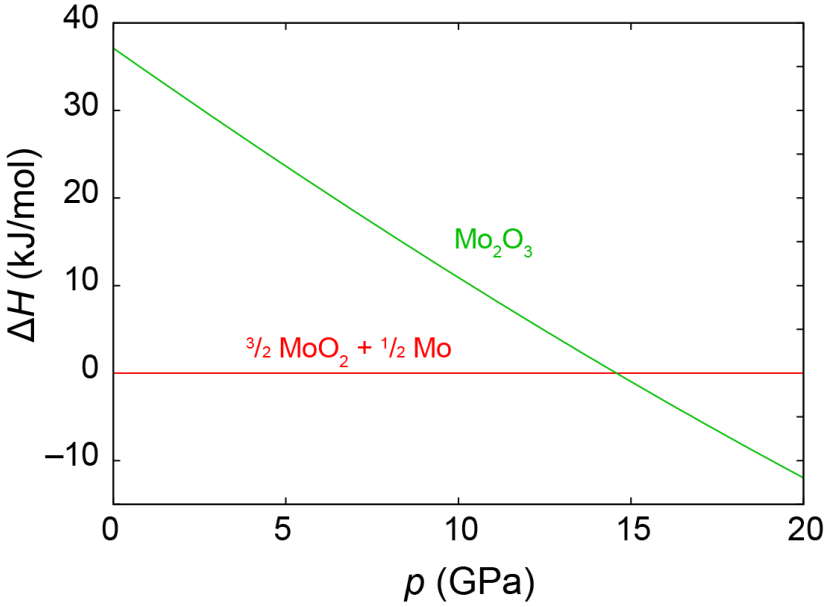

Figure 7.4. Density-functional (VASP-PBE) enthalpy-pressure diagram for the synthesis of Mo_2O_3 in the corundum structure *via* reaction (II).

volume. Hence, only a high-pressure synthesis is a good choice for the tungsten sesquioxides, as well.

To calculate the pressure dependence of all materials, the energy vs. volume curves were calculated for all reactants and products. By fitting the results to the Birch–Murnaghan equation of state[11] and subsequent differentiation, the energy dependence of the pressure is obtained. The pressure-dependent enthalpies can be obtained *via* $H = E + pV$ which are depicted in Figure 7.4 and Figure 7.5 relative to the corresponding reactants. According to Figure 7.4, Mo_2O_3 should form around 15 GPa, not necessarily a routine high-pressure experiment, but still manageable. As mentioned in the introduction, it is impossible to synthesize Mo_2O_3 *via* a conventional synthesis route at ambient pressure. Reduction of MoO_3, $MoO_3{\cdot}H_2O$, molybdenum oxide nitrides, and molybdenum oxide fluorides with various H_2/Ar gas mixtures at temperatures above 548 K always resulted in the formation of MoO_2 and more complex phases like Mo_4O_{11} or $Mo_{18}O_{52}$.

As shown in Figure 7.5, the two possible reaction routes for W_2O_3 require quite different pressures. At a pressure of about 12 GPa the sesquioxide becomes more favorable than the reactants of route (I), while route (II) needs a pressure of more than 60 GPa to yield the sesquioxide. Of course, this huge difference is a direct consequence of the more negative relative volume of reaction (I) (Table 7.4). An attempt to prepare bulk W_2O_3 therefore requires very high pressures of over 60 GPa and is experimentally quite chal-

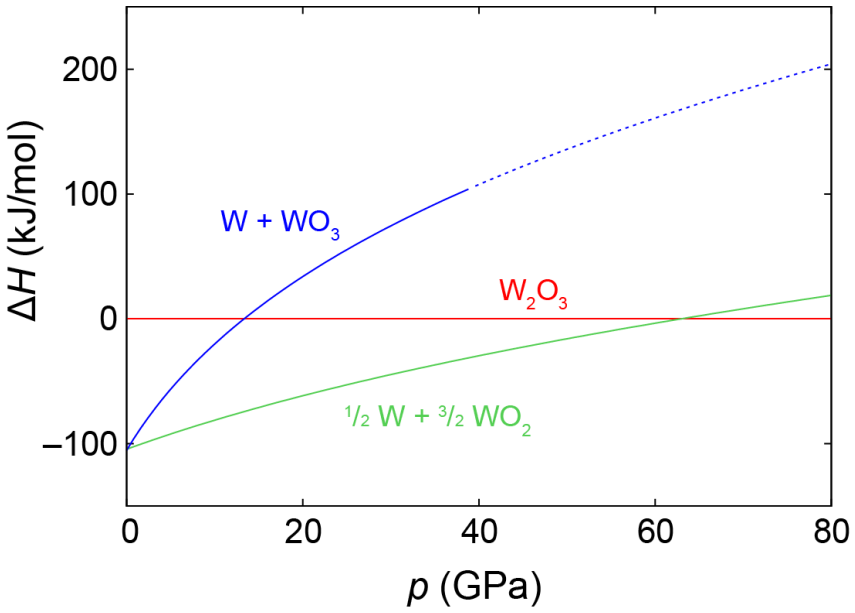

Figure 7.5. Density-functional (VASP-PBE) enthalpy-pressure diagram for the synthesis of W_2O_3 *via* reaction I (blue, extrapolated for $p > 40$ GPa) and reaction II (green).

lenging. The role of the entropy is rather small for both sesquioxides: at 300 K the entropy term is only about 2 kJ·mol^{-1} for the relevant dioxide route (II) and, thus, the influence on the transition pressures is tiny (under 1 GPa). All these findings are reflected by our unsuccessful attempts in synthesizing this phase at ambient pressure. The range of used precursors and reaction conditions were comparable to those of the lighter homologue. Additionally, different oxide chlorides were also tested. Summarizing the results, it can be stated that even at the lowest possible H_2 flow rate (0.01 L·h^{-1}), reduction of the precursor to tungsten metal was observed at temperatures above 873 K. At lower temperatures, WO_2 was the main product.

7.5 Conclusion

Density-functional theory calculations by means of the GGA and a hybrid level on different sesquioxide structures with the composition Mo_2O_3 and W_2O_3 yield the corundum type as the structure with the lowest energy. Upon structural optimization, the monoclinic [V_2O_3] structure transforms into the corundum structure, as was previously also observed for Cr_2O_3. All other investigated structures are energetically much less favorable and therefore are not likely to be found for the sesquioxides of molybdenum and tungsten. Hypothetical synthetic routes were analyzed to estimate the feasibility of the preparation. The synthesis of Mo_2O_3 should be possible *via* the dioxide at a pressure above

15 GPa, while a synthesis of W_2O_3 requires a transition pressure > 60 GPa and should be accomplished *via* the dioxide, as well. Such high-pressure experiments are in progress. Phonon calculations concerning the dynamic stability of both sesquioxides suggest that they are stable.

7.6 Acknowledgement

This work was supported by the DFG within the priority program SPP 1415. We thank the computing center at RWTH Aachen University for providing large amounts of CPU time.

7.7 References

(1) Palatnik, L. S.; Obol'yaninova, O. A.; Naboka, M. N.; Gladkikh, N. T. *Izvestiya Akademii Nauk SSSR, Neorganicheskie Materialy* **1973**, *9* (5), 801–804.

(2) Eristavi, B. G.; Diasamidze, E. M.; Dekanosidze, R. N.; Maisuradze, N. I.; Kutelia, E. R.; Sichinava, A. V.; Menabde, N. E. *Acta Metall. Mater.* **1991**, *39* (7), 1703–1710.

(3) Dezelah, C. L.; El-Kadri, O. M.; Szilágyi, I. M.; Campbell, J. M.; Arstila, K.; Niinistö, L.; Winter, C. H. *J. Am. Chem. Soc.* **2006**, *128* (30), 9638–9639.

(4) Weber, D.; Stork, A.; Nakhal, S.; Wessel, C.; Reimann, C.; Hermes, W.; Müller, A.; Ressler, T.; Pöttgen, R.; Bredow, T.; Dronskowski, R.; Lerch, M. *Inorg. Chem.* **2011**, *50* (14), 6762–6766.

(5) Kresse, G.; Furthmüller, J. *Comput. Mater. Sci.* **1996**, *6* (1), 15–50.

(6) Blöchl, P. E. *Phys. Rev. B* **1994**, *50* (24), 17953–17979.

(7) Perdew, J. P.; Burke, K.; Ernzerhof, M. *Phys. Rev. Lett.* **1997**, *78* (7), 1396–1396.

(8) Perdew, J. P.; Burke, K.; Ernzerhof, M. *Phys. Rev. Lett.* **1996**, *77* (7), 3865–3868.

(9) Grimme, S.; Antony, J.; Ehrlich, S.; Krieg, H. *J. Chem. Phys.* **2010**, *132* (15), 154104-1–19.

(10) Grimme, S.; Ehrlich, S.; Goerigk, L. *J. Comput. Chem.* **2011**, *32* (7), 1456–1465.

(11) Birch, F. *Phys. Rev.* **1947**, *71* (11), 809–824.

(12) Togo, A.; Oba, F.; Tanaka, I. *Phys. Rev. B* **2008**, *78* (13), 134106-1–9.

(13) Stoffel, R. P.; Wessel, C.; Lumey, M.-W.; Dronskowski, R. *Angew. Chem. Int. Ed.* **2010**, *49* (31), 5242–5266.

(14) Dovesi, R.; Orlando, R.; Erba, A.; Zicovich-Wilson, C. M.; Civalleri, B.; Casassa, S.; Maschio, L.; Ferrabone, M.; De La Pierre, M.; D'Arco, P.; Noël, Y.; Causa, M.; Rérat, M.; Kirtman, B. *Int. J. Quantum Chem.* **2014**, *114* (19), 1287–1317.

(15) Wessel, C.; Reimann, C.; Müller, A.; Weber, D.; Lerch, M.; Ressler, T.; Bredow, T.; Dronskowski, R. *J. Comput. Chem.* **2012**, *33* (26), 2102–2107.

(16) Wolff, H.; Bredow, T.; Lerch, M.; Schilling, H.; Irran, E.; Stork, A.; Dronskowski, R. *J. Phys. Chem. A* **2007**, *111* (14), 2745–2749.

(17) Bredow, T.; Gerson, A. R. *Phys. Rev. B* **2000**, *61* (8), 5194–5201.

(18) Cora, F.; Patel, A.; Harrison, N. M.; Roetti, C.; Catlow, C. R. A. *J. Mater. Chem.* **1997**, *7* (6), 959–967.

(19) Cora, F.; Patel, A.; Harrison, N. M.; Dovesi, R.; Catlow, C. R. A. *J. Am. Chem. Soc.* **1996**, *118* (48), 12174–12182.

(20) Ferrari, A. M.; Pisani, C. *J. Phys. Chem. B* **2006**, *110* (15), 7909–7917.

(21) Newnham, R. E.; de Haan, Y. M *Z. Kristallogr.* **1962**, *117* (2–3), 235–237.

(22) Dernier, P. D.; Marezio, M. *Phys. Rev. B* **1970**, *2* (9), 3771–3776.

(23) Ahman, J.; Svensson, G.; Albertsson, J. *Acta Crystallogr., Sect. C* **1996**, *52*, 1336–1338.

(24) Shannon, R. D.; Prewitt, C. T. *J. Solid State Chem.* **1970**, *2* (1), 134–136.

(25) Cromer, D. T. *J. Phys.Chem.* **1957**, *61* (6), 753–755.

(26) Svensson, C. *Acta Crystallogr., Sect. B* **1974**, *30*, 458–461.

(27) Jones, P. G.; Rumpel, H.; Schwarzmann, E.; Sheldrick, G. M.; Paulus, H. *Acta Crystallogr., Sect. B* **1979**, *35*, 1435–1437.

(28) Tronc, E.; Chanéac, C.; Jolivet, J. P. *J. Solid State Chem.* **1998**, *139* (1), 93–104.

(29) Smrčok, L.; Langer, V.; Halvarsson, M.; Ruppi, S. *Z. Kristallogr.* **2001**, *216* (7), 409–412.

(30) Kyono, A.; Kimata, M. *Am. Mineral.* **2004**, *89* (7), 932–940.

(31) Geller, S. *J. Chem. Phys.* **1956**, *24* (6), 1236–1239.

(32) Koehler, W. C.; Wollan, E. O. Neutron-diffraction study of the structure of the A-form of the rare earth sesquioxides. *Acta Crystallogr.* **1953**, *6*, 741–742.

(33) Nakhal, S.; Hermes, W.; Ressler, T.; Pöttgen, R.; Lerch, M. *Z. Naturforsch.* **2009**, *64b*, 281–286.

(34) Stehlík, B.; Weidenthaler, P.; Vlach, J. *Collect. Czech. Chem. Commun.* **1959**, *24*, 1581–1588.

(35) Wessel, C.; Dronskowski, R. *J. Solid State Chem.* **2013**, *199*, 149–153.

7.8 Supporting Information

DFT technicalities. To ensure well-converged structures, the *k*-point grid was increased until the number of *k*-points multiplied with the number of atoms was greater than 5000. A further increase of the *k*-points resulted in marginal changes in the total energies of only about 1 J·mol^{-1}. Such small changes are irrelevant for our investigation, as the lowest observed energy difference between two structure types is about 1 kJ (Sm_2O_3 to Sb_2O_3) and in all other cases at least 1.4 kJ·mol^{-1}. The final *k*-point grid for all structures is listed in Table 7.5.

Table 7.5. Details of the *k*-point mesh and the number of *k*-points in the irreducible Brillouin zone for all investigated polymorphs of Mo_2O_3 and W_2O_3.

Starting structure	Atoms/cell	*k*-point mesh	*k*-points	Atoms x *k*-points
Ag_2O_3	10	30 × 30 × 30	816	8160
Al_2O_3	30	20 × 20 × 6	242	7260
Au_2O_3	40	5 × 9 × 24	195	7800
Bixbyit	80	10 × 10 × 10	76	6080
Fe_2O_3	40	16 × 9 × 7	180	7200
Ga_2O_3	20	6 × 24 × 9	364	7280
$GdFeO_3$	20	16 × 12 × 10	378	7560
La_2O_3	5	18 × 18 × 12	1037	5185
Rh_2O_3	20	14 × 15 × 10	384	7680
Sb_2O_3	20	19 × 8 × 17	450	9000
Sb_2S_3	20	7 × 27 × 10	336	6720
Sm_2O_3	30	5 × 25 × 9	299	8970
V_2O_3	20	9 × 15 × 11	400	8000

Metal bonds in the corundum type. A bonding study of the energetically favored corundum-type structure was performed to analyze the nature of the metal-metal interaction (Figure 7.6 and Figure 7.7). The DOS showed a small amount of electron density at the Fermi level for both compounds (Mo_2O_3 and W_2O_3). The shortest Mo-Mo distances are 2.7 and 2.9 Å while the equivalent W-W distances in the corundum structure are 2.7 and 3.0 Å. The calculated pCOHP (projected Crystal Orbital Hamilton Population) data clearly evidence that the short M-M interactions (2.7 Å) are of bonding nature while the longer interactions also include antibonding contributions.

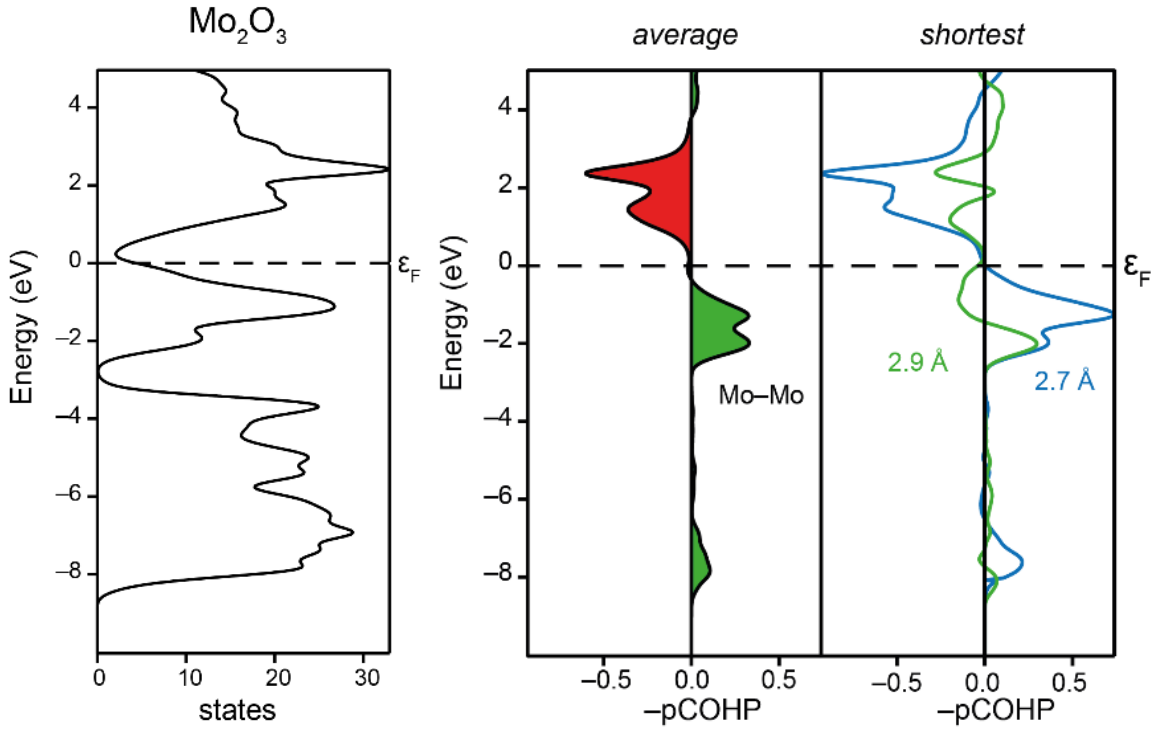

Figure 7.6. Calculated DOS (left) and pCOHP (right) of corundum-type Mo_2O_3.

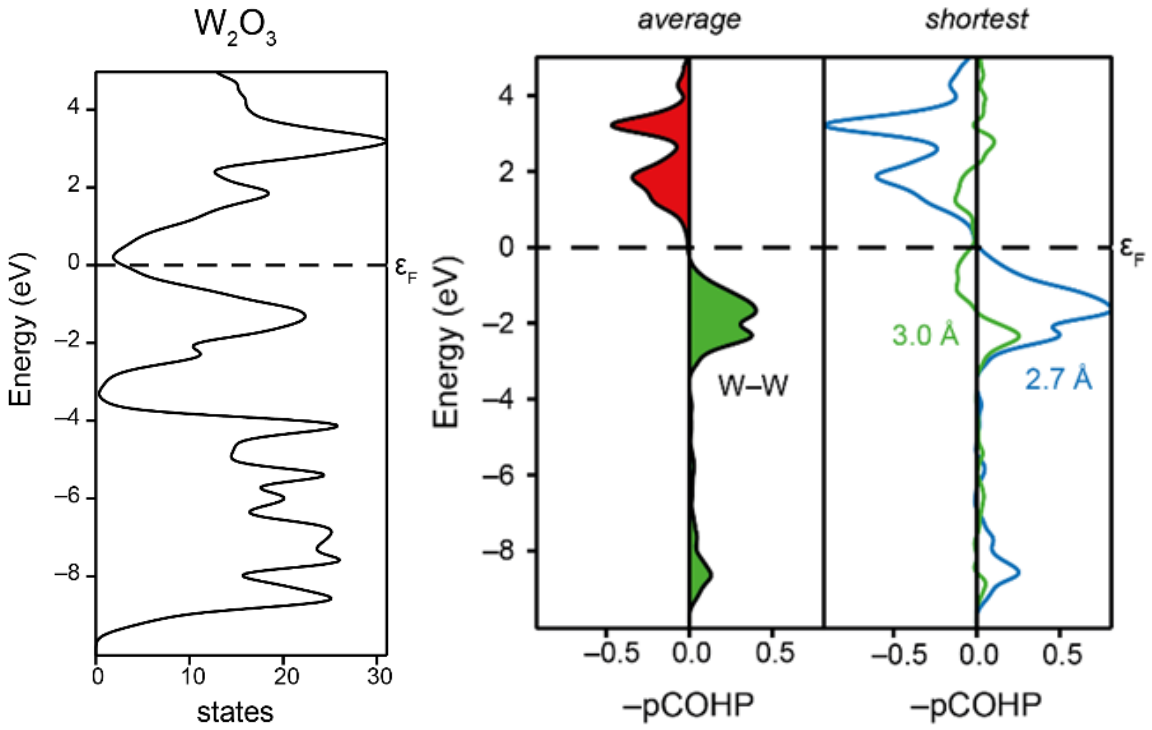

Figure 7.7. Calculated DOS (left) and pCOHP (right) of corundum-type W_2O_3.

8 Publication 5

HP-MoO_2: A High-Pressure Polymorph of Molybdenum Dioxide

Tobias Lüdtke, Dennis Wiedemann, Ilias Efthimiopoulos, Nils Becker, Oliver Janka, Stefan Seidel, Rainer Pöttgen, Richard Dronskowski, Monika Koch-Müller, Martin Lerch

Postprint
Inorganic Chemistry **2017**, *56(4)*, 2321–2327
DOI: 10.1021/acs.inorgchem.6b03067
http://pubs.acs.org/doi/abs/10.1021/acs.inorgchem.6b03067

Contribution to publication:

T. Lüdtke:	Sample preparation (α-MoO_2), characterization (PXRD), writing.
D. Wiedemann:	Single-crystal analysis, writing.
I. Efthimiopoulos	Measurements (Raman spectroscopy), writing.
N. Becker:	Quantum-chemical investigations, writing.
O. Janka:	Measurements (magnetism), writing.
S. Seidel:	Group theory, writing.
R. Pöttgen:	General discussion, proofreading.
R. Dronskowski:	General discussion, proofreading.
M. Koch-Müller:	Sample preparation (HP-MoO_2), general discussion, proofreading.
M. Lerch:	General discussion, proofreading.

Overall contribution of T. Lüdtke to the publication: 25%

Authors. Tobias Lüdtke,[a] Dennis Wiedemann,[a] Ilias Efthimiopoulos,[b] Nils Becker,[c] Oliver Janka,[d] Stefan Seidel,[d] Rainer Pöttgen,[d] Richard Dronskowski,[c,e] Monika Koch-Müller,[*,b] Martin Lerch [*,a]

(a) Institut für Chemie, Technische Universität Berlin, Straße des 17. Juni 135, D-10623 Berlin, Germany
(b) Deutsches GeoForschungsZentrum Potsdam, Telegrafenberg, D-14473 Potsdam, Germany
(c) Institut für Anorganische Chemie, RWTH Aachen University, Landoltweg 1, D-52056 Aachen, Germany
(d) Institut für Anorganische und Analytische Chemie, Universität Münster, Corrensstraße 30, D-48149 Münster, Germany
(e) Jülich-Aachen Research Alliance (JARA-HPC), RWTH Aachen University, D-52074 Aachen, Germany

* Corresponding author

Keywords. High pressure; molybdenum dioxide; single-crystal X-ray diffraction; Raman spectroscopy; density-functional theory computations; magnetism.

Supporting Information. Detailed list with Raman modes and mode-symmetry assignments (PDF). Crystallographic data for the structure refinement of HP-MoO_2 (CIF). The Supporting Information is available free of charge on the ACS Publications website at DOI: 10.1021/acs.inorgchem.6b03067.

Received: 19.12.2016
Accepted: 25.01.2017
Published online: 09.02.2017

8.1 Abstract

High-pressure molybdenum dioxide (HP-MoO_2) was synthesized using a multianvil press at 18 GPa and 1073 K, as motivated by previous first-principles calculations. The crystal structure was determined by single-crystal X-ray diffraction. The new polymorph crystallizes isotypically to HP-WO_2 in the orthorhombic crystal system in space group *Pnma* and was found to be diamagnetic. Theoretical investigations using structure optimization at density-functional theory (DFT) level indicate a transition pressure of 5 GPa at 0 K and identify the new compound as slightly metastable at ambient pressure with respect to the thermodynamically stable monoclinic MoO_2 (α-MoO_2; $\Delta E_m = 2.2\ kJ{\cdot}mol^{-1}$).

8.2 Introduction

Elements of the sixth group of the periodic table form compounds with the metal atom in many different oxidation states. Valence-isoelectronic molybdenum and tungsten have a similar chemistry in consequence of the almost identical ionic radii as one result of the lanthanide contraction. Many binary oxides are known for both elements, but only the di- and trioxides have the element in just one oxidation state (+IV / +VI). MoO_2[1–5] and WO_2[1,2,5] (from now on, we will call those compounds α-MoO_2 and α-WO_2) crystallize isotypically in the monoclinic space group $P2_1/c$. MoO_2 is the eponym for this structure type, which can be described as a distorted rutile type. It is built of chains of MO_6 polyhedra connected *via* opposite edges along the *a* axis with alternating distances between the metal atoms.[5] All vertices are connected with neighboring chains. The distortion is caused by a Peierls-type instability of the electronic structure.[6] Other oxides, like α-ReO_2 and a low-temperature form of VO_2, adopt the same structure type.[3] Reports on tetragonal rutile-type variants (space group $P4_2/mnm$) of α-MoO_2 and α-WO_2, one from 1926 by Goldschmidt *et al.*[1] and a second one regarding the molybdenum dioxide from 2004 by Seisenbaeva *et al.*,[7] are rare. Simulated diffraction patterns indicate that a very good instrumental resolution is necessary to distinguish between monoclinic and tetragonal rutile variants.[8] Additionally, it was proposed that a distorted rutile type, crystallizing in space group $I4_1md$, was the actual product in both reported cases. According to quantum-chemical computation, this variant is *ca.* 7 $kJ{\cdot}mol^{-1}$ less stable than the monoclinic form of the dioxide.[8] Other theoretical studies regarding α-MoO_2 cover a wide range of various aspects.[5,9–13] It can be found in the mineral tugarinovite (named after the geo-

chemist Alexsey Ivanovich Tugarinov)[14] and shows a metal-like electric conductivity being unusual for transition-metal oxides.[15,16] It does not have a variety of technological applications such as MoO_3 but there are some interesting approaches for usage as anode material in lithium-ion batteries,[15,17–20] films for energy storage,[21] soft-magnetic and optical materials,[22–24] and as nanorods.[22,25]

The synthesis of other oxides with metal ions in just one oxidation state probably cannot be achieved by conventional chemical methods, like oxidation or reduction. Another approach to preparing new compounds is the usage of high pressure on existing binary oxides. High-pressure polymorphs are often characterized by a higher density and an increased coordination number of the atoms. For example, the cotunnite type with 9-fold coordinated cations is a common structure type for high-pressure polymorphs of transition-metal oxides[26,27] and oxide nitrides.[28] The synthesis of an orthorhombic high-pressure polymorph of tungsten dioxide (HP-WO_2) is possible at 8 GPa and 1120 K.[29] Remarkably, the crystal structure of this compound has been derived just using powder X-ray diffraction (XRD) data with very weak reflections dominated by the cation substructure. Up to now, only first-principles studies based on quantum-chemical computation at the density-functional theory (DFT) level have been published on a molybdenum analogue. Predicted by calculations, a metastable high-pressure polymorph with an orthorhombic rutile variant should be formed at around 25 GPa.[8] A monoclinic high-pressure polymorph of MoO_3 has been prepared using pressures greater than 6 GPa and temperatures greater than 973 K.[30] In the present work, we report on synthesis and characterization of a new high-pressure polymorph of molybdenum dioxide.

8.3 Experimental Section

Synthesis. As starting material for the high-pressure synthesis, we used α-MoO_2, which we had prepared by reduction of MoO_3 (Sigma-Aldrich, 99.5%) in a tube furnace with direct gas feed at T = 858 K for 18 h with flow rates of 15 $L{\cdot}h^{-1}$ H_2 and 0.7 $L{\cdot}h^{-1}$ O_2. The samples were placed in platinum capsules, which had an outer diameter of 1.4 mm (wall thickness of 0.2 mm) and were 2 mm long. We performed the multianvil run (MA-497) with a 10/5 assembly, rhenium heater, and type C thermocouple at p = 18 GPa and T = 1073 K for 30 h. At the end of the run, the temperature was quenched to ambient conditions within 2 min and the decomposition time was 43 h to avoid breakage of the WC cubes. For more details about the pressure calibration, we refer to Koch-Müller *et al.*[31] After the experiment, the recovered capsule was filed open.

X-ray diffraction. A Rigaku R/AXIS200 SPIDER, a PANalytical X'Pert MPD Pro, and a Rigaku SmartLab diffractometer were used for powder XRD measurements at ambient temperature. The diffractometers operate with unmonochromated Cu-K_α radiation (λ_1 = 154.060 pm, λ_2 = 154.443 pm, $I(\lambda_2)/I(\lambda_1) = 0.500$) at 40 kV and 30 mA (Rigaku)/40 mA (PANalytical). Powder diffraction-pattern simulations, Rietveld refinements,[32] and Le Bail profile decompositions[33] were carried out using the program FULLPROF 2000.[34] Starting values for the refinements were the fractional atomic coordinates and lattice parameters of HP-WO_2.[29] Profiles were fitted with a pseudo-Voigt function. The following parameters were fitted in the Le Bail decomposition process: three unit-cell parameters, one overall temperature displacement factor, three Gaussian half-width (U, V, W) parameters, a mixing and one Lorentzian (η_0, X) parameter, two asymmetry parameters, displacement, and transparency. The background was fitted with 36 points with refinable heights.

Single-crystal diffraction data was collected at 150.0(1) K using an Agilent SuperNova diffractometer equipped with a goniometer in κ geometry, an "Atlas" CCD-detector, and a mirror-monochromated "Nova" Cu-K_α source (λ = 154.184 pm). Diffraction images were integrated with CRYSALISPRO.[35] An analytical numeric absorption correction using a multifaceted crystal model was performed.[36] The structure was solved with SHELXS-2013 using Direct Methods and refined with SHELXL-2016 against F_o^2 data using the full-matrix least-squares algorithm.[37] All atoms were refined anisotropically. An extinction correction was performed as implemented in SHELXL-2016; the corresponding parameter refined to 0.0038(2). Structure graphics were produced using DIAMOND 3.2.[38]

Further details of the crystal structure investigation may be obtained from FIZ Karlsruhe, 76344 Eggenstein-Leopoldshafen, Germany (fax: +49 7247 808-666; e-mail: crysdata@fiz-karlsruhe.de), on quoting the deposition number CSD-432325.

Raman Spectroscopy. Raman spectra of unoriented crystallites were collected in the 100–1200 cm^{-1} wavenumber range with a HORIBA Jobin Yvon LabRAM HR800 UV-vis spectrometer, equipped with a 1800 groove·mm^{-1} grating and a CCD detector. The excitation wavelength was the Ar^+ laser line λ = 514.5 nm with an incident laser power of 0.2 mW, whereas a 50× lens was used for focusing on the sample surface. The acquisition time for each spectrum was 400 s with ten accumulations.

Quantum-Chemical Calculations. The quantum-chemical studies were based on previously published results[8] and supplemented with data acquired from the experiments discussed here. The Vienna *ab initio* simulation package (VASP) was used to perform periodic DFT calculations.[39] Core and valence electrons were separated using projector-augmented waves (PAW).[40] The generalized-gradient approximation as described by Perdew, Burke, and Ernzerhof (GGA-PBE)[41,42] was used to treat the exchange and correlation contributions. As the initial calculations on MoO_2 were carried out with dispersion correction, the herein presented additional calculations also include the corrections for van der Waals forces, namely, Grimme's "D3(BJ)" dispersion correction with Becke–Johnson damping[43,44] as implemented in VASP 5.3.5. The energy cutoff was set to 500 eV, and a *k*-point grid of 12 × 12 × 12 (α-MoO_2) or 6 × 7 × 12 (HP-MoO_2) ensured well-converged structures. All atomic positions and lattice parameters were allowed to relax until the ionic convergence criterion of 10^{-6} eV was reached. The high-pressure behavior was calculated by scaling the cell parameters from 94% to 104% (with fixed $a:b:c$ ratio), and the resulting energy *vs* volume data were fitted to the Birch–Murnaghan equation of state.[45] Thus, the pressure and, eventually, the reaction enthalpies as a function of the pressure were calculated. Additional thermodynamic properties were calculated using PHONOPY.[46] As a first step, supercells of the optimized structures were constructed. All symmetry-inequivalent atoms were then slightly shifted out of their equilibrium positions to calculate the Hellmann–Feynman forces. Subsequently, the force constants and then the dynamical matrices were computed. Through combination of the eigenvalues (phonon wavenumbers) with Bose–Einstein statistics, the free phonon energy was obtained.[47] The thermodynamic properties at finite temperatures are straightforwardly accessible from these theoretical data.

Magnetic Properties. Hand-picked crystals of HP-MoO_2 were packed in a polyethylene (PE) capsule and attached to the sample holder rod of a vibrating sample magnetometer (VSM) unit for measuring the magnetization $M(T)$ in a Quantum Design Physical Property Measurement System (PPMS). The sample was investigated in the temperature range of 3–300 K with magnetic flux densities of 10 and 50 kOe.

8.4 Results and Discussion

Although molybdenum and tungsten show similar behavior, it is surprising that only the dioxide of tungsten is reported to form a high-pressure polymorph. Quantum-chemical calculations on the DFT level were performed to investigate the high-pressure behavior of MoO_2 as described in the previous study on possible new polymorphs of MoO_2.[8] Additionally, the high-pressure polymorph of tungsten dioxide (HP-WO_2) was used as a starting structure for the optimization of MoO_2 and the following investigations. Our calculations reveal an isostructural high-pressure polymorph of MoO_2 based on HP-WO_2. This phase is calculated to be only 2.2 kJ·mol^{-1} less stable than α-MoO_2 and should form at pressures above 5 GPa (Figure 8.1). A second polymorph, with a structure dubbed *ortho*-TiO_2 (for details see ref. 8), is predicted to form between 25 and 30 GPa. The calculated phonon density of states (PDOS) of HP-MoO_2 shows no imaginary modes at ambient or the transition pressure (Figure 8.2) and can, therefore, be identified as a minimum on the potential energy surface. Based on these phonon calculations, we also provide a list of the calculated Raman-active modes in the Supporting Information (Chapter 8.8) for comparison with the experiment. One should note that the calculated pressure is only valid at 0 K, so under experimental conditions with finite temperatures the transition pressure is likely to be different. Based on these theoretical findings, we continued with the corresponding high-pressure synthesis.

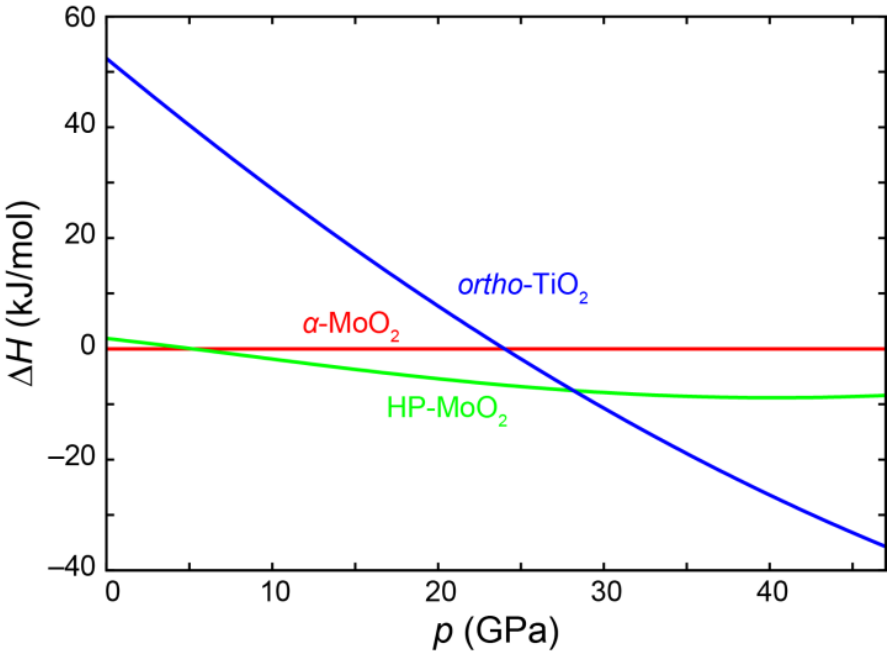

Figure 8.1. Theoretically calculated enthalpy of HP-MoO_2 and the other potential polymorph with *ortho*-TiO_2 structure relative to α-MoO_2.

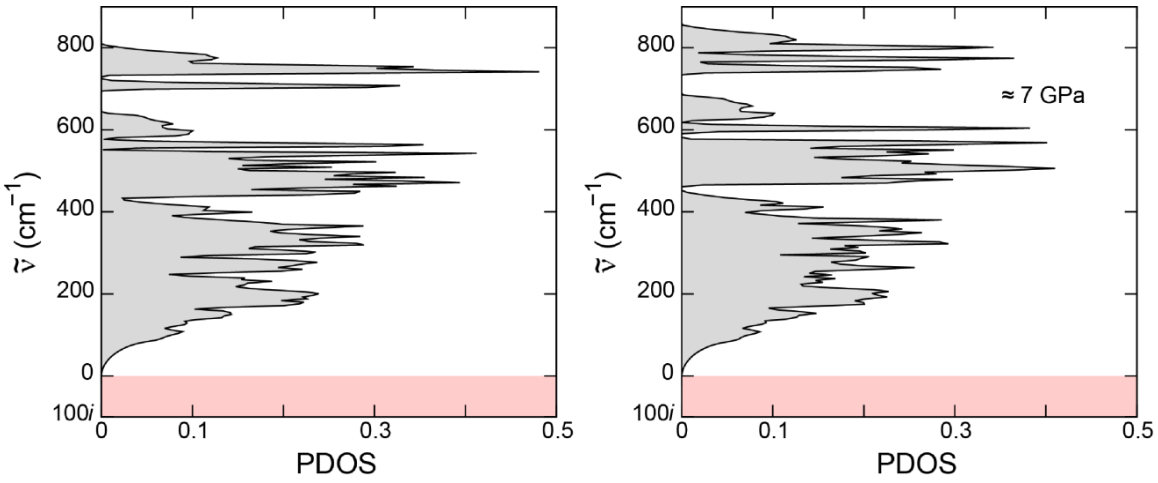

Figure 8.2. Calculated phonon density of states (PDOS) of HP-MoO_2 at ambient pressure (left) and slightly above the calculated transition pressure (right).

The phase purity of the α-MoO_2 starting material was verified using powder XRD on the PANalytical X'Pert MPD Pro. No detectable amounts of MoO_3, suboxides, or elemental molybdenum were found in the precursor for the high-pressure experiments. Optical analysis of the products in reflected light revealed that they consist of a powderlike opaque phase (about 1–4 μm in size), in which additionally some larger crystals 50–100 μm in size occurred; the latter were picked for the single-crystal diffraction experiment, as we discuss below. Several powder X-ray diffraction patterns of the high-pressure product were measured using the Rigaku diffractometer from different portions of the specimen using different preparation strategies. The diffraction patterns taken do not differ in the number and the positions of the reflections, but only in the relative intensities.

All recorded patterns are characterized by sharp reflections and a high background with a maximum at $2\theta \approx 22.5°$. A first phase analysis revealed a close structural relationship to HP-WO_2.[29] Although an *ab initio* structure solution from powder data was unsuccessful, Le Bail whole pattern fitting[33] results in a good accordance of experimental and calculated data. From the different preparation methods, the best results came from a portion of the sample which we had ground for 5 min, mounted on a CryoLoop (Hampton Research), and rotated during the data acquisition of 30 min at a speed of 3° s^{-1} over 360°. The diffraction pattern of this portion is depicted in Figure 8.3 with the results of the Le Bail fit in the range $10° < 2\theta < 120°$.

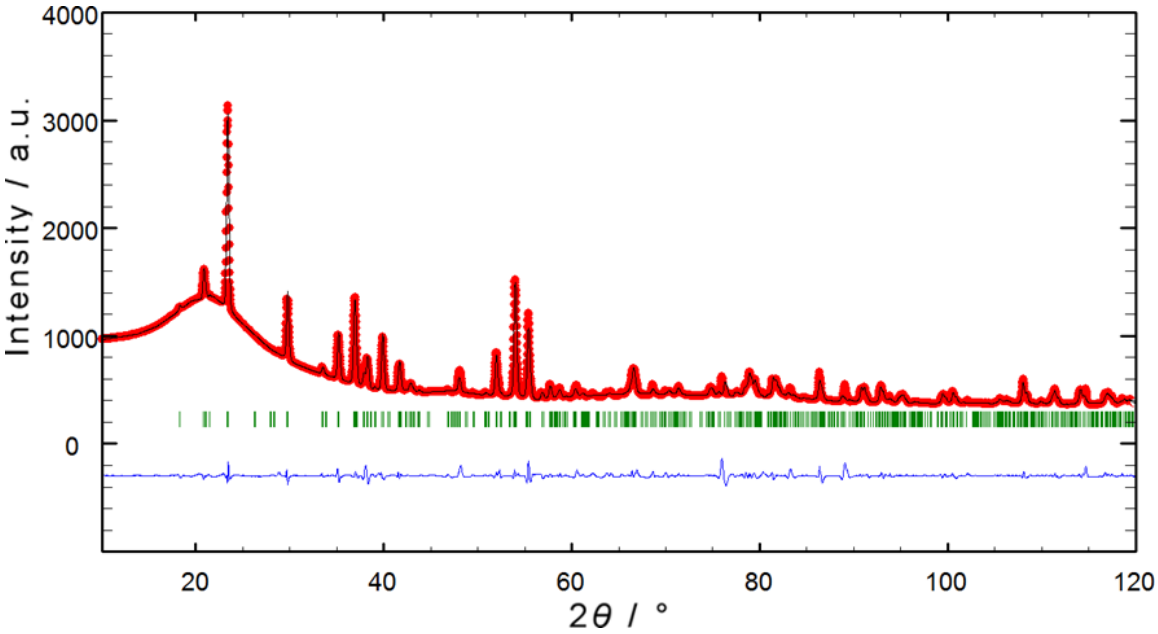

Figure 8.3. X-ray powder diffraction pattern (Cu-K_α radiation) of HP-MoO_2 with the results of the Le Bail profile fit (red: measured; black: calculated; green: Bragg-reflection positions; blue: difference plot).

The problems occurring during Rietveld refinement using a distinct structure model may indicate the presence of multiple preferred orientations of the crystallites. The small amount of substance used for powder diffraction consists of few and relatively large crystallites. This does not comply with the requirements for powder XRD, where a high number of small crystallites with a statistical size distribution is essential. Therefore, the observed intensity deviations of measured and calculated patterns are significant, and the presented diffractogram is unbiased. A solution for this problem might be a synthesis at lower temperatures so that a regular powder is formed.

However, it was possible to isolate a small violet prism with a size of 0.057 × 0.067 × 0.086 mm^3 fit for single-crystal diffraction (see Figure 8.10 in the Supporting Information; Chapter 8.8). Crystallographic details are summarized in Table 8.1. Laue-group determination was unambiguous; the centrosymmetric space-group type *Pnma* was chosen over $Pn2_1a$ for reasons of intensity statistics and commonness. Structure solution using Direct Methods proceeded without problems and yielded the cation positions. Anion positions were deducted from maxima of a difference Fourier map. Refinement proceeded smoothly with an accurate absorption correction and the application of an extinction correction parameter as crucial aspects.

Table 8.1. Results of the single-crystal analysis and Le Bail decomposition of HP-MoO_2.

	Single-crystal	Powder (Le Bail)
λ / pm	154.184	154.060, 154.443
Structure type	HP-WO_2	
Crystal system	Orthorhombic	
Space group	*Pnma* (No. 62)	
Z	12	
Crystal size / mm^3	0.057 × 0.067 × 0.086	
a / pm	969.21(3)	971.62(7)
b / pm	843.22(3)	845.73(6)
c / pm	471.88(2)	475.10(4)
V / 10^6 pm^3	385.65(2)	390.40(5)
ρ_{calc} / $g \cdot cm^{-3}$	6.61	6.53
μ / mm^{-1}	78.4	
$2\theta_{max}$ / °	73.366	120.000
h_{min}, h_{max}	−11, 10	0, 10
k_{min}, k_{max}	−10, 9	0, 9
l_{min}, l_{max}	−5, 5	0, 5
T_{min}, T_{max}	0.020, 0.162	
Measured reflections	1931	632
Independent reflections (R_{int})	403 (0.0276)	316
Observed[a] reflections (R_σ)	393 (0.0122)	
Data, restraints, parameters	403, 0, 47	6516, 0, 45
R_1 | R_F	0.0267	0.0310
wR_2[b] | R_{Bragg}	0.0700	0.0354
R_{wp}		0.0280
R_{exp}		0.0404
u[b], v[b]	0.0507, 0.4034	
S	1.157	0.692
ρ_e(min, max) / 10^{-6} pm^{-3}	−1.57, 1.29	

[a] $I > 2\sigma(I)$.

[b] $w = 1/[\sigma^2(F_o^2) + (uP)^2 + vP]$; $P = [\max(F_o^2, 0) + 2F_c^2]/3$

HP-MoO_2 crystallizes isotypically to HP-WO_2 in the orthorhombic crystal system in space group *Pnma* (No. 62) with 12 formula units per unit cell. As expected, the calculated density of the new high-pressure polymorph (6.61 $g \cdot cm^{-3}$) is slightly higher in com-

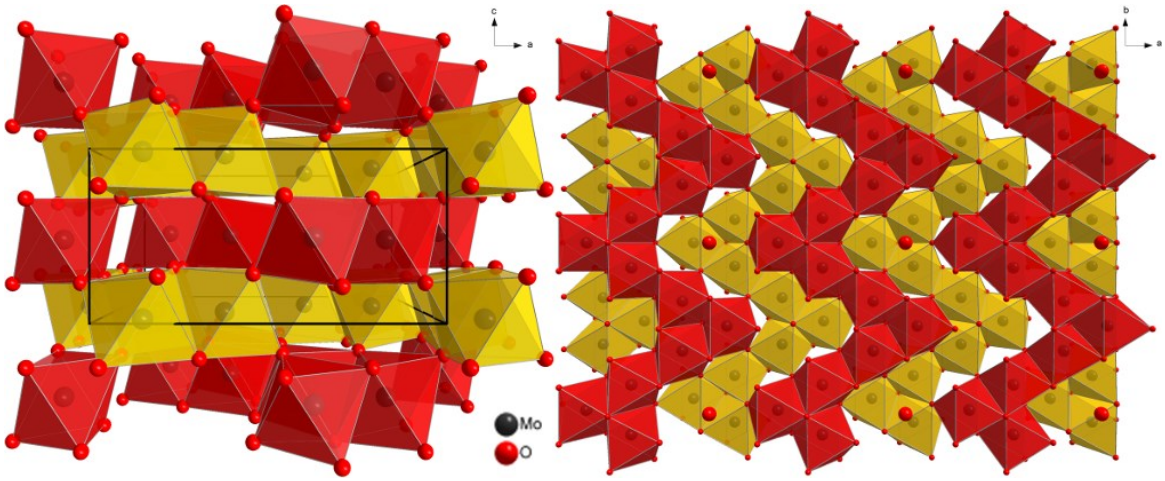

Figure 8.4. Crystal structure of HP-MoO_2. Left: layer-like structure along the *c* axis with unit cell; right: arrangement of the zigzag chains of two layers. Red and yellow polyhedra indicate different layers. Unbound oxide ions indicate the toothing of the layers.

parison to monoclinic α-MoO_2 (6.46 g·cm^{-3}).[4] The crystal structure is built of layers of oxide and molybdenum ions alternating along the *c* axis (Figure 9.4, left). The oxide layers can be described as an almost hexagonal close packing with the metal atoms occupying one half of the octahedral sites. The coordination number of the metal ions is six and therefore not increased with respect to α-MoO_2. Oxide ions are surrounded by three molybdenum ions and do not form perfectly ordered layers, thereby preventing an ideal packing. The distorted MoO_6 octahedra are connected over two edges forming zigzag chains along the *b* axis. Those chains form alternating layers along the *c* axis (indicated as red and yellow polyhedra). Inside one layer, the chains are separated by tunnels but share vertices with chains of neighboring layers *via* O1, O2, and O3 (Figure 9.4, right). One characteristic element of the chains is the sequence of –Mo2–Mo1–Mo2– polyhedra with Mo1 polyhedra as the turning point of the zigzag chains (Figure 9.5). This is possible because the polyhedra around Mo1 are linked over *cis*-positioned edges, while the Mo2 polyhedra are linked *via* edges in *trans* position. All three polyhedra in one sequence are connected *via* O4. This connection extends into the tunnel, which leads to a toothing of the layers. Additionally, the Mo2 polyhedra are connected to the Mo1 polyhedra *via* O1 and to the other Mo2 polyhedra *via* O3. The –Mo2–Mo1–Mo2– chains are linked to each other *via* the O2 ions of the Mo2 polyhedra.

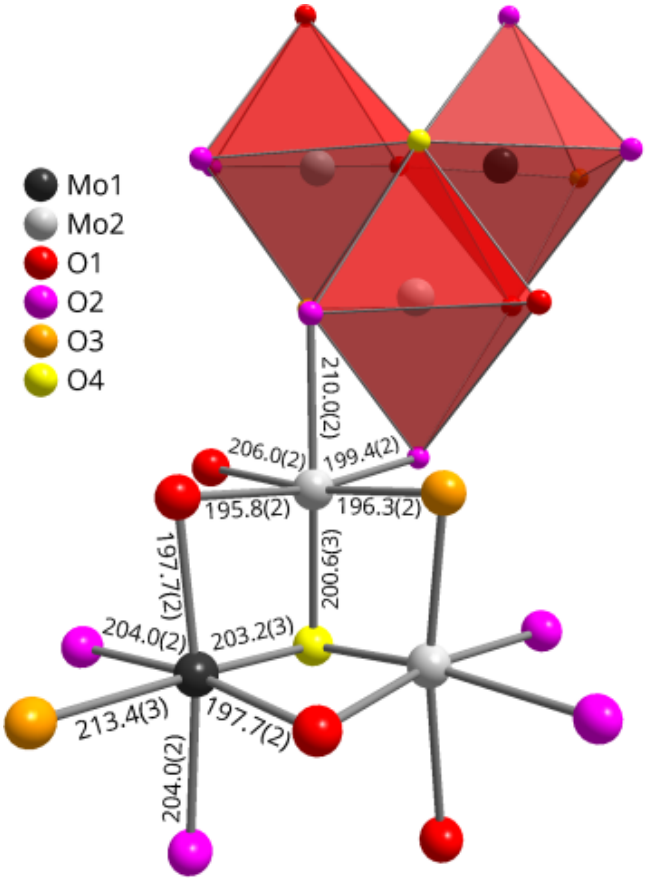

Figure 8.5.
Coordination polyhedra and connectivity of the atoms inside one zigzag chain with bond lengths (in pm).

According to the atomic parameters in Table 9.2, all oxide ions are located very close to a glide plane. Additionally, O3 and O4 are located on a mirror plane. The seemingly differing atomic positions in the original HP-WO_2 publication can be resolved by inverting the *c* axis (*i.e.*, mirroring the atoms at the basal *ab* plane).[29] Figure 9.5 also depicts the corresponding Mo–O bond lengths. The average bond length of 203.3 pm for the $(Mo1)O_6$ polyhedron and 201.4 pm for the $(Mo2)O_6$ polyhedron are in a good agreement with the ionic radii (65 pm for Mo^{4+} in a 6-fold coordination and 136 pm for O^{2-} in a 3-fold coordination).[48] Molybdenum ions are at least 251.60(5) pm apart from each other. Details about distances and angles can be found in the crystallographic information file (CIF).

The almost regular hcp arrangement of the oxide anions in HP-MoO_2 and the ordered molybdenum positions readily call for a close group-theoretical relationship starting from the NiAs structure as aristotype where the octahedral voids of the arsenic substructure are completely filled.

Table 8.2. Experimental and computed (DFT with D3 dispersion correction) atomic parameters of the new high-pressure polymorph of MoO_2.

Atom		Wyckoff	*x*	*y*	*z*
Mo1					
	Experimental	4*c*	0.36523(5)	¼	0.02048(10)
	DFT-D3		0.3638	¼	0.0201
Mo2					
	Experimental	8*d*	0.13305(4)	0.10081(4)	0.00614(5)
	DFT-D3		0.1326	0.1015	0.0077
O1					
	Experimental	8*d*	0.20010(2)	0.57460(2)	0.27710(5)
	DFT-D3		0.2001	0.5740	0.2757
O2					
	Experimental	8*d*	0.45670(2)	0.08630(2)	0.27760(5)
	DFT-D3		0.4559	0.0867	0.2764
O3					
	Experimental	4*c*	0.04340(3)	¼	0.74520(7)
	DFT-D3		0.0418	¼	0.7429
O4					
	Experimental	4*c*	0.20630(3)	¼	0.30120(7)
	DFT-D3		0.2054	¼	0.3034

The corresponding group-subgroup scheme in the Bärnighausen formalism[49–51] is presented in Figure 8.6. We start with space group $P6_3/mmc$ (both *hcp* and NiAs), and the first symmetry reduction goes to space group *Cmcm via* a *translationengleiche* transition of index 3 (t3), leading to the orthohexagonal setting. The following decentering of the lattice (*klassengleiche* transition of index 2 (k2) to *Pmmn*) leads to a first splitting of the oxygen site. The unit cell is then enlarged by another *klassengleiche* transition of index 2 (k2) to *Pnma* followed by an isomorphic transition to *Pnma* upon tripling the *b* parameter. Of the four crystallographically independent molybdenum sites only two are occupied in an ordered manner; two remain empty. Comparison of the calculated and refined positional parameters shows the most pronounced deviation for the *z* parameter of the O4 atoms (connecting three polyhedra). All other atoms show smaller shifts from the subcell sites. These are all a consequence of the molybdenum ordering.

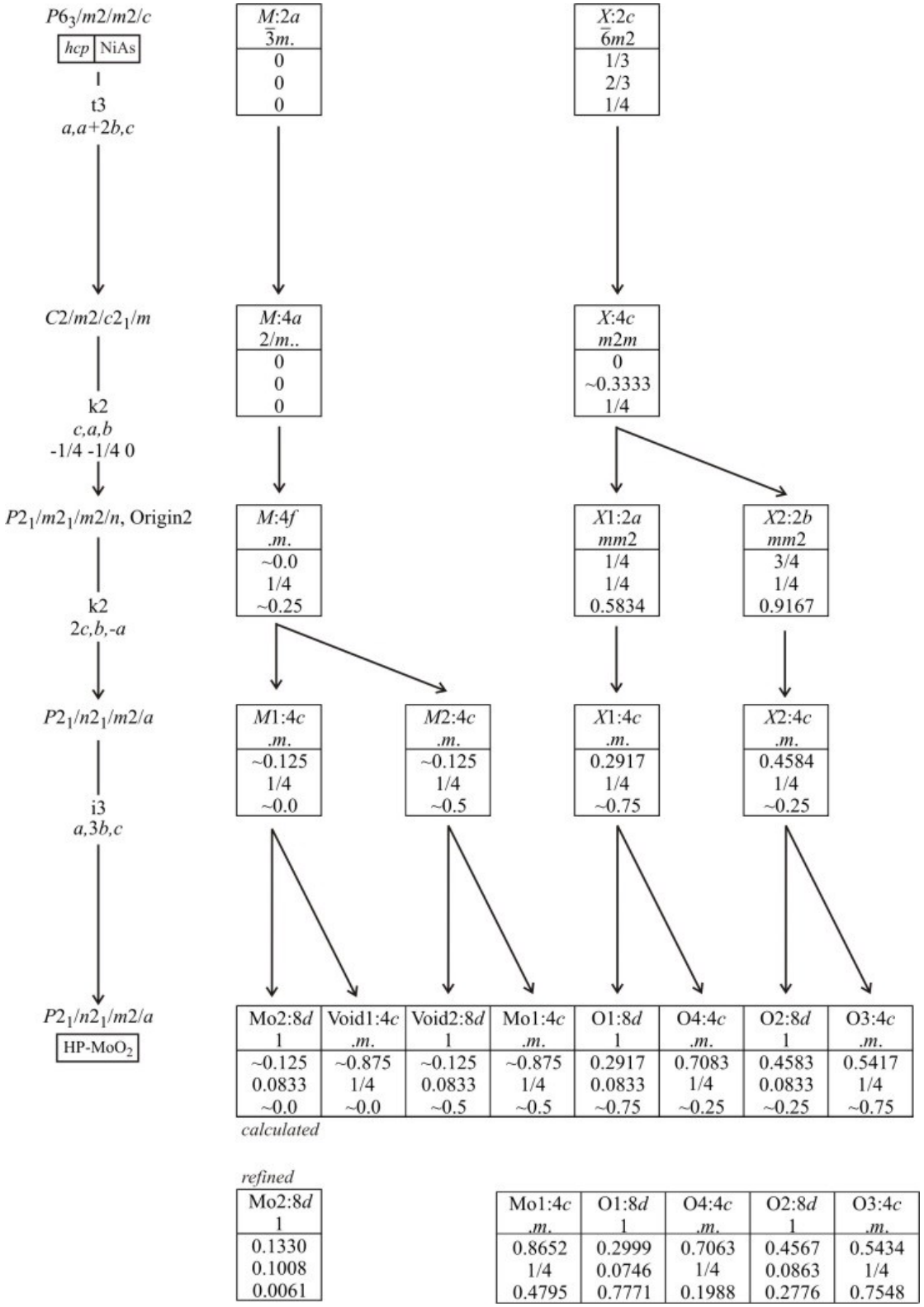

Figure 8.6. Group-subgroup scheme (Bärnighausen formalism) for the group-theoretical relationship between the NiAs structure (aristotype) and the crystal structure of HP-MoO_2.

The calculated HP-MoO_2 structural parameters are in excellent agreement with the experimentally observed results: Table 8.3 lists the cell parameters obtained from the experiment compared to the calculated results. The DFT-D3 results nicely corroborate the experiment, while the exclusion of the dispersion correction leads to a slight overestimation of the cell parameters. When comparing the calculated and measured spatial parameters, the observation remains the same, the theory (DFT-D3) being in nice accord with the experiment. To quantify the conformity, we calculated the root mean square (rms)[52] between the experimental and calculated atomic positions, and the absolute rms = 1.2 pm confirms an excellent agreement.

Table 8.3. Comparison of experimental and DFT-calculated cell parameters (pm) with and without D3 dispersion correction.

	Experimental	DFT(D3)	DFT
a	969.2	971.2	975.5
b	843.2	847.7	850.8
c	471.9	476.2	482.4

Even when starting with large local magnetic moments, spin-polarized electronic-structure calculations using either ferromagnetic (FM) or antiferromagnetic (AFM) orderings immediately converged into nonmagnetic states with identical total energies. It is, therefore, safe to assume either diamagnetic behavior or weak metallic paramagnetism without local moments. This is quite understandable comparing HP-MoO_2 with the ferromagnetic, lighter homologue CrO_2. In HP-MoO_2, the two leftover 4d electrons of Mo^{IV} are well shielded by the filled internal 3d shell, and, because the exchange splitting, which is responsible for spin polarization, scales with the effective nuclear charge, the exchange splitting in HP-MoO_2 is insufficient. The calculated electronic DOS of HP-MoO_2 shows only very few states at the Fermi level, suggesting either a minute overlap between valence and conduction band (*i.e.*, a bad metal) or a semiconductor with a zero band gap, as shown in Figure 8.7. We therefore tentatively suggest HP-MoO_2 as a semimetal with a low electrical conductivity.

As for the vibrational properties, we show the recorded Raman spectrum of HP-MoO_2 in Figure 8.8. According to group theory, a total sum of $\Gamma = 15\,A_g + 12\,B_{1g} + 15\,B_{2g} + 12\,B_{3g}$ first-order Raman-active modes is expected for HP-MoO_2. We could observe 26 Raman-related features; the detailed Raman mode list and a tentative mode-symmetry assignment are given in Table 8.4 in the Supporting Information (Chapter 8.8).

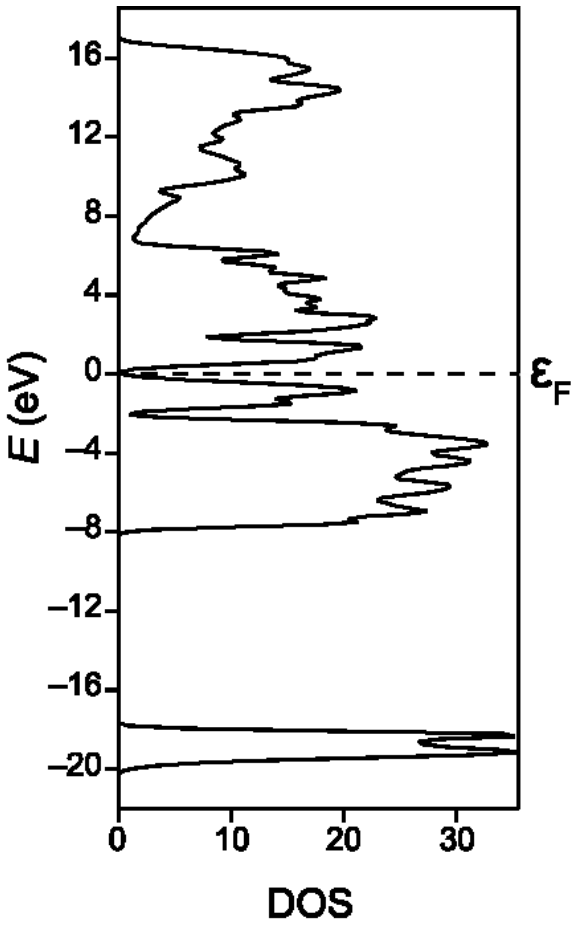

Figure 8.7.
Calculated electronic density of states (DOS) of HP-MoO_2. The minute overlap between the valence and conduction band at the Fermi level classifies the compound as a semimetal.

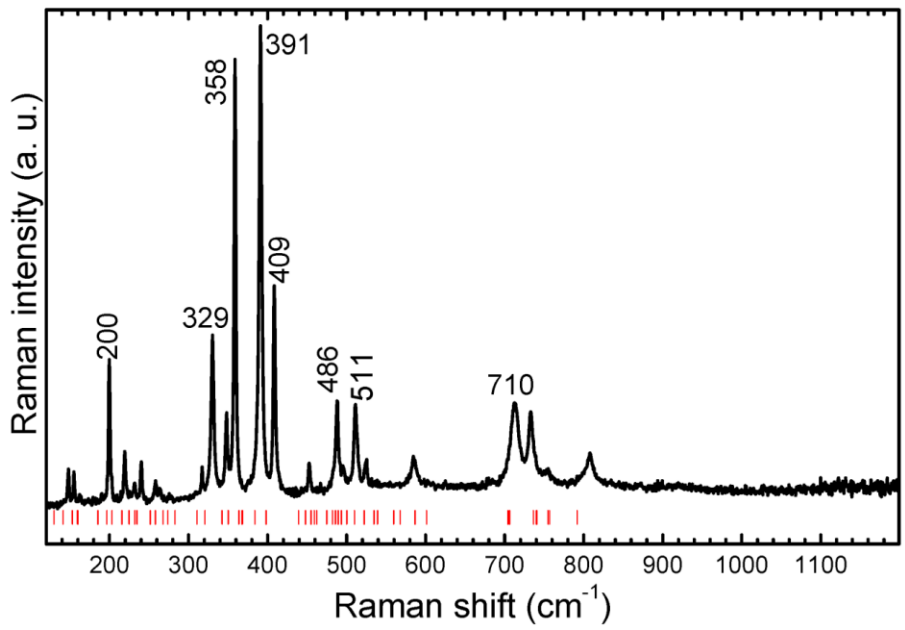

Figure 8.8.
Raman spectrum of HP-MoO_2 at ambient conditions (λ = 514.5 nm). The red tick symbols represent the calculated Raman-mode frequencies (Supporting Information; Chapter 8.8; Table 8.4).

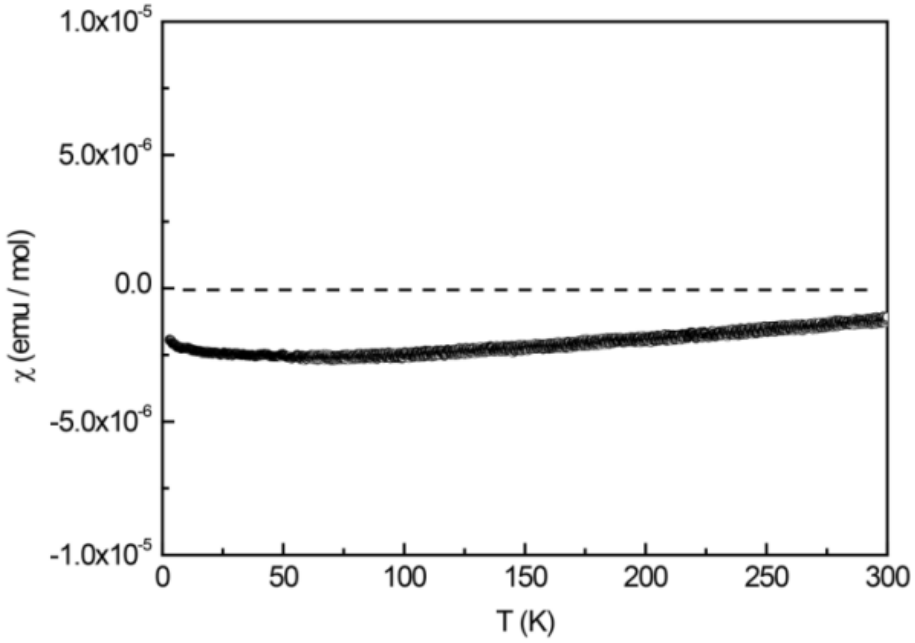

Figure 8.9. Temperature-dependent molar magnetic susceptibility χ of HP-MoO_2, measured with a magnetic field strength of 10 kOe.

In agreement with the calculated phonon DOS (Figure 8.2), the spectrum can be divided into three wavenumber regions: 100–420 cm^{-1}, 420–650 cm^{-1}, and 700–850 cm^{-1}. To the best of our knowledge, this is the first report of the Raman response of an HP-WO_2-type structure. Consequently, our Raman spectra can serve as a basis for the (micro) identification of this phase.

Regarding the vibration-specific Raman-mode assignments, on the other hand, we do not have a reference Raman spectrum for direct comparison. Nevertheless, we can draw some analogies from the Raman mode assignment of the starting material, the monoclinic α-MoO_2 phase.[53] Therefore, we can assign the 100–420 cm^{-1}, 420–650 cm^{-1}, and 700–850 cm^{-1} regions to external vibrations (*e.g.*, translations of the MoO_6 units), and to the Mo–O–Mo bending and Mo–O stretching modes, respectively.

Figure 8.9 shows the temperature dependence of the molar magnetic susceptibility (χ) of the HP-MoO_2 sample measured at 10 kOe; the data obtained at 50 kOe coincides with the 10 kOe data and is therefore not shown. In order to isolate the contribution of the sample, the χ data was corrected by subtracting the susceptibility of an empty PE capsule. The sample shows almost temperature-independent diamagnetic behavior within the whole temperature range. The susceptibility at 300 K exhibits a value of $-1.1(1) \times 10^{-6}$ emu·mol^{-1}. Due to the small sample mass available for this measurement, the relative error of the susceptibility χ(300 K) was estimated to be 10%. The observed diamagnetism is in line with the absence of any localized electron at the Mo^{4+} cation. The

values of the observed susceptibilities are about 1 order of magnitude smaller compared to the calculated ones (-41×10^{-6} emu·mol^{-1}) using the diamagnetic increments ($\chi(Mo^{4+}) = -17 \times 10^{-6}$ emu·mol^{-1}; $\chi(O^{2-}) = -12 \times 10^{-6}$ emu·mol^{-1}) listed in ref. 54. They are, however, in accordance with the outcome of computation (*vide supra*).

8.5 Conclusion

A new high-pressure polymorph of MoO_2 was synthesized using a multianvil press at 18 GPa and 1073 K. Leaving α-MoO_2 for 30 h under these conditions, we transformed the powdered material into single crystals, the structure of which was then determined by means of X-ray diffraction. Measurements of the magnetic susceptibility show diamagnetic behavior. The obtained experimental data are in excellent agreement with our computed results. As the calculations predict an additional phase transition to an *ortho*-TiO_2-type structure at higher pressures (*ca.* 28 GPa), further experiments are in the focus of our interest. Taking into consideration the straightforward synthesis of HP-MoO_2, an extension of our work to other binary transition-metal oxides seems well worth the effort.

8.6 Acknowledgement

This work was supported by the Deutsche Forschungsgemeinschaft (DFG) within the priority program SPP 1415 (LE 781/11-2, DR 342/22-2). We thank Reiner Schulz and Andreas Ebert for technical support during the high-pressure experiments and Hans-Peter Nabein for the help with the powder diffraction measurements. Single-crystal diffraction measurements by Paula Nixdorf are gratefully acknowledged.

8.7 References

(1) Goldschmidt, V. M.; Barth, T.; Holmsen, D.; Lunde, G.; Zachariasen, W. *Skr. Nor. Vidensk.-Akad., Kl. 1: Mater.-Naturvidensk. Kl.* **1926**, *1*, 5–21.

(2) Magnéli, A.; Andersson, G.; Blomberg, B.; Kihlborg, L. *Anal. Chem.* **1952**, *24* (12), 1998–2000.

(3) Magnéli, A.; Andersson, G.; Sundkvist, G. *Acta Chem. Scand.* **1955**, *9*, 1378–1381.

(4) Brandt, B. G.; Skapski, A. C. *Acta Chem. Scand.* **1967**, *21*, 661–672.

(5) Rogers, D. B.; Shannon, R. D.; Sleight, A. W.; Gillson, J. L. *Inorg. Chem.* **1969**, *8* (4), 841–849.

(6) Eyert, V.; Horny, R.; Höck, K.-H.; Horn, S. *J. Phys.: Condens. Matter* **2000**, *12* (23), 4923–4946.

(7) Seisenbaeva, G. A.; Sundberg, M.; Nygren, M.; Dubrovinsky, L.; Kessler, V. G. *Mater. Chem. Phys.* **2004**, *87* (1), 142–148.

(8) Becker, N.; Dronskowski, R. *J. Solid State Chem.* **2016**, *237*, 404–410.

(9) Sasaki, T. A.; Kiuchi, K. *Chem. Phys. Lett.* **1981**, *84* (2), 356–360.

(10) Sasaki, T. A.; Soga, T.; Adachi, H. *Phys. Status Solidi B* **1982** (2), *113*, 647–655.

(11) Burdett, J. K. *Inorg. Chem.* **1985**, *24* (14), 2244–2253.

(12) Yoshino, H.; Shimokoshi, K.; Miyazaki, E. *J. Electron Spectrosc. Relat. Phenom.* **1985**, *36* (3), 269–279.

(13) Scanlon, D. O.; Watson, G. W.; Payne, D. J.; Atkinson, G. R.; Egdell, R. G.; Law, D. S. L. *J. Phys. Chem. C* **2010**, *114* (10), 4636–4645.

(14) Kruglova, A. G. *Int. Geol. Rev.* **1982**, *24* (5), 617–620.

(15) Shi, Y.; Guo, B.; Corr, S. A.; Shi, Q.; Hu, Y.-S.; Heier, K. R.; Chen, L.; Seshadri, R.; Stucky, G. D. *Nano Lett.* **2009**, *9* (12), 4215–4220.

(16) Camacho-López, M. A.; Escobar-Alarcón, L.; Picquart, M.; Arroyo, R.; Córdoba, G.; Haro-Poniatowski, E. *Opt. Mater. (Amsterdam, Neth.).* **2011**, *33* (3), 480–484.

(17) Auborn, J. J.; Barberio, Y. L. *J. Electrochem. Soc.* **1987**, *134* (3), 638–641.

(18) Liang, Y.; Yang, S.; Yi, Z.; Lei, X.; Sun, J.; Zhou, Y. *Mater. Sci. Eng. B* **2005**, *121* (1–2), 152–155.

(19) Yang, L. C.; Gao, Q. S.; Tang, Y.; Wu, Y. P.; Holze, R. *J. Power Sources* **2008**, *179* (1), 357–360.

(20) Sun, Y.; Hu, X.; Luo, W.; Huang, Y. *ACS Nano* **2011**, *5* (9), 7100–7107.

(21) Liang, Y.; Yi, Z.; Yang, S.; Zhou, L.; Sun, J.; Zhou, Y. *Solid State Ionics* **2006**, *177* (5–6), 501–505.

(22) Ma, Y.-R.; Tsai, C.-C.; Lee, S. F.; Cheng, K.-W.; Liou, Y.; Yao, Y. D. *J. Magn. Magn. Mater.* **2006**, *304* (1), e13–e15.

(23) Liu, X.; He, Y.; Wang, S.; Zhang, Q. *J. Alloys Compd.* **2011**, *509* (SUPPL. 1), S408–S411.

(24) Buono-Core, G. E.; Cabello, G.; Klahn, A. H.; Lucero, A.; Nuñez, M. V.; Torrejón, B.; Castillo, C. *Polyhedron* **2010**, *29* (6), 1551–1554.

(25) Hu, B.; Mai, L.; Chen, W.; Yang, F. *ACS Nano* **2009**, *3* (2), 478–482.

(26) Haines, J.; Léger, J. M.; Hull, S.; Petitet, J. P.; Pereira, A. S.; Perottoni, C. A.; Jornada, J. A. H. *J. Am. Ceram. Soc.* **2005**, *80* (7), 1910–1914.

(27) Fu, Z.; Liang, Y.; Wang, S.; Zhong, Z. *Phys. Status Solidi B* **2013**, *250* (10), 2206–2214.

(28) Woodhead, K.; Pascarelli, S.; Hector, A. L.; Briggs, R.; Alderman, N.; McMillan, P. F. *Dalton Trans.* **2014**, *43* (25), 9647–9654.

(29) Sundberg, M.; Werner, P.-E.; Zibrov, I. P. *Z. Kristallogr.* **1994**, *209* (8), 662–666.

(30) McCarron, E. M.; Calabrese, J. C. *J. Solid State Chem.* **1991**, *91* (1), 121–125.

(31) Koch-Müller, M.; Mugnaioli, E.; Rhede, D.; Speziale, S.; Kolb, U.; Wirth, R. *Am. Mineral.* **2014**, *99* (11–12), 2405–2415.

(32) Rietveld, H. M. *Acta Crystallogr.* **1967**, *22* (1), 151–152.

(33) Le Bail, A.; Duroy, H.; Fourquet, J. L. *Mater. Res. Bull.* **1988**, *23* (3), 447–452.

(34) Rodríguez-Carvajal, J. In *Abstracts of the Satellite Meeting on Powder Diffraction of the XV IUCr Congress*; 1990; p 127.

(35) *Rigaku Oxford Diffraction*. Rigaku Corporation: Oxford, U.K., 2015.

(36) Clark, R. C.; Reid, J. S. *Acta Crystallogr. Sect. A* **1995**, *51* (6), 887–897.

(37) Sheldrick, G. M. *Acta Crystallogr. Sect. C* **2015**, *71* (1), 3–8.

(38) Brandenburg, K. *Diamond 3.2;* Crystal Impact GbR: Bonn, Germany, 2012.

(39) Kresse, G.; Furthmüller, J. *Comput. Mater. Sci.* **1996**, *6* (1), 15–50.

(40) Blöchl, P. E. *Phys. Rev. B* **1994**, *50* (24), 17953–17979.

(41) Perdew, J. P.; Burke, K.; Ernzerhof, M. *Phys. Rev. Lett.* **1996**, *77* (7), 3865–3868.

(42) Perdew, J. P.; Burke, K.; Ernzerhof, M. *Phys. Rev. Lett.* **1997**, *78* (7), 1396–1396.

(43) Grimme, S.; Antony, J.; Ehrlich, S.; Krieg, H. *J. Chem. Phys.* **2010**, *132* (15), 154104-1–19.

(44) Grimme, S.; Ehrlich, S.; Goerigk, L. *J. Comput. Chem.* **2011**, *32* (7), 1456–1465.

(45) Birch, F. *Phys. Rev.* **1947**, *71* (11), 809–824.

(46) Togo, A.; Oba, F.; Tanaka, I. *Phys. Rev. B* **2008**, *78* (13), 134106-1–9.

(47) Stoffel, R. P.; Wessel, C.; Lumey, M.-W.; Dronskowski, R. *Angew. Chem. Int. Ed.* **2010**, *49* (31), 5242–5266.

(48) Shannon, R. D. *Acta Crystallogr., Sect. A* **1976**, *32* (5), 751–767.

(49) Bärnighausen, H. *MATCH Commun. Math. Comput. Chem.* **1980**, *9*, 139–175.

(50) Müller, U. *Z. Anorg. Allg. Chem.* **2004**, *630* (11), 1519–1537.

(51) Müller, U. *Symmetriebeziehungen zwischen verwandten Kristallstrukturen*, 1st ed.; Vieweg + Teubner Verlag: Wiesbaden, 2012.

(52) George, J.; Deringer, V. L.; Dronskowski, R. *Inorg. Chem.* **2015**, *54* (3), 956–962.

(53) Dieterle, M.; Mestl, G. *Phys. Chem. Chem. Phys.* **2002**, *4* (5), 822–826.

(54) Bain, G. A.; Berry, J. F. *J. Chem. Educ.* **2008**, *85* (4), 532–536.

8.8 Supporting Information

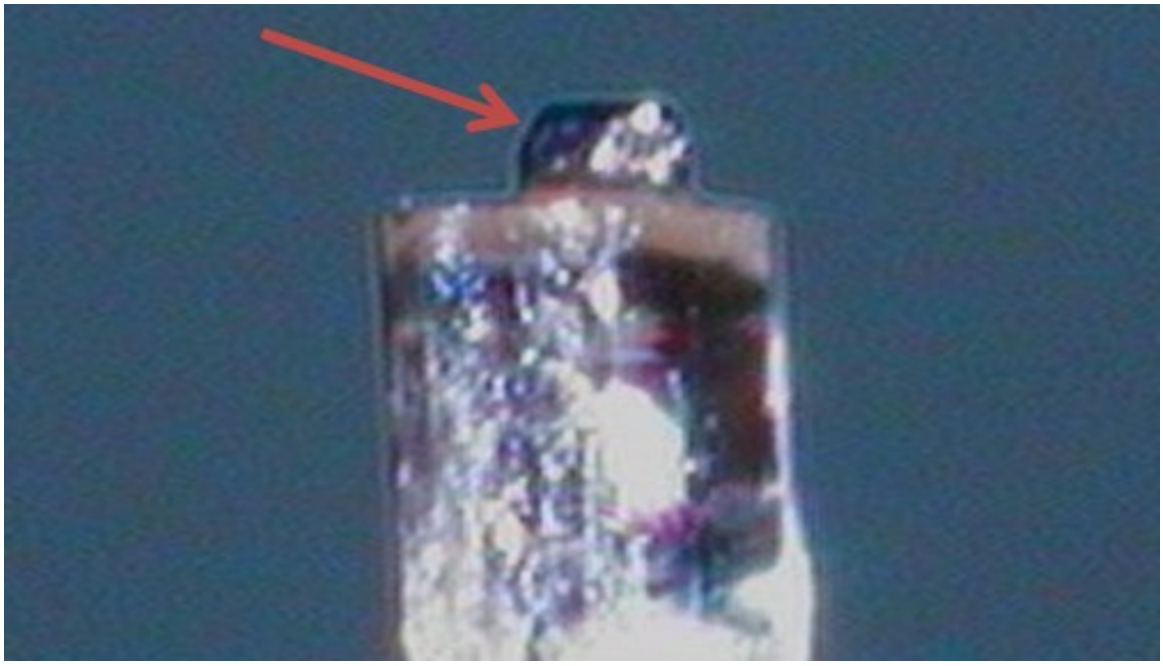

Figure 8.10. HP-MoO_2 single crystal used for X-ray crystal structure determination.

Table 8.4. Assignments, calculated and experimental wavenumbers for the HP-MoO_2 Raman-active modes. The letters in parenthesis indicate the respective relative band intensities: w = weak, vw = very weak, s = strong, vs = very strong, sh = shoulder. The matching between the calculated and experimental Raman mode wavenumbers is tentative.

HP-MoO_2 Raman-active mode wavenumbers (cm^{-1})		
Assignment	Calculated	Observed
B_{3g}	129.80	
A_g	141.29	148 (w)
A_g	153.08	155 (w)
B_{3g}	159.51	
B_{1g}	160.07	163 (vw)
B_{2g}	185.33	
A_g	196.64	200 (s)
B_{1g}	203.03	
B_{2g}	215.79	219 (w)
B_{1g}	224.89	
B_{3g}	232.08	232 (vw)
B_{2g}	234.88	240 (w)
B_{2g}	251.61	
A_g	258.15	258 (w)
B_{3g}	267.83	264 (w)
B_{1g}	273.81	276 (vw)
B_{1g}	282.81	
B_{2g}	310.76	317 (vw)
A_g	320.73	330 (s)
B_{2g}	342.45	348 (w)
A_g	349.92	359 (s)
B_{3g}	350.10	
B_{2g}	363.70	
B_{3g}	367.56	
B_{1g}	368.11	
A_g	383.93	391 (vs)
A_g	398.21	409 (s)
B_{2g}	439.17	
B_{3g}	448.01	
B_{1g}	455.00	453 (w)
B_{1g}	459.25	

Assignment	Calculated	Observed
B_{3g}	462.14	
B_{2g}	474.82	
A_g	482.10	488 (s)
B_{2g}	485.82	
B_{3g}	489.35	496 (vw)
B_{1g}	493.35	
A_g	500.28	511 (s)
B_{2g}	510.00	
A_g	522.31	525 (w)
B_{3g}	534.59	
B_{1g}	539.13	
B_{3g}	559.50	
B_{1g}	567.82	585 (w)
A_g	586.64	
B_{2g}	601.32	
A_g	704.32	713 (s)
B_{2g}	706.23	
A_g	736.34	733 (s)
B_{1g}	740.22	
B_{2g}	740.73	
A_g	754.79	753 (sh)
B_{3g}	756.84	
B_{2g}	791.66	807 (w)

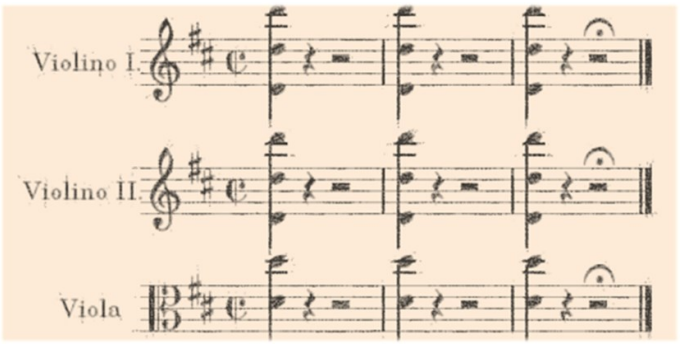

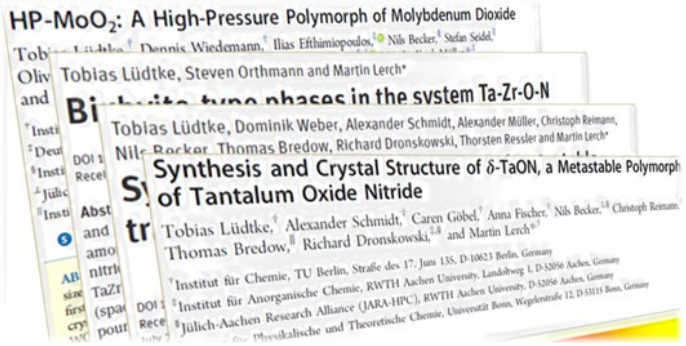

Part III

Conclusion and Prospects

9 Conclusion 163

A Appendices 169

B Bibliography 177

Pictures on the cover sheet:

Top: Conclusion of the *Symphony No. 9 in D minor* by Ludwig van Beethoven with the last three measures for the string instruments.

Center: Artistically modified photo of utilized chemicals.

Bottom: Collage of the printed versions of Publications 1, 2, 3, and 5.

9 Conclusion

δ-TaON (Publications 1 & 2). It was possible to analyze the previously synthesized samples of anatase-type δ-TaON by means of powder X-ray diffraction for structural properties and hot gas extraction for the anion composition. The Rietveld refinement was complemented by additional data of neutron diffraction measurements of $Mg_{0.05}Ta_{0.95}O_{1.15}N_{0.85}$.[51] Unfortunately, no phase-pure samples could be prepared, but fine adjustment of the synthesis parameters of the ammonolysis reaction almost doubled the maximum yield to 82 wt %. A picture of one sample is presented in Figure 9.1. Impurities of γ-TaON and Ta_3N_5 still prevent a comprehensive analysis of the first ternary anatase-type compound without titanium. Nevertheless, this second metastable polymorph of tantalum oxide nitride is, with a calculated stability difference of *ca.* 22 kJ·mol^{-1} to β-TaON,[126] the most unstable polymorph (γ-TaON: *ca.* 17 kJ·mol^{-1}; bixbyite-type V_2O_3: *ca.* 9 kJ·mol^{-1}; anosovite-type V_3O_5: *ca.* 15 kJ·mol^{-1})[6,7,128] obtained throughout the research cluster "Synthesis, characterization, and theoretical description of metastable oxides and oxide nitrides of transition metals" of the SPP 1415. It transforms in a monotropic transition to the baddeleyite-type β-form at temperatures between 1073 and 1123 K. No intermediate steps could be observed. The calculated density is slightly higher compared with γ-TaON, which is a deviation from the Ostwald–Volmer rule. Determined bond lengths are in excellent agreement with experimental and calculated data of anatase-type $Mg_{0.05}Ta_{0.95}O_{1.15}N_{0.85}$.

Quantum-chemical investigations, in association with the successful synthesis, indicate that the most stable configuration in space group $I4_1md$ consists of N–Ta–N and O–Ta–O chains in *a* and *b* direction, which corresponds to the maximum possible distance and lowest repulsion of the N^{3-} ions. These results are consistent with previous

Figure 9.1.
Sample of δ-TaON with γ-TaON and Ta_3N_5 side phases.

studies.[51,266] Calculated relative Gibbs energies show an instability up to 1600 K and consequently a lower transition temperature. Therefore, the transition is controlled by kinetics. The lack of imaginary modes in the PDOS proves the dynamic stability of the phase.

Additional investigations on the synthesized samples by Dr. Sevilay Cosgun showed an indirect band gap of 1.73 eV and a direct of 2.06 eV,[56] compared with calculated 2.52 eV and determined 2.37 eV for the anatase-TaON layers.[132] Surprisingly, no measurable photocatalytic activity was detectable. Due to the often mentioned phase impurities, the results should be considered provisional.

Bixbyite-type phases in the System Ta-Zr-O-N (Publication 3). Motivated by the successful preparation of new compounds based on tantalum oxide nitrides by cation substitution with Mg,[51,52] Sc,[53–56] and Y,[52,57] this approach was extended to the Ta-Zr-O-N system. New phases with bixbyite-type structure, isotypically to Zr_2ON_2 and phases in the system Sc-Ta-O-N, were synthesized. Besides the already known phases with baddeleyite- and anosovite-type structure,[177] these novel compounds extend the already well-studied system by a third structure type. In addition, the pure nitride $TaZrN_3$ was found at an evened ratio of Ta and Zr. The compositional range of the new phases can be expressed by two general sum formulas: $Ta_{1-x}Zr_{1+x}O_{x+3y/2}N_{3-x-y}$ $(0 \le x \le 1,\ 0 \le y \le 2)$ and $Ta_{1+x}Zr_{1-x}O_{3y/2}N_{3+x/3-y}$ $(0 \le x \le 0.33,\ 0 \le y \le 2–2x/3)$. The main focus was set to the Ta:Zr cation ratios of 1:2, 1:1, and 2:1. The latter ratio also represents the highest possible content of Ta for phase pure samples, indicated in the x restriction of the second formula. At even higher amounts of Ta, no morphotropic transition could be observed. Ammonolysis of these precursors resulted in biphasic samples with baddeleyite- or anosovite-type side phases. Details on all experimentally obtained compounds are summarized in Table 9.1.

Table 9.1. Compositional range of all obtained bixbyite-type phases in the system Ta-Zr-O-N.

Ta:Zr	Sum formula	Theoretical y-range	Experimental y-range
2:1	$Ta_{1.33}Zr_{0.67}O_{3y/2}N_{3.11-y}$	$0 \le y \le 1.88$	$0.08 \le y \le 0.20$
1:1	$TaZrO_{3y/2}N_{3-y}$	$0 \le y \le 2$	$0 \le y \le 1.11$
1:2	$Ta_{0.67}Zr_{1.33}O_{0.33+3y/2}N_{2.67-y}$	$0 \le y \le 2$	$0.06 \le y \le 1.04$

Figure 9.2. Synthesized tantalum zirconium oxide nitrides and the nitride $TaZrN_3$. Left to right: $Ta_{0.67}Zr_{1.33}O_{1.89}N_{1.63}$, $Ta_{0.67}Zr_{1.33}O_{1.38}N_{1.97}$, $Ta_{0.67}Zr_{1.33}O_{0.42}N_{2.61}$, $TaZrN_3$, and $Ta_{1.33}Zr_{0.67}O_{0.12}N_{3.03}$.

The varying anion composition has a noticeably effect on the lattice parameter of the cubic unit cell. A change of *ca.* 13 pm could be observed for several different compounds of the same cation series. Another affected variable is the *x* position of the 24*d* cation site, which converges to the ideal value for the fluorine structure with a rising of δ.

Thermal stability under an inert gas atmosphere was observed up to temperatures of at least 1273 K. Under air, the sample starts to amorphousize at temperatures above 600 K. $TaZrN_3$ can be considered as a stable substituted form of metastable Ta_2N_3.

Five selected samples with a distinct difference in anion composition and color (Figure 9.2) were chosen for the investigation of the optical properties by diffuse reflectance UV-vis spectroscopy. Values for the direct band gap of 1.71–2.48 eV and for the indirect band gap of 1.27–1.87 eV were found. The energy difference between the valence and conducting band decreases with an increasing nitrogen content.

HP-MoO_2 (Publications 4 & 5). Efforts to synthesize novel oxide polymorphs of molybdenum and tungsten by conventional synthesis routes were unsuccessful. Those results are supported by first-principle investigations on DFT level of binary dioxides of molybdenum[229] and the sesquioxides (Chapter 8) of both elements by Nils Becker *et al.* A synthesized α-MoO_2 precursor, obtained by reduction of MoO_3 with a H_2/O_2 mixture, was converted in cooperation with Prof. Dr. Monika Koch-Müller of the GFZ Potsdam in a multianvil press at 18 GPa and 1073 K to a new high-pressure polymorph. Investigations by the whole powder pattern decomposition method (Le Bail method) on powder X-ray diffraction data revealed the HP-WO_2 type as the adequate crystal structure. The

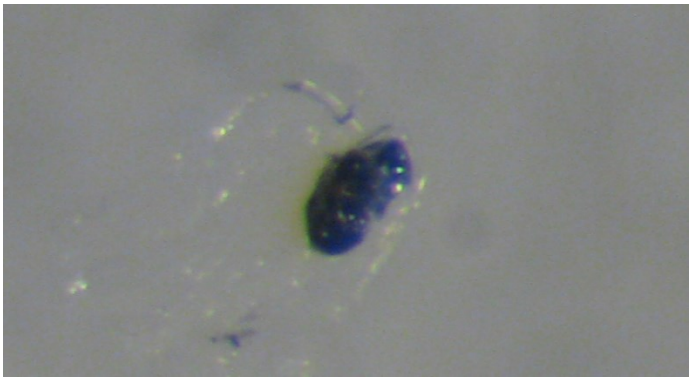

Figure 9.3.
HP-MoO_2 single crystal, photographed through a microscope.

Rietveld refinement did not give any meaningful results due to the coarse crystalline morphology with possible preferred orientations of the sample.

Diffraction analysis of single-crystals (Figure 9.3) confirmed the suggested crystal structure and delivered an entire dataset of crystallographic information. A Bärnighausen-tree shows the relationship of the hettotype to the NiAs aristotype. Computation of the electronic DOS and measurements of the molar magnetic susceptibility classifies the new polymorph as a diamagnetic semimetal with a low electrical conductivity.

9.1 Outlook

Further improvements in synthesis and product quantity per reaction have to be achieved for δ-TaON. If phase-pure samples are available in sufficient quantities, neutron diffraction experiments are recommended to finally elucidate the anion distribution. The preparation of multilayered nanotubes, comparable to anatase TiO_2 nanotubes,[300] might be an interesting alteration of the morphology, which could affect the physical properties.

The aleatory character of the synthesis of novel tantalum oxide nitrides only relates to the exact adjustment of the synthesis conditions. Over all contributions to this topic it can be summarized that the polymorphs require lower reaction temperatures and shorter reaction times with increasing instability. The reaction temperature of 1023 K for δ-TaON is very close to the temperature range where the amorphous precursor starts to crystallize. With the synthesis of the δ-phase it remains uncertain if additional polymorphs of tantalum oxide nitrides can be obtained *via* the here applied synthesis route. Apart from the crystalline phases, another metastable species has not been studied intensively yet. As mentioned in the introduction, the amorphous state is also a metastable condition. Amorphous tantalum oxide nitrides can be considered as a mixture of amor-

phous Ta_2O_5 and Ta_3N_5, therefore the compositional range is not restricted to the common AX_2 composition. These compounds probably offer a wide range of colors and optical bandgaps that could be suitable for the usage as color pigments or photocatalysts.

The novel bixbyite-type oxide nitrides and nitrides of tantalum and zirconium show interesting band gaps for the photocatalytical water splitting. Measurements of the catalytic activity are the logical next step for a further characterization of these promising compounds. A worthwhile effort might be a closer investigation of the orthorhombic side phase reported by Grins *et al.*[177] (Chapter 2.3) as a possible fourth phase in the system Ta-Zr-O-N. Considering the difficulties of structure determination of the ternary oxides (also Chapter 2.3), further studies in this area is highly recommended.

Hafnium, which is closely related in its chemical properties to the lighter homologue Zr, could be another suitable substituent for the modification of tantalum oxide nitrides. Surprisingly, the Ta-Hf-O-N system is rarely explored. Besides investigations on layers and thin films,[301] only the existence of $HfTaO_3N$ has been elucidated theoretically, although the system might be offering interesting properties for optoelectronic devices.[302]

With the successful synthesis of HP-MoO_2, further exploration of the high-pressure area is a promising and well-established approach for novel polymorphs. Another polymorph of MoO_2 with *ortho*-TiO_2 structure is predicted to form at pressures greater than 25 GPa. Other transition metal oxides could also be investigated. As a starting point, theoretical investigations on the sesquioxide high-pressure polymorphs of Nb, Ta,[9,11] and Cr[9,12] have been made within the priority program SPP 1415.

A Appendices

A.1 Additional Information

A.1.1 Chemicals

Table A.1. List of utilized chemicals.

Chemical	Producer	Purity
Tantalum(V) chloride ($TaCl_5$)	Sigma-Aldrich	99.999%
Zirconium(IV) chloride ($ZrCl_4$)	Sigma-Aldrich	99.99%
Molybdenum(VI) oxide (MoO_3)	Sigma-Aldrich	99.5%
Ethanol	Acros Organics	99.5%
Citric acid	Sigma-Aldrich	≥ 99.5%
Ethylene glycol	Alfa Aesar	99%
Ammonia (NH_3)	Air Liquide	99.98%
Oxygen (O_2)	Air Liquide	99.999%
Hydrogen (H_2)	Air Liquide	99.999%

A.1.2 Software

Table A.2. List of utilized software.

Software	Latest version	Producer
WINDOWS 7 PROFESSIONAL	SP 1, 6.1.7601	Microsoft
OFFICE 2010	14.0.7177.5000	Microsoft
X'PERT HIGHSCORE PLUS	4.6a (4.6.1.23823)	PANalytical
FULLPROF	June-2015	JGP - JRC
DIAMOND	4.3.1	Crystal Impact GbR
FINDIT	1.9.6	FIZ Karlsruhe
MERCURY, incl. ENCIFER	3.9	CCDC
ORIGIN	2016G; b9.3.226	OriginLab Corporation
MENDELEY DESKTOP	1.17.8	Mendeley Ltd.
GIMP	2.8.14	GIMP-Team
GRAPHVIZ	2.38	AT&T Labs Research

A.2 Supplementary Material

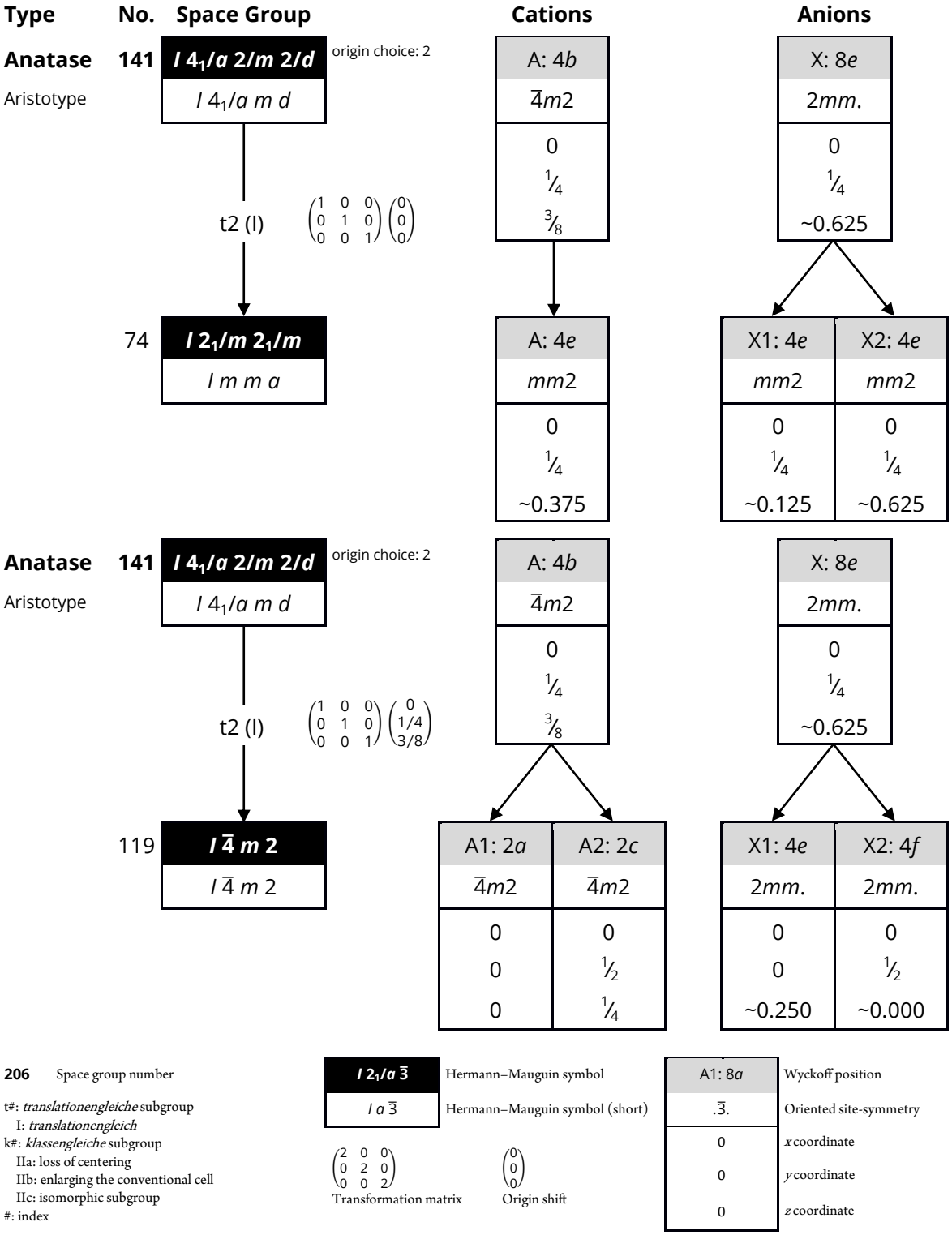

Figure A.1. Group-subgroup relation between anatase ($I4_1/amd$; aristotype) and *Imma* or $I\bar{4}m2$.[250,252,254–256,262,263]

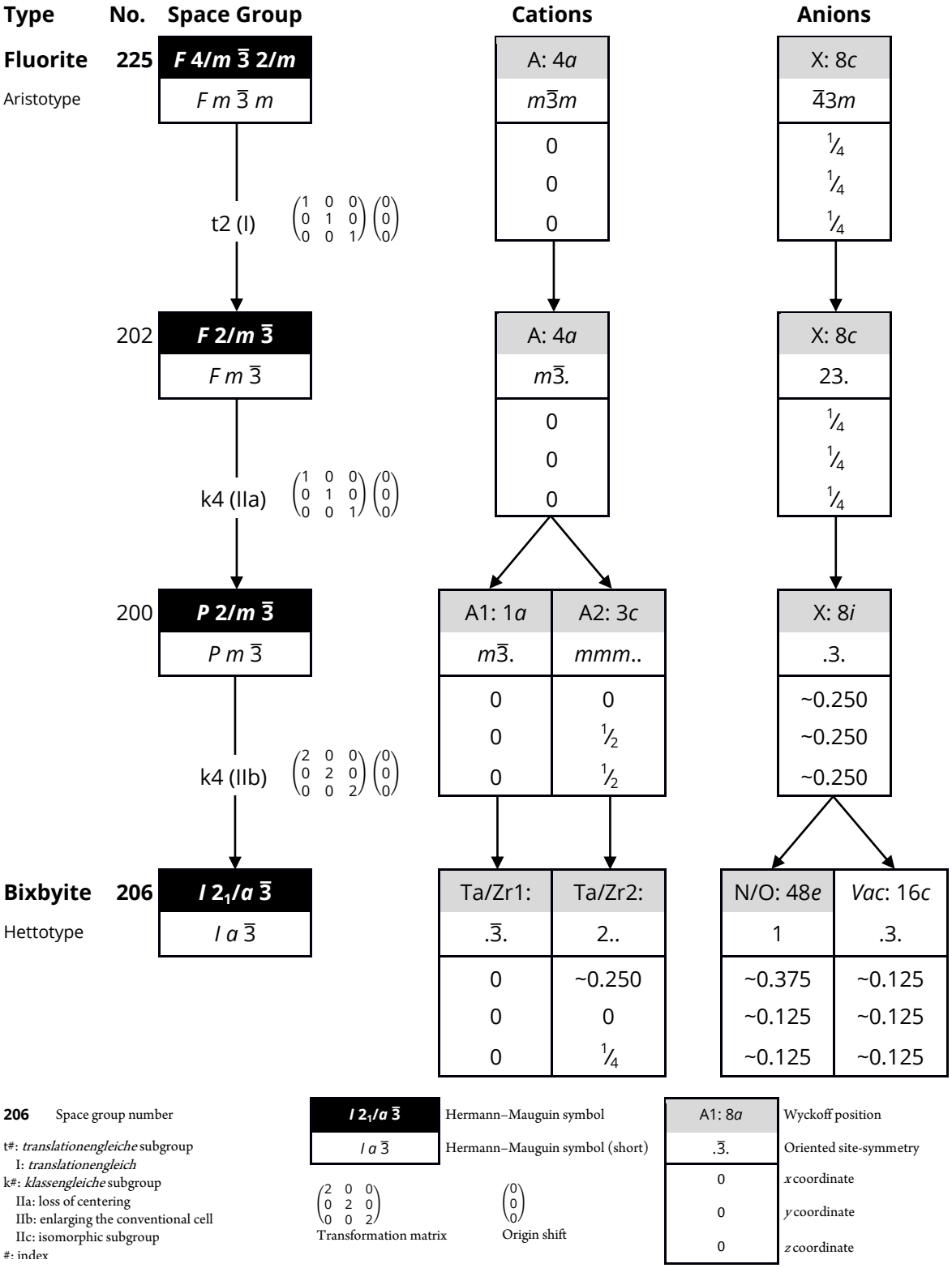

Figure A.2. Second variant of the group-subgroup scheme (Bärnighausen formalism) for the group-theoretical relationship between fluorite (aristotype) and bixbyite-type $(Ta,Zr)_2(O,N)_{3+\delta}$ (hettotype).[250,252,254–256,263]

A.3 Abbreviations, Variables, and Non-SI Units

a	Space groups: glide plane along half the lattice vector of this face
a, b, c	Cell parameters
Å	Ångström; 1 Å = 10^{-10} m
AFM	Antiferromagnetic
anion %	Anion percent; partial fraction of an anionic species of the total anion fraction
a. u.	Arbitrary units
bcc	Body-centered cubic
b	Space groups: glide plane along half the lattice vector of this face
B_{iso}	Isotropic temperature displacement factor (Debye-Waller factor)
c	Space groups: glide plane along half the lattice vector of this face
C	Space groups: base-centered Bravais lattice on *ab* faces only
C	Rietveld residuals: number of parameter linkages
calc	Calculated
CCD	Charge-Coupled Device
CCDC	Cambridge Crystallographic Data Centre
CIF	Crystallographic Information File[303]
CSD	Cambridge Structural Database
Cu-$K_{\alpha(1,2)}$	Emission lines of an electron transitions to the "*K*" shell (principal quantum number 1) from the "*L*" shell (principal quantum number 2) in copper.
Cu-K_{β}	Emission lines of an electron transitions to the "*K*" shell (principal quantum number 1) from the "*M*" shell (principal quantum number 3) in copper.
CVD	Chemical vapor deposition
d	Space groups: glide plane along a quarter of a face diagonal
d	Distance between atomic layers (*hkl*)
DFG	Deutsche Forschungsgemeinschaft (German Science Foundation)
DFT	Density-Functional Theory
DM	Diamagnetic
DOS	Density Of States
D3(BJ)	Dispersion correction with Becke-Johnson damping
EDX	Energy Dispersive X-ray spectroscopy
emu	Electromagnetic unit; in this case, the unit-less magnetic susceptibility is assigned to the CGS unit system, $\chi_{SI} = 4\pi \cdot \chi_{CGS}$
eV	Electronvolt; 1 eV ≈ $1.6021766208 \cdot 10^{-19}$ J

F	In space groups: face-centered Bravais lattice
F	Structure factor amplitudes
fcc	Face-centered cubic
FIZ	Fachinformationszentrum
FM	Ferromagnetic
FWHM	Full Width at Half Maximum
GFZ	GeoForschungsZentrum
GGA	Generalized Gradient Approximation
GPAW	A computer program based on the projector-augmented wave (PAW) method and the atomic simulation environment.
GST	Semiconducting materials used as PCM consisting of the elements Ge, Sb, and Te, *e.g.* $Ge_2Sb_2Te_5$
GW	Combination of a Green function approach with a screened Coulomb potential (W)
H	Enthalpy
h	Hour; 1 h = 3600 s
hcp	Hexagonal close-packing
hkl	Miller indices
H	Enthalpy
HP	High Pressure
HR	High Resolution
I	Space groups: body-centered Bravais lattice
I	Intensity
ICDD	International Centre for Diffraction Data
ICSD	Inorganic Crystal Structure Database
L	Liter; 1 L = 0.001 m^3
LCA	Linear Combination Analysis
m	Space groups: mirror plane
min	Minute; 1 min = 60 s
mol %	Mol percent; amount of substance of a component of the substance
N	Rietveld residuals: Number of measured points
n	Space groups: glide plane along half a face diagonal
obs	Observed
Occ.	Occupation

Oe	Oersted, unit of the magnetic field H; 1 Oe = $1000 \cdot (4\pi)^{-1}$ A·m^{-1} ≈ 79.58 A·m^{-1}
P	Space groups: primitive Bravais lattice
P	Rietveld residuals: Number of parameters
Pa	Pascal; unit of pressure, 1 Pa = 1 N·m^{-2} = kg·m^{-1}·s^{-2}
PAW	Projector-Augmented Waves
PBE	Perdew, Burke, and Ernzerhof
PCM	Phase Change Memory
pCOHP	Projected Crystal Orbital Hamilton Population
PDOS	Phonon Density Of States
PE	Polyethylene
PPMS	Quantum Design Physical Property Measurement System
PW1PW	Perdew–Wang Hartree–Fock hybrid method
R_1	Residual for significantly intense reflections for single-crystal refinements $R_1 = \sqrt{\frac{\sum_{i=1}^{N} \left\| F_i^{obs} - F_i^{calc} \right\|}{\sum_{i=1}^{N} \left\| F_i^{obs} \right\|}}$
R_{Bragg}	Bragg *R* factor (Chapter 2.7.1)
R_{exp}	Expected *R* factor (Chapter 2.7.1)
R_{int}	Independent reflections
R_{wp}	Weighted *R* factor (Chapter 2.7.1)
R_σ	Observed reflections
S	Goodness of Fit (Chapter 2.7.1)
SAED	Selected Area Electron Diffraction
S.O.F.	Site Occupation Factor
SPP	Schwerpunktprogramm (priority program)
SST	Super Sharp Tube
SUTW	Super Ultra Thin Window
T_{min}, T_{max}	Absorption correction
TEM	Transmission Electron Microscopy
UV-vis	Ultraviolet-visible
Vac	Vacancy
VASP	Vienna Ab initio Simulation Package
vol %	Volume percent; volume fraction of a component of the total volume
WDX	Wavelength-Dispersive X-ray spectroscopy

WDXRF	Wavelength-Dispersive X-Ray Fluorescence
w_i	Rietveld residuals: weighting factor at point *i*
wR_2	Weighted residual for significantly intense reflections of single-crystal refinements

$$wR_2 = \sqrt{\frac{\sum_{i=1}^{N} w_i \left[y_i^{\text{obs}} - y_i^{\text{calc}} \right]^2}{\sum_{i=1}^{N} w_i \left[y_i^{\text{obs}} \right]^2}}$$

wt %	Weight percent; mass fraction of a component of the total mass
x, y, z	Atomic positions
XAS	X-ray Absorption Spectroscopy
XANES	X-ray Absorption Near Edge Structure
XRD	X-Ray Diffraction
XRF	X-Ray Fluorescence
y_i	Rietveld residuals: intensity at point *i*
Z	Formula units per unit cell
α, β, γ	Unit cell angles
α	Oxidation degree
θ	Diffraction angle
λ	Wavelength
μ	Absorption coefficient
$\tilde{\nu}$	Wavenumber
ρ_{calc}	Calculated density
ρ_e	Difference electron density
σ^2	Disorder parameter
χ	Magnetic susceptibility
2, 3, 4	Space groups: rotation axes
$2_1, 4_1, 6_3$	Space groups: screw axes
$\bar{3}, \bar{4}$	Space groups: rotoinversion axes

B Bibliography

(1) Bensch, W.; Breu, J. *Kristalline Nichtgleichgewichtsphasen - Präparation, Charakterisierung und in-situ-Untersuchung der Bildungsmechanismen, Antrag auf Einrichtung des Schwerpunktprogramms 1415*; Universität Kiel, Universität Bayreuth, 2007.

(2) Lüdtke, T. *Synthese und Charakterisierung neuer Verbindungen mit Anatasstruktur*; Technische Universität Berlin: Berlin, 2013.

(3) Weber, D. A. *Synthese und Charakterisierung neuer Oxide und Oxidnitride der Elemente der 5. und 6. Gruppe des Periodensystems*; Technische Universität Berlin: Berlin, 2014.

(4) Müller, A. *Solid-state kinetic investigations of vanadium oxides and metastable oxide nitrides: theory and experiments*; Technische Universität Berlin: Berlin, 2015.

(5) Reimann, C. *Quantenchemische Untersuchung metastabiler Phasen von Übergangsmetalloxiden und -oxidnitriden*; Rheinische Friedrich-Wilhelms-Universität Bonn: Bonn, 2014.

(6) Weber, D.; Stork, A.; Nakhal, S.; Wessel, C.; Reimann, C.; Hermes, W.; Muller, A.; Ressler, T.; Pöttgen, R.; Bredow, T.; Dronskowski, R.; Lerch, M. Bixbyite-Type V_2O_3—A Metastable Polymorph of Vanadium Sesquioxide. *Inorg. Chem.* **2011**, *50* (14), 6762–6766.

(7) Weber, D.; Wessel, C.; Reimann, C.; Schwickert, C.; Müller, A.; Ressler, T.; Pöttgen, R.; Bredow, T.; Dronskowski, R.; Lerch, M. Anosovite-Type V_3O_5: A New Binary Oxide of Vanadium. *Inorg. Chem.* **2012**, *51* (15), 8524–8529.

(8) Wessel, C.; Reimann, C.; Müller, A.; Weber, D.; Lerch, M.; Ressler, T.; Bredow, T.; Dronskowski, R. Electronic structure and thermodynamics of V_2O_3 polymorphs. *J. Comput. Chem.* **2012**, *33* (26), 2102–2107.

(9) Wessel, C. *Quantenchemische Untersuchung metastabiler Oxide und Oxidnitride der Vanadium- und Chromgruppe*; RWTH Aachen: Aachen, 2012.

(10) Reimann, C.; Weber, D.; Lerch, M.; Bredow, T. Nonstoichiometry in Bixbyite-Type Vanadium Sesquioxide. *J. Phys. Chem. C* **2013**, *117* (39), 20164–20170.

(11) Wessel, C.; Dronskowski, R. A first-principles study on the existence of niobium and tantalum sesquioxide. *Z. Anorg. Allg. Chem.* **2012**, *638* (12–13), 2117–2122.

(12) Wessel, C.; Dronskowski, R. A first-principles study on chromium sesquioxide, Cr_2O_3. *J. Solid State Chem.* **2013**, *199*, 149–153.

(13) McCrone, W. C. Polymorphism. In *Physics and chemistry of the organic solid state Vol II*; Fox, D., Labes, M. M., Weissberger, A., Eds.; Interscience: New York, 1965; pp 726–767.

(14) IUPAC. *Compendium of Chemical Terminology (the "Gold Book")*, 2nd ed.; McNaught, A. D., Wilkinson, A., Eds.; Blackwell Scientific Publications: Oxford, 2014.

(15) IUPAC Compendium of Chemical Terminology http://goldbook.iupac.org (accessed Jan 14, 2016).

(16) Muller, P. Glossary of terms used in physical organic chemistry (IUPAC Recommendations 1994). *Pure Appl. Chem.* **1994**, *66* (5), 1077–1184.

(17) van de Streek, J. Searching the Cambridge Structural Database for the `best' representative of each unique polymorph. *Acta Crystallogr. Sect. B* **2006**, *62* (4), 567–579.

(18) Jansen, M. A Concept for Synthesis Planning in Solid-State Chemistry. *Angew. Chem. Int. Ed.* **2002**, *41* (20), 3746–3766.

(19) Hollemann, A. F.; Wiberg, N.; Wiberg, E. *Lehrbuch der Anorganischen Chemie*, 102th ed.; de Gruyter: Berlin, Boston, 2008.

(20) Atkins, P.; de Paula, J. *Physical chemistry*, 8th ed.; W. H. Freeman and Company: New York, 2006.

(21) Ovshinsky, S. R. Reversible Electrical Switching Phenomena in Disordered Structures. *Phys. Rev. Lett.* **1968**, *21* (20), 1450–1453.

(22) Simpson, R. E.; Fons, P.; Kolobov, A. V; Fukaya, T.; Krbal, M.; Yagi, T.; Tominaga, J. Interfacial phase-change memory. *Nat. Nanotechnol.* **2011**, *6* (8), 501–505.

(23) Wuttig, M.; Lüsebrink, D.; Wamwangi, D.; Wełnic, W.; Gilleßen, M.;

Dronskowski, R. The role of vacancies and local distortions in the design of new phase-change materials. *Nat. Mater.* **2007**, *6* (2), 122–128.

(24) Ostwald, W. Studien über die Bildung und Umwandlung fester Körper. *Z. Phys. Chem.* **1897**, *22*, 289–330.

(25) Nývlt, J. The Ostwald Rule of Stages. *Cryst. Res. Technol.* **1995**, *30* (4), 443–449.

(26) Threlfall, T. Structural and Thermodynamic Explanations of Ostwald's Rule. *Org. Process Res. Dev.* **2003**, *7* (6), 1017–1027.

(27) Ryall, W. R.; Muan, A. Silicon Oxynitride Stability. *Science* **1969**, *165* (3900), 1363–1364.

(28) Jansen, M.; Letschert, H. P. Inorganic yellow-red pigments without toxic metals. *Nature* **2000**, *404* (6781), 980–982.

(29) Aguiar, R.; Logvinovich, D.; Weidenkaff, A.; Rachel, A.; Reller, A.; Ebbinghaus, S. G. The vast colour spectrum of ternary metal oxynitride pigments. *Dye. Pigment.* **2008**, *76* (1), 70–75.

(30) Hitoki, G.; Takata, T.; Kondo, J. N.; Hara, M.; Kobayashi, H.; Domen, K. An oxynitride, TaON, as an efficient water oxidation photocatalyst under visible light irradiation ($\lambda \leq 500$ nm). *Chem. Commun.* **2002**, *2* (16), 1698–1699.

(31) Hara, M.; Hitoki, G.; Takata, T.; Kondo, J. N.; Kobayashi, H.; Domen, K. TaON and Ta_3N_5 as new visible light driven photocatalysts. *Catal. Today* **2003**, *78* (1–4), 555–560.

(32) Siritanaratkul, B.; Maeda, K.; Hisatomi, T.; Domen, K. Synthesis and photocatalytic activity of perovskite niobium oxynitrides with wide visible-light absorption bands. *ChemSusChem* **2011**, *4* (1), 74–78.

(33) Tessier, F.; Maillard, P.; Cheviré, F.; Domen, K.; Kikkawa, S. Optical properties of oxynitride powders. *J. Ceram. Soc. Japan* **2009**, *117* (1361), 1–5.

(34) Tessier, F.; Marchand, R. Ternary and higher order rare-earth nitride materials: Synthesis and characterization of ionic-covalent oxynitride powders. *J. Solid State Chem.* **2003**, *171* (1–2), 143–151.

(35) Kikkawa, S.; Takeda, T.; Yoshiasa, A.; Maillard, P.; Tessier, F. Crystal structure and optical properties of oxynitride rare-earth tantalates RTa–(O, N) (R=Nd, Gd, Y). *Mater. Res. Bull.* **2008**, *43* (4), 811–818.

(36) Kou, J.; Li, Z.; Yuan, Y.; Zhang, H.; Wang, Y.; Zou, Z. Visible-Light-Induced Photocatalytic Oxidation of Polycyclic Aromatic Hydrocarbons over Tantalum Oxynitride Photocatalysts. *Environ. Sci. Technol.* **2009**, *43* (8), 2919–2924.

(37) Lerch, M.; Lerch, J.; Hock, R.; Wrba, J. Synthesis and Characterization of Oxynitrides in the ZrO_2-Rich Part of the Systems Ca–Zr–O–N and Mg–Zr–O–N. *J. Solid State Chem.* **1997**, *128* (2), 282–288.

(38) Ho, C.-T.; Low, K.-B.; Klie, R. F.; Maeda, K.; Domen, K.; Meyer, R. J.; Snee, P. T. Synthesis and Characterization of Semiconductor Tantalum Nitride Nanoparticles. *J. Phys. Chem. C* **2011**, *115* (3), 647–652.

(39) Münster, A. Eigenschaften und Anwendungen von Titannitrid und Titancarbid. *Angew. Chem.* **1957**, *69* (9), 281–290.

(40) Lerch, M.; Janek, J.; Becker, K. D.; Berendts, S.; Boysen, H.; Bredow, T.; Dronskowski, R.; Ebbinghaus, S. G.; Kilo, M.; Lumey, M. W.; Martin, M.; Reimann, C.; Schweda, E.; Valov, I.; Wiemhöfer, H. D. Oxide nitrides: From oxides to solids with mobile nitrogen ions. *Prog. Solid State Chem.* **2009**, *37* (2–3), 81–131.

(41) Gomathi, A. *Contributions to the Chemistry of Metal Nitrides and Inorganic Nanomaterials*; Bangalore, 2010.

(42) Dobrzhinetskaya, L. F.; Wirth, R.; Yang, J.; Green, H. W.; Hutcheon, I. D.; Weber, P. K.; Grew, E. S. Qingsongite, natural cubic boron nitride: The first boron mineral from the Earth's mantle. *Am. Mineral.* **2014**, *99* (4), 764–772.

(43) Lee, M. R.; Russell, S. S.; Arden, J. W.; Pillinger, C. T. Nierite (Si3N4), a new mineral from ordinary and enstatite chondrites. *Meteoritics* **1995**, *30* (4), 387–398.

(44) Bannister, F. A. Osbornite, Meteoritic Titanium Nitride. *Mineral. Mag.* **1941**, *26* (173), 36–44.

(45) Buchwald, V. F.; Scott, E. R. D. First Nitride (CrN) in Iron Meteorites. *Nat. Phys. Sci.* **1971**, *233* (41), 113–114.

(46) Silvestri, O. Das Vorkommen des Stickstoffeisens unter den Fumarolen - Producten des Aetna und künstliche Darstellung dieser Verbindung. *Ann. d. Phys.* **1876**, *233* (1), 165–172.

(47) Hendricks, S. B.; Kosting, P. R. XXXV. The Crystal Structure of Fe_2P, Fe_2N, Fe_3N

and FeB. *Z. Kristallogr.* **1930**, *74* (1–6).

(48) Buchwald, V. F.; Nielsen, H. P. Roaldite, a New Nitride in Iron Meteorites. In *Abstracts of papers submitted to the Twelfth Lunar and Planetary Science Conference*; Houston, 1981; pp 112–114.

(49) Bayliss, P. Revised unit-cell dimensions, space group, and chemical formula of some metallic minerals. *Can. Miner.* **1990**, *28* (4), 751–755.

(50) Chen, J.; Shi, X.; Zhang, H.; Lü, H.; Fu, Z. The finding of natural GaN crystals in sediments from the East Pacific Ocean. *Chinese Sci. Bull.* **2006**, *51* (9), 1101–1105.

(51) Schilling, H.; Lerch, M.; Börger, A.; Becker, K.-D.; Wolff, H.; Dronskowski, R.; Bredow, T.; Tovar, M.; Baehtz, C. A new anatase-type phase in the system Mg–Ta–O–N. *J. Solid State Chem.* **2006**, *179* (8), 2416–2425.

(52) Schilling, H. *Synthese und Charakterisierung neuartiger Materialien auf der Basis von Oxidnitriden des Tantals*; Technische Universität Berlin: Berlin, 2006.

(53) Stork, A.; Schilling, H.; Wessel, C.; Wolff, H.; Börger, A.; Baehtz, C.; Becker, K.-D.; Dronskowski, R.; Lerch, M. Bixbyite- and anatase-type phases in the system Sc–Ta–O–N. *J. Solid State Chem.* **2010**, *183* (9), 2051–2058.

(54) Stork, A. Neue Oxide und Oxidnitride von Übergangsmetallen, Technische Universität Berlin, Berlin, 2011.

(55) Cosgun, S.; Rohloff, M.; Göbel, C.; Gernert, U.; Fischer, A.; Lerch, M. Synthesis and Crystal Structure of Rutile-type $ScTa_2O_5N$. *Z. Anorg. Allg. Chem.* **2014**, *640* (14), 2771–2775.

(56) Cosgun, S. *Synthese und Charakterisierung Tantaloxidnitrid-basierter Verbindungen für die photokatalytische Wasserspaltung*; Technische Universität Berlin: Berlin, 2015.

(57) Schilling, H.; Wolff, H.; Dronskowski, R.; Lerch, M. Fluorite-type solid solutions in the system Y-Ta-O-N: A nitrogen-rich analogue to yttria-stabilized zirconia (YSZ). *Z. Naturforsch.* **2006**, *61b* (6), 660–664.

(58) Nakhal, S.; Hermes, W.; Ressler, T.; Pöttgen, R.; Lerch, M. Synthesis, Crystal Structure and Magnetic Properties of Bixbyite-type Vanadium Oxide Nitrides. *Z. Naturforsch.* **2009**, *64b*, 281–286.

(59) Nakhal, S.; Hermes, W.; Ressler, T.; Pöttgen, R.; Lerch, M. Synthesis, Crystal Structure, and Magnetic Properties of a Vanadium Oxide Nitride with Pseudobrookite-type Structure. *Z. Anorg. Allg. Chem.* **2009**, *635* (12), 2016–2020.

(60) Ercit, T. S.; Wise, M. A.; Cerny, P. Compositional and structural systematics of the columbite group. *Am. Mineral.* **1995**, *80* (5–6), 613–619.

(61) Ekeberg, A. G. Of the Properties of the Earth Yttria, compared with those of Glucine; of Fossils, in which the first of these Earths in contained; and of the Discovery of a metallic Nature (Tantalium). *J. Nat. Philos. Chem. Arts* **1802**, *3*, 251–255.

(62) Ekeberg, A. G. Ueber ein neues Metall, Tantalum, welches zugleich mit der Yttererde in einigen schwedischen Fossilien entdeckt worden ist; nebst einigen Anmerkungen über die Eigenschaften der Yttererde, in Vergleichung mit der Beryllerde. *Crells Ann. d. Chem.* **1803**, *1*, 3–21.

(63) Hatchett, C. An Analysis of a Mineral Substance from North America, Containing a Metal Hitherto Unknown. *Philos. Trans. R. Soc. London* **1802**, *92*, 49–66.

(64) Wollaston, W. H. On the Identity of Columbium and Tantalum. *Philos. Trans. R. Soc. London* **1809**, *99*, 246–252.

(65) Rose, H. Ueber die Zusammensetzung der Tantalite und ein im Tantalite von Baiern enthaltenes neues Metall. *Ann. Phys.* **1844**, *139* (10), 317–341.

(66) Schönberg, N. An X-Ray Investigation of the Tantalum-Oxygen System. *Acta Chem. Scand.* **1954**, *8* (2), 240–245.

(67) Keller, C. Über ternäre Oxide des Niobs und Tantals vom Typ ABO_4. *Z. Anorg. Allg. Chem.* **1962**, *318* (1–2), 89–106.

(68) Rooksby, H. P.; White, E. A. D. The structures of 1:1 compounds of rare earth oxides with niobia and tantala. *Acta Crystallogr.* **1963**, *16* (9), 888–890.

(69) Syono, Y.; Kikuchi, M.; Goto, T.; Fukuoka, K. Formation of rutile-type $Ta(IV)O_2$ by shock reduction and cation-deficient $Ta_{0.8}O_2$ by subsequent oxidation. *J. Solid State Chem.* **1983**, *50* (2), 133–137.

(70) Lehovec, K. Lattice structure of β-Ta_2O_5. *J. Less Common Met.* **1964**, *7* (6), 397–410.

(71) Wolten, G. M.; Chase, A. B. Single-crystal data for β Ta_2O_5 and A KPO_3. *Z. Kristallogr.* **1969**, *129* (5–6), 365–368.

(72) Aleshina, L. A.; Loginova, S. V. Rietveld analysis of X-ray diffraction pattern from β-Ta_2O_5 oxide. *Crystallogr. Reports* **2002**, *47* (3), 415–419.

(73) Stephenson, N. C.; Roth, R. S. Structural systematics in the binary system The Crystal Structure of the High Temperature Form of Ta_2O_5–WO_3. V. The structure of the low-temperature form of tantalum oxide L-The Crystal Structure of the High Temperature Fo. *Acta Crystallogr. Sect. B* **1971**, *27* (5), 1037–1044.

(74) Hummel, H.-U.; Fackler, R.; Remmert, P. Tantaloxide durch Gasphasenhydrolyse, Druckhydrolyse und Transportreaktion aus 2H-TaS_2: Synthesen von TT-Ta_2O_5 und T-Ta_2O_5 und Kristallstruktur von T-Ta_2O_5. *Chem. Ber.* **1992**, *125* (3), 551–556.

(75) Voloshin, A. V.; Pakhomovskii, Y. A.; Perlina, G. A. New mineral names. Tantite. *Am. Mineral.* **1984**, *69*, 1193–1193.

(76) Moser, R. Growth of single crystals and polymorphism of Nb_2O_5 and Ta_2O_5. *Schweiz. Min. Petrog. Mitt.* **1965**, *45*, 35–101.

(77) Terao, N. Structure des Oxides de Tantale. *Jpn. J. Appl. Phys.* **1967**, *6* (1), 21–34.

(78) Lagergren, S.; Magnéli, A. On the Tantalum - Oxygen System. *Acta Chem. Scand.* **1952**, *6*, 444–446.

(79) Laves, F.; Petter, W. Eine displazive Umwandlung bei α-Ta_2O_5. *Helv. Phys. Acta* **1964**, *37*, 617–617.

(80) Waring, J. L.; Roth, R. S. Effect of Oxide Additions on the Polymorphism of Tantalum Pentoxide. *J. Res. Natl. Bur. Stand. (1934).* **1968**, *72A* (2), 175–186.

(81) Stephenson, N. C.; Roth, R. S. The Crystal Structure of the High Temperature Form of Ta_2O_5. *J. Solid State Chem.* **1971**, *3* (2), 145–153.

(82) Plies, V.; Gruehn, R. Beiträge zur Untersuchung anorganischer nichstöchiometrischer Verbindungen. X. Zum thermischen Verhalten metastabiler H-Ta_2O_5-Varianten im System Ta_2O_5-TiO_2. *Z. Anorg. Allg. Chem.* **1980**, *463* (1), 32–44.

(83) Liu, X. Q.; Han, X. D.; Zhang, Z.; Ji, L. F.; Jiang, Y. J. The crystal structure of high temperature phase Ta_2O_5. *Acta Mater.* **2007**, *55* (7), 2385–2396.

(84) Izumi, F.; Kodama, H. A new modification of tantalum(V) oxide. *J. Less Common Met.* **1979**, *63* (2), 305–307.

(85) Zibrov, I. P.; Filonenko, V. P.; Sundberg, M.; Werner, P.-E. Structures and phase transitions of B-Ta_2O_5 and Z-Ta_2O_5: two high-pressure forms of Ta_2O_5. *Acta Crystallogr. Sect. B* **2000**, *56* (4), 659–665.

(86) Schönberg, N. An X-Ray Study of the Tantalum-Nitrogen System. *Acta Chem. Scand.* **1954**, *8*, 199–203.

(87) Brauer, G.; Zapp, K. H. Die Kristallstruktur des Tantalnitrids TaN. *Naturwissenschaften* **1953**, *40* (23), 604–604.

(88) Brauer, G.; Zapp, K. H. Die Nitride des Tantals. *Z. Anorg. Allg. Chem.* **1954**, *277* (3–4), 129–139.

(89) Gatterer, J.; Dufek, G.; Ettmayer, P.; Kieffer, R. Das kubische Tantalmononitrid (B 1-Typ) und seine Mischbarkeit mit den isotypen Übergangsmetallnitriden und-carbiden. *Monatsh. Chem.* **1975**, *106* (5), 1137–1147.

(90) Mashimo, T.; Tashiro, S.; Toya, T.; Nishida, M.; Yamazaki, H.; Yamaya, S.; Oh-Ishi, K.; Syono, Y. Synthesis of the B1-type tantalum nitride by shock compression. *J. Mater. Sci.* **1993**, *28* (13), 3439–3443.

(91) Terao, N. Structure of Tantalum Nitrides. *Jpn. J. Appl. Phys.* **1971**, *10* (2), 248–259.

(92) Christensen, A. N.; Lebech, B. A reinvestigation of the structure of ε-tantalum nitride. *Acta Crystallogr. Sect. B* **1978**, *34* (1), 261–263.

(93) Brauer, G.; Mohr, E.; Neuhaus, A.; Skokan, A. θ-TaN, eine Hochdruckform von Tantalnitrid. *Monatsh. Chem.* **1972**, *103* (3), 794–798.

(94) Mashimo, T.; Tashiro, S. Synthesis of the WC-type tantalum nitride by mechanical alloying. *J. Mater. Sci. Lett.* **1994**, *13* (3), 174–176.

(95) Buvinger, E. A. Analysis of Thin Films of Tantalum Reactively Sputtered in Nitrogen Atmosphere. *Appl. Phys. Lett.* **1965**, *7* (1), 14–15.

(96) Coyne, H. J.; Tauber, R. N. Preparation, Structure, and Properties of Sputtered, Highly Nitrided Tantalum Films. *J. Appl. Phys.* **1968**, *39* (12), 5585–5593.

(97) Ganin, A. Y.; Kienle, L.; Vajenine, G. V. Plasma-Enhanced CVD Synthesis and Structural Characterization of Ta_2N_3. *Eur. J. Inorg. Chem.* **2004**, *2004* (16), 3233–

3239.

(98) Salamon, K.; Očko, M.; Radić, N.; Bogdanović Radović, I.; Despoja, V.; Bernstorff, S. Bixbyite-Ta_2N_3 thin films: Characterization and electrical properties. *J. Alloys Compd.* **2016**, *682*, 98–106.

(99) Zerr, A.; Miehe, G.; Li, J.; Dzivenko, D. A.; Bulatov, V. K.; Höfer, H.; Bolfan-Casanova, N.; Fialin, M.; Brey, G.; Watanabe, T.; Yoshimura, M. High-Pressure Synthesis of Tantalum Nitride Having Orthorhombic U_2S_3 Structure. *Adv. Funct. Mater.* **2009**, *19* (14), 2282–2288.

(100) Friedrich, A.; Winkler, B.; Bayarjargal, L.; Juarez Arellano, E. A.; Morgenroth, W.; Biehler, J.; Schröder, F.; Yan, J.; Clark, S. M. In situ observation of the reaction of tantalum with nitrogen in a laser heated diamond anvil cell. *J. Alloys Compd.* **2010**, *502* (1), 5–12.

(101) Brauer, G.; Weidlein, J. R. Synthesis and Properties of Red Tantalum Nitride Ta_3N_5. *Angew. Chem. Int. Ed.* **1965**, *4* (3), 241–242.

(102) Strähle, J. Die Kristallstruktur des Tantal(V)-nitrids Ta_3N_5. *Z. Anorg. Allg. Chem.* **1973**, *402* (1), 47–57.

(103) Kerlau, M.; Merdrignac-Conanec, O.; Guilloux-Viry, M.; Perrin, A. Synthesis of crystallized TaON and Ta_3N_5 by nitridation of Ta_2O_5 thin films grown by pulsed laser deposition. *Solid State Sci.* **2004**, *6* (1), 101–107.

(104) Gilles, J.-C. Sur deux nouveaux nitrures de tantale. *Comptes Rendus Hebd. des Séances l'Académie des Sci. Série C, Sci. Chim.* **1968**, *266*, 546–547.

(105) Fontbonne, A.; Gilles, J.-C. Nouveaux Nitrures de Tantale. Nitrure et Oxynitrures Mixtes de Tantale et de Niobium. *Rev. Int. des hautes températures des réfractaires* **1969**, *6*, 181–191.

(106) Salamat, A.; Woodhead, K.; Shah, S. I. U.; Hector, A. L.; McMillan, P. F. Synthesis of U_3Se_5 and U_3Te_5 type polymorphs of Ta_3N_5 by combining high pressure–temperature pathways with a chemical precursor approach. *Chem. Commun.* **2014**, *50* (70), 10041–10044.

(107) Conroy, L. E.; Christensen, A. N. Preparation and crystal structure of β-Ta_2N. *J. Solid State Chem.* **1977**, *20* (2), 205–207.

(108) Schönberg, N. Ternary Metallic Phases in the Ta-C-N, Ta-C-O, and Ta-N-O Systems. *Acta Chem. Scand.* **1954**, *8*, 620–623.

(109) Buslaev, Y. A.; Glushkova, M. A.; Ershova, M. M.; Shustorovich, E. M. Synthesis and Properties of Tantalum Chloronitride, Ta_2N_3Cl, and Tantalum Oxynitride, TaON. *Neorg. Mater. (Engl. Transl.)* **1966**, *2*, 2120–2123.

(110) Brauer, G.; Weidlein, J. R. Synthesis and Properties of Tantalum Oxide Nitride, TaON. *Angew. Chem. Int. Ed.* **1965**, *4* (10), 875–875.

(111) Brauer, G.; Weidlein, J.; Strähle, J. Über das Tantalnitrid Ta_3N_5 und das Tantaloxidnitrid TaON. *Z. Anorg. Allg. Chem.* **1966**, *348* (5–6), 298–308.

(112) Buslaev, Y. A.; Safronov, G. M.; Pakhomov, V. I.; Glushkova, M. A.; Repko, V. P.; Ershova, M. M.; Zhukov, A. N.; Zhdanova, T. A. Production of Single Crystals and the Structure of TaON. *Neorg. Mater. (Engl. Transl.)* **1969**, *5*, 45–48.

(113) Lumey, M.-W.; Dronskowski, R. The Electronic Structure of Tantalum Oxynitride and the Falsification of α-TaON. *Z. Anorg. Allg. Chem.* **2003**, *629* (12–13), 2173–2179.

(114) Armytage, D.; Fender, B. E. F. Anion ordering in TaON: a powder neutron-diffraction investigation. *Acta Crystallogr. Sect. B* **1974**, *30* (3), 809–812.

(115) Pauling, L. The Principles Determining the Structure of Complex Ionic Crystals. *J. Am. Chem. Soc.* **1929**, *51* (4), 1010–1026.

(116) Weishaupt, M.; Strähle, J. Darstellung der Oxidnitride VON, NbON und TaON. Die Kristallstruktur von NbON und TaON. *Z. Anorg. Allg. Chem.* **1977**, *429* (1), 261–269.

(117) Brese, N. E.; O'Keeffe, M. Crystal Chemistry of Inorganic Nitrides. In *Structure and Bonding 79*; Springer Verlag: Berlin, Heidelberg, 1992; pp 309–381.

(118) Harb, M.; Sautet, P.; Nurlaela, E.; Raybaud, P.; Cavallo, L.; Domen, K.; Basset, J.-M.; Takanabe, K. Tuning the properties of visible-light-responsive tantalum (oxy)nitride photocatalysts by non-stoichiometric compositions: a first-principles viewpoint. *Phys. Chem. Chem. Phys.* **2014**, *16* (38), 20548–20560.

(119) Orhan, E.; Tessier, F.; Marchand, R. Synthesis and energetics of yellow TaON. *Solid State Sci.* **2002**, *4* (8), 1071–1076.

(120) Chun, W.-J.; Ishikawa, A.; Fujisawa, H.; Takata, T.; Kondo, J. N.; Hara, M.; Kawai, M.; Matsumoto, Y.; Domen, K. Conduction and Valence Band Positions of Ta_2O_5, TaON, and Ta_3N_5 by UPS and Electrochemical Methods. *J. Phys. Chem. B* **2003**, *107* (8), 1798–1803.

(121) Fang, C. M.; Orhan, E.; de Wijs, G. A.; Hintzen, H. T.; de Groot, R. A.; Marchand, R.; Saillard, J.-Y.; de With, G. The electronic structure of tantalum (oxy)nitrides TaON and Ta_3N_5. *J. Mater. Chem.* **2001**, *11* (4), 1248–1252.

(122) Abe, R.; Takata, T.; Sugihara, H.; Domen, K. Photocatalytic overall water splitting under visible light by TaON and WO_3 with an IO_3^-/I^- shuttle redox mediator. *Chem. Commun.* **2005**, No. 30, 3829–3831.

(123) Phillips, J. C. Bonds and Bands in Semiconductors. *Science* **1970**, *169* (3950), 1035–1042.

(124) Phillips, J. C.; Van Vechten, J. A. Spectroscopic Analysis of Cohesive Energies and Heats of Formation of Tetrahedrally Coordinated Semiconductors. *Phys. Rev. B* **1970**, *2* (6), 2147–2160.

(125) Jørgensen, C. K. *Molekülverbindungen und Koordinationsverbindungen in Einzeldarstellungen*; Briegleb, G., Cramer, F., Hartmann, H., Eds.; Springer Verlag: Berlin, 1969.

(126) Bredow, T.; Lumey, M.-W.; Dronskowski, R.; Schilling, H.; Pickardt, J.; Lerch, M. Structure and Stability of TaON Polymorphs. *Z. Anorg. Allg. Chem.* **2006**, *632* (7), 1157–1162.

(127) Schilling, H.; Stork, A.; Irran, E.; Wolff, H.; Bredow, T.; Dronskowski, R.; Lerch, M. γ-TaON: A Metastable Polymorph of Tantalum Oxynitride. *Angew. Chem. Int. Ed.* **2007**, *46* (16), 2931–2934.

(128) Wolff, H.; Bredow, T.; Lerch, M.; Schilling, H.; Irran, E.; Stork, A.; Dronskowski, R. A First-Principles Study of the Electronic and Structural Properties of γ-TaON. *J. Phys. Chem. A* **2007**, *111* (14), 2745–2749.

(129) Gao, Q.; Liu, N.; Wang, S.; Tang, Y. Metal non-oxide nanostructures developed from organic–inorganic hybrids and their catalytic application. *Nanoscale* **2014**, *6* (23), 14106–14120.

(130) Qiu, Y.; Gao, L. Novel Synthesis of Nanocrystalline Gallium Nitride Powder from Gallium(III)-Urea Complex. *Chem. Lett.* **2003**, *32* (8), 774–775.

(131) Wang, Z.; Hou, J.; Yang, C.; Jiao, S.; Huang, K.; Zhu, H. Hierarchical metastable γ-TaON hollow structures for efficient visible-light water splitting. *Energy Environ. Sci.* **2013**, *6* (7), 2134–2144.

(132) Suzuki, A.; Hirose, Y.; Oka, D.; Nakao, S.; Fukumura, T.; Ishii, S.; Sasa, K.;

Matsuzaki, H.; Hasegawa, T. High-mobility electron conduction in oxynitride: Anatase TaON. *Chem. Mater.* **2014**, *26* (2), 976–981.

(133) Suzuki, A.; Hirose, Y.; Oka, D.; Nakao, S.; Fukumura, T.; Hasegawa, T. Low temperature epitaxial growth of anatase TaON using anatase TiO_2 seed layer. *Jpn. J. Appl. Phys.* **2015**, *54* (8), 80303-1–3.

(134) Nakhal, S.; Lumey, M.-W.; Bredow, T.; Dronskowski, R.; Lerch, M. Synthesis and Approximated Crystal and Electronic Structure of a Proposed New Tantalum Oxide Nitride Ta_3O_6N. *Z. Anorg. Allg. Chem.* **2010**, *636* (6), 1006–1012.

(135) Nakhal, S. *Synthese, Kristallstruktur und Eigenschaften von neuen Übergangsmetalloxiden, -oxidhydroxiden und -oxidnitriden*; Technische Universität Berlin: Berlin, 2008.

(136) Houmes, J. D.; zur Loye, H.-C. Iron-Promoted Synthesis of Tantalum and Niobium Oxynitrides. *J. Solid State Chem.* **1996**, *127* (2), 267–275.

(137) Lumey, M.-W.; Dronskowski, R. First-Principles Electronic Structure, Chemical Bonding, and High-Pressure Phase Prediction of the Oxynitrides of Vanadium, Niobium, and Tantalum. *Z. Anorg. Allg. Chem.* **2005**, *631* (5), 887–893.

(138) Lowther, J. E. Theoretical study of potential high-pressure phases of TaON and a quaternary $ZrTaO_3N$. *Phys. Rev. B* **2006**, *73* (13), 134110-1–8.

(139) Woodhead, K.; Pascarelli, S.; Hector, A. L.; Briggs, R.; Alderman, N.; McMillan, P. F. High pressure polymorphism of β-TaON. *Dalton Trans.* **2014**, *43* (25), 9647–9654.

(140) van Arkel, A. E.; de Boer, J. H. Darstellung von reinem Titanium-, Zirkonium-, Hafnium- und Thoriummetall. *Z. Anorg. Allg. Chem.* **1925**, *148* (1), 345–350.

(141) Kroll, W. Method for manufacturing titanium and alloys thereof. USPTO 2205854, 1940.

(142) Holmberg, B.; Dagerhamn, T.; Leppänen, K. X-Ray Studies on Solid Solutions of Oxygen in α-Zirconium. *Acta Chem. Scand.* **1961**, *15*, 919–925.

(143) Yamaguchi, S. Ordered Arrangement of Oxygen in the Interstitial Solid Solution of Zirconium-Oxygen System. *J. Phys. Soc. Japan* **1968**, *24* (4), 855–868.

(144) Böhm, J. Über das Verglimmen einiger Metalloxyde. *Z. Anorg. Allg. Chem.* **1925**, *149* (1), 217–222.

(145) Davey, W. P. The crystal structure of zirconium oxide. *Phys. Rev.* **1926**, *23* (6), 798–798.

(146) Goldschmidt, V. M. Geochemische Verteilungsgesetze VI–VIII. *Skr. Nor. Vidensk.-Akad., Kl. 1: Mat.-Naturvidensk. Kl.* **1926**.

(147) Ruff, O.; Ebert, F. Beiträge zur Keramik hochfeuerfester Stoffe. l. Die Formen des Zirkondioxyds. *Z. Anorg. Allg. Chem.* **1929**, *180* (1), 19–41.

(148) Ruff, O.; Ebert, F.; Stephan, E. Beiträge zur Keramik hochfeuerfester Stoffe II. Das System ZrO_2–CaO. *Z. Anorg. Allg. Chem.* **1929**, *180* (1), 215–224.

(149) Duwez, P.; Brown, F. H.; Odell, F. The Zirconia-Yttria System. *J. Electrochem. Soc.* **1951**, *98* (9), 356–362.

(150) Duwez, P.; Odell, F.; Brown, F. H. Stabilization of Zirconia with Calcia and Magnesia. *J. Am. Ceram. Soc.* **1952**, *35* (5), 107–113.

(151) Kröger, F. A.; Vink, H. J. Relations between the Concentrations of Imperfections in Crystalline Solids. *Solid State Phys.* **1956**, *3*, 307–435.

(152) Kröger, F. A. *Chemistry of Imperfect Crystals*, 1st ed.; Interscience (Wiley): Amsterdam, 1964.

(153) Bocquillon, G.; Susse, C. High pressure phase diagram of zirconium oxide. *Rev. Int. Hautes Temp. Refract* **1969**, *6*, 263–266.

(154) Suyama, R.; Ashida, T.; Kume, S. Synthesis of the Orthorhombic Phase of ZrO2. *J. Am. Ceram. Soc.* **1985**, *68* (12), C-314–C-315.

(155) Kudoh, Y.; Takeda, H.; Arashi, H. In situ determination of crystal structure for high pressure phase of ZrO_2 using a diamond anvil and single crystal X-ray diffraction method. *Phys. Chem. Miner.* **1986**, *13* (4), 233–237.

(156) Suyama, R.; Horiuchi, H.; Kume, S. Structural Refinements of ZrO_2 and HfO_2 Treated at 600°C·6GPa. *J. Ceram. Assoc. Japan* **1987**, *95* (1102), 567–568.

(157) Liu, L.-G. High-pressure phase transformations in baddeleyite and zircon, with geophysical implications. *Earth Planet. Sci. Lett.* **1979**, *44* (3), 390–396.

(158) Liu, L.-G. New high pressure phases of ZrO_2 and HfO_2. *J. Phys. Chem. Solids* **1980**, *41* (4), 331–334.

(159) Haines, J.; Léger, J. M.; Atouf, A. Crystal Structure and Equation of State of Cotunnite-Type Zirconia. *J. Am. Ceram. Soc.* **1995**, *78* (2), 445–448.

(160) Haines, J.; Léger, J. M.; Hull, S.; Petitet, J. P.; Pereira, A. S.; Perottoni, C. A.; Jornada, J. A. H. Characterization of the Cotunnite-Type Phases of Zirconia and Hafnia by Neutron Diffraction and Raman Spectroscopy. *J. Am. Ceram. Soc.* **1997**, *80* (7), 1910–1914.

(161) Van Arkel, A. E. Crystal structure and physical properties. *Phys. (The Hague)* **1924**, *4*, 286–301.

(162) Becker, K.; Ebert, F. Die Kristallstruktur einiger binärer Carbide und Nitride. *Z. Phys.* **1925**, *31* (1), 268–272.

(163) Schönberg, N. The Structure of the Metallic Quaternary Phase ZrTaNO. *Acta Chem. Scand.* **1954**, *8*, 627–629.

(164) Juza, R.; Rabenau, A.; Nitschke, I. Über ein braunes Zirkonnitrid Zr_3N_4. *Z. Anorg. Allg. Chem.* **1964**, *332* (1–2), 1–4.

(165) Lerch, M.; Füglein, E.; Wrba, J. Synthesis, crystal structure, and high temperature behavior of Zr_3N_4. *Z. Anorg. Allg. Chem.* **1996**, *622* (2), 367–372.

(166) Zerr, A.; Miehe, G.; Riedel, R. Synthesis of cubic zirconium and hafnium nitride having Th_3P_4 structure. *Nat. Mater.* **2003**, *2* (3), 185–189.

(167) Gilles, J.-C. Préparation par réaction à l'état solide et structures des oxynitrures de zirconium. *Bull. Soc. Chim. Fr.* **1962**, *22*, 2118–2122.

(168) Gilles, J.-C. Préparation par réaction à l'état solide et structures des oxynitrures de zirconium. *Corros. Anticorros.* **1964**, *12*, 15–22.

(169) Collongues, R.; Gilles, J. C.; Lejus, A. M.; Perez y Jorba, M.; Michel, D. Recherches sur les oxynitrures metalliques. *Mater. Res. Bull.* **1967**, *2* (9), 837–848.

(170) Cheng, Y. B.; Thompson, D. P. The Nitriding of Zirconia. *Spec. Ceram.* **1992**, *9*, 149–162.

(171) Lerch, M. Nitridation of Zirconia. *J. Am. Ceram. Soc.* **1996**, *79* (10), 2641–2644.

(172) Bredow, T.; Lerch, M. Anion Distribution in $Zr_7O_8N_4$. *Z. Anorg. Allg. Chem.* **2007**, *633* (15), 2598–2602.

(173) Füglein, E.; Hock, R.; Lerch, M. Über Kristallstruktur und Hochtemperaturverhalten von Zr_2ON_2. *Z. Anorg. Allg. Chem.* **1997**, *623* (1–6), 304–308.

(174) Clarke, S. J.; Michie, C. W.; Rosseinsky, M. J. Structure of Zr_2ON_2 by Neutron

Powder Diffraction: The Absence of Nitride–Oxide Ordering. *J. Solid State Chem.* **1999**, *146* (2), 399–405.

(175) Bredow, T.; Lerch, M. Anion Distribution in Zr_2ON_2. *Z. Anorg. Allg. Chem.* **2004**, *630* (13–14), 2262–2266.

(176) Michie, C. W.; Claridge, J. B.; Clarke, S. J.; Rosseinsky, M. J. $Zr_4O_5N_2$ – Intergrowth of Fluorite and Bixbyite Anion Layers Formed by Coupled Site-Selective Anion and Vacancy Ordering. *Chem. Mater.* **2003**, *15* (7), 1547–1553.

(177) Grins, J.; Käll, P.-O.; Svensson, G. Phases in the $Zr_xTa_{1-x}(O,N)_y$ system, formed by ammonolysis of Zr-Ta gels: preparation of a baddeleyite-type solid solution phase $Zr_xTa_{1-x}O_{1+x}N_{1-x}$, $0 \leq x \leq 1$. *J. Mater. Chem.* **1994**, *4* (8), 1293–1301.

(178) Guenther, E.; Jansen, M. Optical properties of $Ta_{(3-x)}Zr_{(x)}N_{(5-x)}O_{(x)}$ semiconductor pigments. *Mater. Res. Bull.* **2001**, *36* (7–8), 1399–1405.

(179) Pastrana-Fábregas, R.; Isasi-Marín, J.; Sáez-Puche, R. Synthesis and characterization of inorganic pigments based on transition metal oxynitrides. *J. Mater. Res.* **2006**, *21* (9), 2255–2260.

(180) Pastrana-Fabregas, R.; Isasi-Marin, J.; Fernandez-Martinez, F.; Saez-Puche, R. Preparation and characterization of inorganic colored pigments without toxic metals. *Phys. Chem. News* **2008**, *44*, 21–26.

(181) Lerch, M.; Lerch, J. Nitrogen incorporation into Ta_2O_5-containing zirconia ceramics. *J. Mater. Sci. Lett.* **1997**, *16* (17), 1454–1456.

(182) Maeda, K.; Terashima, H.; Kase, K.; Domen, K. Nanoparticulate precursor route to fine particles of TaON and ZrO_2-TaON solid solution and their photocatalytic activity for hydrogen evolution under visible light. *Appl. Catal. A Gen.* **2009**, *357* (2), 206–212.

(183) Ma, S. S. K.; Maeda, K.; Domen, K. Modification of TaON with ZrO2 to improve photocatalytic hydrogen evolution activity under visible light: influence of preparation conditions on activity. *Catal. Sci. Technol.* **2012**, *2* (4), 818–823.

(184) Kisi, E. H.; Howard, C. J.; Hill, R. J. Crystal Structure of Orthorhombic Zirconia in Partially Stabilized Zirconia. *J. Am. Ceram. Soc.* **1989**, *72* (9), 1757–1760.

(185) Tuenge, R. T.; Eyring, L. On the structures of the intermediate phases in the terbium oxide system. *J. Solid State Chem.* **1982**, *41* (1), 75–89.

(186) Ruan, J.-L.; Huang, J.-L.; Lu, H.-H.; Chen, J. S.; Lii, D.-F. Effects of the Ta content on the microstructure and electrical property of reactively sputtered $Ta_xZr_{1-x}N$ thin films. *Thin Solid Films* **2011**, *519* (15), 4987–4991.

(187) Aouadi, S. M.; Filip, P.; Debessai, M. Characterization of tantalum zirconium nitride sputter-deposited nanocrystalline coatings. *Surf. Coatings Technol.* **2004**, *187* (2–3), 177–184.

(188) Zhang, H.; Liu, S. Optical compound film deposited by a double e-gun. *Thin Solid Films* **1992**, *209* (2), 148–149.

(189) Zheng, C.; West, A. Private Communication. **1990**.

(190) Sellar, J. R. Observation of in-situ reduction and oxygen transport in zirconia-tantala ceramic alloys. In *Science and Technology of Zirconia V*; 1993; pp 198–206.

(191) Gritzner, G.; Puchner, C. V_2O_5, Nb_2O_5 and Ta_2O_5 doped zirconia ceramics. *J. Eur. Ceram. Soc.* **1994**, *13* (5), 387–394.

(192) Pissenberger, A.; Gritzner, G. Preparation and properties of niobia- and tantala-doped orthorhombic zirconia. *J. Mater. Sci. Lett.* **1995**, *14* (22), 1580–1582.

(193) Höftberger, M.; Gritzner, G. Niobia and tantala codoped orthorhombic zirconia ceramics. *Scr. Metall. Mater.* **1995**, *32* (8), 1237–1241.

(194) Spiridonov, F. M.; Mulenkova, M. N.; Tsirel'nikov, V. I.; Komissarova, L. N. Intermediate phases in the hafnium dioxide-tantalum pentoxide system. *Russ. J. Inorg. Chem.* **1981**, *26*, 922–923.

(195) Chan, F. L.; Johnson, G. G. X-Ray Diffraction Study of New Hafnium Compounds. In *Developments in Applied Spectroscopy*; Springer US: Boston, MA, 1972; pp 307–329.

(196) Roth, R. S.; Coughanour, L. W. Phase equilibrium relations in the systems titania-niobia and zirconia-niobia. *J. Res. Natl. Bur. Stand. (1934).* **1955**, *55* (4), 209–213.

(197) Trunov, V. K.; Vladimirova, Z. A.; Kovba, L. M.; Komissarova, L. N. Double Oxides in the ZrO_2 - Nb_2O_5 System. *Neorg. Mater. (Engl. Transl.)* **1965**, *1*, 1055–1057.

(198) Newnham, R. E. Crystal Structure of $ZrTiO_4$. *J. Am. Ceram. Soc.* **1967**, *50* (4),

216–216.

(199) Roth, R. S.; Waring, J. L.; Brower, W. S.; Parker, H. S. Superstructure of the Orthorhombic $Nb_2O_5{\cdot}6ZrO_2$ Type Phase(s) in the Nb_2O_5 and Ta_2O_5 Systems. In *Solid State Chemistry. Proceedings of the 5th Materials Research Symposium*; Roth, R.S., Schneider, S. J., Ed.; NBS: Washington, 1972; Vol. 364, pp 183–195.

(200) Hyde, B. G.; Bursill, L. A.; O'Keeffe, M.; Andersson, S. Continuous Topological Variation of Coordination in Crystals: Structural Relations and Possible Transformation Mechanisms. *Nat. Phys. Sci.* **1972**, *237* (72), 35–38.

(201) Galy, J.; Roth, R. S. The Crystal Structure of $Nb_2Zr_6O_{17}$. *J. Solid State Chem.* **1973**, *7* (3), 277–285.

(202) Hyde, B. G.; Bagshaw, A. N.; Andersson, S.; O'Keeffe, M. Some Defect Structures in Crystalline Solids. *Annu. Rev. Mater. Sci.* **1974**, *4* (1), 43–92.

(203) Kanade, K. G.; Baeg, J.-O.; Kale, B. B.; Milee, S. M.; Moon, S.-J.; Kong, K. Rose-red color oxynitride $Nb_2Zr_6O_{17-x}N_x$: A visible light photocatalyst to hydrogen production. *Int. J. Hydrogen Energy* **2007**, *32* (18), 4678–4684.

(204) Thompson, J. G.; Withers, R. L.; Sellar, J.; Barlow, P. J.; Hyde, B. G. Incommensurate composite modulated $Nb_2Zr_{x-2}O_{2x+y}$: x = 7.1–10.3. *J. Solid State Chem.* **1990**, *88* (2), 465–475.

(205) Fütterer, K.; Schmid, S.; Thompson, J. G.; Withers, R. L.; Ishizawa, N.; Kishimoto, S. The structure refinement of compositely modulated $Nb_2Zr_{x-2}O_{2x+1}$ (x = 12). *Acta Crystallogr. Sect. B* **1995**, *51* (5), 688–697.

(206) Withers, R. L.; Thompson, J. G.; Hyde, B. G. A Modulation-Wave Approach to the Structural Description of the Nb_2Zr_{x-2} O_{2x+1} (x = 7.1–10.3) Solid-Solution Field. *Acta Crystallogr. Sect. B* **1991**, *47* (2), 166–174.

(207) Schmid, S.; Thompson, J. G.; Withers, R. L.; Petříček, V.; Ishizawa, N.; Kishimoto, S. Re-Refinement of Composite Modulated Nb2Zrx−2O2x+y (x = 8) Using Synchrotron Radiation Data. *Acta Crystallogr. Sect. B* **1997**, *53* (6), 851–860.

(208) Sellar, J. R. Disorder, superlattice canting and chiral domains in zirconia–niobia ceramic alloys. *Acta Crystallogr. Sect. A* **1999**, *55* (2), 220–227.

(209) Sellar, J. R. A frustrated planar XY model for niobia–zirconia ceramic alloys. *Micron* **2001**, *32* (8), 871–877.

(210) Scheele, C. W. Versuche mit Wasserbley. *Sven. vetensk. Acad. Handl.* **1778**, *40*, 238–248.

(211) Hjelm, P. J. Ueber Molybdäna und Reduction derselben Erde. *Sven. vetensk. Acad. Handl.* **1788**, *49*, 268–279.

(212) Schönberg, N. On the Existence of a Metallic Molybdenum Oxide. *Acta Chem. Scand.* **1954**, *8*, 617–619.

(213) Huber, J. M. *Oxidnitride als Katalysatoren zur Methanaktivierung*; Technische Universität Berlin: Berlin, 2011.

(214) Wooster, N. The crystal structure of Molybdenum Trioxide, MoO_3. *Z. Kristallogr.* **1931**, *80* (1–6), 504–512.

(215) Bräkken, H. Die Kristallstrukturen der Trioxyde von Chrom, Molybdän und Wolfram. *Z. Kristallogr.* **1931**, *78* (1–6), 484–489.

(216) Andersson, G.; Magnéli, A. On the Crystal Structure of Molybdenum Trioxide. *Acta Chem. Scand.* **1950**, *4*, 793–797.

(217) Kihlborg, L. Least squares refinement of the crystal structure of molybdenum trioxide. *Ark. foer Kemi* **1963**, *21*, 357–364.

(218) McCarron, E. M.; Calabrese, J. C. The growth and single crystal structure of a high pressure phase of molybdenum trioxide: MoO_3-II. *J. Solid State Chem.* **1991**, *91* (1), 121–125.

(219) McCarron, E. M. β-MoO_3: a metastable analogue of WO_3. *J. Chem. Soc., Chem. Commun.* **1986**, No. 4, 336–338.

(220) Parise, J. B.; McCarron, E. M.; Von Dreele, R.; Goldstone, J. A. β-MoO_3 produced from a novel freeze drying route. *J. Solid State Chem.* **1991**, *93* (1), 193–201.

(221) Parise, J. B.; McCarron, E. M.; Sleight, A. W. A new modification of ReO_3-type MoO_3 and the deuterated intercalation compound from which it is derived: $D_{0.99}MoO_3$. *Mater. Res. Bull.* **1987**, *22* (6), 803–811.

(222) Parise, J. B.; McCarron, E. M.; Sleight, A. W.; Prince, E. Refinement of the Structure of Beta'-MoO_3. *Mater. Sci. Forum* **1988**, *27–28*, 85–88.

(223) Goldschmidt, V. M.; Barth, T.; Holmsen, D.; Lunde, G.; Zachariasen, W. Geochemische Verteilungsgesetze der Elemente. VI. Ueber die Krystallstrukturen vom Rutiltypus, mit Bemerkungen zur Geochemie zweiwertiger und vierwertiger

Elemente. *Skr. Nor. Vidensk.-Akad., Kl. 1: Mat.-Naturvidensk. Kl.* **1926**, *1*, 5–21.

(224) Magnéli, A.; Andersson, G.; Blomberg, B.; Kihlborg, L. Identification of Molybdenum and Tungsten Oxides by X-Ray Powder Patterns. *Anal. Chem.* **1952**, *24* (12), 1998–2000.

(225) Magnéli, A.; Andersson, G.; Sundkvist, G. On the MoO_2 Structure Type. *Acta Chem. Scand.* **1955**, *9*, 1378–1381.

(226) Brandt, B. G.; Skapski, A. C. A Refinement of the Crystal Structure of Molybdenum Dioxide. *Acta Chem. Scand.* **1967**, *21*, 661–672.

(227) Rogers, D. B.; Shannon, R. D.; Sleight, A. W.; Gillson, J. L. Crystal chemistry of metal dioxides with rutile-related structures. *Inorg. Chem.* **1969**, *8* (4), 841–849.

(228) Seisenbaeva, G. A.; Sundberg, M.; Nygren, M.; Dubrovinsky, L.; Kessler, V. G. Thermal decomposition of the methoxide complexes $MoO(OMe)_4$, $Re_4O_6(OMe)_{12}$ and $(Re_{1-x}Mo_x)O_6(OMe)_{12}$ ($0.24 \leq x \leq 0.55$). *Mater. Chem. Phys.* **2004**, *87* (1), 142–148.

(229) Becker, N.; Dronskowski, R. A first-principles study on new high-pressure metastable polymorphs of MoO_2. *J. Solid State Chem.* **2016**, *237*, 404–410.

(230) Magnéli, A. The Crystal Structure of Mo_4O_{11} (γ-Molybdenum Oxide). *Acta Chem. Scand.* **1948**, *2*, 861–871.

(231) Kihlborg, L. Crystal structure studies on monoclinic and orthorhombic Mo_4O_{11}. *Ark. foer Kemi* **1963**, *21*, 365–377.

(232) Åsbrink, S.; Kihlborg, L.; Jackman, L. M.; Sparrow, D. R. A Study of the Crystal Symmetry and Structure of Orthorhombic Mo_4O_{11} by Least-squares Techniques. *Acta Chem. Scand.* **1964**, *18*, 1571–1573.

(233) Ghedira, M.; Vincent, H.; Marezio, M.; Marcus, J.; Furcaudot, G. Structure cristalline du conducteur métallique bidimensionnel Mo_4O_{11}-γ. *J. Solid State Chem.* **1985**, *56* (1), 66–73.

(234) Knorr, R.; Müller, U. η-Mo_4O_{11} und $Mg_2Mo_3O_8$: eine neue Synthese und Verfeinerung ihrer Kristallstrukturen. *Z. Anorg. Allg. Chem.* **1995**, *621* (4), 541–545.

(235) Magnéli, A. The Crystal Structures of Mo_9O_{26} (beta'-Molybdenum Oxide) and Mo_8O_{23} (beta-molybdenum Oxide). *Acta Chem. Scand.* **1948**, *2*, 501–517.

(236) Magnéli, A. Structures of the ReO_3-type with recurrent dislocations of atoms: `homologous series' of molybdenum and tungsten oxides. *Acta Crystallogr.* **1953**, *6* (6), 495–500.

(237) Kihlborg, L. Crystal structure on Mo_5O_{14}, a compound exhibiting two-dimensional disorder. *Ark. foer Kemi* **1963**, *21*, 427–437.

(238) Ekström, T. Formation of ternary phases of Mo_5O_{14} and $Mo_{17}O_{47}$ structure in the molybdenum-wolfram-oxygen system. *Mater. Res. Bull.* **1972**, *7* (1), 19–26.

(239) Ekström, T.; Cyvin, S. J.; Enzell, C. R.; Olli, M.; Pilotti, Å. The Magnetic Susceptibility of Phases with the $Mo_{17}O_{47}$ and Mo_5O_{14} Types of Structure. *Acta Chem. Scand.* **1972**, *26*, 3381–3382.

(240) Portemer, F.; Sundberg, M.; Kihlborg, L.; Figlarz, M. Homologues of Mo_4O_{11}(mon) in the Mo-W-O System Prepared by Soft Chemistry. *J. Solid State Chem.* **1993**, *103* (2), 403–414.

(241) Kihlborg, L. The Crystal Structure of $Mo_{17}O_{47}$. *Acta Chem. Scand.* **1960**, *14*, 1612–1622.

(242) Kihlborg, L. Least Squares Refinement of the Structure of $Mo_{17}O_{47}$. *Acta Chem. Scand.* **1963**, *17* (5), 1485–1487.

(243) Yamazoe, N.; Ekström, T.; Kihlborg, L.; Granberg, M.; Karlsson, F.; Edlund, K.; Eliasen, M.; Herskind, C.; Laursen, T.; Pedersen, P. M. Structural Effects of Vanadium Substitution in $Mo_{17}O_{47}$. *Acta Chem. Scand.* **1975**, *29a*, 404–408.

(244) Freedman, M. L.; Leber, S. Identification of tungstic and molybdic "acids" by X-ray powder diffraction. *J. Less-Common Met.* **1964**, *7* (6), 427–432.

(245) Peters, H.; Till, L.; Radeke, K. H. Fällungsprodukte beim Ansäuern von Molybdatlösungen. *Z. Anorg. Allg. Chem.* **1969**, *365* (1–2), 14–21.

(246) Caiger, N. A.; Crouch-Baker, S.; Dickens, P. G.; James, G. S. Preparation and structure of hexagonal molybdenum trioxide. *J. Solid State Chem.* **1987**, *67* (2), 369–373.

(247) Lunk, H. J.; Hartl, H.; Hartl, M. A.; Fait, M. J. G.; Shenderovich, I. G.; Feist, M.; Frisk, T. A.; Daemen, L. L.; Mauder, D.; Eckelt, R.; Gurinov, A. A. "Hexagonal molybdenum trioxide" - Known for 100 years and still a fount of new discoveries. *Inorg. Chem.* **2010**, *49* (20), 9400–9408.

(248) Megaw, H. D. *Crystal Structures: A Working Approach*; W.B. Saunders Co: Philadelphia, 1973.

(249) Buerger, M. J. Derivative Crystal Structures. *J. Chem. Phys.* **1947**, *15* (1), 1–16.

(250) Bärnighausen, H. Group-Subgroup Relations between Space Groups: A Useful Tool in Crystal Chemistry. *MATCH Commun. Math. Comput. Chem.* **1980**, *9*, 139–175.

(251) Hermann, C. XXXV. Zur systematischen Strukturtheorie. *Zeitschrift für Krist. - Cryst. Mater.* **1929**, *69* (1–6), 533–555.

(252) Müller, U. Kristallographische Gruppe-Untergruppe-Beziehungen und ihre Anwendung in der Kristallchemie. *Z. Anorg. Allg. Chem.* **2004**, *630* (11), 1519–1537.

(253) Wyckoff, R. W. G. *The analytical expression of the results of the theory of space-groups*; Carnegie Institution of Washington: Washington, 1922.

(254) Hahn, T. *International Tables for Crystallography, Vol. A Space Group Symmetry*, 5th ed.; Springer: Dordrecht, 2005.

(255) Aroyo, M. I.; Perez-Mato, J. M.; Capillas, C.; Kroumova, E.; Ivantchev, S.; Madariaga, G.; Kirov, A.; Wondratschek, H. Bilbao Crystallographic Server: I. Databases and crystallographic computing programs. *Z. Kristallogr.* **2006**, *221* (1), 15–27.

(256) Aroyo, M. I.; Kirov, A.; Capillas, C.; Perez-Mato, J. M.; Wondratschek, H. Bilbao Crystallographic Server. II. Representations of crystallographic point groups and space groups. *Acta Crystallogr. Sect. A* **2006**, *62* (2), 115–128.

(257) Aroyo, M. I.; Perez-Mato, J. M.; Orobengoa, D.; Tasci, E.; De La Flor, G.; Kirov, A. Crystallography online: Bilbao crystallographic server. *Bulg. Chem. Commun.* **2011**, *43* (2), 183–197.

(258) Parker, R. L. I. Zur Kristallographie von Anatas und Rutil. *Zeitschrift für Krist. - Cryst. Mater.* **1923**, *59* (1–6), 1–54.

(259) Burdett, J. K. Electronic control of the geometry of rutile and related structures. *Inorg. Chem.* **1985**, *24* (14), 2244–2253.

(260) Burdett, J. K.; Hughbanks, T.; Miller, G. J.; Richardson, J. W.; Smith, J. V. Structural-electronic relationships in inorganic solids: powder neutron diffraction

studies of the rutile and anatase polymorphs of titanium dioxide at 15 and 295 K. *J. Am. Chem. Soc.* **1987**, *109* (12), 3639–3646.

(261) Ivantchev, S.; Kroumova, E.; Madariaga, G.; Pérez-Mato, J. M.; Aroyo, M. I. SUBGROUPGRAPH : a computer program for analysis of group–subgroup relations between space groups. *J. Appl. Crystallogr.* **2000**, *33* (4), 1190–1191.

(262) Sens, I.; Müller, U. Die Zahl der Substitutions- und Leerstellenvarianten des NaCl-Typs bei verdoppelter Elementarzelle (a, b, 2c). *Z. Anorg. Allg. Chem.* **2003**, *629* (3), 487–492.

(263) Müller, U. *Symmetriebeziehungen zwischen verwandten Kristallstrukturen*, 1st ed.; Vieweg + Teubner Verlag: Wiesbaden, 2012.

(264) Meyer, A. *Symmetriebeziehungen zwischen Kristallstrukturen des Formeltyps AX_2, ABX_4 und AB_2X_6 sowie deren Ordnungs- und Leerstellenvarianten*; Universität Karlsruhe: Karlsruhe, 1981.

(265) Grins, J. $Ti_xTa_{1-x}(O,N)_y$ phases formed by ammonolysis of Ti-Ta gels: Preparation of an anatase-type solid solution phase $Ti_xTa_{1-x}O_{1+x}N_{1-x}$, $0.52 \leq x \leq 0.87$. *J. Eur. Ceram. Soc.* **1997**, *17* (15–16), 1819–1824.

(266) Wolff, H.; Lerch, M.; Schilling, H.; Bähtz, C.; Dronskowski, R. A density-functional study on the stability of anatase-type phases in the system Mg–Ta–O–N. *J. Solid State Chem.* **2008**, *181* (10), 2684–2689.

(267) Wolff, H.; Schilling, H.; Lerch, M.; Dronskowski, R. A density-functional and molecular-dynamics study on the physical properties of yttrium-doped tantalum oxynitride. *J. Solid State Chem.* **2006**, *179* (8), 2265–2270.

(268) Wüstefeld, C.; Vogt, T.; Löchner, U.; Strähle, J.; Fuess, H. Synthesis of TiNF and Structure Determination by Powder Diffraction using Synchrotron Radiation. *Angew. Chem. Int. Ed.* **1988**, *27* (7), 929–930.

(269) Penfield, S. L.; Poote, H. W. XXXIV. Ueber Bixbyit, ein neues Mineral, mit einer Notiz über den begleitenden Topas. *Z. Kristallogr.* **1897**, *28* (1–6), 13–16.

(270) Zachariasen, W. Über die Kristallstruktur von Bixbyit, sowie vom künstlichen Mn_2O_3. *Z. Kristallogr.* **1928**, *67* (1–6), 455–464.

(271) Pauling, L.; Shappell, M. D. The Crystal Structure of Bixbyite and the C-Modification of the Sesquioxides. *Z. Kristallogr.* **1930**, *75* (1), 128–142.

(272) Mitchell, R. S. Who's Who in Mineral Names. *Rocks Miner.* **1987**, *62* (2), 120–123.

(273) Geller, S. Structure of α-Mn_2O_3, $(Mn_{0.983}Fe_{0.017})_2O_3$ and $(Mn_{0.37}Fe_{0.63})_2O_3$ and relation to magnetic ordering. *Acta Crystallogr. Sect. B* **1971**, *27* (4), 821–828.

(274) Ramos-Gallardo, A.; Vegas, A. The cation array in the bixbyite-type structures. *J. Solid State Chem.* **1995**, *119* (1), 131–133.

(275) Rundle, R. E.; Baenziger, N. C.; Wilson, A. S.; McDonald, R. A. The Structures of the Carbides, Nitrides and Oxides of Uranium 1. *J. Am. Chem. Soc.* **1948**, *70* (1), 99–105.

(276) Tobisch, J.; Hase, W. Structure Investigations of Two Uranium Nitrides U_2N_{3+x}. *Phys. status solidi* **1967**, *21* (1), K11–K12.

(277) Masaki, N.; Tagawa, H. Diffraction study of α U_2N_{3+x}. *J. Nucl. Mater.* **1975**, *57* (2), 187–192.

(278) Hostachy, A.; Coing-Boyat, J. Structure cristalline de Cu_3TeO_6. *Comptes Rendus Hebd. des Séances l'Académie des Sci. Série B, Sci. Phys.* **1968**, 1435–1438.

(279) Falck, L.; Lindqvist, O.; Moret, J. Tricopper(II) tellurate(VI). *Acta Crystallogr. Sect. B* **1978**, *34* (3), 896–897.

(280) Rayaprol, S.; Kaushik, S. D.; Babu, P. D.; Siruguri, V. Structure and magnetism of $FeMnO_3$. In *AIP Conference Proceedings*; 2013; pp 1132–1133.

(281) Juza, R.; Hund, F. Die ternären Nitride Li_3AlN_2 und Li_3GaN_2. *Z. Anorg. Allg. Chem.* **1948**, *257* (1–3), 13–25.

(282) Juza, R.; Langer, K.; Von Benda, K. Ternary Nitrides, Phosphides, and Arsenides of Lithium. *Angew. Chem. Int. Ed.* **1968**, *7* (5), 360–370.

(283) Goglio, G.; Denis, A.; Gaudin, E.; Labrugère, C.; Foy, D.; Largeteau, A. Solvothermal processes for nitride synthesis: Examples of Li_3GaN_2 and graphitic C_3N_4 elaboration. *Z. Naturforsch.* **2008**, *63b* (6), 730–738.

(284) Niewa, R.; Zherebtsov, D. A.; Leoni, S. $Li_3[ScN_2]$: The First Nitridoscandate(III)—Tetrahedral Sc Coordination and Unusual MX_2 Framework. *Chem. A Eur. J.* **2003**, *9* (17), 4255–4259.

(285) Sundberg, M.; Werner, P.-E.; Zibrov, I. P. X-ray powder crystal structure analysis of high pressure tungsten dioxide. On the information in weak reflections. *Z.*

Kristallogr. **1994**, *209* (8), 662–666.

(286) Schmidt, H. K. Das Sol-Gel-Verfahren: Anorganische Synthesemethoden. *Chemie unserer Zeit* **2001**, *35* (3), 176–184.

(287) Pechini, M. P. Method of Preparing Lead and Alkaline Earth Titanates and Niobates and Coating Method using the same to form a capacitor. USPTO 3330697, 1967.

(288) Okubo, T.; Kakihana, M. Low temperature synthesis of Y_3NbO_7 by polymerizable complex method: Utilization of a methanol-citric acid solution of $NbCl_5$ as a novel niobium precursor. *J. Alloys Compd.* **1997**, *256* (1–2), 151–154.

(289) Bragg, W. L. The Diffraction of Short Electromagnetic Waves by a Crystal. *Proc. Camb. Phil. Soc.* **1913**, *17*, 43–57.

(290) Rietveld, H. M. Line profiles of neutron powder-diffraction peaks for structure refinement. *Acta Crystallogr.* **1967**, *22* (1), 151–152.

(291) Rietveld, H. M. A profile refinement method for nuclear and magnetic structures. *J. Appl. Crystallogr.* **1969**, *2* (2), 65–71.

(292) Rietveld, H. M. The Rietveld method. *Phys. Scr.* **2014**, *89* (9), 98002-1–6.

(293) David, W. I. F. Powder diffraction: Least-squares and beyond. *J. Res. Natl. Inst. Stand. Technol.* **2004**, *109* (1), 107–123.

(294) Toby, B. H. R factors in Rietveld analysis: How good is good enough? *Powder Diffr.* **2006**, *21* (1), 67–70.

(295) Le Bail, A.; Duroy, H.; Fourquet, J. L. Ab-initio structure determination of $LiSbWO_6$ by X-ray powder diffraction. *Mater. Res. Bull.* **1988**, *23* (3), 447–452.

(296) Le Bail, A. Whole powder pattern decomposition methods and applications: A retrospection. *Powder Diffr.* **2005**, *20* (4), 316–326.

(297) Rodríguez-Carvajal, J. FULLPROF: A Program for Rietveld Refinement and Pattern Matching Analysis. In *Abstracts of the Satellite Meeting on Powder Diffraction of the XV IUCr Congress*; 1990; p 127.

(298) Rodríguez-Carvajal, J. Recent advances in magnetic structure determination by neutron powder diffraction. *Phys. B Condens. Matter* **1993**, *192*, 55–69.

(299) Kubelka, P.; Munk, F. Ein Beitrag Zur Optik Der Farbanstriche. *Z. Techn. Phys.* **1931**, *12*, 593–601.

(300) Mogilevsky, G.; Chen, Q.; Kleinhammes, A.; Wu, Y. The structure of multilayered titania nanotubes based on delaminated anatase. *Chem. Phys. Lett.* **2008**, *460* (4–6), 517–520.

(301) Gaobo, X.; Qiuxia, X. Thermal stability of HfTaON films prepared by physical vapor deposition. *J. Semicond.* **2009**, *30* (2), 23002-1–5.

(302) Liu, Q.-J.; Liu, Z.-T.; Feng, L.-P.; Tian, H. First-principles study of the structural, elastic and electronic properties of $HfTaO_3N$. *Comput. Mater. Sci.* **2010**, *50* (1), 114–117.

(303) Hall, S. R.; Allen, F. H.; Brown, I. D. The crystallographic information file (CIF): a new standard archive file for crystallography. *Acta Crystallogr. Sect. A* **1991**, *47* (6), 655–685.

List of Publications

(Ordered by date of acceptance)

1. Lüdtke, T.; Schmidt, A.; Becker, N.; Reimann, C.; Bredow, T.; Dronskowski, R.; Lerch, M. Kristallstruktur von δ-TaON. *Zeitschrift für Anorganische und Allgemeine Chemie* **2014**, *640* (11), 2349–2349. DOI: 10.1002/zaac.201404025.
2. Lüdtke, T.; Schmidt, A.; Göbel, C.; Fischer, A.; Becker, N.; Reimann, C.; Bredow, T.; Dronskowski, R.; Lerch, M. Synthesis and Crystal Structure of δ-TaON, a Metastable Polymorph of Tantalum Oxide Nitride. *Inorganic Chemistry* **2014**, *53* (21), 11691–11698. DOI: 10.1021/ic501726m.
3. Lüdtke, T.; Lerch, M. Synthese und Kristallstruktur neuer Oxidnitride vom Bixbyit-Typ. *Zeitschrift für Anorganische und Allgemeine Chemie* **2016**, *642* (18), 1035–1035. DOI: 10.1002/zaac.201605033.
4. Lüdtke, T.; Weber, D.; Schmidt, A.; Müller, A.; Reimann, C.; Becker, N.; Bredow, T.; Dronskowski, R.; Ressler, T.; Lerch, M. Synthesis and characterization of metastable transition metal oxides and oxide nitrides. *Zeitschrift für Kristallographie – Crystalline Materials* **2017**, *232* (1–3), 3–14. DOI: 10.1515/zkri-2016-1961.
5. Becker, N.; Reimann, C.; Weber, D.; Lüdtke, T.; Lerch, M.; Bredow, T.; Dronskowski, R. A density-functional theory approach to the existence and stability of molybdenum and tungsten sesquioxide polymorphs. *Zeitschrift für Kristallographie – Crystalline Materials* **2017**, *232* (1–3), 69–75. DOI: 10.1515/zkri-2016-1960.
6. Lüdtke, T.; Wiedemann, D.; Efthimiopoulos, I.; Becker, N.; Janka, O.; Seidel, S.; Pöttgen, R.; Dronskowski, R.; Koch-Müller, M.; Lerch, M. HP-MoO_2: A High-Pressure Polymorph of Molybdenum Dioxide. *Inorganic Chemistry* **2017**, *56* (4), 2321–2327. DOI: 10.1021/acs.inorgchem.6b03067.
7. Lüdtke, T.; Orthmann, S.; Lerch, M. Bixbyite-type phases in the system Ta-Zr-O-N. *Zeitschrift für Naturforschung B – Chemical Sciences* **2017**, *72b*(4), 305–311. DOI: 10.1515/znb-2017-0014.

List of Conference Contributions

09.2014 18. Vortragstagung Fachgruppe Festkörperchemie und Materialforschung, *Dresden, Germany* – Poster

05.2015 Berichtskolloquium für die zweite Periode, *Bad Sooden-Allendorf, Germany* – Poster

06.2016 Abschlusskolloquium des SPP1415, *Wetzlar, Germany* – Poster

09.2016 19. Vortragstagung Fachgruppe Festkörperchemie und Materialforschung, *Innsbruck, Austria* – Poster

List of Figures

Figure 1.1. Schematic representation of an energy landscape for a one-component system depending on two arbitrary parameters x_1 and x_2. The minima in energy (blue and violet regions) indicate viable stable or metastable polymorphs. 4

Figure 2.1. Coordination polyhedra (left) and unit cell (right) of the baddeleyite-type structure of β-TaON 13

Figure 2.2. Group-subgroup relation of $Fm\bar{3}m$ and $I4_1/amd$ with possible transformation pathways.[261] The relevant transition steps are marked gray. 22

Figure 2.3. Group-subgroup scheme (Bärnighausen formalism) and graphical development of the unit cell for the group-theoretical relationship between rock salt (aristotype) and anatase-type δ-TaON (hettotype).[250,252,254–256,262–264] See Figure A.1 or Figure A.2 for legend. 24

Figure 2.4. Maximal non-isomorphic subgroups (all *translationengleich*) of space group $I4_1/amd$. All subgroups allowing an ordered anion arrangement are marked gray.[261] 26

Figure 2.5. Coordination polyhedra and anion arrangement for δ-TaON in different space groups. Two different polyhedra are created during the transformation to space group $I\bar{4}m2$.[51,52,262,266] 26

Figure 2.6. Group-subgroup scheme (Bärnighausen formalism) for the group-theoretical relationship between the anatase structure and the subgroup $I4_1md$.[51,52,250,252,254–256,263,267] See Figure A.1 or Figure A.2 for legend. 27

Figure 2.7. Group-subgroup relation of $Fm\bar{3}m$ and $Ia\bar{3}$ with possible transformation pathways.[261] The relevant transition steps are marked gray. 28

Figure 2.8. First variant of the group-subgroup scheme (Bärnighausen formalism) and graphical development of the unit cell for the group-theoretical relationship between fluorite (aristotype) and bixbyite-type $(Ta,Zr)_2(O,N)_{3+\delta}$ (hettotype).[250,252,254–256,263] See Figure A.1 or Figure A.2 for legend. 30

Figure 2.9. Group-subgroup scheme (Bärnighausen formalism) for the group-theoretical relationship between the bixbyite structure and the subgroup *Ibca*.[173,250,252,254–256,263] See Figure A.1 or Figure A.2 for legend. 32

Figure 2.10. Group-subgroup relation of space groups $P6_3/mmc$ (NiAs, hcp) and *Pnma* (HP-WO_2) with possible transformation pathways.[261] The relevant transition steps are marked gray. 33

Figure 2.11. Group-subgroup scheme (Bärnighausen formalism) and graphical development of the unit cell for the group-theoretical relationship between NiAs (aristotype) and HP-WO_2-type HP-MoO_2 (hettotype).[250,252,254–256,263] See Figure A.1 or Figure A.2 for legend. 34

Figure 3.1. Synthesis apparatus with the gas mixing unit (right) and the tube furnace with the control unit (left). 45

Figure 3.2. Schematic representation of the used reaction tube with direct gas feed. 45

Figure 4.1. X-ray powder diffraction pattern (Cu-K_α radiation) with results of the Rietveld refinement (red: measured; black: calculated; blue: measured – calculated). The vertical bars indicate the reflection positions of anatase-type δ-TaON (top, blue), Ta_3N_5 (middle, red), and β-TaON (bottom, green).* 58

Figure 4.2. TEM-images of the as synthesized sample containing δ-TaON, β-TaON and Ta_3N_5: a), b) porous sponge-like structure. SAED pattern given as inset, demonstrate the presence of multiple crystal phases. 59

Figure 4.3. HRTEM-images (a,e) from the marked region in Figure 5.2 with corresponding FFT patterns (b,f). Filtered HRTEM-images of (a) evidencing the presence of δ-TaON (c) and β-TaON (d) and

filtered HRTEM-images of (e) evidencing the presence of δ-TaON (g) and Ta_3N_5 (h). 60

Figure 4.4. Crystal structure of anatase-type TaON. Left: unit cell with coordination octahedra. Right: Ta–O/N bond lengths in pm.* 61

Figure 4.5. Supercell of δ-TaON with the most stable N/O distribution.* 62

Figure 4.6. Energy per formula unit versus volume of the three known phases of TaON at ambient pressure (top), and relative Gibbs energy versus temperature for the different TaON phases (VASP/PBE) (bottom). 63

Figure 4.7. Phonon density of states of δ-TaON at ambient pressure calculated *via* density-functional theory. 65

Figure 5.1. X-ray powder diffraction pattern (Cu-K_α radiation) of bixbyite-type V_2O_3 with results of the Rietveld refinement (red: measured; black: calculated; green: Bragg-reflection positions; blue: measured – calculated).* 79

Figure 5.2. Coordination polyhedra of bixbyite-type V_2O_3. Bond lengths are presented in pm. 81

Figure 5.3. *In situ* V *K* edge XANES spectra measured during isothermal treatment of corundum-type V_2O_3 under catalytic conditions (5 vol % propene, 5 vol % oxygen in helium) at 633 K. 82

Figure 5.4. Evolution of oxidation degree during isothermal oxidation as a function of time during isothermal oxidation of oxide nitride with bixbyite structure with the stoichiometry $V_2O_{3.08}N_{0.06}$ in 5 vol % propene, 5 vol % oxygen in helium at 623 K, 633 K, 643 K, and 653 K. Traces were extracted from *in situ* X-ray diffraction measurements. 83

Figure 5.5. Linearization of oxidation degree *α* traces for isothermal oxidation of $V_2O_{3.08}N_{0.06}$ with bixbyite to VO_2(R) using three-dimensional diffusion models (D3, Jander; D4, Ginstling-Brounshtein). Isothermal measurements were performed under catalytic conditions (5 vol % propene, 5 vol % oxygen in helium) at 623 K, 633 K, 643 K, and 653 K. 83

Figure 5.6. Evolution of apparent activation energies $E_{a\alpha}$ of the rate determining step g(α) for the oxidation of oxide nitrides $V_2O_{3.03}N_{0.02}$, $V_2O_{3.08}N_{0.06}$, and corundum-type V_2O_3 under catalytic conditions (5 vol % propene, 5 vol % oxygen in helium). 84

Figure 5.7. X-ray powder diffraction pattern (Cu-$K_{\alpha1}$ radiation) of γ-TaON with results of the Rietveld refinement. The vertical bars indicate the positions of the Bragg reflections (red: measured; black: calculated; green: Bragg-reflection positions; blue: measured – calculated).* 86

Figure 5.8. Crystal structure with eight unit cells of γ-TaON.* 88

Figure 5.9. Coordination polyhedra of γ-TaON. Bond lengths are presented in pm.* 89

Figure 5.10. X-ray powder diffraction pattern (Cu-K_{α} radiation) of δ-TaON with results of the Rietveld refinement. The vertical bars indicate the positions of the Bragg reflections (blue: δ-TaON 82 wt %, red: Ta_3N_5 12 wt %, green: γ-TaON 6 wt %). 91

Figure 5.11. Crystal structure of anatase-type TaON. Left: unit cell with coordination polyhedra. Right: Ta–O/N bond lengths. Bond lengths are presented in pm.* 93

Figure 6.1. Crystal structure of the bixbyite-type tantalum zirconium oxide nitrides. Only two of 16 possible vacancies (Vac) have been marked.* 107

Figure 6.2. X-ray powder diffraction pattern (Cu-K_{α} radiation) of $TaZrN_3$ with results of the Rietveld refinement (red: measured; black: calculated; green: Bragg-reflection positions; blue: difference between measured and calculated).* 108

Figure 6.3. Dependency of unit cell parameter a and cation position x (24d) from the nitrogen content of the new bixbyite-type phases with an even cation ratio. 111

Figure 6.4. UV-vis spectrum/Tauc plot (black) of $Ta_{0.67}Zr_{1.33}O_{1.89}N_{1.63}$ with Tauc plot determination of the direct optical band gap (blue). 112

Figure 7.1. Relaxed crystal structure of Mo_2O_3 (and W_2O_3) in the corundum structure (left) displaying the lowest energy. The [V_2O_3] starting

structure (right) transforms into the corundum structure (left) upon structural relaxation.* 125

Figure 7.2. Projected density of states for both sesquioxides in the corundum structure according to CRYSTAL-PW1PW. The orbital energy is given relative to the Fermi energy. 127

Figure 7.3. Calculated phonon DOS of both sesquioxides in the corundum structure based on VASP-PBE results. 128

Figure 7.4. Density-functional (VASP-PBE) enthalpy-pressure diagram for the synthesis of Mo_2O_3 in the corundum structure *via* reaction (II). 129

Figure 7.5. Density-functional (VASP-PBE) enthalpy-pressure diagram for the synthesis of W_2O_3 *via* reaction I (blue, extrapolated for $p > 40$ GPa) and reaction II (green). 130

Figure 7.6. Calculated DOS (left) and pCOHP (right) of corundum-type Mo_2O_3. 134

Figure 7.7. Calculated DOS (left) and pCOHP (right) of corundum-type W_2O_3. 135

Figure 8.1. Theoretically calculated enthalpy of HP-MoO_2 and the other potential polymorph with *ortho*-TiO_2 structure relative to α-MoO_2. 143

Figure 8.2. Calculated phonon density of states (PDOS) of HP-MoO_2 at ambient pressure (left) and slightly above the calculated transition pressure (right). 144

Figure 8.3. X-ray powder diffraction pattern (Cu-K_α radiation) of HP-MoO_2 with the results of the Le Bail profile fit (red: measured; black: calculated; green: Bragg-reflection positions; blue: difference plot). 145

Figure 8.4. Crystal structure of HP-MoO_2. Left: layer-like structure along the *c* axis with unit cell; right: arrangement of the zigzag chains of two layers. Red and yellow polyhedra indicate different layers. Unbound oxide ions indicate the toothing of the layers. 147

Figure 8.5. Coordination polyhedra and connectivity of the atoms inside one zigzag chain with bond lengths (in pm). 148

Figure 8.6. Group-subgroup scheme (Bärnighausen formalism) for the group-theoretical relationship between the NiAs structure (aristotype) and the crystal structure of HP-MoO_2. 150

Figure 8.7. Calculated electronic density of states (DOS) of HP-MoO_2. The minute overlap between the valence and conduction band at the Fermi level classifies the compound as a semimetal. 152

Figure 8.8. Raman spectrum of HP-MoO_2 at ambient conditions ($\lambda = 514.5$ nm). The red tick symbols represent the calculated Raman-mode frequencies (Supporting Information; Chapter 8.8; Table 8.4). 152

Figure 8.9. Temperature-dependent molar magnetic susceptibility χ of HP-MoO_2, measured with a magnetic field strength of 10 kOe. 153

Figure 8.10. HP-MoO_2 single crystal used for X-ray crystal structure determination. 157

Figure 9.1. Sample of δ-TaON with γ-TaON and Ta_3N_5 side phases. 163

Figure 9.2. Synthesized tantalum zirconium oxide nitrides and the nitride $TaZrN_3$. Left to right: $Ta_{0.67}Zr_{1.33}O_{1.89}N_{1.63}$, $Ta_{0.67}Zr_{1.33}O_{1.38}N_{1.97}$, $Ta_{0.67}Zr_{1.33}O_{0.42}N_{2.61}$, $TaZrN_3$, and $Ta_{1.33}Zr_{0.67}O_{0.12}N_{3.03}$. 165

Figure 9.3. HP-MoO_2 single crystal, photographed through a microscope. 166

Figure A.1. Group-subgroup relation between anatase ($I4_1/amd$; aristotype) and *Imma* or $I\bar{4}m2$.[250,252,254–256,262,263] 170

Figure A.2. Second variant of the group-subgroup scheme (Bärnighausen formalism) for the group-theoretical relationship between fluorite (aristotype) and bixbyite-type $(Ta,Zr)_2(O,N)_{3+\delta}$ (hettotype).[250,252,254–256,263] 171

List of Tables

Table 2.1. Binary oxides of tantalum (sorted by ascending oxidation state of Ta). 10

Table 2.2. Binary nitrides of tantalum (sorted by ascending oxidation state of Ta). 11

Table 2.3. Ternary oxide nitrides of tantalum (sorted by ascending oxidation state of Ta). 14

Table 2.4. Binary oxides of zirconium (sorted by ascending oxidation state of Zr). 16

Table 2.5. Binary nitrides of zirconium (sorted by ascending oxidation state of Zr). 16

Table 2.6. Ternary oxide nitrides of zirconium. 17

Table 2.7. Binary oxides of molybdenum (sorted by ascending oxidation state of Mo). 20

Table 4.1. Results of the Rietveld refinement for δ-TaON in comparison with selected results for $Mg_{0.05}Ta_{0.95}O_{1.15}N_{0.85}$. 59

Table 4.2. Refined atomic parameters for anatase-type TaON. 60

Table 4.3. Gaussian-type basis sets for Ta, O, and N. 70

Table 5.1. Results of the Rietveld refinement for bixbyite-type V_2O_3. 80

Table 5.2. Refined atomic parameters of bixbyite-type V_2O_3. 80

Table 5.3. Results of the Rietveld refinement for γ-TaON. 87

Table 5.4. Refined atomic parameters of γ-TaON. 87

Table 5.5. Results of the Rietveld refinement for δ-TaON. 92

Table 5.6. Refined atomic parameters of δ -TaON. 92

Table 5.7. Fundamental band gaps (eV) of TaON polymorphs calculated with the plasmon-pole approximation to GW implemented in GPAW. All calculated gaps obtained in this work correspond to indirect transitions. The corresponding direct gaps are given in parentheses. 94

Table 6.1. Results of the Rietveld refinements for selected bixbyite-type phases in comparison with results for Zr_2ON_2. 109

Table 6.2. Refined atomic parameters for TaZrN3. 109

Table 6.3. Cell parameter *a* and cation coordinate *x* of selected samples with a Ta:Zr ratio of 1:1. 110

Table 6.4. Optical band gaps of different bixbyite-type compounds. 111

Table 7.1. Molar volumes and relative energies per formula unit for hypothetical molybdenum sesquioxide Mo_2O_3 polymorphs as a function of computational methodology and magnetic state (DM = diamagnetic, FM = ferromagnetic, AFM = antiferromagnetic). The listed structures represent the starting structures. 124

Table 7.2. Molar volumes and relative energies per formula unit for hypothetical tungsten sesquioxide W_2O_3 polymorphs as a function of computational methodology and magnetic state (DM = diamagnetic, FM = ferromagnetic, AFM = antiferromagnetic). The listed structures represent the starting structures. 124

Table 7.3. Structural details and molar volumes of molybdenum and tungsten sesquioxide in the corundum structure based on VASP-PBE calculations. 126

Table 7.4. Relative theoretical reaction enthalpies and volumes of M_2O_3 for the hypothetical reaction routes I and II based on VASP-PBE results. 128

Table 7.5. Details of the *k*-point mesh and the number of *k*-points in the irreducible Brillouin zone for all investigated polymorphs of Mo_2O_3 and W_2O_3. 133

Table 8.1. Results of the single-crystal analysis and Le Bail decomposition of HP-MoO_2. 146

Table 8.2. Experimental and computed (DFT with D3 dispersion correction) atomic parameters of the new high-pressure polymorph of MoO_2. 149

Table 8.3. Comparison of experimental and DFT-calculated cell parameters (pm) with and without D3 dispersion correction. 151

Table 8.4. Assignments, calculated and experimental wavenumbers for the HP-MoO_2 Raman-active modes. The letters in parenthesis indicate the respective relative band intensities: w = weak, vw = very weak, s = strong, vs = very strong, sh = shoulder. The matching between the calculated and experimental Raman mode wavenumbers is tentative. 158

Table 9.1. Compositional range of all obtained bixbyite-type phases in the system Ta-Zr-O-N. 164

Table A.1. List of utilized chemicals. 169

Table A.2. List of utilized software. 169

Index

Ammonolysis 37, 54, 85, 90, 105
Anatase 21
Anatase structure 22, 61, 92
  anion ordering 26, 60, 91
Baddeleyite 15
Bärnighausen, Hartmut 20
Berzelius, Jöns Jacob 15
Bixby, Maynard 27
Bixbyite 27
Bixbyite structure 27, 79, 106
  N/O ordering 106
Bixbyite-type V_2O_3 78
Ekeberg, Anders Gustaf 9
Hatchett, Charles 9
Hjelm, Peter Jacob 19
HP-MoO_2 33, 143, 165
  crystal structure 33, 146
  structure determination 144
  synthesis 140
HP-WO_2 32, 140, 143
Klaproth, Martin Heinrich 3, 15
Kröger–Vink notation 15, 29, 38
Kubelka–Munk function 41, 106
Le Bail 40, 141, 144
  HP-MoO_2 144
McCrone, Walter C. 4
Ostwald, Friedrich Wilhelm 5
Ostwald–Volmer rule 6, 87, 92
Pauling's rule 12, 14
Pechini method 36, 43, 54, 85, 105
Pechini, Maggio 36
Phillips–Van Vechten 13, 111
Rietveld refinement 39
  bixbyite-type V_2O_3 79
  $TaZrN_3$ 108
  γ-TaON 86
  δ-TaON 57, 91
Rose, Heinrich 9
Scheele, Carl Wilhelm 19
Tauc plot 41, 106, 111
$TaZrN_3$ 107, 164
UV-vis spectroscopy 40, 46, 105
Wyckoff, Ralph Walter Graystone 21
X-ray diffraction 38, 46, 55, 77, 105, 141
Zirconia 15, 16, 103
α-TaON 12, 53, 85
β-TaON 12, 53, 85
γ-TaON 13, 85
  crystal structure 13, 88
  N/O analysis 89
  Rietveld refinement 86
  synthesis 85
δ-TaON 14, 57, 90, 163
  crystal structure 21, 58, 92
  N/O analysis 57
  Rietveld refinement 57, 91
  synthesis 54, 90